Dissertation
submitted to the
Combined Faculty of Mathematics, Engineering and Natural Sciences
of Heidelberg University, Germany
for the degree of
Doctor of Natural Sciences

Put forward by
Petar Andrejić
born in: Kruševac, Serbia
Oral examination: 11.01.2023

Control of high frequency electromagnetic radiation

Referees: Prof. Dr. Adriana Pálffy-Buß
Prof. Dr. Maurits Haverkort

Abstract

Mössbauer nuclei in thin film nanostructures are an established platform for X-ray quantum optics, and provide novel methods for the narrowband control of hard X-rays. However, quantum optical models for these nanostructures have so far only considered grazing incidence geometry, in a regime of idealized plane wave propagation, and homogeneous nuclear hyper-fine environments. We develop a theoretical description for the interaction of X-rays with Mössbauer nuclei in arbitrary geometries, including dispersive effects, using macroscopic quantum electrodynamics to derive Maxwell-Bloch equations. We use this formalism to study:

(i) the effects of beam divergence and inhomogeneous hyper-fine distributions on energy spectra at grazing incidence. In particular, we demonstrate that the collective Lamb shift and broadening of single mode super-radiance can be used to overcome the effects of inhomogeneous broadening, and result in a single line spectrum in the large collective coupling limit.

(ii) the equations of motion for guided modes coupled to Mössbauer nuclei. We show that these modes obey equations of motion analogous to nuclear forward scattering. We study the interference of multiple modes coupled to a longitudinally structured layer of nuclei, and demonstrate selective super and sub radiant emission. This demonstrates that front coupling to thin film nanostructures opens the door for a vast new space of techniques for the control of hard X-rays.

Zusammenfassung

Mössbauer-Kerne in Dünnschicht-Nanostrukturen sind eine etablierte Plattform für die Röntgenquantenoptik und bieten neuartige Methoden für die schmalbandige Kontrolle harter Röntgenstrahlung. Jedoch haben quantenoptische Modelle für diese Nanostrukturen bisher nur die Geometrie des streifenden Einfalls, eine idealisierte ebene Wellenausbreitung und homogene Hyperfeinstrukturumgebungen im Kern berücksichtigt. Wir entwickeln eine theoretische Beschreibung der Wechselwirkung von Röntgenstrahlen mit Mössbauer-Kernen in beliebigen Geometrien, einschließlich dispersiver Effekte, unter Verwendung der makroskopischen Quantenelektrodynamik zur Herleitung der Maxwell-Bloch-Gleichungen. Wir verwenden diesen Formalismus zur Untersuchung:

(i) der Auswirkungen von Strahldivergenz und inhomogenen Hyperfein-Verteilungen auf Energiespektren bei streifendem Einfall. Insbesondere zeigen wir, dass die kollektive Lamb-Verschiebung und die Verbreiterung einer Einzelmoden-Superradianz genutzt werden können, um die Auswirkungen der inhomogenen Verbreiterung zu überwinden und ein einzelnes Linienspektrum im großen kollektiven Kopplungslimit zu erhalten.

(ii) der Bewegungsgleichungen für geführte Moden gekoppelt an Mössbauer-Kerne. Wir zeigen, dass sie Bewegungsgleichungen gehorchen, welche analog zur Kernvorwärtsstreuung sind. Wir untersuchen die Interferenz mehrerer Moden, die an eine longitudinal strukturiereten Schicht von Kernen gekoppelt sind, und demonstrieren selektive Super- und Subradianz. Dies zeigt, dass die Vorwärtskopplung an Dünnfilm-Nanostrukturen die Tür zu einem riesigen neuen Raum geometrischer Techniken für die Kontrolle harter Röntgenstrahlung öffnet.

Within the framework of this thesis, the following article was published in a refereed journal:

- *Superradiance and anomalous hyperfine splitting in inhomogeneous ensembles*
  Petar Andrejić and Adriana Pálffy,
  Phys. Rev. A **104**, 033702 (2021).

The following articles are in preparation for submission to refereed journals:

- *Waveguide QED with Mössbauer nuclei*
  Petar Andrejić, Leon M. Lohse and Adriana Pálffy.
- *Effects of quantum cooperativity on hyperfine spectra*
  Petar Andrejić, Xiangjin Kong, Lars Bocklage, Xinchao Huang, Olaf Leupold, Aleksandr Chumakov, Ralf Röhlsberger and Adriana Pálffy.
- *Optical theory of x-ray waveguides*
  Leon M. Lohse and Petar Andrejić.
- *Observation of nuclear forward scattering in a single-mode x-ray waveguide*
  Leon M. Lohse, Ankita Negi, Anjali Panchwanee, Olaf Leupold, Ilya Sergeev, Petar Andrejić, Adriana Pálffy, Tim Salditt, and Ralf Röhlsberger.

Contents

Chapter 1

Introduction

Theodore Maiman, the inventor of the ruby laser, once remarked "A laser is a solution seeking a problem" [1]. Despite his misgivings, the use of lasers as a coherent source has enabled precise optical control of the quantum states of matter, and ushered in the modern era of quantum optics. Although considerable experimental progress has been made in the microwave, optical, and ultraviolet domain, creation of coherent X-ray sources has been far more difficult. In the past two decades however, the advent of high brilliance, highly coherent third generation synchrotron sources as well as X-ray free electron lasers (XFEL) has finally allowed X-rays to join the stable of modern quantum optics. Due to the high energy, short length and time scales, and low attenuation of X-rays, this has led to the development of powerful new techniques in ultra-fast spectroscopy [2, 3], nano-scale imaging [4–6], excitation of inner shell atomic transitions [7, 8], and could in the future lead to innovations in quantum communication, macroscopic entanglement [9], and beyond.

Quantum optics is a broad field, and a thorough overview of the interesting phenomena that have been studied would merit a book of its own. Nevertheless, let us briefly touch on some key results. Historically, some of the earliest experimental evidence of the quantized nature of atomic transitions involved the fluorescence of atoms under incoherent illumination. In this regime, the energy levels of the atom are randomly populated, and emit photons irreversibly via spontaneous decay. Under illumination by periodic, coherent sources however, the situation is drastically different. Instead of random population and decay, the atom undergoes Rabi oscillations; periodically oscillating between the ground and excited state that are resonant to the driving field. The introduction of multiple driving fields introduces counterintuitive and powerful control techniques, such as electromagnetically induced transparency (EIT) [10], or stimulated Raman adiabatic passage (STIRAP) [11]. In EIT, the interference between two Rabi oscillations causes a window of transparency where an atom would otherwise be opaque, while in STIRAP, population can be transferred between two dipole-forbidden states, via an intermediate coupling to a third state. However, with careful design of the pulse sequences used to excite the intermediate transitions, the population transfer can occur without populating the intermediate state, bypassing the inefficiencies that would be incurred by spontaneous decay from the intermediate state.

In parallel with these developments in single atom control, the collective interaction of large ensembles of atoms has been a field of great interest too. The most fa-

mous effect in collective quantum optics is perhaps Dicke super-radiance. In 1954, Dicke demonstrated that ensembles of N atoms placed in a cloud smaller than the wavelength of a transition emit and absorb collectively, with their spontaneous decay rate enhanced by a factor of N [12]. Later, it was demonstrated that this effect holds if the atoms interact only via a single electromagnetic mode [13]. In more recent years, there has been considerable interest in collective interactions beyond the single mode, or large wavelength regimes. It has been shown that in general, collective emission can be described via the eigenfunctions of an effective dipole-dipole interaction potential, and is highly geometry dependent [14–18]. This has opened a new door for the design of optical metamaterials, via the geometric placement of atomic arrays. For example, it has been demonstrated that sub-wavelength, square lattices of atoms can be used as mirrors for photons resonant to their dipole transitions [19], while 1D arrays have been proposed as efficient photon storage devices [20, 21], or to achieve ultra-strong coupling, such that single photon Rabi oscillations could be observed [22].

X-ray quantum optics and its advantages

Transitions between nuclear isomeric states and the nuclear ground state provide the analogue of atomic transitions at hard X-ray energies, on the order of 10 keV and higher. Third generation synchrotron, and XFEL sources provide coherent stimulation of these transitions, and this combination has brought quantum optics to the hard X-ray domain.

Nuclei in solid state environments are particularly suitable for quantum optical control due to the Mössbauer effect. As the recoil energy of isomeric transitions lies below the phonon band-gap of the surrounding crystal, the nuclei emit and absorb light elastically, with zero recoil. Thus, Mössbauer nuclei do not have the challenges of Doppler broadening that can often plague quantum optics in the visible spectrum.

The high energies of the nuclear isomeric transitions also mean there is essentially zero thermal noise to consider. For example, a quick calculation using the black-body spectrum gives the integrated thermal photon number density above 10 keV to be hundreds of orders of magnitude smaller than $1\,\mathrm{m}^{-3}$ at any experimentally relevant temperature. Thus, if techniques for efficient generation, switching and measurement of entangled X-ray states could be developed, they would present an ideal platform for quantum communication. Finally, the fact that the nuclei are embedded in a solid state environment allows for a great degree of control of their spatial structure, down to the nanometre scale.

Using forward scattering in thin foils enriched with Mössbauer nuclei, Kocharovskaya *et al.* have demonstrated numerous quantum optical and optomechanical phenomena, such as coherent pulse shaping [23], electromagnetically induced transparency [24], acoustically induced transparency [25], optical control of the hyperfine spectrum [26], and have recently proposed an X-ray quantum memory device [27].

For control over the optical environment, it has been shown that placing Mössbauer nuclei in thin film nanostructures provides the analogue of atoms in an optical cavity. High atomic number (Z) materials deflect X-rays stronger than low Z materials, and form the capping layers. Low Z materials are used as filler, and thin layers of resonant nuclei placed in the middle act as the 'atoms'. At grazing incidence, this acts analogously to atoms placed between the mirrors of a Fabry-Pérot resonator.

Multiple layers can be coupled together, and their scattered fields used as 'con-

trol fields', allowing one to implement multiple source models from quantum optics in the X-ray domain. Using this model, cavities exhibiting a diverse range of quantum optical phenomena have been developed both experimentally and theoretically. These include Rabi oscillations [28], slow light and coherent population trapping [29], EIT [30], spontaneously generated coherences [31], coherent pulse shaping [32], Fano resonances and interferometry [33], subluminal pulse propagation [34], optomechanical coupling [35], and more.

On the collective side, super-radiance has been shown to be significant in both forward scattering off of bulk foils, and grazing incidence scattering off of thin films. In nuclear forward scattering, the collective emission and absorption of Mössbauer nuclei results in pronounced collective Rabi oscillations, while at grazing incidence, the high collimation of synchrotron radiation results in a single Fourier mode of the thin-film stack being excited. As such, thin-films grazing incidence scattering is described by the single mode Dicke model, and the resulting collective effects play a large role. This was demonstrated clearly in 2010 by an experiment of Röhlsberger *et al.* [36], who measured a collective Lamb shift, and in addition significant collective broadening of such a system, on the order of 61 times the natural linewidth. A 2018 experiment at the SACLA XFEL by Chumakov *et al.* measured the multi-photon statistics of the forward scattering from a foil target, providing the first direct experimental verification of the photon decay statistics of the Dicke model [37]. The interplay between Dicke super-radiance and hyperfine interactions has been shown to lead to anomalous spectra with exceptional points [38], and it has been demonstrated that the combination of angle of incidence control as well as cavity design can result in a large range of coupling regimes [39, 40].

Now that we have seen the advantages and successes of X-ray quantum optics, we will turn our attention to the current limitations, and how we will address some of these in this thesis. Specifically, we will focus on two topics:

A: understanding the limitations of the approximations used to model the thin-film nanostructures as single mode cavities, and the nuclei within as identical emitters.

B: investigating the viability of, and developing a theoretical model for waveguide QED with Mössbauer nuclei, and demonstrating that it may be used for novel methods of X-ray control.

Limitations of X-ray quantum optics, and how we will address them

Compared to the visible wavelengths, working with Mössbauer nuclei in thin-film cavities poses new challenges, both experimental and theoretical. For both the single mode cavity picture, and Dicke super-radiance picture of thin-film nanostructures, it is important that the incident field excites a single Fourier mode. For this to be valid, the angular width of the incident beam must be narrower than the resonance being driven. On the other hand, the resonances of thin-film nano-structures can be incredibly narrow, on the order of ten µrad in angular width, while the incident beams used for Mössbauer grazing incidence experiments are configured for angular divergences from 20 µrad to 200 µrad at the ID18 beam-line at ESRF [1], and approximately 60 µrad or more at the P01 beam-line at PETRA III [2]. As such, for the first part of topic **A**, we investigate the effect of beam divergence on the experimentally measured spectra, and the validity of the single mode approximation. We

[1] Parameters for ID18 at ESRF, November 2018, beam-time ID HC-4028

[2] Parameters for P01 at PETRA III, August 2020, beam-time ID 11008029

find that divergences on the order of 5 µrad can be treated as single modes, but at larger beam divergences the spectrum is substantially broadened and distorted. This could result in erroneous conclusions for the spatial structure and hyperfine parameters of the thin film being measured, and thus is crucial to consider in theoretical predictions.

The other approximation used, in particular to model the nuclei as obeying Dicke model dynamics, is that the nuclei are identical, with no inhomogeneous broadening. As the thin-films are formed through a sputter deposition process, the resonant layer is polycrystalline, and thus a random distribution of hyperfine parameters is present, and thus we cannot treat the nuclei as identical in general. This is relevant not only to the X-ray regime, as atomic systems also have many sources of inhomogeneous broadening, i.e. Doppler broadening, background electric and magnetic field gradients. However, for nuclei, this broadening is small compared to the collective coupling strength, and we do not expect this effect to ruin the Dicke model dynamics entirely. Thus, the second focus of topic **A** is to develop a model for Dicke model dynamics in the presence of small inhomogeneities, and derive analytic expressions for the resultant spectra. We show that the collective Lamb shift can be used to overcome inhomogeneous broadening, and in the limit of strong collective coupling the spectrum tends toward a single line, with only super-radiant broadening in the line-width.

The biggest experimental challenge, however, is in the driving fields. Although synchrotrons are incredibly narrowband, down to the order of 10^{-4} of their frequency, their bandwidth is still large compared to Mössbauer transitions, which have a bandwidth on the order of 10^{-12} times their frequency. As such, even the most brilliant synchrotron sources still have only a few resonant photons per shot, putting Mössbauer quantum optics firmly in the linear regime. This situation has improved with the introduction of XFEL sources, which have on the order of hundreds of resonant photons per shot, and with diamond cavities for seeding [23, 41, 42], this could rise by orders of magnitude still. The other challenge is that due to the incredibly large size of the sources, and the limited availability of passive optics in the X-ray regime, experiments are largely limited to either single sources, or must use methods such as optomechanical coupling mechanisms [23, 32] for pulse shaping. This connects us back to topic **B**; waveguides support multiple modes, and it is possible to excite these simultaneously with a single incident beam. Thus, let us now turn our attention to the waveguide QED of Mössbauer nuclei.

Waveguide QED of X-rays

A field that has been relatively neglected in comparison to nuclear forward scattering and grazing incidence, is X-ray quantum optics in the waveguide regime. It is our view however, that some key limitations of current approaches can be addressed in the waveguide regime, and thus the focus of this thesis is to develop theoretical models for the use of Mössbauer nuclei in waveguide structures for the narrowband control of X-rays.

So far, tapered and channelled X-ray waveguides have been studied, and shown to be powerful options for focusing and guiding, down to the nanometre scale [43–49]. Used as guides for synchrotron radiation, [50–54] they have been successfully used as point-like hard x-ray sources for imaging, in particular for holographical imaging [55]. A recent proposal for embedding Mössbauer nuclei in tapered waveguides has showing the potential for reaching inversion of the isomeric tran-

sitions [56]. On the other hand, the excitation of Mössbauer nuclei embedded in tapered and channelled waveguides have not yet been experimentally demonstrated, and we shall instead turn our attention to thin-film nanostructures. Because of their use in grazing incidence experiments, their design, fabrication, and control is well understood and validated. Additionally, recent exploratory work has demonstrated the viability of directly driving guided modes in such thin-films with synchrotron radiation, and coupling to Mössbauer nuclei within the film [57].

Although thin-film nano-structures act as slab waveguides, as mentioned previously, a well collimated incoming beam at grazing incidence only excites a single Fourier mode, acting as a cavity, which severely restricts the implementation of models that require multiple modes, or effects that result from radiation into a continuum. This also restricts their spatial structure to effectively one dimensional, and rules out higher dimensional geometric effects.

In this thesis, we derive a theoretical description for the front coupling of thin-film nanostructures, beginning *ab initio* with the Grüner-Welsch quantization of macroscopic quantum electrodynamics. This allows us to derive generic Maxwell-Bloch equations for the X-ray – nucleus interaction, in terms of the dyadic Green's functions of their surrounding nano-structure. We then specialize these equations for thin-film waveguides, and derive analytic expressions for the guided mode propagation using the complex analytic structure of the Fourier transformed Green's function.

We then show that the resultant equations of motion for the single mode regime are identical in form to nuclear forward scattering, and analogous to the interaction of atoms coupled to a single waveguide mode, thus demonstrating the equivalence of the dynamical beat of nuclear forward scattering to collective Rabi oscillations.

We then consider the case of multiple modes coupled to a thin layer of Mössbauer nuclei, and demonstrate that the nuclei emit into a collective super-position of the individual guided modes. We then consider structuring the layer longitudinally into an array of micro-strips, and demonstrate that coupled to two modes, the resulting interference pattern can be used for selective super-radiance and sub-radiance. This demonstrates that guided modes can be used for effective two-beam control techniques, and opens the door for a vast possibility of new methods of narrowband X-ray control via the engineering of collective radiation patterns.

Outline

We begin in Chapter 2 with an overview of nuclear isomeric transitions, the Mössbauer effect, and how coherent X-ray sources are used to populate nuclear isomeric states. We then discuss the collective interactions present in Mössbauer quantum optics. Finally, we introduce the three experimental geometries that will be considered in this work. These are bulk foil nuclear forward scattering, thin film grazing incidence, and thin film front coupling.

In Chapter 3, we give an overview of Grüner-Welsch quantized macroscopic QED. This quantizes the macroscopic Maxwell's equations using the dyadic Green's functions of the medium. This forms the basis of our theoretical description.

In Chapter 4, we introduce the well known analytic solution for the Green's function of slab waveguides, and discuss the spectral properties of its Fourier transform. This encodes the resonances, and hence guided modes of the waveguide, and allows us to obtain analytic expressions for the guided mode contribution to the Green's function.

In Chapter 5, we define the nuclear Hamiltonian and Lindblad super-operators, the nuclear-magnetic dipole interaction Hamiltonian, and give an overview of the hyperfine interactions present. We then use these in Chapter 6 to derive the equations of motion for general interactions between Mössbauer nuclei and electromagnetic fields in linear media. In Section 6.1 we derive the nuclear isomeric Bloch equations, while in Section 6.2 we show that the field obeys the macroscopic Maxwell's equations, with the fields promoted to operators, and we specialize the Kirchoff integral for the three experimental geometries, to obtain expressions for the incident field in terms of its free space expression and the Green's function of the X-ray medium. Following this, in Section 6.3 we discuss the effects of dispersion, and the rotating wave approximation. We show that the rotating wave approximation remains valid as long as it is performed *after* obtaining the Fourier space equation of motion for the field. However, dispersive effects cannot be neglected in general, and are shown to lead to non-Markovian dynamics.

Armed with the equations of motion, we proceed to specialize them in our two areas of focus: grazing incidence in Chapter 7, and front coupling in Chapter 8. In Chapter 7, we consider two inhomogeneities for grazing incidence geometry, that arise in realistic experimental conditions: angular divergence and inhomogeneous broadening. Firstly, in Section 7.1 we show that although the beam divergence at synchrotrons is approximately the angular width of a guided mode resonance, the beam can nevertheless be considered well collimated and single mode. On the other hand, we show that angular instabilities can result in far more dramatic effects, with distortions of the measured spectra and erroneous conclusions for the sample structure and hyperfine parameters. Secondly, in Section 7.2 we show that in the presence of inhomogeneous hyperfine interactions, the collective interaction cannot be considered as an overall frequency shift and broadening, and the resulting energy spectra have anomalous line shapes. In particular, we show that in the limit of strong collective coupling, the effect of inhomogeneous broadening is diminished, and the line-width tends towards the super-radiant line-width that would be observed in the absence of inhomogeneity.

In Chapter 8, we consider the equations of motion for guided modes interacting with Mössbauer nuclei, in the front coupling geometry. We begin in Section 8.1 with a derivation from our Green's function approach of the existing well known expressions for nuclear forward scattering. We show that including the effects of

dispersion introduces the proper retarded time into the solution. This also allows us to compare the existing approaches of nuclear forward scattering to the Green's function model of single mode super-radiance of linear geometries, and show that they are equivalent, thus demonstrating that the dynamical beat of nuclear forward scattering, and collective Rabi oscillation [16, 58] of atomic optics, are one and the same. Next in Section 8.2 we develop forward scattering equations for front coupled thin film waveguides, and demonstrate that the equation of motion for each mode resembles that of nuclear forward scattering, with the effective resonant length scaled by the spectral parameters of the modes. We then consider the equations for multiple modes coupled to a thin layer, and show that super-radiance and sub-radiance play a large role, with the nuclei emitting collectively into a single bright mode. In Section 8.3 we consider in detail the specialization of these effects to a two mode waveguide, and demonstrate that the interference pattern of the collective radiation mode allows for selective super-radiance and sub-radiance via engineering of micro-patterns into the resonant layer. This opens the door for a vast possibility of new models in X-ray quantum optics, as well as demonstrates that Mössbauer waveguides are an ideal platform for investigating geometric light matter interactions.

Finally, in Chapter 9 we give our concluding remarks, and an outlook for future research in the Green's function formalism, inhomogeneous Dicke model dynamics, and waveguide X-ray QED.

Chapter 2

Background

In this chapter, we give a brief overview of quantum optics with Mössbauer nuclei. We begin in Section 2.1 with an overview of nuclear isomeric states, their hyperfine structure, and the Mössbauer effect. We give a brief introduction to modern synchrotron and X-ray free electron laser (XFEL) X-ray sources and their use in driving nuclear isomeric transitions in Section 2.1.3.

Following this, in Section 2.2 we give a background to the theoretical models that are currently used in X-ray quantum optics, as well an overview of Dicke superradiance in Section 2.3, which is an important collective effect in Mössbauer optics.

Finally, in Section 2.4, we describe the three experimental configurations of Mössbauer nuclei that will be considered in this thesis.

2.1 Mössbauer nuclei

First discovered by Rudolf Mössbauer in 1958 [59], the eponymous Mössbauer effect refers to the recoil-free emission of gamma radiation from nuclei in a solid state environment.

As with all many-body quantum systems, a nucleus has many possible quantized internal states, referred to as isomeric states. These states correspond to the different possible meta-stable arrangements of the nucleons, and for the purposes of Mössbauer transitions the most relevant structural quantities are the nuclear spin quantum number I, parity π, magnetic dipole moment μ, and electric quadrupole moment Q.

The nuclear isomeric states have a total angular momentum that is the combination of the spin angular momentum of the constituent nucleons, and the orbital angular momentum of their macroscopic arrangement. Thus, different isomeric states have different total spin. The different internal arrangements of charge and current also change the electric and magnetic multipole moments of the nucleus, which are used both to predict the splitting due to hyperfine interactions, and predict the transition rates between different isomeric states. For these transitions, the familiar selection rules from atomic optics also hold.

Firstly, one must consider parity. The parity of a state reflects whether it is even or odd under a point reflection. For many low-lying isomeric states, the parity is unchanged. Due to the fact that the selection rules for electric dipole transitions require a change in parity between the initial and final states [60], most Mössbauer

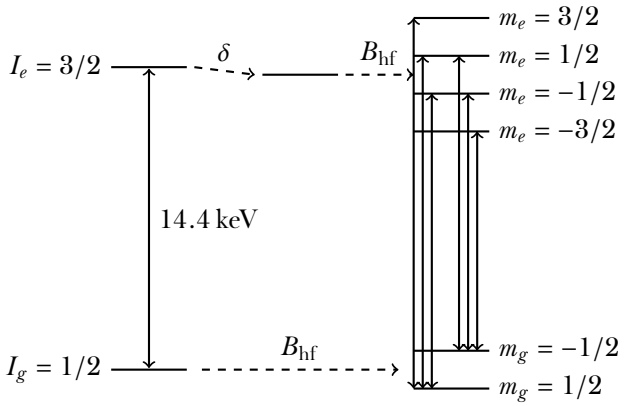

Figure 2.1: The level scheme of ^{57}Fe. The isomer shift δ shifts all excited states equally, and is due to a monopole interaction with the local electric field. The addition of an external magnetic field B_{hf} results in a hyperfine splitting of the magnetic sublevels according to their spin projection m_g or m_e on the quantization axis. The six magnetic dipole transitions are illustrated.

transitions are electric dipole forbidden, and thus the lowest order multipole transition is due to magnetic dipole coupling. For these, the selection rules require that the change in spin quantum number obeys $\Delta I = 0, \pm 1$, and *no* parity change [60]. In addition to magnetic dipole transitions, electric quadrupole transitions play a small role, put as they are much smaller in transition rate, we will not consider them in this work, except when accounting for the spontaneous decay rate of the nuclear transitions.

2.1.1 Hyperfine structure

The isomeric states have a hyperfine structure, Figure 2.1, which are split by interactions between the nucleus and its local electronic environment. These can be expressed in terms of interactions between the local electric and magnetic fields with the electric and magnetic multipole moments of the isomeric level. The most significant of these are the isomer shift, the magnetic dipole splitting, and the electric quadrupole splitting, all of which will be discussed in detail in Section 5.4. These provide an incredibly sensitive probe of the local electronic structure, and is used to non-destructively identify metallurgical structures, as well as investigate the chemical structure of iron containing molecules, including haemoglobin.

2.1.2 Recoil and the Mössbauer effect

Transition energies between the isomeric states lie in the gamma ray range, and as with atomic transitions, a nuclear excited state will spontaneously decay to its ground state. This occurs through gamma radiation, as well as internal conversion. In internal conversion, an inner-shell electron is excited by the nuclear transition, and is ionized. In both the gamma and internal conversion decay channels, there must be recoil to balance the resultant change of momentum. Thus, in general, some portion of the transition energy is taken up by the kinetic energy of this recoil, Doppler

shifting the emitted photon in the case of gamma radiation. There is a continuum of possible Doppler shifts, resulting in Doppler broadening of the resulting spectrum. This is problematic for spectroscopic purposes, as this broadening makes the hyperfine structure completely unresolvable.

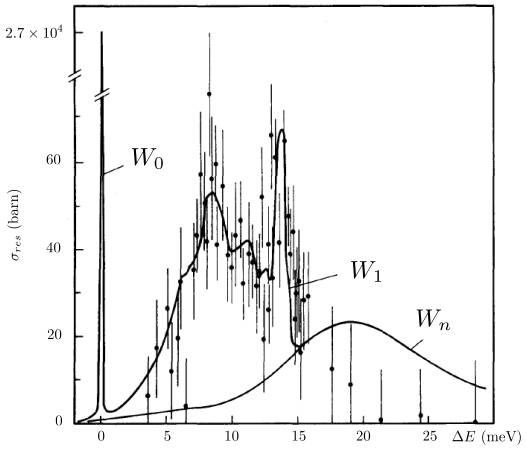

Figure 2.2: Fluorescence spectrum of the 58 keV isomeric transition in crystalline ^{159}Tb [61]. Note the broad Doppler shifted bands, corresponding to transitions coupled to one phonon, W_1, or multiple, W_n. A sharp Mössbauer peak is also present, W_0, corresponding to recoil energies below the phonon gap.

For a nucleus embedded in a solid, any recoil motion relative to the crystal lattice is quantized as phonons. The phononic spectrum of a crystal is gapped, and therefore any recoil energy below this gap will not result in a phononic vibration. Rather, the recoil energy is taken up by the kinetic motion of the entire solid uniformly. Due to the immensely larger mass of the solid compared to an individual nucleus, the resultant Doppler velocity is suppressed by a factor of Avogadro's number, and is effectively zero. It is this effect that Mössbauer first measured in 1958, and it is the key reason for the viability of Mössbauer spectroscopy.

The recoil free fraction of transitions is referred to as the 'Lamb-Mössbauer factor', f_{LM}. It is dependent on both the chemical structure and temperature of a sample, but can be estimated using a Debye model for the phononic modes.

2.1.3 Populating the isomeric states

Due to the large transition energies, populating the excited isomeric states is challenging. The initial method used was radioactive decay. The archetypical example of this is the use of ^{57}Co, which decays via electron capture to ^{57}Fe. The resultant ^{57}Fe is in an excited state, and will emit a cascade of gamma rays. The final gamma in the cascade is from the 14.4 keV transition, which is used for Mössbauer spectroscopy.

The drawback of this method is that it requires radioactive sources, and that the cobalt source has a different electronic structure to iron, making it impractical for

use in experiments requiring ionic iron.

On the other hand, the development of high brilliance synchrotron and XFEL sources has resulted in the widespread use of direct gamma ray excitation of the desired transitions. These sources generate gamma radiation via the Bremsstrahlung of electrons, that is, the radiation emitted by an accelerating charge.

This is achieved using undulators, periodic arrangements of alternating magnetic fields. An electron beam entering an undulator is forced into sinusoidal transverse motion, producing intense Bremsstrahlung as it reaches peak displacement. This radiation is highly collimated, and directed along the beam axis, with an on-axis fundamental wavelength of

$$\lambda = \frac{\lambda_u}{2\gamma^2}\left(1 + \frac{K^2}{2}\right), \tag{2.1}$$

where λ_u is the undulator magnet spacing, γ the Lorentz factor of the electron beam, and the dimensionless undulator deflection parameter is given by

$$K = \frac{eB_u\lambda_u}{2\pi m_e c}, \tag{2.2}$$

with B_u the undulator magnetic field, and m_e the electron mass. In addition to the fundamental wavelength, harmonics are produced, with the odd harmonics directed along the beam axis.

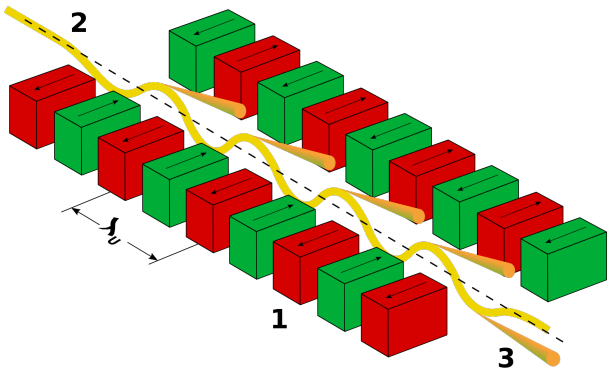

Figure 2.3: Working principle of an undulator. High power magnets of alternating polarity (1) are placed at intervals of length λ_u. An incident electron beam (2) is forced into transverse sinusoidal motion, emitting highly collimated on-axis radiation at maximum deflection (3).

The dependence of the fundamental wavelength on both the electron beam velocity and undulator magnetic field strength allows for tuning to a wide range of X-ray energies, allowing for high brilliance in a relatively narrow band around a desired wavelength.

In a synchrotron, the electron beam is accelerated in a circular storage ring. At certain locations in the ring undulators are placed, providing the X-ray source for the beam-lines.

In contrast, an XFEL uses a linear accelerator, with undulators lining the entire beam-line. The emitted radiation from an electron in the beam, travelling at c, will 'overtake' the beam, and therefore interact with electrons further ahead in the beam. This causes electrons slightly further ahead than a resonant wavelength λ to be decelerated, and electrons slightly further behind to be accelerated, creating bunches spaced a distance λ apart. As a result, the emitted radiation of the electron bunches is in phase with the radiation of the previous bunches, resulting in the coherent enhancement of the beam intensity. The result is a beam of substantially lower bandwidth, and higher peak brilliance than a synchrotron source.

2.2 Theoretical approaches

2.2.1 Scattering models

The earliest theoretical models of Mössbauer optics focused on multiple scattering descriptions of single photon propagation through a crystalline sample. This was developed in great detail by Hannon and Trammel [62–66], as well as Kagan *et al.* [67–69]. In this approach, the nuclei are modelled via their linear susceptibility, as a contribution to the single photon scattering amplitudes of a crystal. This method was employed in frequency domain by Kagan *et al.* [68] to derive the analytic expression for the delayed response of nuclear forward scattering, which we will discuss in Section 2.4.1. Using the Fourier inversion of the nuclear susceptibility, Shvyd'ko obtained time domain equations of motion for forward scattering [70], and also modelled phenomena such as magnetic switching of the nuclear hyperfine interactions for photon storage [71]. Sturhahn and Kohn further extended the scattering description to include incoherent scattering processes [72].

The primary limitation of this approach is that it is expressed in terms of Feynman diagrams for the photon propagator, with the nuclei modelled via their linear susceptibilities. As such, the underlying level schemes and collective interactions between nuclei are modelled implicitly rather than explicitly, which is undesirable when developing a qualitative picture of the underlying quantum optical phenomena. With the advent of XFEL sources, ultra-narrowband sources, capable of inverting the isomeric transitions could be in reach. With such strong excitation, the response of the nuclei is no longer linear, posing new challenges for their theoretical description. A Feynman diagram approach is far less useful in this regime, due to the fact that as composite structures, the isomeric states obey the 'mixed' statistics of atomic transitions rather than the Bosonic or Fermionic statistics of fundamental particles. As such, Wicks theorem does not hold in its usual form, leading to an exponential increase in the number of Feynman diagrams to consider at each scattering order.

Due to these factors, it is desirable to use a fully quantum optical mode to describe the nucleus-photon interaction, and we will now proceed to give an overview of the existing approaches.

2.2.2 Quantum optical models

To address the cavity-like aspects of grazing incidence thin-film nanostructures, Heeg developed a phenomenological model for describing thin film structures from a cavity QED point of view [73]. This model takes into account the collective be-

haviour of the nuclei by employing the single mode Dicke model. Due to its phenomenological nature, the coupling parameters for Heeg's model have to be determined by curve fitting either to an experimental spectrum, or to a numerical simulation of the linear response of the cavity. Due to this limitation, Lentrodt *et al.* [74] as well as Kong *et al.* [75], have instead successfully used a dipole-dipole formalism developed by Dung *et al.* [76] to model the cavity system. This formalism has been widely used in visible optics, and models the cavity field as an effective interaction potential between the nuclear layers, which can be obtained from the dyadic Green's function of the macroscopic Maxwell's equations for the cavity. This is particularly advantageous for thin films, as explicit analytic expressions for the Green's function are known, and numerically efficient. Diekmann *et al.* [40] have further developed this into a few-mode model by curve-fitting poles to the Fourier transformed Green's function, thus providing an ab initio method of obtaining the coupling parameters for Heeg's phenomenological model.

However, for our purposes, we desire analytic expressions for the equations of motion of the guided modes, as well as a complex analytic method of finding the spectral parameters such as mode locations, radiation modes etc. In addition, the coupled dipole-dipole model assumes the waveguide is non-dispersive, and thus neglects the effects of time delay due to the mode propagation. This is a good approximation to make at grazing incidence, where a single Fourier mode is excited, however as we are considering propagating modes explicitly, it is not at all clear if this is valid in the waveguide regime.

Because of these limitations, we will work *ab initio* from the Grüner-Welsch quantization of the macroscopic Maxwell's equations [77], which is presented in Chapter 3. This method treats the linear, lossy macroscopic medium as a bosonic noise field. Because of this, the electric and magnetic displacement fields obey bosonic statistics, and thus one can proceed with canonical quantization of the macroscopic Maxwell's equations. The resulting expressions then give the electromagnetic field and their commutators in terms of the dyadic Green's function of the medium. This forms the basis of the coupled dipole-dipole formalism of Dung *et al.* [76], which makes the further assumption that the medium is non-dispersive and adiabatically eliminates the electromagnetic field. As mentioned previously, we will not be making this approximation, and we instead explicitly model the field throughout.

2.3 Collective radiation and super-radiance

As discussed in Chapter 1, collective emission and absorption plays a large role in the interaction of Mössbauer nuclei and the electromagnetic field. Synchrotron radiation is well collimated, and thus large ensembles of nuclei are uniformly illuminated. This creates the conditions for super-radiant absorption and emission, which we shall now discuss.

2.3.1 Dicke super-radiance

In his seminal 1954 paper [12], Dicke demonstrated that an ensemble of identical atoms interacting with light of wavelength much larger than the ensemble size, would absorb and emit radiation collectively. He showed that the atoms would emit and absorb in phase and coherently, resulting in N such atoms having a factor of N speed up in their spontaneous emission rate compared to their single particle value.

While Dicke's original work considered primarily the long wavelength condition for super-radiance, it is not a necessity. Indeed, the key physical requirement is permutation invariance: any two atoms must be able to have their locations swapped without experiencing a different field amplitude. Thus, one can achieve super-radiance in other schemes. One such method is to place the atoms periodically in a single mode cavity, spaced an integer multiple of the mode wavelength apart. Then, due to periodicity, the illumination will be uniform, and the atoms super-radiantly driven.

Super-radiance is also achieved in 'pencil' geometries, as well as waveguides. Here, the atoms are placed in a linear arrangement, and driven by a pulsed excitation. Uniform illumination is achieved through a large *envelope* compared to the ensemble size. In these geometries, translational symmetry plays the role of permutation invariance, allowing for super-radiance without restrictions on the wavelength in relation to the ensemble size.

2.3.2 Radiation modes and sub-radiance

The classic Dicke picture of super-radiance deals with only a single unidirectional electromagnetic mode. However, in free space, one must consider the full continuum of electromagnetic modes, particularly the full directionality of these modes.

In such scenarios, it has been shown that the exchange of resonant photons between atoms leads to a dipole-dipole interaction, described by the electromagnetic dyadic Green's function $\overleftrightarrow{G}$, with the non-Hermitian effective potential given by

$$\hat{V}_{dd} = \frac{k_0^2}{\epsilon_0} \sum_{i,j} \hat{p}_i \cdot \overleftrightarrow{G}(\vec{r}_i, \vec{r}_j, \omega_0) \cdot \hat{p}_j^\dagger, \tag{2.3}$$

where $\vec{p}_i$ the transition dipole operator of the ith atom, $\vec{r}_i$ its position, and ω_0 the transition frequency. The dyadic Green's function and its derivation will be discussed in detail in Chapter 3.

The ensemble radiates collectively through the eigenmodes of this potential, with the complex eigenvalue of each mode describing its frequency shift and decay rate via the real and imaginary parts respectively. The magnitude of the imaginary part of the main diagonal of the potential gives the single particle decay rate of each atom [78, eq. 8.115],

$$\gamma_i = \frac{k_0^2}{\epsilon_0} \vec{p}_i \cdot \mathrm{Im}\{\overleftrightarrow{G}(\vec{r}_i, \vec{r}_i, , \omega_0)\} \cdot \vec{p}_i^*, \tag{2.4}$$

where $\vec{p}_i$ denotes the vector magnitude of the transition dipole operator. Thus, for indistinguishable atoms, we must have

$$\sum_n \mathrm{Im}\{\lambda_n\} = N\gamma_0, \tag{2.5}$$

where λ_n is the nth radiation eigenvalue, γ_0 the uniform single particle decay rate, and N the number of atoms. In addition, the imaginary part of $\hat{V}_{dd}$ is a positive semi-definite operator, and thus $\mathrm{Im}\{\lambda\} \geq 0$ for each eigenvalue.

We can see that this implies the existence of *sub-radiance*: for every super-radiant mode, that decays faster than γ_0, there must be at least one mode that decays slower

than γ_0. In such modes, rather than the emitted radiation from different atoms constructively interfering, the atoms emit out of phase, and destructively interfere, trapping the excitation within the ensemble. While hard to prepare experimentally, such states are highly desirable due to the prospects of radiation with very narrow line-widths.

2.4 Experimental schemes

2.4.1 Nuclear forward scattering

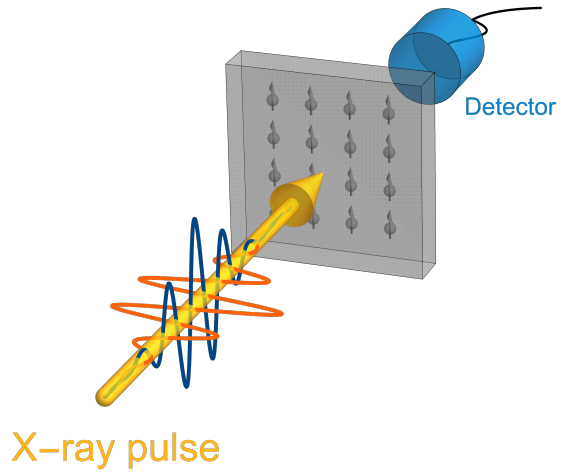

Figure 2.4: Experimental geometry of nuclear forward scattering. A well collimated beam at normal incidence illuminates a thin foil containing resonant nuclei. The transmitted field is measured, while back-reflection is minimal due to the extremely high frequency of the incident radiation.

In nuclear forward scattering, Figure 2.4, a thin foil enriched with resonant nuclei is used as the target, with the beam arriving at normal incidence. Nuclei further ahead in the target are not just driven directly by the incident beam, but also interact with the scattered field of nuclei behind them. The result is an interference pattern known as the dynamical beat, with the scattered field described by [68, 79]

$$E_{sc}(t) \propto e^{-i(\omega_0 - i\frac{\gamma}{2})t} \frac{J_1(\sqrt{\Omega t})}{\sqrt{\Omega t}}, \tag{2.6}$$

where ω_0, γ are the transition frequency and decay rate, J_1 is a Bessel function of the first kind,

$$\Omega = \gamma \sigma_0 \rho_N L \tag{2.7}$$

is the dynamical beat frequency, ρ_N the number density of resonant nuclei, L the foil thickness, and

$$\sigma_0 = \frac{2\pi}{k_0^2} \cdot \frac{f_{LM}}{1+\alpha} \cdot \frac{2I_e + 1}{2I_g + 1} \tag{2.8}$$

is the nuclear scattering cross-section [79].

For short times, the scattered response envelope is approximately exponential,

$$\frac{J_1(\sqrt{\Omega t})}{\sqrt{\Omega t}} \approx e^{-\frac{\gamma}{2} T_{eff} t}, \quad \gamma t T_{eff} \leq 3, \tag{2.9}$$

where

$$T_{eff} = \frac{\sigma_0 \rho_N L}{4} = \frac{\Omega}{4\gamma} \tag{2.10}$$

is the 'effective resonant thickness' of the sample. Thus, for short times the sample is super-radiant, with an enhancement of the decay-rate given by the effect resonant thickness.

2.4.2 Grazing incidence thin-film scattering

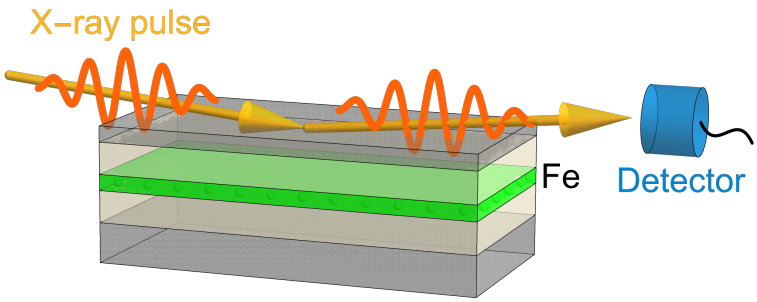

Figure 2.5: Experimental geometry of grazing incidence thin-film scattering. A well collimated beam incident at a very small angle illuminates a multi-layer containing resonant nuclei. Due to translational symmetry, the planar wave-vector is conserved, exciting a single Fourier mode. The layer is nano-structured, creating a 'cavity' in the transverse direction z. Both the reflected and transmitted components can be measured.

In grazing incidence scattering, Figure 2.5, the target is a thin film multi-layer structure. Layers of varying atomic number Z are placed in nanometre scale layers, with layers of high Z deflecting X-rays stronger than layers of low Z. This allows for the creation of resonance structures, with high Z capping layers and a low Z filler.

For a plane wave incident at a small angle of incidence (on the order of milliradians), the transverse component of the wave-vector will be of a similar magnitude to the thin-film layer depths. As such, the thin-film structure acts as a 'cavity' for the plane wave, and the angle of incidence can be adjusted to drive a resonance of the 'cavity' mode structure.

If a thin film of resonant nuclei is placed at the maximum of one of these cavity modes, due to the plane wave driving, the nuclei are uniformly illuminated, and thus are super-radiant.

2.4.3 Thin-film front coupling

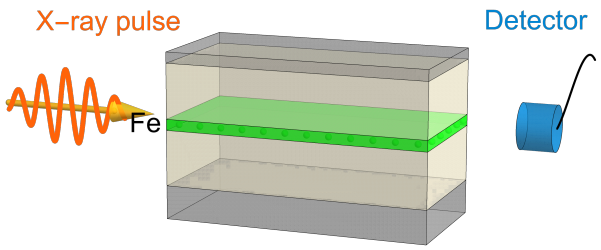

Figure 2.6: Experimental geometry of front coupling thin-film scattering. Translational symmetry is broken at the interface, and thus the planar wave-vector is not conserved. The layer is nano-structured, creating a waveguide, and the guided modes are excited by the input beam directly.

In thin-film front coupling, Figure 2.6, the same type of multi-layer structure as grazing incidence is used. However, the incident light is now coupled directly parallel with the layer planes, such that it enters from the side of the thin-film slab.

This allows for the use of thicker capping layers for greater field confinement, without reducing the in-coupling strength as would occur in grazing incidence.

In Chapter 8 we will derive the equations of motion for front coupling, and demonstrate that it shares features from both conventional nuclear forward scattering and grazing incidence. The resonance structure from grazing incidence appears as the collection of guided modes that can be excited by the incident beam. The guided modes themselves display the same dynamical beat phenomenon as nuclear forward scattering,

Chapter 3

Macroscopic QED of multi-layers

In this chapter, we introduce the theoretical description of the electromagnetic field in multi-layered dielectric media. We begin by reviewing the macroscopic formulation of Maxwell's equations, and their formal solution in terms of dyadic Green's functions. Following this, we introduce the Grüner-Welsch [77] quantization of macroscopic QED, which uses the dyadic Green's functions of the medium to define the second quantized medium-assisted electromagnetic field. This method is particularly suitable for planar layered media, as analytic expressions for the dyadic Green's functions are well known [80–83]. We will review their derivation in Chapter 4.

Finally, we give an overview of the Kirchoff's integral formula for the electromagnetic field, and how it allows us to obtain the input field in a medium from a given free space solution of Maxwell's equations, using the Green's functions of the media. We will use this in Chapter 6 to evaluate the input fields for the three experimental configurations introduced in Chapter 2: grazing incidence, forward scattering, and waveguide front coupling.

3.1 Maxwell's equations in macroscopic media

In a macroscopic medium, instead of working with the fundamental fields $\vec{E}, \vec{B}$, and electric and magnetic dipole sources $\vec{P}, \vec{M}$ directly, one may instead work with the so-called 'electric displacement' field $\vec{D}$, and 'magnetizing field' $\vec{H}$, which are defined via the constitutive relations

$$\vec{D}(\vec{r}, t) = \varepsilon_0 \vec{E}(\vec{r}, t) + \vec{P}(\vec{r}, t), \tag{3.1}$$

$$\vec{H}(\vec{r}, t) = \frac{1}{\mu_0} \vec{B}(\vec{r}, t) - \vec{M}(\vec{r}, t). \tag{3.2}$$

The fields obey the macroscopic Maxwell's equations [82–84],

$$\nabla \cdot \vec{D}(\vec{r}, t) = \rho_e(\vec{r}, t), \tag{3.3}$$
$$\nabla \cdot \vec{B}(\vec{r}, t) = \rho_m(\vec{r}, t), \tag{3.4}$$
$$\nabla \times \vec{E}(\vec{r}, t) = -\vec{j}_m(\vec{r}, t) - \partial_t \vec{B}(\vec{r}, t), \tag{3.5}$$
$$\nabla \times \vec{H}(\vec{r}, t) = \vec{j}_e(\vec{r}, t) + \partial_t \vec{D}(\vec{r}, t), \tag{3.6}$$

with free electric charge and current densities $\rho_e, \vec{j}_e$ measured in Coulombs and Amperes, respectively, and free magnetic charge and current densities $\rho_m, \vec{j}_m$ measured in Webers and Volts, respectively. So far, magnetic charges have never been observed in nature. Nevertheless, keeping in fictitious magnetic charges makes Maxwell's equations invariant under duality transformations [82, 83],

$$\begin{pmatrix} \rho_e \\ \rho_m \end{pmatrix} \to R(\theta) \begin{pmatrix} \rho_e \\ \rho_m \end{pmatrix}, \tag{3.7}$$
$$\begin{pmatrix} \vec{j}_e \\ \vec{j}_m \end{pmatrix} \to R(\theta) \begin{pmatrix} \vec{j}_e \\ \vec{j}_m \end{pmatrix}, \tag{3.8}$$
$$\begin{pmatrix} \vec{E} \\ \vec{H} \end{pmatrix} \to R(\theta) \begin{pmatrix} \vec{E} \\ \vec{H} \end{pmatrix}, \tag{3.9}$$
$$\begin{pmatrix} \vec{D} \\ \vec{B} \end{pmatrix} \to R(\theta) \begin{pmatrix} \vec{D} \\ \vec{B} \end{pmatrix}, \tag{3.10}$$
$$R(\theta) = \begin{pmatrix} \cos\theta & -\sin\theta \\ \sin\theta & \cos\theta \end{pmatrix}. \tag{3.11}$$

This is particularly useful in situations with no free charges, $\rho_e, \rho_m, \vec{j}_e, \vec{j}_m = 0$, as we can see that the duality transformation then holds exactly. In any case, as we shall see, finding the dyadic Green's function can be done using arbitrary choices of electric or magnetic sources, and as such, we will continue using the fictitious magnetic sources.

Taking a temporal Fourier transform of (3.3) through (3.6) gives

$$\nabla \cdot \vec{D}(\vec{r}, \omega) = \rho_e(\vec{r}, \omega), \tag{3.12}$$
$$\nabla \cdot \vec{B}(\vec{r}, \omega) = \rho_m(\vec{r}, \omega), \tag{3.13}$$
$$\nabla \times \vec{E}(\vec{r}, \omega) = -\vec{j}_m(\vec{r}, \omega) + i\omega \vec{B}(\vec{r}, \omega), \tag{3.14}$$
$$\nabla \times \vec{H}(\vec{r}, \omega) = \vec{j}_e(\vec{r}, \omega) - i\omega \vec{D}(\vec{r}, \omega), \tag{3.15}$$

where we have distinguished the time and frequency domain forms of a function by its arguments. Our choice of Fourier conventions is summarized in Appendix C.1.

In a linear medium, the electric and magnetic dipole fields can be obtained from the fundamental fields via susceptibility dyads,

$$\vec{P}(\vec{r}, \omega) = \varepsilon_0 \overleftrightarrow{\chi}_e(\vec{r}, \omega) \cdot \vec{E}(\vec{r}, \omega), \tag{3.16}$$
$$\vec{M}(\vec{r}, \omega) = \frac{1}{\mu_0} \overleftrightarrow{\chi}_m(\vec{r}, \omega) \cdot \vec{B}(\vec{r}, \omega). \tag{3.17}$$

In an isotropic medium, the susceptibilities are diagonal and rotationally symmetric, and thus can be taken to be scalar. For hard X-ray scattering the magnetic scattering is negligible, and we will therefore take $\chi_m = 0$. In principle, the electric susceptibility is not isotropic, as it is highly sensitive to the crystal structure of the medium due to Bragg scattering. However, for thin films formed through sputter deposition, which are the experimental realization of the systems we consider, the samples are polycrystalline and highly disordered. The bulk electric susceptibility is therefore the disorder average of the individual crystal grains susceptibility, and is thus isotropic, and homogeneous within a particular medium. We will therefore take χ_e to be scalar. In addition, the dipole responses must be causal. In frequency domain, this is enforced by Kramers-Kronig consistency,

$$\mathrm{Re}(\chi_\lambda(\vec{r},\omega)) = \frac{1}{\pi}\mathscr{P}\int \mathrm{d}\omega' \, \frac{\mathrm{Im}(\chi_\lambda(\vec{r},\omega'))}{\omega'-\omega}, \tag{3.18}$$

$$\mathrm{Im}(\chi_\lambda(\vec{r},\omega)) = -\frac{1}{\pi}\mathscr{P}\int \mathrm{d}\omega' \, \frac{\mathrm{Re}(\chi_\lambda(\vec{r},\omega'))}{\omega'-\omega}, \tag{3.19}$$

where $\mathscr{P}$ denotes the Cauchy principal value, and $\lambda = e, m$. Substituting (3.16), (3.17) into (3.1) and (3.2) gives [82]

$$\vec{D}(\vec{r},\omega) = \varepsilon_0\varepsilon(\vec{r},\omega)\vec{E}(\vec{r},\omega), \tag{3.20}$$

$$\vec{H}(\vec{r},\omega) = \frac{1}{\mu_0\mu(\vec{r},\omega)}\vec{B}(\vec{r},\omega), \tag{3.21}$$

$$\mu(\vec{r},\omega) = \frac{1}{1-\chi_m(\vec{r},\omega)}, \tag{3.22}$$

$$\varepsilon(\vec{r},\omega) = 1+\chi_e(\vec{r},\omega). \tag{3.23}$$

One can then use (3.12) through (3.15), combined with (3.20) through (3.23) to show [83, eq. 1.21, 1.22] [82, p. 2.149]

$$\mu\nabla\times\mu^{-1}\nabla\times\vec{E} - n^2\frac{\omega^2}{c^2}\vec{E} = i\omega\mu_0\mu\vec{j}_e - \mu\nabla\times\mu^{-1}\vec{j}_m, \tag{3.24}$$

$$\varepsilon\nabla\times\varepsilon^{-1}\nabla\times\vec{H} - n^2\frac{\omega^2}{c^2}\vec{H} = i\omega\varepsilon_0\varepsilon\vec{j}_m + \varepsilon\nabla\times\varepsilon^{-1}\vec{j}_e \tag{3.25}$$

where we have defined the refractive index

$$n(\vec{r},\omega) = \sqrt{\mu(\vec{r},\omega)\varepsilon(\vec{r},\omega)}. \tag{3.26}$$

The solutions are then given in terms of dyadic Green's functions as

$$\vec{E}(\vec{r},\omega) = \int \mathrm{d}^3r' \, \overleftrightarrow{\mathscr{G}}_e(\vec{r},\vec{r}',\omega)\cdot\vec{i}_e(\vec{r}',\omega), \tag{3.27}$$

$$\vec{H}(\vec{r},\omega) = \int \mathrm{d}^3r' \, \overleftrightarrow{\mathscr{G}}_m(\vec{r},\vec{r}',\omega)\cdot\vec{i}_m(\vec{r}',\omega) \tag{3.28}$$

where

$$i_e(\vec{r},\omega) = i\omega\mu_0\vec{j}_e - \nabla\times\mu^{-1}\vec{j}_m, \tag{3.29}$$

$$i_m(\vec{r},\omega) = i\omega\varepsilon_0\vec{j}_m + \nabla\times\varepsilon^{-1}\vec{j}_e, \tag{3.30}$$

$$(\nabla\times\mu^{-1}\nabla\times - \frac{\omega^2}{c^2}\varepsilon)\overleftrightarrow{\mathscr{G}}_e(\vec{r},\vec{r}',\omega) = \delta^3(\vec{r}-\vec{r}'), \tag{3.31}$$

$$(\nabla\times\varepsilon^{-1}\nabla\times - \frac{\omega^2}{c^2}\mu)\overleftrightarrow{\mathscr{G}}_m(\vec{r},\vec{r}',\omega) = \delta^3(\vec{r}-\vec{r}'). \tag{3.32}$$

In defining the sources, (3.29), (3.30), we can now see why the fictitious sources can be used to derive the Green's function for real sources: a time harmonic electric current is an equivalent source to the curl of a magnetic current, while a time harmonic magnetic current is an equivalent source to the curl of an electric current.

Dimensionally, as the relative susceptibilities μ, ε are dimensionless, we can see that the dyadic Green's functions $\overleftrightarrow{\mathcal{G}}_\lambda$, $\lambda = e, m$ have the dimension of inverse length. Due to singularities in the Green's function for $\vec{r} = \vec{r'}$ [83], the integrals in (3.27), (3.28) should be interpreted in the principle value sense, by excluding an infinitesimal volume of variable size but fixed shape around the source region, and taking the limit as this volume shrinks to zero. Written out explicitly, performing this procedure on (3.27) is then given by

$$\vec{E}(\vec{r},\omega) = \mathcal{P}\int \mathrm{d}^3 r'\, \overleftrightarrow{\mathcal{G}}_e(\vec{r},\vec{r}',\omega)\cdot\vec{i}_e(\vec{r}',\omega) - \overleftrightarrow{L}_e\cdot\vec{i}_e(\vec{r},\omega). \tag{3.33}$$

Here, $\mathcal{P}$ denotes the principal value procedure, and $\overleftrightarrow{L}$ is the positive semi-definite 'depolarizing dyadic' [83], that accounts for the surface boundary terms of the infinitesimal exclusion volume [83]. In a nuclear or atomic system, this term contributes to the Lamb shift of the scatterer [81, 83], and as such we can absorb it into our definition of single particle frequencies. Therefore, we can neglect $\overleftrightarrow{L}$ for our purposes, and implicitly assume that the principal value is performed as needed.

The two Green's functions $\overleftrightarrow{\mathcal{G}}_e$, $\overleftrightarrow{\mathcal{G}}_m$ are not independent. Their relation can easily be found by consider purely electric, and purely magnetic sources respectively.

Firstly, for purely magnetic sources, we may take a curl of (3.28), and use (3.17), (3.23), (3.28), (3.29) and (3.30) to write (c.f. [82, eq. 2.204])

$$\nabla\times\vec{H} = \vec{j}_e - i\omega\vec{D}, \tag{3.34}$$

$$-\int \mathrm{d}^3 r'\, \nabla\times\overleftrightarrow{\mathcal{G}}_m(\vec{r},\vec{r}',\omega)\times\nabla'\cdot\frac{1}{\varepsilon(\vec{r}',\omega)}\vec{j}_e(\vec{r}',\omega) = \vec{j}_e(\vec{r}',\omega) \tag{3.35}$$

$$-\frac{\mu_0\varepsilon_0\varepsilon}{\omega^2}\int \mathrm{d}^3 r'\, \overleftrightarrow{\mathcal{G}}_e(\vec{r},\vec{r}',\omega)\cdot\vec{j}_e(\vec{r}',\omega)$$

$$\overleftrightarrow{\mathcal{G}}_e = \frac{1}{\varepsilon(\vec{r},\omega)k^2}\delta^3(\vec{r}-\vec{r}') + \frac{1}{\varepsilon(\vec{r},\omega)k}\nabla\times\overleftrightarrow{\mathcal{G}}_m\times\nabla'\frac{1}{\varepsilon(\vec{r}',\omega)k} \tag{3.36}$$

where $k = \omega c^{-1}$.

A dual derivation for the case of purely electric sources shows

$$\overleftrightarrow{\mathcal{G}}_m = \frac{1}{\mu(\vec{r},\omega)k^2}\delta^3(\vec{r}-\vec{r}') + \frac{1}{\mu(\vec{r},\omega)k}\nabla\times\overleftrightarrow{\mathcal{G}}_e\times\nabla'\frac{1}{\mu(\vec{r}',\omega)k}. \tag{3.37}$$

Therefore, we can solve for either the electric or magnetic fields, whichever is simpler, and use (3.36), (3.37) to obtain the dual. We will from this point work in terms of the electric Green's function, and denote it

$$\overleftrightarrow{G} \equiv \overleftrightarrow{\mathcal{G}}_e, \tag{3.38}$$

and denote the electric current simply as $\vec{j}$, with the magnetic charges and currents zero, as is physically the case.

3.1.1 Response from dipole currents

The free current density can be expressed in terms of electric and magnetic multipole density fields, $\vec{P}, \vec{M}$. To dipole order, we have

$$\vec{j}(\vec{r},\omega) = -i\omega\vec{P}(\vec{r},\omega) + \nabla\times\vec{M}(\vec{r},\omega). \tag{3.39}$$

For a continuous ensemble of scatterers with uniform density, the dipole densities are found as the product of the polarization fields of the scatterers with the source number density $\rho_N(\vec{r})$,

$$\vec{P}(\vec{r},\omega) = \rho_N(\vec{r})\vec{p}(\vec{r},\omega), \tag{3.40}$$

$$\vec{M}(\vec{r},\omega) = \rho_N(\vec{r})\vec{m}(\vec{r},\omega), \tag{3.41}$$

For point scatterers, we may substitute the density with the point particle density and polarization operators,

$$\rho_N(\vec{r}) \to \sum_i \delta^3(\vec{r}-\vec{r}_i), \tag{3.42}$$

$$\vec{P}(\vec{r},\omega) = \sum_i \vec{p}_i(\omega)\delta^3(\vec{r}-\vec{r}_i), \tag{3.43}$$

$$\vec{M}(\vec{r},\omega) = \sum_i \vec{m}_i(\omega)\delta^3(\vec{r}-\vec{r}_i). \tag{3.44}$$

We can therefore write the electric field as the sum of the electric and magnetic dipole contributions, with their own corresponding Green's function [82, eq. 2.194],

$$\begin{aligned}\vec{E}(\vec{r},\omega) = &-\mathcal{P}\int \mathrm{d}^3r'\,\rho_N(\vec{r})\frac{1}{\varepsilon_0}\overleftrightarrow{G}_{ee}(\vec{r},\vec{r}',\omega)\cdot\hat{p}(\vec{r}',\omega)\\ &-\mathcal{P}\int \mathrm{d}^3r'\,\rho_N(\vec{r})\mu_0 c\overleftrightarrow{G}_{em}(\vec{r},\vec{r}',\omega)\cdot\hat{m}(\vec{r},\omega).\end{aligned} \tag{3.45}$$

These Green's functions are defined as [82, eq. 2.198, 2.200]

$$\overleftrightarrow{G}_{ee}(\vec{r},\vec{r}',\omega) = \frac{i\omega}{c}\overleftrightarrow{G}(\vec{r},\vec{r}',\omega)\frac{i\omega}{c}, \tag{3.46}$$

$$\overleftrightarrow{G}_{em}(\vec{r},\vec{r}',\omega) = \frac{i\omega}{c}\overleftrightarrow{G}(\vec{r},\vec{r}',\omega)\times\overleftarrow{\nabla}'. \tag{3.47}$$

Note that we have used integration by parts to obtain the *em* Green's function, which assumes $G(\vec{r},\vec{r}',\omega)$ vanishes at spatial infinity.

We can further obtain the *me* and *mm* Green's functions, giving the magnetic response from electric and magnetic dipoles respectively, by using Maxwell's equations, (3.14). The magnetic field response is therefore given by [82, eq. 2.195]

$$\begin{aligned}\vec{B}(\vec{r},\omega) = &-\mathcal{P}\int \mathrm{d}^3r'\,\rho_N(\vec{r'})\mu_0 c\overleftrightarrow{G}_{me}(\vec{r},\vec{r}',\omega)\cdot\hat{p}(\vec{r}',\omega)\\ &-\mathcal{P}\int \mathrm{d}^3r'\,\rho_N(\vec{r'})\mu_0\overleftrightarrow{G}_{mm}(\vec{r},\vec{r}',\omega)\cdot\hat{m}(\vec{r},\omega),\end{aligned} \tag{3.48}$$

where [82, eq. 2.199, 2.201]

$$\overleftrightarrow{G}_{me}(\vec{r},\vec{r}',\omega) = \overrightarrow{\nabla}\times\overleftrightarrow{G}(\vec{r},\vec{r}',\omega)\frac{i\omega}{c} \tag{3.49}$$

$$\overleftrightarrow{G}_{mm}(\vec{r},\vec{r}',\omega) = \overrightarrow{\nabla}\times\overleftrightarrow{G}(\vec{r},\vec{r}',\omega)\times\overleftarrow{\nabla}'. \tag{3.50}$$

These Green's functions have the dimension of inverse volume.

3.2 Quantization of field in linear medium

In linear media, the electromagnetic field can be quantized in terms of the dyadic Green's function of the material. Below we summarize the main results, following the derivation of Buhmann [82].

First, Bosonic noise fields are introduced, corresponding to electric and magnetic noise, $\lambda = e, m$, and satisfying the following commutation relations

$$[\hat{f}_\lambda(\vec{r},\nu),\hat{f}^\dagger_{\lambda'}(\vec{r}',\nu')] = \delta_{\lambda\lambda'}\delta^3(\vec{r}-\vec{r}')\delta(\nu-\nu'), \tag{3.51}$$

$$[\hat{f}_\lambda(\vec{r},\nu),\hat{f}_{\lambda'}(\vec{r}',\nu')] = 0. \tag{3.52}$$

The noise field frequency ν is at this stage formal parameter, as in the Schrödinger picture operators have no time dependence. However, we desire that this frequency parameter corresponds to a Fourier component for the free field in the Heisenberg picture, i.e.

$$\partial_t\hat{f}_\lambda(\vec{r},\nu,t) = -\frac{i}{\hbar}[f_\lambda(\vec{r},\nu,t),H_F] = -i\nu\hat{f}_\lambda(\vec{r},\nu,t), \tag{3.53}$$

where H_F is the noise field Hamiltonian. In order for this to hold, the following Hamiltonian is required [82, eq. 2.271]

$$H_F = \sum_{\lambda=e,m}\int_0^\infty \mathrm{d}\nu\int \mathrm{d}^3r\,\hbar\nu f^\dagger_\lambda(\vec{r},\nu)f_\lambda(\vec{r},\nu). \tag{3.54}$$

Under this Hamiltonian, the noise fields then have a Heisenberg picture time dependence of

$$\hat{f}_\lambda(\vec{r},\nu,t) = \hat{f}_\lambda(\vec{r},\nu,0)^{-i\nu t}. \tag{3.55}$$

In terms of the noise fields, the electric and magnetic fields are given by [82, eq.

2.259, 2.263]:

$$\hat{E}_+(\vec{r},\nu) = \sum_{\lambda=e,m}\int \mathrm{d}^3 s\, \overleftrightarrow{\zeta}_\lambda(\vec{r},\vec{s},\nu)\cdot\hat{f}_\lambda(\vec{s},\nu), \tag{3.56}$$

$$\hat{E}_-(\vec{r},\nu) = \hat{E}_+(\vec{r},\nu)^\dagger, \tag{3.57}$$

$$\hat{E}(\vec{r}) = \int_0^\infty \mathrm{d}\nu \left(\hat{E}_+(\vec{r},\nu)+\hat{E}_-(\vec{r},\nu)\right), \tag{3.58}$$

$$\hat{B}_+(\vec{r},\nu) = \frac{1}{i\nu}\sum_{\lambda=e,m}\int \mathrm{d}^3 s\, \nabla\times\overleftrightarrow{\zeta}_\lambda(\vec{r},\vec{s},\nu)\cdot\hat{f}_\lambda(\vec{s},\nu), \tag{3.59}$$

$$\hat{B}_-(\vec{r},\nu) = \hat{B}_+(\vec{r},\nu)^\dagger, \tag{3.60}$$

$$\hat{B}(\vec{r}) = \int_0^\infty \mathrm{d}\nu \left(\hat{B}_-(\vec{r},\nu)+\hat{B}_+(\vec{r},\nu)\right), \tag{3.61}$$

$$\overleftrightarrow{\zeta}_e(\vec{r},\vec{r}',\nu) = i\frac{\nu^2}{c^2}\sqrt{\frac{\hbar}{\pi\varepsilon_0}\operatorname{Im}\varepsilon(\vec{r}',\nu)}\overleftrightarrow{G}(\vec{r},\vec{r}',\nu), \tag{3.62}$$

$$\overleftrightarrow{\zeta}_m(\vec{r},\vec{r}',\nu) = i\frac{\nu}{c}\sqrt{\frac{\hbar}{\pi\varepsilon_0}\frac{\operatorname{Im}\mu(\vec{r}',\nu)}{|\mu(\vec{r}',\nu)|^2}}\overleftrightarrow{G}(\vec{r},\vec{r}',\nu)\times\nabla'. \tag{3.63}$$

We have introduced the notation $E_\pm$ to denote positive and negative frequency field components, having noted that our choice of Fourier convention results in annihilation operators corresponding to positive frequencies (Appendix C.1). The electric field obeys the equal time commutation relations [82, eq. A.2]

$$[\hat{E}_+(\vec{r},\nu),\hat{E}_-(\vec{r}',\nu')] = \frac{\hbar\mu_0\nu^2}{\pi}\operatorname{Im}\{\overleftrightarrow{G}(\vec{r},\vec{r'},\nu)\}\delta(\nu-\nu'). \tag{3.64}$$

This can be easily seen to be equal to

$$[\hat{E}_+(\vec{r},\nu),\hat{E}_-(\vec{r}',\nu')] = -\frac{\hbar}{\pi\varepsilon_0}\operatorname{Im}\{\overleftrightarrow{G}_{ee}(\vec{r},\vec{r}',\nu)\}\delta(\nu-\nu'). \tag{3.65}$$

Using

$$\hat{B}_+(\vec{r},\nu) = \frac{1}{i\nu}\nabla\times\hat{E}_+(\vec{r},\nu), \tag{3.66}$$

and

$$\hat{B}_-(\vec{r},\nu) = -\frac{1}{i\nu}\nabla\times\hat{E}_-(\vec{r},\nu) = \frac{1}{i\nu}\hat{E}_+(\vec{r},\nu)\times\nabla, \tag{3.67}$$

one can then show that the magnetic field obeys the following equal time commutator

$$[\hat{B}_+(\vec{r},\nu),\hat{B}_-(\vec{r}',\nu')] = -\frac{\hbar\mu_0}{\pi}\operatorname{Im}\{\overleftrightarrow{G}_{mm}(\vec{r},\vec{r'},\nu)\}\delta(\nu-\nu'). \tag{3.68}$$

These commutators in turn show that the field is consistent with the fluctuation-dissipation theorem [82, eq. 2.268].

3.3 Input/output fields

In order to evaluate observables such as the scattered intensity, reflectivity, transmission etc. we need to be able to determine the propagation of both incoming

and outgoing fields in the medium. In particular, the incident beam is specified as a free space solution of Maxwell's equations, while the detectors in an experiment are placed far away from the sample, and measure both the field scattered directly by the medium, in addition the field scattered by the nuclei. We must therefore be able to evaluate the incoming and outgoing fields scattering by the electronic medium, in terms of their free space expressions and vice versa.

To do this, we will use the method of fictitious sources. This is based on the vector-dyadic form of Kirchoff's integral formula [83]. In free space, the electric field obeys the differential equation

$$\nabla \times \nabla \times \vec{E}_0(\vec{r},\omega) - \frac{\omega^2}{c^2}\vec{E}_0(\vec{r},\omega) = i\omega\mu_0\vec{j}(\vec{r},\omega). \tag{3.69}$$

The free space Green's dyadic obeys

$$\nabla \times \nabla \times \overleftrightarrow{G}_0(\vec{r},\vec{r}',\omega) - \frac{\omega^2}{c^2}\overleftrightarrow{G}_0(\vec{r},\vec{r}',\omega) = \overleftrightarrow{\mathbb{1}}\,\delta^3(\vec{r}-\vec{r}'). \tag{3.70}$$

In the case that the entire source current $\vec{j}$ is enclosed by a volume V, using Green's second theorem, the solution at a position $\vec{r}$ that lies outside V can be written in the form [83, eq. 1.95]

$$\begin{aligned}\vec{E}_0(\vec{r},\omega) &= i\omega\mu_0\int_V \mathrm{d}^3r'\,\overleftrightarrow{G}_0(\vec{r},\vec{r}',\omega)\cdot\vec{j}(\vec{r}',\omega)\\ &+\oint_{\partial V}\mathrm{d}^2s\,\overleftrightarrow{G}_0(\vec{r},s,\omega)\cdot\hat{n}(s)\times\nabla\times\vec{E}_0(\vec{s},\omega)+\overleftrightarrow{G}_0(\vec{r},s,\omega)\times\nabla\cdot\hat{n}(s)\times\vec{E}_0(\vec{s},\omega).\end{aligned} \tag{3.71}$$

Note that we have dropped the principal value notation, as we are only considering observation points outside the source region, which allows the integrals to converge in the usual way. In addition, we note that although Hanson and Yakovlev define (3.71) in terms of an observation point *inside* the source region [83, fig. 1.1], (3.71) holds even for observation points *outside* the source position, Figure 3.1.

The case $\vec{j} = 0$ gives the Kirchoff integral formula for the homogeneous solution,

$$\vec{E}_0(\vec{r},\omega) = \oint_{\partial V}\mathrm{d}^2s\,\overleftrightarrow{G}_0(\vec{r},s,\omega)\cdot\hat{n}(s)\times\nabla\times\vec{E}_0(\vec{s},\omega)+\overleftrightarrow{G}_0(\vec{r},s,\omega)\times\nabla\cdot\hat{n}(s)\times\vec{E}_0(\vec{s},\omega). \tag{3.72}$$

We can use (3.46), (3.47) and (3.5) to write this as

$$\begin{aligned}\vec{E}_0(\vec{r},\omega) = -\int_{\partial V}\mathrm{d}^2s\,\Bigg(&\frac{c^2}{i\omega}\overleftrightarrow{G}_{0,ee}(\vec{r},\vec{s},\omega)\cdot\vec{B}_0(\vec{s},\omega)\times\hat{n}(\vec{s})\\ &+\frac{c}{i\omega}\overleftrightarrow{G}_{0,em}(\vec{r},\vec{s},\omega)\cdot\vec{E}_0(\vec{s},\omega)\times\hat{n}(\vec{s})\Bigg).\end{aligned} \tag{3.73}$$

Comparing with equation (3.45), we see that this is equivalent to the response from fictitious electric and magnetic polarization densities

$$\vec{P}_0(\vec{r},\omega) = \frac{1}{i\mu_0\omega}\vec{B}_0(\vec{r},\omega)\times\vec{S}(\vec{r}), \tag{3.74}$$

$$\vec{M}_0(\vec{r},\omega) = \frac{1}{i\mu_0\omega}\vec{E}_0(\vec{r},\omega)\times\vec{S}(\vec{r}), \tag{3.75}$$

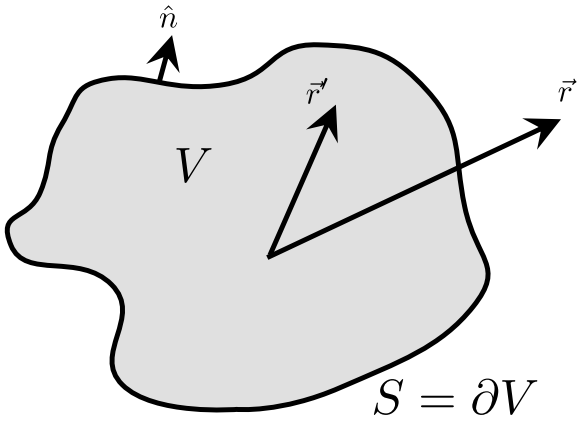

Figure 3.1: Geometry considered in Equation (3.71). All sources $\vec{r}'$ are bounded by a surface S, with normal vectors $\hat{n}$ and interior volume V, while the observation point under consideration $\vec{r}$ lies in the exterior of V.

where $\vec{S}(\vec{r})$ is the surface normal distribution for the boundary ∂V, equal to the indicator distribution for the surface times the field of normal vectors along the surface.

This allows us, given a desired incident field in free space, to obtain the scattered field via the Green's function of the system. Specifically, we enclose both the observation position $\vec{r}$ and all scatterers in a bounding volume V, such that the boundary of the volume lies in free space. We then specify the desired free fields along the surface. We then construct the full scattered field from the fictitious sources using the full Green's function,

$$\begin{aligned}\vec{E}(\vec{r},\omega) = &-\int \mathrm{d}^3 r' \, \frac{1}{\varepsilon_0} \overleftrightarrow{G}_{ee}(\vec{r},\vec{r}'\omega)\cdot\vec{P}_0(\vec{r}',\omega) \\ &-\int \mathrm{d}^3 r' \, \mu_0 c \overleftrightarrow{G}_{em}(\vec{r},\vec{r}',\omega)\cdot\vec{M}_0(\vec{r},\omega).\end{aligned} \tag{3.76}$$

Substituting back (3.74), (3.75), and using (3.5) gives

$$\begin{aligned}\vec{E}(\vec{r},\omega) = &-\int_{\partial V} \mathrm{d}^2 s \, \frac{c}{ik} \overleftrightarrow{G}_{ee}(\vec{r},\vec{s},\omega)\cdot\vec{B}_0(\vec{s},\omega)\times\hat{n}(\vec{s}) \\ &-\int_{\partial V} \mathrm{d}^2 s \, \frac{1}{ik} \overleftrightarrow{G}_{em}(\vec{r},\vec{s},\omega)\cdot\vec{E}_0(\vec{s},\omega)\times\vec{n}(\vec{s}),\end{aligned} \tag{3.77}$$

$$\begin{aligned}\vec{B}(\vec{r},\omega) = &-\int_{\partial V} \mathrm{d}^2 s \, \frac{1}{ik} \overleftrightarrow{G}_{me}(\vec{r},\vec{s},\omega)\cdot\vec{B}_0(\vec{s},\omega)\times\hat{n}(\vec{s}) \\ &-\int_{\partial V} \mathrm{d}^2 s \, \frac{1}{ikc} \overleftrightarrow{G}_{mm}(\vec{r},\vec{s},\omega)\cdot\vec{E}_0(\vec{s},\omega)\times\vec{n}(\vec{s}).\end{aligned} \tag{3.78}$$

With this, we have completed our specification of the electromagnetic fields and their quantization in linear media, and we shall now proceed to specify the quantum model for the nuclei, and their interaction with the magnetic field.

Chapter 4

The Green's function and its resonant structure

Whether we are interested in nuclear forward scattering, grazing incidence scattering, or front coupled waveguide scattering, the relevant Green's function is that of a multi-layered dielectric, with the scattering geometry affecting the boundary conditions of the incident and outgoing fields.

In this section, we therefore give an overview of the well known analytic expressions for the multi-layer Green's functions, which appear in various works, such as Tomaš [80], Hanson and Yakovlev [83], Johansson [81], Buhmann [82], and others. As we will make use of various analytic properties of this solution, we therefore give an overview of its derivation, and discuss its structure as a complex function. In particular, we illustrate that guided modes of the structure appear as poles of the spatially Fourier transformed Green's function, with branch cuts appearing for each capping layer, corresponding to the radiative modes that propagate in the capping layers.

Finally, in order to inform the experimental design of X-ray waveguides, it is important to have simple, easy to calculate figures of merit. We therefore show how various important figures of merit can be given in terms of the Green's function and its spatial Fourier transform, thus allowing for qualitative and quantitative comparison of the merit of different candidate designs.

4.1 Analytic expression for multi-layers

The coordinate system we will use for our multi-layers is such that the layers are stacked in the z direction, and uniform in the xy plane, Figure 4.1.

Experimentally, thin film waveguides are formed through a sputter deposition process [30, 36] and therefore the layers are polycrystalline, and highly disordered. As such, the Bragg contribution to scattering is negligible. In addition, at hard X-ray wavelengths, the magnetic contribution to electronic scattering is negligible, while the electric contribution is far from any electronic resonances. We can therefore describe the media as linear dielectrics, given as a spatially varying refractive index $n(z)$. These refractive indices are well studied, and highly accurate estimations have been implemented in software libraries such as 'xraylib' [85].

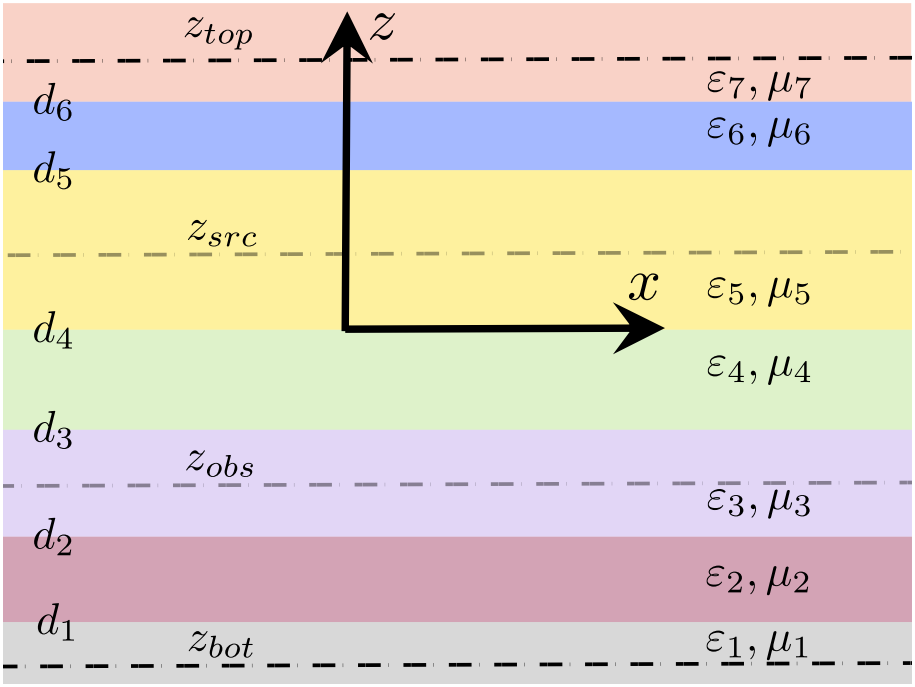

Figure 4.1: Geometry of a multi-layer slab waveguide, used to evaluate the Green's function. Each layer l has its own relative permittivity and permeability ε_l, μ_l. The upper interface of layer l is labelled d_l. In dashed lines we have highlighted four particular z coordinates of importance: z_{src}, the source position, z_{obs}, the observation position (i.e. where the scattered field is being evaluated), and z_{top}, z_{bot}, which arbitrary reference positions above and below all sources and interfaces, respectively. z_{top} and z_{bot} are used for setting the normalization of the fields used in computing the Green's function.

As the layers are translationally symmetric in the x, y directions, we have an overall cylindrical symmetry. We can therefore express the dyadic Green's function as

$$\overleftrightarrow{G}(\vec{r}, \vec{r'}, \omega) = \int \frac{\mathrm{d}^2 q}{(2\pi)^2} e^{i\vec{q}\cdot(\vec{\rho}-\vec{\rho}')} \overleftrightarrow{G}(\vec{q}, z, z', \omega), \tag{4.1}$$

where we distinguish the real space and $\vec{q}$ space Green's function by their arguments, $\vec{\rho}$ is the projection of $\vec{r}$ to the x, y plane, and $\vec{q}$ a wave-vector for this plane. In cylindrical coordinates, we can express the planar wave-vector as

$$\vec{q} = q(\cos(\phi_q)\hat{x} + \sin(\phi_q)\hat{y}), \tag{4.2}$$

and due to cylindrical symmetry, we can express the $\vec{q}$ space Green's function for arbitrary ϕ_q in terms of rotation matrices and the solution for $\phi_q = 0$,

$$\overleftrightarrow{G}(q, \phi_q, z, z', \omega) = U(\phi_q) \overleftrightarrow{G}(q, \phi_q = 0, z, z', \omega) U(\phi_q)^\top, \tag{4.3}$$

where $U(\phi_q)$ is a rotation matrix in the q_x, q_y plane. As such, the problem can be solved as two-dimensional, which we will do so in the following section.

4.1.1 Transfer matrix derivation

In this section, we will give a derivation of the multi-layered Green's function in terms of transfer matrices, following largely Johansson [81] as well as Hanson and Yakovlev [83].

The Fourier transformed Green's function can be separated according to the polarization of the scattered plane waves being considered, s and p. These correspond to transverse electric (TE) and transverse magnetic (TM) fields respectively.

Our geometry is such that we consider the fields propagating along x with transverse wave-vector q, with the layer stacked along the z axis, Figure 4.1. The TE field therefore has electric field E polarized along $\hat{y}$, while the TM field has magnetic field H polarized along $\hat{y}$. As we will be considering a particular transverse wave-vector q, and single frequency ω, we will omit their notation in the function arguments for the rest of this section.

The TE and TM fields obey the equations of motion [83]

$$(\partial_z^2 + n(z)^2k^2 - q^2)E_y = i\omega\mu_0 j_{e,y} - \partial_x j_{m,z} + \partial_z j_{m,x} \tag{4.4}$$

$$(\varepsilon\partial_z\varepsilon^{-1}\partial_z + n(z)^2k^2 - q^2)H_y = i\omega\epsilon_0\varepsilon j_{m,y} + \partial_x j_{e,z} - \varepsilon\partial_z\varepsilon^{-1} j_{e,x}, \tag{4.5}$$

where we note that we have set $\mu = 1$, as the magnetic scattering of the layers is negligible. The refractive index is therefore given by $n(z)^2 = \varepsilon(z)$ in this regime.

We can therefore separately solve for the scalar Green's function $\mathcal{G}_{TE}$, $\mathcal{G}_{TM}$ of (4.4) and (4.5) respectively, and use (3.36) to obtain the full dyadic Green's function,

$$\overleftrightarrow{G}(q, z, z', \omega) = \hat{y} \otimes \hat{y}\mathcal{G}_{TE} + \frac{1}{\varepsilon(z)\varepsilon(z')k^2}(\hat{y} \times \nabla \otimes \nabla' \times \hat{y})\,\mathcal{G}_{TM}, \tag{4.6}$$

where we have ignored the delta contribution in (4.5), as it can be absorbed into the depolarizing dyadic, which we argued in Section 3.1 will only contribute physically via small shifts of the single particle frequencies and decay rates of resonant nuclei placed in the waveguide.

In particular, if we consider as input

$$\vec{j}_e = \hat{y}\frac{1}{i\omega\mu_0}\delta(z - z'), \tag{4.7}$$

$$\vec{j}_m = \hat{y}\frac{1}{i\omega\epsilon_0}\delta(z - z'), \tag{4.8}$$

we can see that they will drive only the TE and TM fields respectively, and the resulting solutions of E_y, H_y will give the corresponding Green's functions by their definitions, (3.31), (3.32).

Transfer matrices

The general solution to (4.4) and (4.5) can be given in terms of a superposition of upward and downward propagating waves,

$$E_y(z) = A^s(z) + B^s(z), H_y(z) = A^p(z) + B^p(z), \tag{4.9}$$

where A is the upward and B the downward propagating solution respectively. We first consider E_y, H_y within the lth layer. Within a layer, ε, n are constant, and we

will denote them as ε_l, n_l. The homogeneous solutions to (4.4), (4.5) are then given within layer l as

$$E_l(z) = A_l^s(d_l)e^{ip_l(z-d_l)} + B_l^s(d_l)e^{-ip_l(z-d_l)}, \tag{4.10}$$
$$H_l(z) = A_l^p(d_l)e^{ip_l(z-d_l)} + B_l^p(d_l)e^{-ip_l(z-d_l)}, \tag{4.11}$$
$$p_l^2 + q^2 = n_l^2 k^2, \tag{4.12}$$

where E_l, H_l denote the field evaluated within the layer, and d_l is the coordinate of the top of the lth layer.

We can represent this via a vector of the two components,

$$E_l(z) = \begin{pmatrix}1 & 1\end{pmatrix} \cdot \vec{\mathscr{E}}(z), \tag{4.13}$$
$$\vec{\mathscr{E}}(z) \equiv \begin{pmatrix}A_l^s(z)\\ B_l^s(z)\end{pmatrix}, \tag{4.14}$$

and similarly

$$H_l(z) = \begin{pmatrix}1 & 1\end{pmatrix} \cdot \vec{\mathscr{H}}(z), \tag{4.15}$$
$$\vec{\mathscr{H}}(z) \equiv \begin{pmatrix}A_l^p(z)\\ B_l^p(z)\end{pmatrix}. \tag{4.16}$$

Within a layer, we can see that propagation from position z', z within the layer is given by the matrix

$$\vec{\mathscr{E}}_l(z) = S_l(z, z')\vec{\mathscr{E}}_l(z') \tag{4.17}$$
$$\vec{\mathscr{H}}_l(z) = S_l(z, z')\vec{\mathscr{H}}_l(z') \tag{4.18}$$
$$S_l(z, z') = \begin{pmatrix}e^{ip_l(z-z')} & 0\\ 0 & e^{-ip_l(z-z')}\end{pmatrix}, \tag{4.19}$$

which we can see is the same for both TE and TM fields. On the other hand, to relate propagation across a layer boundary, we must make use of the respective boundary conditions of (4.4) and (4.5), which we will now show give the Fresnel matrices for s and p polarizations respectively.

Fresnel matrices

We now will consider the transfer matrix for the boundary between layers l and n. These are found from the boundary conditions that both derivatives in (4.5), (4.5) should have continuous arguments.

The boundary condition for TE waves from (4.4) is that E_y and $\partial_z E_y$ must be continuous at a layer boundary. This gives

$$A_l^s + B_l^s = A_n^s + B_n^s, \tag{4.20}$$
$$ip_l A_l^s - ip_l B_l^s = ip_n A_n^s - ip_n B_n^s, \tag{4.21}$$

where we are implicitly evaluating A, B at the layer boundary. In matrix notation, we have

$$\begin{pmatrix}1 & 1\\ ip_l & -ip_l\end{pmatrix}\vec{\mathscr{E}}_l = \begin{pmatrix}1 & 1\\ ip_n & -ip_n\end{pmatrix}\vec{\mathscr{E}}_n. \tag{4.22}$$

This can be rearranged to give

$$\vec{\mathscr{E}}_l = T^s_{ln}\vec{\mathscr{E}}_n, \tag{4.23}$$

$$T^s_{ln} = \frac{1}{2p_l}\begin{pmatrix} p_l + p_n & p_l - p_n \\ p_l - p_n & p_l + p_n \end{pmatrix}, \tag{4.24}$$

which is the matrix of Fresnel coefficients for s polarization as expected.

For TM waves, (4.5) gives the boundary condition that H_y, and $\varepsilon^{-1}\partial_z H_y$ must be continuous at the layer boundary. This gives

$$A^p_l + B^p_l = A^p_n + B^p_n, \tag{4.25}$$

$$i\frac{p_l}{\varepsilon_l}A^p_l - i\frac{p_l}{\varepsilon_l}B^p_l = i\frac{p_l}{\varepsilon_n}A^p_n - i\frac{p_n}{\varepsilon_n}B^p_n. \tag{4.26}$$

In matrix form, we then have,

$$\begin{pmatrix} 1 & 1 \\ i\frac{p_l}{\varepsilon_l} & -i\frac{p_l}{\varepsilon_l} \end{pmatrix}\vec{\mathscr{H}}_l = \begin{pmatrix} 1 & 1 \\ i\frac{p_n}{\varepsilon_n} & -i\frac{p_n}{\varepsilon_n} \end{pmatrix}\vec{\mathscr{H}}_n. \tag{4.27}$$

This can be rearranged to give

$$\vec{\mathscr{H}}_l = T^p_{ln}\vec{\mathscr{H}}_n, \tag{4.28}$$

$$T^p_{ln} = \frac{1}{2p_l\varepsilon_n}\begin{pmatrix} p_l\varepsilon_n + p_n\varepsilon_l & p_l\varepsilon_n - p_n\varepsilon_l \\ p_l\varepsilon_n - p_n\varepsilon_l & p_l\varepsilon_n + p_n\varepsilon_l \end{pmatrix}, \tag{4.29}$$

which is the matrix of Fresnel coefficients for p polarization as expected. We note the difference in expressions compared with Johansson [81] arises from the fact that we have considered the H field, as opposed to the E field for the TM mode.

Full transfer matrix

Combining the S and T matrices, we can define the full transfer matrix W, that relates the field components at arbitrary positions z to arbitrary positions z', including in different layers. Let l be the layer index of the observation position z, n the layer of the source position z', and d_l the coordinates of the upper interface of the lth layer (Figure 4.1). We then have

$$\mathscr{E}_l(z) = W^{s,+}(z, z')\mathscr{E}_n(z'), \tag{4.30}$$

$$W^{s,+}(z, z') = S_l(z, d_{l-1})T^s_{l,l-1}S_{l-1}(d_{l-1}, d_{l-2})\ldots T^s_{n+1,n}S_n(d_n, z'), \tag{4.31}$$

for $z > z'$, and

$$\mathscr{E}_l(z) = W^{s,-}(z, z')\mathscr{E}_n(z'), \tag{4.32}$$

$$W^{s,-}(z, z') = \left[W^{s,+}(z', z)\right]^{-1}, \tag{4.33}$$

for $z < z'$. Analogous expressions give $W^{p,\pm}$ for the TM field.

Now that we have determined the propagation of the field through the layers, we must impose appropriate boundary conditions. The scattered field for $z > z'$ should be outgoing in the top layer. This is imposed by setting

$$B^s(z_{top}) = B^p(z_{top}) = 0, \tag{4.34}$$

$$A^s(z_{top}) = A^p(z_{top}) = 1, \tag{4.35}$$

where z_{top} is an arbitrary position within the top layer, above z,z'. Note that at this stage, the normalization of the fields is arbitrary, so we have set them to unit amplitude in the outgoing layer for convenience. Denoting this field solution as E_+, H_+, we have [81]

$$E_+(z) = \begin{pmatrix}1 & 1\end{pmatrix} W^{s,-}(z, z_{top}) \begin{pmatrix}1\\0\end{pmatrix} \tag{4.36}$$

$$= W^{s,-}_{1,1}(z, z_{top}) + W^{s,-}_{2,1}(z, z_{top}),$$

$$H_+(z) = W^{p,-}_{1,1}(z, z_{top}) + W^{p,-}_{2,1}(z, z_{top}), \tag{4.37}$$

where W_{ij} refers to the matrix element i, j. Similarly, we require the scattered field for $z < z'$ to be outgoing in the bottom layer. We therefore set

$$B^s(z_{bot}) = B^p(z_{bot}) = 1, \tag{4.38}$$

$$A^s(z_{bot}) = A^p(z_{bot}) = 0, \tag{4.39}$$

where z_{bot} is an arbitrary reference position in the bottom layer, below z, z'.

Denoting this solution as E_-, H_-, we then have

$$E_-(z) = W^{s,+}_{1,2}(z, z_{bot}) + W^{s,+}_{2,2}(z, z_{bot}), \tag{4.40}$$

$$H_-(z) = W^{p,+}_{1,2}(z, z_{bot}) + W^{p,+}_{2,2}(z, z_{bot}). \tag{4.41}$$

Green's functions

Finally, we must determine the normalization of the solution. The general outgoing solution for E_y is given by

$$E_y(z) = \alpha E_+(z)\Theta(z - z') + \beta E_-(z)\Theta(z' - z), \tag{4.42}$$

where Θ is the Heaviside step function, and α, β are some yet to be determined coefficients. As the source is a delta distribution, we require only continuity of the field, but not its derivative at $z = z'$. This requires

$$\alpha E_+(z') = \beta E_-(z'). \tag{4.43}$$

We can therefore write

$$E_y(z) = \frac{E_+(z)E_-(z')\Theta(z - z') + E_+(z')E_-(z)\Theta(z' - z)}{D^s}, \tag{4.44}$$

for a single yet to be determined coefficient D^s.

A similar argument shows

$$H_y(z) = \frac{H_+(z)H_-(z')\Theta(z - z') + H_+(z')H_-(z)\Theta(z' - z)}{D^p}. \tag{4.45}$$

The second boundary condition is obtained by combining our source equations, (4.7), (4.8) with the TE, TM equations, (4.4), (4.5) give

$$(\partial_z^2 + \varepsilon k^2 - q^2)E_y(z) = \delta(z - z'), \tag{4.46}$$

$$(\partial_z \varepsilon^{-1} \partial_z H_y(z) + k^2 - q^2)H_y = \delta(z - z'). \tag{4.47}$$

Integrating these over an infinitesimal interval $[z'-dz, z'+dz]$, and taking the limit $\delta \to 0$ gives

$$\lim_{dz\to 0} \partial_z E_y(z'+dz) - \partial_z E_y(z'-dz) = 1, \tag{4.48}$$

$$\lim_{dz\to 0} \varepsilon(z'+dz)^{-1}\partial_z H_y(z'+dz) - \varepsilon(z'-dz)^{-1}\partial_z H_y(z'-dz) = 1. \tag{4.49}$$

Using (4.44), (4.45), these evaluate to

$$\partial_z E_+(z')E_-(z') - E_+(z')\partial_z E_-(z') = D^s, \tag{4.50}$$

$$\frac{1}{\varepsilon(z')}\left(\partial_z H_+(z')H_-(z') - H_+(z')\partial_z H_-(z')\right) = D^p, \tag{4.51}$$

i.e. the denominators are proportional to the Wronskian of the solutions. In particular, Vassallo shows [86] that the denominators are constant, and evaluate to

$$D^s = -2ip_+T^s_+, \tag{4.52}$$

$$D^p = -\frac{2ip_+}{\varepsilon_+}T^\sigma_+, \tag{4.53}$$

$$T^\sigma_+ = W^{\sigma,+}_{12}(z_{top}, z_{bot}), \tag{4.54}$$

where p_+ is the z wave-vector in the top layer, ε_+ the permittivity, and T^σ_+ the transmission coefficients for propagating σ polarized light upward from the bottom layer to the top. We finally have

$$\mathcal{G}_{TE}(z,z') = \frac{E_+(z)E_-(z')\Theta(z-z') + E_+(z')E_-(z)\Theta(z'-z)}{-2ip_+T^s_+}, \tag{4.55}$$

$$\mathcal{G}_{TM}(z,z') = \frac{H_+(z)H_-(z')\Theta(z-z') + H_+(z')H_-(z)\Theta(z'-z)}{-2ip_+T^p_+/\varepsilon_+}. \tag{4.56}$$

To obtain the dyadic Green's function, we can use (3.36), to obtain

$$\overleftrightarrow{G}(z,z') = \hat{y}\otimes\hat{y}\mathcal{G}_{TE}(z,z') + \frac{1}{\varepsilon(z)\varepsilon(z')k^2}\left(\hat{y}\times\bar{\nabla}\otimes\bar{\nabla}'\times\hat{y}\right)\mathcal{G}_{TM}(z,z'), \tag{4.57}$$

where we have defined

$$\bar{\nabla} = iq\hat{x} + \partial_z\hat{z}, \tag{4.58}$$

$$\bar{\nabla}' = -iq\hat{x} + \partial'_z\hat{z}, \tag{4.59}$$

which give the gradient in the partially Fourier transformed space. We note that the denominator of $\varepsilon(z)\varepsilon(z')k^2$ accounts for the difference in Fresnel matrices between E and H, as we mentioned previously.

Explicitly, let us write $H_+(z)$ in the shorthand

$$H_+(z) = W_1(z) + W_2(z), \tag{4.60}$$

$$W_i(z) = W^{s,-}_{i1}(z, z_{top}). \tag{4.61}$$

We then have

$$\bar{\nabla}H_+(z) = iq(W_1(z)+W_2(z))\hat{x} + ip_l(W_1(z)-W_2(z))\hat{z}, \tag{4.62}$$

where l is the layer containing z. By definition,

$$k_l^{\pm} = q\hat{x} \pm p_l\hat{z} \tag{4.63}$$

is the wave-vector for upward (+) and downward (-) propagating solutions. We can therefore write (4.62) as

$$\begin{aligned}\bar{\nabla}H_+(z) &= iq(W_1(z)+W_2(z))\hat{x} + ip_l(W_1(z)-W_2(z))\hat{z} \\ &= in_lk\left(\hat{k}_l^+W_1(z) + \hat{k}_l^-W_2(z)\right),\end{aligned} \tag{4.64}$$

where we note that

$$q^2 + p_l^2 = n_l^2k^2. \tag{4.65}$$

On the other hand, we note that since $\hat{y}$ is the unit vector for s polarization, it's curl with $\hat{k}_l^{\pm}$ gives the corresponding unit vector for p polarization,

$$\hat{y}\times\hat{k}_l^{\pm} = \hat{p}_l^{\pm} = \frac{\pm p_l\hat{x} + q\hat{z}}{n_lk}. \tag{4.66}$$

We therefore have

$$\frac{1}{\varepsilon(z)k}\hat{y}\times\bar{\nabla}H_+(z) = \frac{i}{n_l}\hat{p}_l^+W_{11}^{p,-}(z) + \frac{i}{n_l}\hat{p}_l^-W_{21}^{p,-}(z). \tag{4.67}$$

For both grazing incidence and front coupling, the z component of the wave-vectors are negligible compared with q. As a result, the Fresnel coefficients of both p and s polarized components are approximately equal, and the p polarization vector is approximately $\hat{z}$. We therefore approximate

$$\overleftrightarrow{G}(q,z,z',\omega) \approx \overleftrightarrow{\mathbb{1}}_{\perp}\mathcal{G}_{TE}(q,z,z',\omega), \tag{4.68}$$

where $\overleftrightarrow{\mathbb{1}}_{\perp} = \hat{y}\otimes\hat{y} + \hat{z}\otimes\hat{z}$.

4.2 Spectral theory and resonances of the Green's function

Maxwell's equations in dielectric media form a Sturm-Liouville system of equations, and as such admit a spectral representation. This is discussed in great detail by Hanson and Yakovlev [83], in particular in Chapter 8. We will first demonstrate how the Fourier integral for the real space Green's function is obtained from the complex structure of $\mathcal{G}_{TE}$, and then proceed to compare with the eigenfunction expansions of Hanson and Yakovlev.

To begin, we consider the real space form of the Green's function,

$$\overleftrightarrow{G}(\vec{\rho}-\vec{\rho}',z,z') = \int\frac{\mathrm{d}^2q}{(2\pi)^2}\overleftrightarrow{G}(\vec{q},z,z')e^{i\vec{q}\cdot(\rho-\vec{\rho}')}, \tag{4.69}$$

where

$$\vec{\rho} = x\hat{x} + y\hat{y}. \tag{4.70}$$

We will consider the case $y = y'$, such that we are left with the effectively two-dimensional Green's function

$$\overleftrightarrow{G}_{2D}(x - x', z, z') = \int \frac{\mathrm{d}q}{2\pi} \overleftrightarrow{\mathbb{1}}_{\perp} \mathcal{G}_{TE}(q, z, z') e^{iq(x-x')}, \tag{4.71}$$

where we have reintroduced the explicit notation of q, but are continuing to suppress the notation of the frequency ω, as we are still considering the Green's function for a particular fixed frequency.

Let us consider for now the case $x > x'$. Then, we may close the q integral contour in upper half of the complex q plane, with the arc portion of the contour vanishing due to the exponential decay of $e^{iq(x-x')}$, Figure 4.2. However, we must take care with the complex structure of $\mathcal{G}_{TE}$ when we choose our contour, as it contains both poles and branch cuts. We will consider these now.

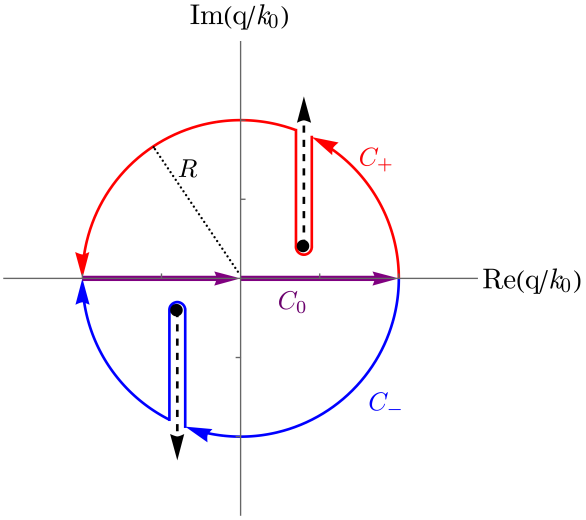

Figure 4.2: Arc contour for evaluating (4.71). The horizontal contribution C_0 (purple) corresponds to the original Fourier integral, while the arc contributions C_+ (red) and C_- (blue) correspond to the closures for $x > x'$ and $x < x'$ respectively, and vanish as $R \to \infty$, due to the exponential decay of $e^{iq(x-x')}$. However, the contour must be deformed to avoid the branch cuts (black dashed lines), which give rises to the radiative modes of the Green's function.

4.2.1 Poles

$\mathcal{G}_{TE}$ has poles whenever

$$E_+(q, z) = E_-(q, z), \tag{4.72}$$

which can be seen by the vanishing of the Wronskian D^s, and hence divergence of (4.55). As E_+ and E_- are equal for a pole, we will label them both as

$$E_\lambda(z) = E_+(q_\lambda, z) = E_-(q_\lambda, z), \tag{4.73}$$

where λ index the poles q_λ. By construction E_+ is purely outgoing in the top layer, and E_- is purely outgoing in the bottom layer. Therefore, at a pole, the mode

function E_λ is purely outgoing, and thus exponentially attenuated, in both capping layers. As such, E_λ normalizable.

The order M_λ of a given pole q_λ, as well as its location can be determined by applying the argument principle [87] to the Wronskian $D^s(q)$: as a holomorphic function $D^s(q)$ has no singularities, therefore evaluating

$$M_\lambda = \frac{1}{2\pi i} \oint_C \mathrm{d}q \, \frac{\partial_q D^s(q)}{D^s(q)}, \tag{4.74}$$

for a closed contour C gives the sum of the multiplicity of each zero within. As the zeroes of D^s are the poles of the Green's function, this therefore gives the sum of the orders of all poles within C.

To obtain the location of all poles within a given contour, one can therefore proceed as follows: start with the initial contour C and subdivide it. Evaluate the zero number of the Wronskian within each subdivision with (4.74). Discard subdivisions without zeros, and proceed with recursive subdivisions on the rest. Subdivision can be halted when the size of the remaining contours reaches a desired tolerance, giving an approximate location and multiplicity for the zeroes. Finally, these can be refined using a root finding algorithm such as Newton's algorithm from this initial starting point. There is no physical restriction on the order of the poles [83], however, as we shall see in Chapter 8, for realistic layer structures we only find simple poles, $M = 1$.

4.2.2 Branch cuts

The second complex structure to consider are the branch cuts of $\mathcal{G}_{TE}$. The transfer matrices, and hence $\mathcal{G}_{TE}$ implicitly depend on the z wave-vector in each layer l,

$$p_l = i\sqrt{q^2 - \varepsilon_l k^2}, \tag{4.75}$$

each of which has a branch cut. Nevertheless, it can be shown that the branch cut for each inner layer is cancelled due to the fact that it appears in both T_{ll-1}, and the denominator of T_{l+1l}, and thus the only physical branch cuts are in the capping layers [86, 88–91].

The only branch cuts which are not cancelled are therefore those that appear only in a single Fresnel matrix, which is the case for the top and bottom layers. Therefore, the branch cuts of $\mathcal{G}_{TE}$ are precisely those of

$$p_{top} = i\sqrt{q^2 - \varepsilon_{top} k^2}, \tag{4.76}$$

$$p_{bot} = i\sqrt{q^2 - \varepsilon_{bot} k^2}. \tag{4.77}$$

For a physical choice of branch cut, we require outward propagating solutions to be exponentially decaying solutions in both capping layers. This is achieved in (4.75) if one makes the standard choice of branch cut for the function $\sqrt{z}$, which is along the negative real z axis. With this choice of cut, $\mathrm{Im}(p_l) \geq 0$ everywhere in the upper half plane as desired. This results in the form seen in Figure 4.3. The cut asymptotically tends toward a vertical line, and thus we must deform our arc to avoid the cut. The integration along this cut corresponds to 'radiative' modes, that is, the continuum of electromagnetic modes that propagate out into the capping

layers. Close to the branch cut, the imaginary part of p_l tends to zero, while the real part changes sign as one crosses the cut, Figure 4.4. As a result, these solutions correspond to radiation modes, fields that propagate unattenuated out into the z direction. q remains complex however, and hence the resulting fields are attenuated in the x direction.

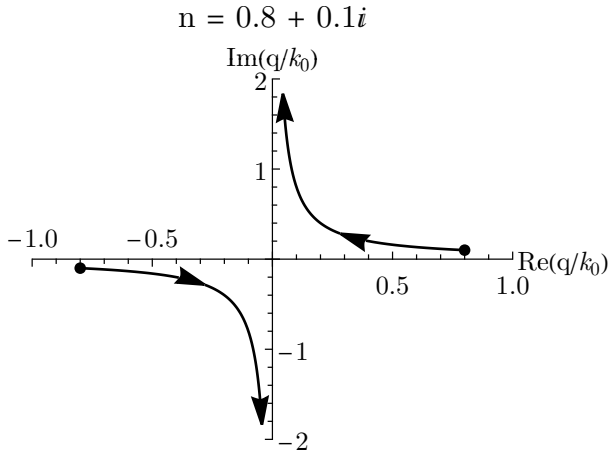

Figure 4.3: Physical choice of branch cut for the z wave-vector $p(q)$as a function of complex q. This choice results in the outward propagating field being exponentially attenuated in the capping layers. The branch cuts initially are approximately horizontal, then tend asymptotically toward a vertical line. Note however that integrals involving e^{iqx} will be oscillatory when performed on a contour around this cut.

For numerical purposes, this branch cut is not ideal, as the detour will have oscillatory behaviour due to the fact that $\mathrm{Re}(q)$ is not constant, and therefore for x fixed, e^{iqx} will have oscillatory contributions, that will grow in frequency as x increases. As the only physical constraint on our branch cut is that it does not cross the real q axis, we are free to choose an arbitrary cut, not just the exponentially damped choice.

For numerical efficiency, the best choice is a vertical line upward from the branch point, Figure 4.5, which can be achieved by rearranging the expressions for p_l to

$$p_l = i\sqrt{-i(kn_l - q)}\sqrt{-i(kn_l + q)}, \tag{4.78}$$

$$n_l = \sqrt{\varepsilon_l}, \tag{4.79}$$

where the square roots have the usual branch cut along the negative real axis. With this choice of branch cut, the real part of q is constant along the detour, and therefore $e^{i\,\mathrm{Re}(q)x}$ can be factored out, leaving a purely exponentially decaying integrand. The integrand will decay exponentially, and far more rapidly as x increases, thus making this choice of branch cut highly numerically efficient.

On the other hand, manipulating the branch cut exposes new poles to the integrand. These poles correspond to 'leaky' modes, which are exponentially growing in the capping layers, rather than attenuated. As such, one may be concerned that their inclusion results in a diverging expression for the Green's function if one considers observation points z in the capping layers.

This is not the case however, as the choice of branch cut does not affect the values of $\mathcal{G}_{1D}$ along the real q axis, which is the only determinant of the final Fourier

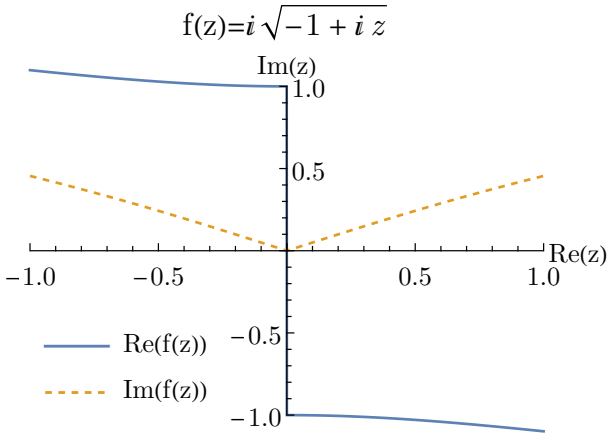

Figure 4.4: Real and imaginary values of $f(z) = i\sqrt{-1+iz}$ as one crosses the branch cut at $z = 0$. One can see that the imaginary part of $f(z)$ vanishes at the cut, while the real part changes sign as z crosses the cut. This demonstrates that as one approaches the branch cut of Figure 4.3, the attenuation/exponential growth in the capping layer vanishes, and thus the solutions correspond to radiating modes.

transformed result. Indeed, it has been shown that even though the leaky modes are individually divergent as $z \to \infty$, their contribution can be divided into two regimes [90]: the evanescent, and diffractive regime. In the evanescent regime, z close to the capping interfaces, the leaky modes interfere constructively, and the overall real space Green's function will grow exponentially. However, for sufficiently large z, one enters the diffractive regime. In this regime, the contribution from the leaky modes interfere destructively and the real space Green's function then decays with a power law attenuation [90].

Real space Green's function

While we have discussed the case $x > x'$ so far, similar arguments can be made for the complex structure $x < x'$, except that one closes the integration contour in the lower half plane of q. Since $\mathcal{G}_{TE}$ is even in q,

$$\mathcal{G}_{TE}(q, z, z') = \mathcal{G}_{TE}(-q, z, z'), \tag{4.80}$$

and thus for each pole q_λ, in the upper half plane, $-q_\lambda$ is also a pole in the lower half plane. As we have seen in Figures 4.3 and 4.5, the same applies to the branch cuts, giving us

$$\overleftrightarrow{G}_{2D}(x - x', z, z') = i\overleftrightarrow{\mathbb{1}}_{\perp} \sum_{\lambda} g_\lambda(z, z') e^{iq_\lambda |x-x'|} + i\overleftrightarrow{\mathbb{1}}_{\perp} g_{rad}(x - x', z, z'), \tag{4.81}$$

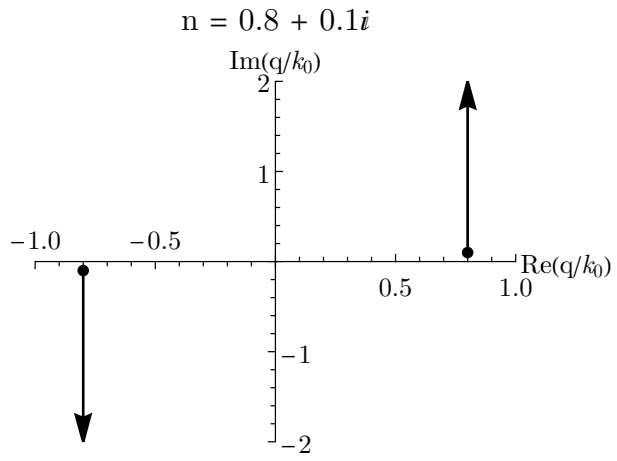

Figure 4.5: Vertical branch cut for the z wave-vector $p(q)$ as a function of complex q. This choice is numerically efficient when computing the real space Green's function, at the expense of uncovering poles corresponding to 'leaky' modes, which are exponentially divergent in the capping layers.

where $g_\lambda(z, z')$ is the residue of $G_{2D}(q, z, z')$ at the pole q_λ, and

$$g_{rad}(x - x', z, z') = g_{top}(x - x, z, z') + g_{bot}(x - x, z, z') \tag{4.82}$$

$$g_{top}(x - x', z, z') = e^{in_{top}k_0|x-x'|} \tag{4.83}$$
$$\times \lim_{\epsilon\to 0} \int_0^\infty \frac{\mathrm{d}s}{2\pi} e^{-s|x-x'|} \left(\mathcal{G}_{TE}(n_{top} - \epsilon + is) - \mathcal{G}_{TE}(n_{top} + \epsilon + is)\right)$$

$$g_{bot}(x - x', z, z') = e^{in_{bot}k|x-x'|} \tag{4.84}$$
$$\times \lim_{\epsilon\to 0} \int_0^\infty \frac{\mathrm{d}s}{2\pi} e^{-s|x-x'|} \left(\mathcal{G}_{TE}(n_{bot}k - \epsilon + is) - \mathcal{G}_{TE}(n_{bot}k + \epsilon + is)\right)$$

are the branch cut contributions. Physically, g_{top} and g_{bot} correspond to the continuum of modes that are outward radiating in the top and bottom layers respectively.

Note that in the case $n_{top} = n_{bot}$, the branch cuts become degenerate, and there is an ambiguity about the separation of radiation modes into top and bottom contributions [86, 90]. If the waveguide is symmetric, one can instead separate the radiation modes into odd and even solutions [86, 90], but the general situation is more challenging to analyse. One potential solution is to introduce a small increase in loss ϵ in one of the layers, such that the two branch cuts are infinitesimally separated [86]. One can then evaluate the two branch cuts separately, and consider the limit as ϵ approaches zero.

4.2.3 Spectral theory

We are now ready to identify the components of (4.81) with the results of spectral theory, which are explained in detail in Chapter 8 of Hanson and Yakovlev [83], as well as Vassallo [86].

Hanson and Yakovlev identify the spectral solution of (4.4) and (4.5) with two classes of modes: modes that are proper in z forming a discrete set, which we index

with λ, and modes that are improper in z, that form a continuum, that we index with ν. The expansion in terms of these modes is then given by [83, p. 8.154][86, eq. 17]

$$\mathcal{G}_{TE}(q,z,z') = \sum_{\lambda} \frac{u_\lambda(z)u_\lambda(z')}{2iq_\lambda(q-q_\lambda)} + \sum_{\sigma=\pm}\int_0^\infty \frac{\mathrm{d}\nu}{2\pi}\frac{w_\sigma(\nu,z)w_\sigma(\nu,z)}{4i\kappa(\nu,z)W_{11}^{s,-}(\kappa(\nu,z_{top}),z_{top},z_{top})}\delta(q-\kappa(\nu,z)) \quad (4.85)$$

where $\kappa = \sqrt{n(z)^2k^2-\nu^2}$, and $w_\pm$ refers to improper modes which radiate into the top (+) and bottom (-) cladding. By inspection, we can immediately identify this spectral expansion with our expansion (4.81) in terms of the poles and branch cut respectively. However, for this expansion to converge, one requires that the modes are normalizable, in the sense that there exists an inner product such that

$$\langle u_\lambda, u_{\lambda'})\rangle = \delta_{\lambda\lambda'}, \quad (4.86)$$
$$\langle w_+(\nu,\cdot), w_+(\nu',\cdot)\rangle = \delta(\nu-\nu'), \quad (4.87)$$
$$\langle w_-(\nu,\cdot), w_-(\nu',\cdot)\rangle = \delta(\nu-\nu'), \quad (4.88)$$
$$\langle w_+(\nu,\cdot), w_-(\nu',\cdot)\rangle = 0, \quad (4.89)$$
$$\langle u_\lambda, w_+(\nu,\cdot)\rangle = 0, \quad (4.90)$$
$$\langle u_\lambda, w_-(\nu,\cdot)\rangle = 0, \quad (4.91)$$

where the dot in the notation for $w_+(\nu,\cdot)$ denotes that it is the z argument that is being integrated over by the inner product.

If such an inner product exists, then the resolution of the identity is given by

$$\delta(z-z') = \sum_\lambda u_\lambda(z)u_\lambda(z') + \int_0^\infty \mathrm{d}\nu\, w_+(\nu,z)w_+(\nu,z') + \int_0^\infty \mathrm{d}\nu\, w_-(\nu,z)w_-(\nu,z'). \quad (4.92)$$

Now that we have introduced the modes of the waveguide, let us proceed to analyse the proper and improper modes in detail.

Proper modes

The proper modes form a countable set, and are normalizable with the inner product

$$\langle u_{\lambda'}, u_\lambda\rangle_{TE} = \int_{-\infty}^\infty \mathrm{d}z\, u_\lambda(z)u_{\lambda'}(z) = \delta_{\lambda\lambda'} \quad (4.93)$$

for TE modes [83, 86], and

$$\langle u_{\lambda'}, u_\lambda\rangle_{TM} = \int_{-\infty}^\infty \frac{\mathrm{d}z}{\varepsilon(z)}u_\lambda(z)u_{\lambda'}(z) = \delta_{\lambda\lambda'} \quad (4.94)$$

for TM modes [83, 86]. Note that these are *not* the L^2 inner products: one does not take the complex conjugate of $u_{\lambda'}$. This is due to the fact that for lossy dielectrics, $\overleftrightarrow{\mathcal{G}}_{TE}$ is the kernel of a symmetric integral operator, but not Hermitian [83].

These inner products are convergent for lossy capping layers, and the "physical" choice of branch cut, as all poles correspond to exponentially decaying solutions. On the other hand, for capping layers without loss, e.g. air, or choosing a branch cut that exposes leaky modes, the outgoing solutions are not normalizable.

However, it has been shown that one may modify the inner product in such a way that all proper modes are orthonormal [92–94], even for leaky modes. Specifically, we note that in the outer capping layers, the modes are of the form

$$u_\lambda(z) \propto \begin{cases} e^{ip_{+,\lambda}z}, & z > z_{top}, \\ e^{-ip_{-,\lambda}z}, & z < z_{bot}, \end{cases} \tag{4.95}$$

where $p_{+,\lambda}$, $p_{-,\lambda}$ are the z wave-vectors for q_λ in the top and bottom capping layers respectively. One then finds that the integral over the top layer in (4.93) gives, for an attenuated, guided mode,

$$\begin{aligned} \int_{z_{top}}^{\infty} \mathrm{d}z\, u_\lambda(z) u_{\lambda'}(z) &= u_\lambda(z_{top}) u_{\lambda'}(z_{top}) \int_{z_{top}}^{\infty} \mathrm{d}z\, e^{i(p_{+,\lambda}+p_{+,\lambda'})(z-z_{top})} \\ &= -\frac{u_\lambda(z_{top}) u_{\lambda'}(z_{top})}{i(p_{+,\lambda}+p_{+,\lambda'})}, \end{aligned} \tag{4.96}$$

where we have used continuity to write

$$u_\lambda(z) = u_\lambda(z_{top}) e^{ip_{+,\lambda}(z-z_{top})}, \quad z > z_{top}. \tag{4.97}$$

We also have

$$\begin{aligned} \int_{-\infty}^{z_{bot}} \mathrm{d}z\, u_\lambda(z) u_{\lambda'}(z) &= u_\lambda(z_{bot}) u_{\lambda'}(z_{bot}) \int_{-\infty}^{z_{bot}} \mathrm{d}z\, e^{-i(p_{-,\lambda}+p_{-,\lambda'})(z-z_{bot})} \\ &= -\frac{u_\lambda(z_{bot}) u_{\lambda'}(z_{bot})}{i(p_{-,\lambda}+p_{-,\lambda'})}. \end{aligned} \tag{4.98}$$

One can therefore rewrite (4.93) as

$$\begin{aligned} \langle u_{\lambda'}, u_\lambda \rangle_{TE} &= \int_{z_{bot}}^{z_{top}} \mathrm{d}z\, u_\lambda(z) u_{\lambda'}(z) - \frac{u_\lambda(z_{top}) u_{\lambda'}(z_{top})}{i(p_{+,\lambda}+p_{+,\lambda'})} - \frac{u_\lambda(z_{bot}) u_{\lambda'}(z_{bot})}{i(p_{-,\lambda}+p_{-,\lambda'})} \\ &= \delta_{\lambda\lambda'}. \end{aligned} \tag{4.99}$$

Unlike (4.93), this form is finite for *all* proper modes, even leaky modes [92–94].

As the proper modes correspond to the pole contributions of (4.81), we can see that we have

$$u_\lambda(z) = \frac{E_\lambda(z)}{\sqrt{\langle E_\lambda, E_\lambda \rangle}}. \tag{4.100}$$

Now that we have described the proper modes, let us focus on the improper modes, which correspond to modes that radiate out of the core of the waveguide, into the cladding.

Improper modes

The improper mode contribution in (4.85) can immediately be identified with the integral over the branch cut contributions, for the physical choice of branch cut [86]. However, as we have deformed the branch cuts to the vertical cut, Figure 4.5, this

expression will no longer hold. In particular, with the vertical choice of branch cuts, $\mathrm{Im}(p_\pm)$ is no longer zero along the cut, and the radiation modes are exponentially divergent in the capping layers. As such, it is not clear if one can define an inner product and hence proper spectral expansion in the sense of (4.86) through (4.91). Nevertheless, for our purposes, this is not necessary. The extent of the radiative modes is short, as they are attenuated with at least the attenuation length of the corresponding cladding material. Therefore, for evaluating the input fields, we can neglect their contribution away from the front and back interfaces. In addition, in Appendix A, we show that over the bandwidth of the fields that we will consider, the remaining branch cut contributions can be approximated as a constant background plus a series of poles, and the resulting coupling to the resonant nuclei is negligible in practice. As such, we can safely ignore the radiative modes, as their dominant contribution has already been extracted as the leaky modes.

We can therefore model the Green's function as

$$\mathcal{G}_{TE}(q, z, z') \approx \sum_\lambda \frac{u_\lambda(z)u_\lambda(z')}{2iq_\lambda(q - q_\lambda)}, \tag{4.101}$$

where λ indexes the poles of the vertical choice of branch cut, and the mode functions are orthonormal with the inner product (4.99).

4.3 Figures of merit

In this section, we will consider three important figures of merit for the interaction of a dipole with a waveguide mode: the Q factor, the mode volume and the scattering cross-section. The Q factor is defined as the ratio of the energy stored to the energy dissipated per oscillation period of the mode. The mode volume measures the spatial confinement of the mode, and is obtainable from the normalization of the mode functions for finite resonators. However, for unbounded resonators, such as our multi-layer planar waveguides, the definition of mode volume is more ambiguous. Finally, the scattering cross-section gives the ratio of scattered power to the incident intensity for a photon interacting with an atomic/nuclear transition dipole.

4.3.1 Q factor

Given an oscillator with a Lorentzian response function,

$$f(\omega) \propto \frac{1}{\omega - \omega_\lambda + i\frac{\Gamma_\lambda}{2}}, \tag{4.102}$$

the Q factor can be shown to be equal to

$$Q_\lambda = \frac{\omega_\lambda}{\Gamma_\lambda}. \tag{4.103}$$

If there exists a proper eigenmode, with wave-vector q_λ, the frequency response of a proper mode is then the superposition of two Lorentzians, one giving the positive frequency and the other the negative frequency response:

$$\frac{1}{\omega^2/c^2 - q_\lambda^2} = \frac{c}{2q_\lambda}\left(\frac{1}{\omega - \omega_\lambda} - \frac{1}{\omega + \omega_\lambda}\right), \tag{4.104}$$

where $\omega_\lambda = q_\lambda c$. Comparing this to (4.102) and (4.103) we see that

$$Q_\lambda = \left|\frac{\mathrm{Re}\{\omega_\lambda\}}{2\,\mathrm{Im}\{\omega_\lambda\}}\right| = \left|\frac{\mathrm{Re}\{q_\lambda\}}{2\,\mathrm{Im}\{q_\lambda\}}\right|. \tag{4.105}$$

However, for improper modes, the modes are infinite in extent, and both the power stored and power dissipated are infinite. The frequency response will be of the form

$$f(\omega) \propto \int \mathrm{d}\nu\, \frac{w(\nu)}{\omega^2 - \nu^2} \tag{4.106}$$

for some $w(\nu)$ that gives the weighting of the continuum of proper modes that make up the improper mode. In particular, for a guided mode of our slab waveguide, we have

$$f(\omega) = \int \frac{\mathrm{d}q}{2\pi} \frac{\mathrm{Re}\{g_\lambda(\omega)\}q_\lambda(\omega) + i\,\mathrm{Im}\{g_\lambda(\omega)\}q}{2(q^2 - q_\lambda(\omega)^2)}, \tag{4.107}$$

which is a divergent quantity. Therefore, there is no sensible Q factor for a coupling directly to a guided mode.

On the other hand, at grazing incidence, for a sufficiently well collimated beam, we pick out a particular angle of incidence θ for all frequency components, giving

$$f(\theta, \omega) = \frac{g_\lambda(\omega)}{\omega\cos\theta/c - q_\lambda(\omega)} - \frac{g_\lambda(\omega)^*}{\omega\cos\theta/c + q_\lambda(\omega)}. \tag{4.108}$$

In particular, if the dispersion of g_λ, q_λ is sufficiently small compared with $1/c$, we can neglect dispersion, and obtain a Lorentzian frequency response. The Q factor in this case is given by

$$Q(\theta) = \left|\frac{\mathrm{Re}\{q_\lambda\}}{2\,\mathrm{Im}\{q_\lambda\}}\right| \tag{4.109}$$

as before, where we note that the $\cos\theta$ factor appears in both the numerator and denominator, and therefore cancels. As this is thus independent of the angle of incidence, we can therefore consider it to be an intrinsic Q factor of the mode.

Mode volume

For the mode volume, Kristensen *et al.* [92] have derived expressions in terms of an outward radiating normalization condition for the resonant modes. However, we desire an expression in terms of the dyadic Green's function, and will therefore derive this now.

Our starting point is the Purcell factor. In his 1946 note [95], Purcell considered the maximal possible decay rate of an atom embedded in a cavity, compared with the free space rate. He demonstrated that this was given by the eponymous Purcell factor,

$$\frac{\Gamma_\lambda}{\Gamma_0} = \frac{6\pi Q_\lambda}{V_\lambda k_0^3}, \tag{4.110}$$

where Γ_λ is the decay rate of a two-level atom placed at the maximum of the mode, Γ_0 the free space decay rate, k_0 the wave-number of the transition, and Q_λ, V_λ the Q factor and mode volume respectively.

To link this to the Green's function, we can use the spontaneous decay rate of an electric dipole transition in terms of the Green's function, given by [78, eq. 8.115]

$$\Gamma = \frac{2\wp^2}{3\hbar\epsilon_0}\left|\mathrm{tr}\left[\mathrm{Im}\{\overleftrightarrow{G}_{ee}(\vec{r}_0, \vec{r}_0, \omega_0)\}\right]\right|, \tag{4.111}$$

where $\vec{r}_0$ is the atomic position, $\wp$ the magnitude of the dipole matrix element, and the trace is with respect to the polarization indices of the dyadic Green's function. Note that we are considering general Green's functions here, not just free space.

In free space, the trace of the Green's function gives [78, eq. 8.119]

$$\left|\mathrm{tr}\left[\mathrm{Im}\{\overleftrightarrow{G}_{ee}(\vec{r}_0,\vec{r}_0,\omega_0)\}\right]\right| = \frac{k_0^3}{2\pi}. \tag{4.112}$$

Defining

$$\overleftrightarrow{G}_{ee,\lambda}(\vec{r},\vec{r}',\omega) = -k_0^2\frac{\vec{u}_\lambda(\vec{r})\otimes\vec{u}_\lambda(\vec{r}')}{\omega^2/c^2-q_\lambda^2}, \tag{4.113}$$

we see that

$$\frac{\Gamma_\lambda}{\Gamma_0} = \frac{2\pi}{k_0^3}\left|\mathrm{tr}\left[\mathrm{Im}\{\overleftrightarrow{G}_{ee,\lambda}(\vec{r}_0,\vec{r}_0,\omega_0)\}\right]\right|. \tag{4.114}$$

Combining (4.105), (4.110) and (4.114) gives us the mode volume in terms of the Green's function at the mode maximum,

$$V_\lambda = \left|\frac{\mathrm{Re}\{q_\lambda\}}{2\,\mathrm{Im}\{q_\lambda\}}\right|\cdot\left|\frac{1}{3}\,\mathrm{tr}\left[\mathrm{Im}\{\overleftrightarrow{G}_{ee,\lambda}(\vec{r}_c,\vec{r}_c,\omega_0)\}\right]\right|^{-1}, \tag{4.115}$$

where $\vec{r}_c$ is the position at the mode maximum. Rearranging this gives the following identity:

$$\left|\frac{1}{3}\,\mathrm{tr}\left[\mathrm{Im}\{\overleftrightarrow{G}_{ee,\lambda}(\vec{r}_c,\vec{r}_c,\omega_0)\}\right]\right| = \frac{Q_\lambda}{V_\lambda}. \tag{4.116}$$

For an unconfined mode, such as a Fourier mode of free space, the mode volume is formally divergent, as the mode is unconfined. However, for partially confined modes, such as guided modes of a waveguide, we can nevertheless define a 'mode volume' for the directions that are confined. For example, for a thin-film nanostructure, the guided modes are confined in the z direction, and thus we can define a mode length for this axis.

4.3.2 Scattering cross-section

The scattering cross-section of the photon-atom/nucleus interaction is defined as the ratio of scattered power to incident intensity. The calculation of this is a textbook exercise, and one can show in particular that for a monochromatic driving field the scattered power is given by [60, p. 5.271]

$$P_{sc} = \hbar\omega_0\Gamma\rho_{ee}(t\to\infty), \tag{4.117}$$

where ρ_{ee} is the density matrix element for the excited state population, and $t\to\infty$ denotes the steady state value.

Considering a monochromatic driving field with amplitude E_0 and detuning Δ, the steady state solution of the optical Bloch equations is given by [60, p. 5.273]

$$\rho_{ee}(t\to\infty) = \frac{1}{2}\frac{I/I_{sat}}{1+\Delta^2/\Gamma^2+I/I_{sat}}, \tag{4.118}$$

where the intensity is given by

$$I = \frac{1}{2}\epsilon_0 c E_0^2, \tag{4.119}$$

and the saturation intensity is defined as

$$I_{sat} = \frac{\Gamma^2 I}{2\Omega^2}, \tag{4.120}$$

where

$$\Omega = \frac{\wp E_0}{\hbar} \tag{4.121}$$

is the Rabi frequency of the transition.

On resonance, $\Delta = 0$, and for linear driving $I/I_{sat} \ll 1$, this reduces to

$$\rho_{ee}(t \to \infty) \approx \frac{I}{I_{sat}}, \tag{4.122}$$

thus giving a cross-section of

$$\sigma_0 = \frac{P_{sc}}{I} = \frac{\hbar\omega_0\Gamma}{2I_{sat}}. \tag{4.123}$$

One can show [60, eq. 5.254] that in free space this gives the usual expression of

$$\sigma_0 = \frac{2\pi}{k_0^2}. \tag{4.124}$$

However, we are interested in particular in the *partial* cross-sections, that is to say, the cross-section for scattering from a particular mode. This is done by considering the contribution to the scattered power only from the given mode. This is therefore given by substituting the total decay rate in (4.117) with the partial decay rate for the mode,

$$P_\lambda = \hbar\omega_0\Gamma_\lambda\,\rho_{ee}(t \to \infty). \tag{4.125}$$

The steady state solution and hence saturation intensity remain the same, and we therefore find that the partial cross-section σ_λ is given by

$$\sigma_\lambda = \frac{P_\lambda}{P_{sc}}\sigma_0 = \frac{2\pi}{k_0^2}\cdot\frac{\Gamma_\lambda}{\Gamma}. \tag{4.126}$$

Chapter 5

Quantum model for nucleus-field interaction

In this chapter, we introduce the quantum model to model the nuclei, and their interaction with the magnetic field. We begin by introducing the state transition operators of the nuclei in Section 5.1. Then, in Section 5.2 we give an overview of the magnetic dipole coupling Hamiltonian for the nucleus-field interaction.

The nuclei undergo spontaneous decay both due to electromagnetic radiation, and their interaction with their solid state environment. We therefore discuss these incoherent processes in Section 5.3, and give the Lindblad super-operators that we use to describe them.

Finally, the magnetic field can be decomposed into an overall plane-wave phase factor times a slowly varying envelope, therefore in Section 5.5 we introduce the interaction picture that is used to transform into the slowly varying 'co-rotating' frame of the fields and nuclei.

5.1 Transition operators

For the purposes of evaluating the equations of motion of the nuclei, it is useful to introduce the single particle transition operators,

$$\hat{\Pi}_{ab}^{(i)} = |a\rangle\langle b| \,, \tag{5.1}$$

where the bra–ket notation is implied to only act on the Hilbert space of the ith particle, and a, b label states in this Hilbert space. These transition operators obey the following algebra:

$$[\hat{\Pi}_{ab}^{(i)}, \hat{\Pi}_{cd}^{(j)}] = \delta_{ij}\left(\hat{\Pi}_{ad}^{(i)}\delta_{bc} - \hat{\Pi}_{cb}^{(i)}\delta_{ad}\right), \tag{5.2}$$

$$\hat{\Pi}_{ab}^{(i)}\hat{\Pi}_{bc}^{(i)} = \hat{\Pi}_{ac}^{(i)}, \tag{5.3}$$

$$\sum_a \hat{\Pi}_{aa}^{(i)} = \mathbb{1}. \tag{5.4}$$

We can use this notation to express the basis expansion of the transition dipole operators,

$$\hat{m}^{(i)} = m_0 \sum_{\mu,j} \vec{d}_{\mu j}\hat{\Pi}_{\mu j}^{(i)} + \text{h.c.} = \hat{m}_+^{(i)} + \hat{m}_-^{(i)}, \tag{5.5}$$

where μ indexes excited states, and j indexes ground states.

For the case of a single particle, the expectation value of a transition operator can be easily seen to be equivalent to the density matrix elements,

$$\left\langle \hat{\Pi}_{ab} \right\rangle \equiv \mathrm{tr}\{\hat{\rho}\,\hat{\Pi}_{ab}\} = \rho_{ba}. \tag{5.6}$$

However, for an entangled many-particle state, the density matrix elements are not so straightforward to analytically compute with, whereas correlations of the transition operators can be systematically expanded through the cumulant expansion method, allowing for a hierarchy of equations of motion to be obtained and analysed.

5.2 Magnetic dipole Hamiltonian

The wavelength of the resonant X-rays are substantially larger than the nuclear radius. Therefore, we may use the long wave-length approximation and use a dipole interaction Hamiltonian. The nucleus can interact with the field through either recoil free elastic scattering, or couple with phonons and undergo inelastic scattering. The latter case will be discussed in the following section on incoherent processes. Therefore, we model only the recoil free portion in our Hamiltonian, via the Lamb-Mössbauer factor f_{LM}, the fraction of radiative interaction that occurs through the elastic channel. As f_{LM} describes the overall *transition* fraction, which is proportional to the modulus square of the interaction Hamiltonian elements via Fermi's golden rule, we therefore multiply the Hamiltonian by an overall pre-factor of $\sqrt{f_{LM}}$, giving

$$H_I = \sqrt{f_{LM}} \sum_i \hat{p}_i \cdot \hat{E}(\vec{r}_i) - \sqrt{f_{LM}} \sum_i \hat{m}_i \cdot \hat{B}(\vec{r}_i), \tag{5.7}$$

where $\hat{p}_i$, $\hat{m}_i$ are the electric/magnetic transition dipole operators of the ith nucleus respectively. For commonly used nuclei such as ^{57}Fe, the transitions are electric dipole forbidden, so we may take $\hat{p}_i = 0$.

The matrix elements for the transition dipole operator $\hat{m}$ can be obtained via the Wigner–Eckart theorem [96, eq. B.29],

$$\left\langle I_e, m_e \middle| \hat{m} \middle| I_g, m_g \right\rangle = \sqrt{(2I_e+1)\mathcal{B}(\mathcal{M}1, I_e \to I_g)} \sum_{q=-1}^{1} \hat{e}_q (-1)^{I_e - m_e} \begin{pmatrix} I_e & 1 & I_g \\ -m_e & q & m_g \end{pmatrix}, \tag{5.8}$$

where [96, eq. B.74]

$$\mathcal{B}(\mathcal{M}1, I_e \to I_g) = \frac{1}{2I_e+1} |\left\langle I_e \middle\| \hat{m} \middle\| I_g \right\rangle|^2 \tag{5.9}$$

is the reduced transition probability, in Weisskopf units, and $\hat{e}_q$ are the spherical basis vectors.

More generally, for the qth component of a spherical rank k tensor, arbitrary excited state μ, and arbitrary ground state j, it will be useful to introduce the notation

$$\langle \mu | T^{(k)}_q | j \rangle = \frac{1}{\sqrt{2I_e+1}} \left\langle I_e \middle\| T^{(k)} \middle\| I_g \right\rangle C(kq, \mu \to j), \tag{5.10}$$

where $\langle I_e||T^{(k)}||I_g\rangle$ is the usual reduced matrix element, and

$$C(kq, \mu \to j) = \sqrt{2I_e + 1} \sum_{m_e, m_g} (-1)^{I_e - m_e} \langle \mu | I_e, m_e \rangle \langle I_g, m_g | j \rangle \begin{pmatrix} I_e & 1 & I_g \\ -m_e & q & m_g \end{pmatrix}, \tag{5.11}$$

reducing to the Clebsch-Gordan coefficients when μ, j are angular momentum eigenstates. In general, under hyperfine interactions, the energy eigenstates are not angular momentum eigenstates. However, using the notation of (5.10) and (5.11), we have for a given excited state μ and ground state j,

$$\langle \mu | \hat{m} | j \rangle = m_0 \vec{d}_{\mu j}, \tag{5.12}$$

$$\vec{d}_{\mu j} = \sum_{q=-1}^{1} \hat{e}_q C(kq, \mu \to j) \tag{5.13}$$

$$m_0 = \sqrt{f_{LM} \mathscr{B}(\mathscr{M}1, 3/2 \to 1/2)}, \tag{5.14}$$

generalizing the Wigner–Eckart decomposition. Experimentally measured values for the reduced matrix elements are commonly tabulated. For example, for $\mathscr{M}1$ transitions, the corresponding Weisskopf unit is [96, tab. B1]

$$\mathscr{B}_{sp}(\mathscr{M}1) = 1.790 \mu_N^2, \tag{5.15}$$

where we use $\mu_N = e\hbar(2m_p)^{-1}$ as the nuclear magneton in SI units. For the 14.4 keV transition in ^{57}Fe, the experimentally measured reduced transition probability is [97]

$$\mathscr{B}(\mathscr{M}1, 3/2 \to 1/2) = 0.0078 \mathscr{B}_{sp}(\mathscr{M}1) = 0.013962 \mu_N^2, \tag{5.16}$$

giving an effective magnetic moment of

$$m_0 \approx \sqrt{f_{LM}} 0.118161 \mu_N. \tag{5.17}$$

5.3 Incoherent processes

The nucleus undergoes spontaneous decay from the excited states to the ground states, via incoherent processes. These occur with transitions coupled via various multi-polarities, which we denote with the transition rates

$$\Gamma(\lambda k, I_e \to I_g), \tag{5.18}$$

where $\lambda = \mathscr{E}, \mathscr{M}$ denotes the electric or magnetic character, and k denotes the multipole order.

The rates for transitions between a specific excited state μ and ground state j will of course depend on the magnitude of the multipole moment for these transitions, which can be expressed via the Wigner–Eckart theorem in the form

$$\Gamma(\lambda l, \mu \to j) = \Gamma(\lambda l, I_e \to I_g) \mathscr{R}(\lambda l, \mu \to j), \tag{5.19}$$

where we have defined the rate fractions

$$\mathscr{R}(\lambda l, \mu \to j) = \sum_q |C(lq, \mu \to j)|^2. \tag{5.20}$$

Using the orthogonality of Wigner 3j symbols, one can show that under a sum over the excited eigenstates μ, and ground eigenstates j, and l projection q (see Section C.2),

$$\sum_{\mu,q} |C(lq,\, \mu \to j)|^2 = \frac{2I_e + 1}{2I_g + 1}, \tag{5.21}$$

$$\sum_{j,q} |C(lq,\, \mu \to j)|^2 = 1, \tag{5.22}$$

$$\sum_{\mu,j,q} |C(lq,\, \mu \to j)|^2 = 2I_e + 1, \tag{5.23}$$

and thus summing over ground state decay channels from a given excited state gives

$$\sum_{j} \Gamma(\lambda l,\, \mu \to j) = \Gamma(\lambda l,\, I_e \to I_g), \tag{5.24}$$

as expected. We can therefore model these incoherent processes as proportional to Lindblad super-operators of the form

$$\mathscr{L}_{\lambda l}[\hat{\rho}] = \sum_i \sum_{\mu,j} \mathscr{R}(\lambda l,\, \mu \to j) \left(\hat{\Pi}^{(i)}_{j\mu} \hat{\rho} \hat{\Pi}^{(i)}_{\mu j} - \frac{1}{2} \{ \hat{\rho},\, \hat{\Pi}^{(i)}_{\mu\mu} \} \right), \tag{5.25}$$

$$\mathscr{L}^H_{\lambda l}[\hat{O}] = \sum_i \sum_{\mu,j} \mathscr{R}(\lambda l,\, \mu \to j) \left(\hat{\Pi}^{(i)}_{\mu j} \hat{O} \hat{\Pi}^{(i)}_{j\mu} - \frac{1}{2} \{ \hat{O},\, \hat{\Pi}^{(i)}_{\mu\mu} \} \right), \tag{5.26}$$

where L^H denotes the Heisenberg form, acting on operators rather than density matrices.

The largest decay channel for nuclei is through internal conversion. This is a process where inner shell electrons interact with the nucleus, absorb the energy of the excited state, and are ionized, relaxing the nucleus to the ground state. This is given by

$$L_{IC}[\hat{\rho}] = \sum_{\lambda,l} \Gamma_{IC}(\lambda l,\, I_e \to I_g) \mathscr{L}_{\lambda l}[\hat{\rho}]. \tag{5.27}$$

The internal conversion coefficients are proportional to the product of the transition multipole operator of the nuclei, and the corresponding transition multipole operator of the inner shell electrons. However, estimating the electron multipole operators experimentally is challenging, and in practice these are estimated numerically instead.

However, the total fraction of decay via internal conversion can readily be measured by observing the X-ray spectrum created by the relaxation of the ejected electrons. This is then commonly tabulated as the total internal conversion coefficient α, defined as the ratio of total internal conversion rate to total radiative decay rate,

$$\alpha = \frac{\Gamma_{IC}}{\Gamma_{rad}}. \tag{5.28}$$

In terms of the tabulated total transition decay rate $\Gamma(I_e \to I_g)$, we therefore have

$$\sum_{\lambda,l} \Gamma_{IC}(\lambda l,\, I_e \to I_g) = \Gamma(I_e \to I_g) \frac{\alpha}{1 + \alpha}. \tag{5.29}$$

For radiative decay via gamma emission, the total radiative line-width Γ_{rad} is the combination of the elastic (recoil free) and inelastic (phonon coupled) radiation channels. These have the same multi-polarities, with the dominant contributions being $\mathscr{M}1$ and $\mathscr{E}2$.

The Lamb-Mössbauer factor is defined as the recoil free fraction of decay, thus giving us

$$\Gamma_{elas.} = f_{LM}\Gamma_{rad}, \tag{5.30}$$
$$\Gamma_{inel.} = (1 - f_{LM})\Gamma_{rad} \tag{5.31}$$
$$\Gamma_{rad} = \frac{1}{1+\alpha}\Gamma(I_e \to I_g). \tag{5.32}$$

The radiative decay rates have the dominant multipolarities of $\mathscr{M}1$ and $\mathscr{E}2$, giving the following for the radiative Lindblad terms:

$$L_{rad}[\hat{\rho}] = \Gamma_{rad.}(\mathscr{M}1, I_e \to I_g)\mathscr{L}_{\mathscr{M}1}[\hat{\rho}] + \Gamma_{rad.}(\mathscr{E}2, I_e \to I_g)\mathscr{L}_{\mathscr{E}2}[\hat{\rho}]. \tag{5.33}$$

The ratio of $\mathscr{E}2$ to $\mathscr{M}1$ decay rates is commonly tabulated as the mixing ratio δ,

$$\delta^2 = \frac{\Gamma_{rad.}(\mathscr{E}2, I_e \to I_g)}{\Gamma_{rad.}(\mathscr{M}1, I_e \to I_g)}, \tag{5.34}$$

with the total rate given by (5.32). Thus, we can write

$$L_{rad.}[\hat{\rho}] = \Gamma(I_e \to I_g)\frac{1}{1+\alpha}\left(\frac{1}{1+\delta^2}\mathscr{L}_{\mathscr{M}1}[\hat{\rho}] + \frac{\delta^2}{1+\delta^2}\mathscr{L}_{\mathscr{E}2}[\hat{\rho}]\right). \tag{5.35}$$

The full Lindblad term is therefore given by the sum of (5.27) and (5.35),

$$L[\hat{\rho}] = L_{rad.}[\hat{\rho}] + L_{IC}[\hat{\rho}]. \tag{5.36}$$

5.4 Nuclear Hamiltonian

The nuclear Hamiltonian has the general form

$$H_N = \sum_{\mu}\hbar(\omega_0 + \Delta_\mu)\,|\mu\rangle\langle\mu| + \sum_j \hbar\Delta_j\,|j\rangle\langle j|\,, \tag{5.37}$$

where μ indexes the excited eigenstates, and j indexes the ground eigenstates. Here, ω_0 is the overall (zero splitting) transition frequency while Δ_μ, Δ_j are the hyperfine splittings of states μ, j.

The origin of these hyperfine splittings are from interactions with the surrounding electronic environment of the nucleus. The first is the isomer shift, originating from the monopole interaction with the surrounding electronic environment. This can always be modelled as a constant shift of all excited sublevels. Ab initio calculations generally use density functional theory to model the electron density of a given compound of interest, using measured values of the nuclear radius for the ground and excited levels as theoretical inputs. In practice, for thin films this is not particularly useful due to the sputter deposition process introducing irregularities in the material structure, and as such this must usually be fitted from experimental data.

The most important splitting is from the magnetic hyperfine field B experienced by the nucleus. This is given by the following Hamiltonian,

$$H_M = -\mu_N g_I \vec{I} \cdot \vec{B}, \tag{5.38}$$

where g_I is the g factor for the ground or excited manifold, **I** the nuclear spin operator, and μ_N the nuclear magneton. Note the magnitude of splitting between the states is given by $\mu_N g_I |B|$.

The final source of splitting commonly observed is the quadrupole splitting, due to the electric field gradient (EFG) experienced by the nucleus. This can be expressed in terms of the second derivative tensor of the electric potential,

$$V_{ij} = \partial_{x_i} \partial_{x_j} V. \tag{5.39}$$

As the electric potential obeys Laplace's equation,

$$\nabla^2 V = 0, \tag{5.40}$$

this tensor is traceless,

$$\sum_i V_{ii} = 0. \tag{5.41}$$

It is always possible to choose a coordinate system such that the maximum gradient is along z, and that the off-diagonal components vanish (i.e. $V_{zx} = 0$ etc). The interaction Hamiltonian is then given by

$$H_Q = \frac{eQ_I}{2I(2I-1)} (V_{xx}^2 I_x^2 + V_{yy} I_y^2 + V_{zz} I_x^2), \tag{5.42}$$

with e the electron charge, and Q_I the quadrupole moment (i.e. reduced matrix element of the nuclear quadrupole tensor). In practice however, one instead usually defines the interaction in terms of the principle axis gradient, V_{zz}, and the so-called asymmetry parameter,

$$\eta = \frac{V_{xx} - V_{yy}}{V_{zz}}. \tag{5.43}$$

By convention this is chosen to be such that $0 \leq \eta \leq 1$. We then have

$$H_Q = \frac{eQ_I V_{zz}}{4I(2I-1)} (3I_z^2 - I^2 + \eta (I_x^2 - I_y^2)). \tag{5.44}$$

Note that states with $I = 1/2$ have no quadrupole interaction. A general orientation of quadrupole can be obtained by a unitary rotation transformation. Unlike the magnetic case, the splitting between states will grow as the I_z eigenvalue m grows, and will depend on the total spin of the state. As such, we will define the quadrupole splitting to simply be

$$\Delta_Q = eQ_I V_{zz}. \tag{5.45}$$

This gives

$$H_Q = \frac{\Delta_Q}{4I(2I-1)} (3I_z^2 + -I^2 + \eta (I_x^2 - I_y^2)). \tag{5.46}$$

5.5 Interaction picture

The total Hamiltonian is given

$$H = H_F + H_N + H_I, \quad H_N = \sum_i H_N^{(i)}. \tag{5.47}$$

Here, H_F is the field Hamiltonian given by (3.54), H_N is the sum over the individual nuclear Hamiltonians, each having the form of (5.37), and H_I is the interaction Hamiltonian given by (5.7).

In general, the nuclear transition operators will have a phase factor evolving with the overall transition frequency ω_0, plus or minus a small detuning due to the hyperfine splittings. The remaining time dependence will consist of a slowly varying envelope, that evolves over the timescale of the spontaneous decay rate γ rather than the transition frequency. In addition, the scattered field will also consist of a similarly slowly varying envelope times $e^{i\omega_0 t}$ phase factor. We therefore wish to eliminate the resonant phase of both the nuclear and field operators. To eliminate the resonant phase, we adopt the transformation Hamiltonian

$$H_T = \sum_i \sum_\mu \hbar\omega_0 \hat{\Pi}^{(i)}_{\mu\mu} + \hbar\omega_0 \sum_{\lambda=e,m} \int_0^\infty \mathrm{d}\nu \int \mathrm{d}^3 r\, \hat{f}^\dagger_\lambda(\vec{r},\nu)\hat{f}_\lambda(\vec{r},\nu). \tag{5.48}$$

This then defines a unitary evolution operator $U_T(t) = \exp\left(\frac{i}{\hbar}H_T t\right)$, that can be used to obtain the interaction picture of the operators,

$$U_T(t)\hat{\Pi}^{(i)}_{\mu\mu'}U_T^\dagger(t) = \tilde{\Pi}^{(i)}_{\mu\mu'} \tag{5.49}$$

$$U_T(t)\hat{\Pi}^{(i)}_{jj'}U_T^\dagger(t) = \tilde{\Pi}^{(i)}_{jj'}, \tag{5.50}$$

$$U_T(t)\hat{\Pi}^{(i)}_{\mu j}U_T^\dagger(t) = \tilde{\Pi}^{(i)}_{\mu j}e^{i\omega_0 t}, \tag{5.51}$$

$$U_T(t)\hat{f}^\dagger_\lambda(\vec{r},\nu)U_T^\dagger(t) = \tilde{f}^\dagger_\lambda(\vec{r},\nu)e^{i\omega_0 t}, \tag{5.52}$$

$$U_T(t)\hat{B}(\vec{r})U_T^\dagger(t) = \tilde{B}_+(\vec{r})e^{-i\omega_0 t} + \text{h.c}, \tag{5.53}$$

$$\hat{B}_\pm(\vec{r}) \equiv \hat{B}^\dagger_\mp(\vec{r}) = \int_0^\infty \mathrm{d}\nu\, \hat{B}_\pm(\vec{r},\nu), \tag{5.54}$$

where we have defined the total positive and negative fields in the last line, and use $\tilde{O}$ to denote the transformation picture quantity associated with operator $\hat{O}$. The transformed nuclear and field Hamiltonians read

$$\tilde{H}_N + \tilde{H}_F = U_I(t)\,(H_N + H_F)\,U_I^\dagger(t) - H_T, \tag{5.55}$$

$$\tilde{H}_N^{(i)} = \sum_\mu \hbar\Delta_\mu \tilde{\Pi}^{(i)}_{\mu\mu} + \sum_j \hbar\Delta_j \tilde{\Pi}^{(i)}_{jj}, \tag{5.56}$$

$$\tilde{H}_F = \sum_{\lambda=e,m} \int_0^\infty \mathrm{d}\nu \int \mathrm{d}^3 r\, \hbar(\nu-\omega_0)\tilde{f}^\dagger_\lambda(\vec{r},\nu)\tilde{f}_\lambda(\vec{r},\nu).$$

The dipole interaction Hamiltonian reads

$$\tilde{H}_I(t) = -m_0 \sum_i \sum_{\mu,j} \left(\vec{d}_{\mu j}\tilde{\Pi}^{(i)}_{\mu j}e^{i\omega_0 t} + \text{h.c.}\right)\cdot\left(\tilde{B}_+(\vec{r}_i)e^{-i\omega_0 t} + \text{h.c.}\right). \tag{5.57}$$

5.6 Continuum limit

In the continuum limit, we replace the discrete nuclear positions with a continuum field, with a density of $\rho_N(\vec{r})$

Sums over indices are replaced by integration over the density

$$\sum_i \to \int \mathrm{d}^3 r\, \rho(\vec{r}) \tag{5.58}$$

The normalization of the density gives

$$\int \mathrm{d}^3 r\, \rho(\vec{r}) = N. \tag{5.59}$$

Similarly, we replace the Kronecker delta with a distribution proportional to the Dirac delta,

$$\delta_{ij} \to \mathcal{D}(\vec{r} - \vec{r}') \propto \delta^3(\vec{r} - \vec{r}'). \tag{5.60}$$

The proportionality is found by noting that the following must hold,

$$\sum_i \delta_{ij} = \int \mathrm{d}^3 r\, \mathcal{D}(\vec{r} - \vec{r}') = 1, \tag{5.61}$$

and using (5.58) we see that the proportionality constant must therefore be ρ_N^{-1}, giving

$$\delta_{ij} \to \frac{1}{\rho_N(\vec{r})} \delta^3(\vec{r} - \vec{r}'). \tag{5.62}$$

For homogeneous resonant layers, we can take a uniform density of $\rho_N = \frac{N}{V}$. Thus, we have

$$\hat{\Pi}^{(i)}_{ab}(t) \to \hat{\Pi}_{ab}(\vec{r}, t), \tag{5.63}$$

$$\sum_i \to \rho_N \int \mathrm{d}^3 r\,, \tag{5.64}$$

$$\delta_{ij} \to \frac{1}{\rho_N} \delta^3(\vec{r} - \vec{r}'). \tag{5.65}$$

The commutation relation between transition operators then become

$$[\hat{\Pi}_{ab}(\vec{r}, t), \hat{\Pi}_{cd}(\vec{r}', t)] = \frac{1}{\rho_N} \delta^3(\vec{r} - \vec{r}') \left(\hat{\Pi}_{ad}(\vec{r}, t)\delta_{bc} - \hat{\Pi}_{cb}(\vec{r}, t)\delta_{ad} \right), \tag{5.66}$$

with the interaction Hamiltonian now given by

$$\tilde{H}_I(t) = -\rho_N m_0 \sum_{\mu,j} \int \mathrm{d}^3 r \left(\tilde{\Pi}_{\mu j}(\vec{r}, t) \vec{d}_{\mu j} e^{i\omega_0 t} + \mathrm{h.c} \right) \cdot \left(\tilde{B}_+(\vec{r}) e^{-i\omega_0 t} + \mathrm{h.c.} \right). \tag{5.67}$$

Now that we fully specified both the fields and nuclei and their Hamiltonians, we can proceed to evaluate their equations of motion.

Chapter 6

Equations of motion and their solution

In the following chapter, we will implicitly work in the transformed frame of Section 5.5, and as such drop the $\tilde{O}$ notation.

6.1 Nuclear Bloch equations

We begin with the master equation for an arbitrary operator $\hat{O}$,

$$\partial_t \hat{O} = \frac{i}{\hbar}[\hat{H}_N + \hat{H}_F + \hat{H}_I(t), \hat{O}] + L^H[\hat{O}], \tag{6.1}$$

where L^H is the Heisenberg form of the Lindblad terms. For the transition operators, we find the following commutators with the interaction Hamiltonian,

$$[\hat{H}_I(t), \hat{\Pi}_{\mu\nu}(\vec{r}, t)] = m_0 \sum_j \left(\hat{\Pi}_{\mu j}(\vec{r}, t)\vec{d}_{\nu j} e^{i\omega_0 t} - \hat{\Pi}_{j\nu}(\vec{r}, t)\vec{d}^*_{\mu j} e^{-i\omega_0 t}\right) \cdot \hat{B}(\vec{r}, t) \tag{6.2}$$

$$[\hat{H}_I(t), \hat{\Pi}_{jk}(\vec{r}, t)] = -m_0 \sum_\mu \left(\hat{\Pi}_{\mu k}(\vec{r}, t)\vec{d}_{\mu j} e^{i\omega_0 t} - \hat{\Pi}_{j\mu}(\vec{r}, t)\vec{d}^*_{\mu k} e^{-i\omega_0 t}\right) \cdot \hat{B}(\vec{r}, t), \tag{6.3}$$

$$[\hat{H}_I(t), \hat{\Pi}_{\mu j}(\vec{r}, t)] = m_0 \left(\sum_\nu \hat{\Pi}_{\mu\nu}(\vec{r}, t)\vec{d}^*_{\nu j} e^{-i\omega_0 t} - \sum_k \hat{\Pi}_{kj}\vec{d}^*_{\mu k} e^{-i\omega_0 t}\right) \cdot \hat{B}(\vec{r}, t), \tag{6.4}$$

$$[\hat{H}_I(t), \hat{\Pi}_{j\mu}(\vec{r}, t)] = -m_0 \left(\sum_\nu \hat{\Pi}_{\nu\mu}(\vec{r}, t)\vec{d}_{\nu j} e^{i\omega_0 t} - \sum_k \hat{\Pi}_{jk}\vec{d}_{\mu k} e^{i\omega_0 t}\right) \cdot \hat{B}(\vec{r}, t), \tag{6.5}$$

where μ, ν index excited states, j, k index ground states, and

$$\hat{B}(\vec{r}, t) = \hat{B}_+(\vec{r}, t)e^{-i\omega_0 t} + \hat{B}_-(\vec{r}, t)e^{i\omega_0 t} \tag{6.6}$$

is the total magnetic field. The nuclear Hamiltonian commutators give

$$[\hat{H}_N, \hat{\Pi}_{\mu\nu}(\vec{r}, t)] = \hbar(\Delta_\mu - \Delta_\nu)\hat{\Pi}_{\mu\nu}(\vec{r}, t), \tag{6.7}$$
$$[\hat{H}_N, \hat{\Pi}_{jk}(\vec{r}, t)] = \hbar(\Delta_j - \Delta_k)\hat{\Pi}_{jk}(\vec{r}, t), \tag{6.8}$$
$$[\hat{H}_N, \hat{\Pi}_{\mu j}(\vec{r}, t)] = \hbar(\Delta_\mu - \Delta_j)\hat{\Pi}_{\mu j}(\vec{r}, t). \tag{6.9}$$

The Lindblad terms acting on excited state transition operators give

$$L^H[\hat{\Pi}_{\mu\nu}(\vec{r}, t)] = -\gamma\hat{\Pi}_{\mu\nu}(\vec{r}, t), \tag{6.10}$$

where γ is the total line-width, summed over all multi-polarities.

For ground state transition operators they give

$$L^H[\hat{\Pi}_{jk}(\vec{r}, t)] = \delta_{jk}\sum_\mu \Gamma(\mu \to j)\hat{\Pi}_{\mu\mu}(\vec{r}, t), \tag{6.11}$$

where the partial line-width is given by

$$\Gamma(\mu \to j) = \sum_{\lambda=\mathscr{E},\mathscr{M}}\sum_l \Gamma(\lambda l, \mu \to j), \tag{6.12}$$

with the multipolar line-widths given by (5.19).

Finally, for excited-ground state transition operators they give

$$L^H[\hat{\Pi}_{\mu j}(\vec{r}, t)] = -\frac{\gamma}{2}\hat{\Pi}_{\mu j}(\vec{r}, t). \tag{6.13}$$

Combined, we have the following nuclear Bloch equations,

$$\begin{aligned}\partial_t\hat{\Pi}_{\mu\nu}(\vec{r}, t) = &\left(i(\Delta_\mu - \Delta_k) - \gamma\right)\hat{\Pi}_{\mu\nu}(\vec{r}, t) \\ &+ \frac{im_0}{\hbar}\sum_j\left(\hat{\Pi}_{\mu j}(\vec{r}, t)\vec{d}_{\nu j}e^{i\omega_0 t} - \hat{\Pi}_{j\nu}(\vec{r}, t)\vec{d}^{\,*}_{\mu j}e^{-i\omega_0 t}\right)\cdot\hat{B}(\vec{r}, t),\end{aligned} \tag{6.14}$$

$$\begin{aligned}\partial_t\hat{\Pi}_{jk}(\vec{r}, t) = &\, i(\Delta_j - \Delta_k)\hat{\Pi}_{jk}(\vec{r}, t) + \delta_{jk}\sum_\mu \Gamma(\mu \to j)\hat{\Pi}_{\mu\mu}(\vec{r}, t) \\ &- \frac{im_0}{\hbar}\sum_\mu\left(\hat{\Pi}_{\mu k}(\vec{r}, t)\vec{d}_{\mu j}e^{i\omega_0 t} - \hat{\Pi}_{j\mu}(\vec{r}, t)\vec{d}^{\,*}_{\mu k}e^{-i\omega_0 t}\right)\cdot\hat{B}(\vec{r}, t),\end{aligned} \tag{6.15}$$

$$\begin{aligned}\partial_t\hat{\Pi}_{\mu j}(\vec{r}, t) = &\left(i(\Delta_\mu - \Delta_j) - \frac{\gamma}{2}\right)\hat{\Pi}_{\mu j}(\vec{r}, t) \\ &+ \frac{im_0}{\hbar}\left(\sum_\nu \hat{\Pi}_{\mu\nu}(\vec{r}, t)\vec{d}^{\,*}_{\nu j}e^{-i\omega_0 t} - \sum_k \hat{\Pi}_{kj}\vec{d}^{\,*}_{\mu k}e^{-i\omega_0 t}\right)\cdot\hat{B}(\vec{r}, t),\end{aligned} \tag{6.16}$$

$$\begin{aligned}\partial_t\hat{\Pi}_{j\mu}(\vec{r}, t) = &\left(-i(\Delta_\mu - \Delta_j) - \frac{\gamma}{2}\right)\hat{\Pi}_{j\mu}(\vec{r}, t) \\ &- \frac{im_0}{\hbar}\left(\sum_\nu \hat{\Pi}_{\nu\mu}(\vec{r}, t)\vec{d}_{\nu j}e^{i\omega_0 t} - \sum_k \hat{\Pi}_{jk}\vec{d}_{\mu k}e^{i\omega_0 t}\right)\cdot\hat{B}(\vec{r}, t).\end{aligned} \tag{6.17}$$

With the nuclear Bloch equations derived, we will proceed to evaluate the equation of motion for the field.

6.2 Field equation of motion

Recall that the frequency parameter of each field component is a formal parameter, with the frequency components of the field acting as Fourier components only for the free field. The interaction with the nuclei gives rise to additional time dynamics for each frequency component. As such, we include an explicit time dependence in our notation of the field components, as well as the formal frequency parameter,

$$\hat{B}_+(\vec{r}, \nu) \to \hat{B}_+(\vec{r}, \nu, t). \tag{6.18}$$

The Heisenberg equation of motion for the magnetic field envelope is given by

$$\begin{aligned}\partial_t \hat{B}_+(\vec{r}, \nu, t) =& \frac{i}{\hbar}[H_F' + H_I(t), \hat{B}_+(\vec{r}, \nu, t)] \\ =& -i(\nu - \omega_0)\hat{B}_+(\vec{r}, \nu, t) \\ & - \frac{i\mu_0}{\pi} e^{i\omega_0 t} \int \mathrm{d}^3 r'\, \rho(r') \,\mathrm{Im}\{\overleftrightarrow{G}_{mm}(\vec{r}, \vec{r}', \nu)\} \cdot \hat{m}(\vec{r}', t),\end{aligned} \tag{6.19}$$

where

$$\hat{m}(\vec{r}, t) = m_0 \sum_{\mu j} \vec{d}_{\mu j} \hat{\Pi}_{\mu j}(\vec{r}, t) e^{i\omega_0 t} + \mathrm{h.c.} \tag{6.20}$$

is the transition magnetization. This is formally solved as

$$\begin{aligned}&\hat{B}_+(\vec{r}, \nu, t) = \hat{B}_+(\vec{r}, \nu, -\infty) e^{-i(\nu-\omega_0)t} \\ &- \frac{i\mu_0}{\pi} e^{i\omega t} \int_{-\infty}^{t} \mathrm{d}t'\, e^{-i\nu(t-t')} \int \mathrm{d}^3 r'\, \rho(r') \,\mathrm{Im}\{\overleftrightarrow{G}_{mm}(\vec{r}, \vec{r}', \nu)\} \cdot \hat{m}(\vec{r}, t).\end{aligned} \tag{6.21}$$

The total field is then given by

$$\hat{B}(\vec{r}, t) = \int_0^\infty \mathrm{d}\nu \left(\hat{B}_+(\vec{r}, \nu, t) e^{-i\omega_0 t} + \hat{B}_-(\vec{r}, \nu, t) e^{i\omega_0 t}\right) \tag{6.22}$$

We substitute (6.21) and its Hermitian conjugate into (6.22), to obtain

$$\begin{aligned}\hat{B}(\vec{r}, t) =& \hat{B}_{in}(\vec{r}, t) \\ & + \frac{\mu_0}{\pi} \int_0^\infty \mathrm{d}\nu \int_{-\infty}^{t} \mathrm{d}t' \left(i e^{i\nu(t-t')} - i e^{-i\nu(t-t')}\right) \\ & \times \int \mathrm{d}^3 r'\, \rho(r') \,\mathrm{Im}\{\overleftrightarrow{G}_{mm}(\vec{r}, \vec{r}', \nu)\} \cdot \hat{m}(\vec{r}', t),\end{aligned} \tag{6.23}$$

where we have defined the input field $\hat{B}_{in}$ to be the homogeneous solution

$$\hat{B}_{in}(\vec{r}, t) = \int_0^\infty \mathrm{d}\nu\, \hat{B}_+(\vec{r}, \nu, -\infty) e^{-i\nu t} + \mathrm{h.c.} \tag{6.24}$$

All that remains is to evaluate the scattering term. We first note that as $\overleftrightarrow{G}_{mm}$ obeys the Schwarz reflection principle [82],

$$\overleftrightarrow{G}_{mm}(\vec{r}, \vec{r'}, \omega)^* = \overleftrightarrow{G}_{mm}(\vec{r}, \vec{r'}, -\omega^*), \tag{6.25}$$

that we have

$$\mathrm{Im}\{\overleftrightarrow{G}_{mm}(\vec{r}, \vec{r'}, \nu)\} = -\,\mathrm{Im}\{\overleftrightarrow{G}_{mm}(\vec{r}, \vec{r'}, -\nu)\}. \tag{6.26}$$

We can then make use of this to show that

$$\int_0^\infty \mathrm{d}\nu \int_{-\infty}^t \mathrm{d}t' \left(ie^{i\nu(t-t')} - ie^{-i\nu(t-t')}\right) \mathrm{Im}\{\overleftrightarrow{G}_{mm}(\vec{r},\vec{r}',\nu)\} \\ = i\int_{-\infty}^\infty \mathrm{d}\nu \int_{-\infty}^t \mathrm{d}t'\, e^{i\nu(t-t')}\, \mathrm{Im}\{\overleftrightarrow{G}_{mm}(\vec{r},\vec{r}',\nu)\} \quad (6.27)$$

This allows us to rewrite (6.27) as

$$\hat{B}_{sc}(\vec{r},t) = \frac{i\mu_0}{\pi}\int_{-\infty}^\infty \mathrm{d}\nu \int_{-\infty}^\infty \mathrm{d}t'\,\Theta(t-t')e^{i\nu(t-t')} \\ \times \int \mathrm{d}^3r'\,\rho(\vec{r}')\,\mathrm{Im}\{\overleftrightarrow{G}_{mm}(\vec{r},\vec{r}',\nu)\}\cdot\hat{m}(\vec{r}',t'). \quad (6.28)$$

Taking a temporal Fourier transform, we see that

$$\hat{B}_{sc}(\vec{r},\omega) = \frac{\mu_0\rho_N}{\pi}\int_{-\infty}^\infty \mathrm{d}\nu\,\frac{1}{\nu-\omega+i0^+}\int \mathrm{d}^3r'\,\mathrm{Im}\{\overleftrightarrow{G}_{mm}(\vec{r},\vec{r}',\nu)\}\cdot\hat{m}(\vec{r}',\omega). \quad (6.29)$$

We can then use the Sokhotski–Plemelj theorem [98],

$$\frac{1}{x+i0^+} = -i\pi\delta(x) + \mathcal{P}\frac{1}{x}, \quad (6.30)$$

combined with the Kramers–Kronig relations [84, Sec. 7.10D]

$$\pi\,\mathrm{Re}\{\overleftrightarrow{G}_{mm}(\vec{r},\vec{r}',\nu)\} = \mathcal{P}\int_{-\infty}^\infty \mathrm{d}\nu\,\frac{1}{\omega-\nu}\,\mathrm{Im}\{\overleftrightarrow{G}_{mm}(\vec{r},\vec{r}',\nu)\}, \quad (6.31)$$

to obtain

$$\hat{B}_{sc}(\vec{r},\omega) = -\mu_0\int \mathrm{d}^3r'\,\rho(\vec{r}')\overleftrightarrow{G}_{mm}(\vec{r},\vec{r}',\omega)\cdot\hat{m}(\vec{r},\omega). \quad (6.32)$$

Thus, we can see that the scattered field obeys the macroscopic Maxwell's equations (3.48), with the nuclear transition dipoles as the source. We also see that this demonstrates that the noise current frequency parameter ν is not a Fourier parameter for the interacting system,

$$\hat{B}_{in}(\vec{r},\omega) + \hat{B}_{sc}(\vec{r},\omega) \neq \hat{B}(\vec{r},\nu)\big|_{\nu=\omega}. \quad (6.33)$$

In addition, we note once again that as the Fourier transform of a Hermitian operator, $\hat{m}$ obeys the Schwarz reflection principle,

$$\hat{m}(\vec{r},\omega)^\dagger = \hat{m}(\vec{r},-\omega^*), \quad (6.34)$$

and combined with the Schwarz reflection of $\overleftrightarrow{G}_{mm}$ we see that this also holds for B_{sc}, thus showing that our expression for B_{sc} is consistent with it being the Fourier transform of a Hermitian operator.

6.2.1 Beam description

To describe the input field, we will first specify the incident beam description in free space, and then apply (3.72) to obtain the electronically scattered field. We

first specify the beam in a coordinate system such that z is along the beam propagation direction, and make an appropriate coordinate transformation to obtain its expression in the coordinate system relevant to the geometry being considered.

The general expression for the far field of a beam propagating along $\hat{z}$ is given in terms of the Fourier components as

$$\vec{E}(\vec{r},\omega) = \int \frac{\mathrm{d}^2 q}{(2\pi)^2} \vec{E}(\vec{q},\omega) e^{i\sqrt{k^2-q^2}z + i\vec{q}\cdot\vec{\rho}}, \tag{6.35}$$

where the integration range is over $0 \le q \le k$, and

$$\vec{\rho} = x\hat{x} + y\hat{y}. \tag{6.36}$$

The transversality of the field components is given by the constraint

$$\vec{E}(\vec{q},\omega)\cdot\vec{k} = 0, \tag{6.37}$$

where

$$\vec{k} = \sqrt{k^2 - q^2}\hat{z} + \vec{q}. \tag{6.38}$$

We assume that the beam envelope is uniform along the y axis, so that we may consider an effectively two-dimensional problem. This is a good approximation for synchrotron beams, which are tightly focused only in one direction. In this case, we can write

$$\vec{E}(\vec{r},\omega) = \int_{-k}^{k} \frac{\mathrm{d}q}{2\pi} \vec{E}(q,\omega) e^{i\sqrt{k^2-q^2}z + iqx}, \tag{6.39}$$

An alternate choice of representation is the angular spectrum representation, using $q = k\sin\theta_B$. This gives

$$\vec{E}(\vec{r},\omega) = \int_{-\pi/2}^{\pi/2} \frac{\mathrm{d}\theta_B}{2\pi} \vec{E}(\theta_B,\omega) e^{i(z\cos\theta_B + x\sin\theta_B)}, \tag{6.40}$$

where

$$\vec{E}(\theta_B,\omega) = k\cos\theta_B \vec{E}(q = k\sin\theta_B,\omega). \tag{6.41}$$

We may now use the Kirchoff integral (3.72) to obtain the scattered field, which we will do so for grazing incidence, nuclear forward scattering, and waveguide front coupling.

Grazing incidence

For grazing incidence, the relevant bounding surface in (3.72) is a plane $z = z_\infty$, placed in the air layer, above both the sample and the observation z coordinate. As the surface is considered as the limit of a sphere enclosing the incident beam source, located at some distant positive z coordinate, we take the surface normal to be $-\hat{z}$. Due to translational symmetry in the x, y plane, we can express everything in terms of the x, y wave-vector $\vec{q}$, giving

$$\vec{B}(\vec{q},z,\omega) = -\frac{c}{i\omega} \overleftrightarrow{G}_{me}(\vec{q},z,z_\infty,\omega)\cdot\vec{B}_0(\vec{q},z_\infty,\omega)\times\hat{z} - \frac{1}{i\omega} \overleftrightarrow{G}_{mm}(\vec{q},z,z_\infty,\omega)\cdot\vec{E}_0(\vec{q},z_\infty,\omega)\times\hat{z}. \tag{6.42}$$

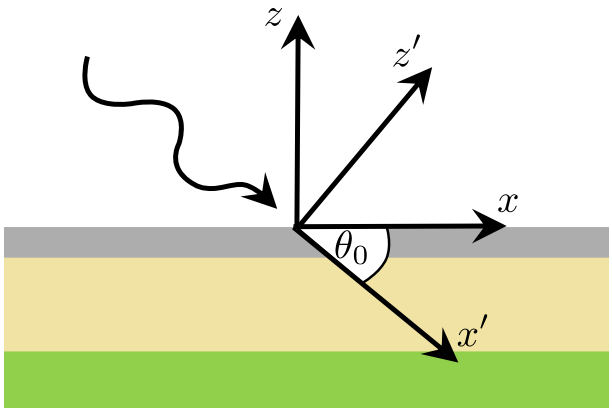

Figure 6.1: Coordinate geometry of grazing incidence. Relation of beam coordinates x', z' to layer coordinates x, z at an angle of incidence θ_0 is shown.

For the input field, we consider a beam propagating at an angle of incidence θ_0 in the x, z plane, uniform in the y plane. In the beam coordinates, such that $\hat{x}'$ is the beam propagation direction, we have

$$\vec{E}_0(x', z', \omega) = cB_{in} \int_{-\pi/2}^{\pi/2} \mathrm{d}\theta_B \left(\hat{s} f_s(\theta_B) + \hat{p}(\theta_B) f_p(\theta_B)\right) e^{i\frac{\omega}{c}(x' \cos\theta_B + z' \sin\theta_B)} \quad (6.43)$$

where B_{in} is the field amplitude in magnetic units, $\hat{s}$, $\hat{p}(\theta_B)$ are the s, p polarization unit vectors, and $f_s(\theta)$, $f_p(\theta)$ are dimensionless expansion functions.

The beam coordinates are given in terms of the layer coordinates via (see Fig. 6.1)

$$x' = x \cos\theta_0 - z \sin\theta_0, \quad (6.44)$$
$$z' = x \sin\theta_0 + z \cos\theta_0. \quad (6.45)$$

Thus, we can simply rotate (6.43) by an angle θ_0 about the y axis, to obtain its expression in the layer coordinates,

$$\vec{E}_0(x, z, \omega) = cB_{in} \int_{-\pi/2}^{\pi/2} \mathrm{d}\theta_B \left(\hat{s} f_s(\theta_B) + \hat{p}(\theta_B - \theta_0) f_p(\theta_B)\right) e^{i\frac{\omega}{c}(x \cos(\theta_B - \theta_0) + z \sin(\theta_B - \theta_0))} \quad (6.46)$$

$$= cB_{in} \int_{-\pi/2-\theta_0}^{\pi/2-\theta_0} \mathrm{d}\theta \left(\hat{s} f_s(\theta + \theta_0) + \hat{p}(\theta) f_p(\theta + \theta_0)\right) e^{i\frac{\omega}{c}(x \cos(\theta) + z \sin(\theta))} \quad (6.47)$$

where we have defined $\theta = \theta_B + \theta_0$, and noted that $\hat{s}$, being parallel to y, is unaffected by a rotation in the x, z plane, while $\hat{p}$ is rotated by θ_0.

Taking a curl and dividing by $i\omega$ gives the magnetic field,

$$\vec{B}_0(x, z, \omega) = B_{in} \int_{-\pi/2-\theta_0}^{\pi/2-\theta_0} \mathrm{d}\theta \left(\hat{p}(\theta) f_s(\theta + \theta_0) - \hat{s} f_p(\theta + \theta_0)\right) e^{i\frac{\omega}{c}(x \cos(\theta) + z \sin(\theta))}, \quad (6.48)$$

where we have used the fact that since $\hat{k}, \hat{s}, \hat{p}$ correspond to a rotation of $\hat{x}, \hat{y}, \hat{z}$, their curl identity is

$$\hat{k}(\theta) \times \hat{s} = \hat{p}(\theta). \tag{6.49}$$

Since $\hat{s} = \hat{y}$, we simply have

$$\hat{s} \times \hat{z} = \hat{x}. \tag{6.50}$$

We note that

$$\hat{p}(\theta) = \cos\theta\hat{z} - \sin\theta\hat{x}. \tag{6.51}$$

We therefore have

$$\hat{p}(\theta) \times \hat{z} = \sin\theta\hat{y}. \tag{6.52}$$

From (4.68), we have

$$\overleftrightarrow{G}(q, z, z') \approx (\hat{y} \otimes \hat{y} + \hat{z} \otimes \hat{z})\mathcal{G}_{TE}. \tag{6.53}$$

The curl is approximately given by

$$\nabla \times \overleftrightarrow{G}(q, z, z', \omega) \approx ik\hat{x} \times \overleftrightarrow{G}(q, z, z', \omega). \tag{6.54}$$

Therefore, using (3.49), (3.50) gives

$$\overleftrightarrow{G}_{me} \approx -k^2\mathcal{G}_{TE}(\hat{z} \otimes \hat{y} - \hat{y} \otimes \hat{z}), \tag{6.55}$$

$$\overleftrightarrow{G}_{mm} \approx -k^2\mathcal{G}_{TE}(\hat{y} \otimes \hat{y} + \hat{z} \otimes \hat{z}). \tag{6.56}$$

We finally obtain for the spatial Fourier components, in angular coordinates $q = k\cos\theta$,

$$\begin{aligned}\vec{B}(k\cos\theta, z, \omega) \approx &- ik\sin(\theta)\hat{z}\mathcal{G}_{TE}(k\cos\theta, z, z_\infty, \omega)f_s(\theta + \theta_0)e^{iz_\infty \sin(\theta)}B_{in} \\ &- ik\sin(\theta)\hat{y}\mathcal{G}_{TE}(k\cos\theta, z, z_\infty, \omega)f_p(\theta + \theta_0)e^{iz_\infty \sin(\theta)}B_{in}.\end{aligned} \tag{6.57}$$

For grazing incidence, with a well collimated beam, one can take $f_s(\theta)$, $f_p(\theta)$ to be proportional to $\delta(\theta)$.

Forward scattering

For regular nuclear forward scattering, we take a bulk sample, with infinite extent in the yz plane. The normal vector is taken to be $\hat{x}$, which is also the direction the of propagation the incident field, which can be approximated as a plane wave,

$$\vec{E}_0(q, x, \omega) = 2\pi c\delta(q)B_{in}\hat{e}_{in}e^{-ikx}, \tag{6.58}$$

where q is now the z Fourier component, with B_{in} the field amplitude in magnetic units, and $\hat{e}_{in} \cdot \hat{x} = 0$ the field polarization. The magnetic field is given by

$$\vec{B}_0(q, x, \omega) = 2\pi\delta(q)B_{in}(\hat{x} \times \hat{e}_{in})e^{-ikx}. \tag{6.59}$$

If we are interested in only the transmitted field, we can without loss of generality take x_∞ to be the incident air-sample interface, $x_\infty = 0$. The full field is then given by

$$\vec{B}(q, x, \omega) = -2\pi\delta(q)B_{in}\left(\overleftrightarrow{G}_{me}(q, x, 0, \omega) \cdot \hat{e}_{in} + \overleftrightarrow{G}_{mm}(q, x, 0, \omega) \cdot (\hat{e}_{in} \times \hat{x})\right) \tag{6.60}$$

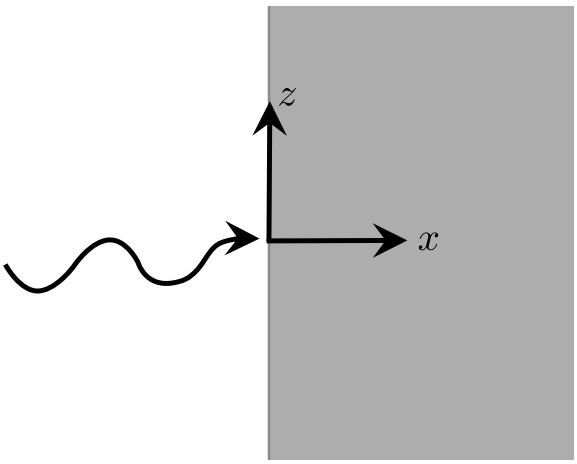

Figure 6.2: Coordinate geometry for forward scattering. The beam propagates at normal incidence along the z direction through a bulk sample.

Front coupling

For waveguide front coupling, we can no longer treat the medium as infinite in the x extent. Thus, we must consider the interface between the air and the waveguide explicitly.

One must consider the scattering problem between the slab waveguide system and air interfaces on either side. For normal incidence scattering at X-ray wavelengths, the reflectivity is negligible. As such, we may consider the Green's functions for source and observation points both in the same subsystem (i.e. waveguide or air) to be the homogeneous Green's functions for the homogeneous medium. We therefore take the bounding plane to be the plane of incidence at the air-waveguide boundary, and find the incident field by imposing continuity at the boundary.

To evaluate the field in the interior, we must expand the transverse beam profile into the waveguide mode basis of Section 4.2. Specifically, the Green's function is of the form

$$\overleftrightarrow{G}_{me} \approx k^2(\hat{y}\otimes\hat{z}+\hat{z}\otimes\hat{y})\mathcal{G}_{TE}, \tag{6.61}$$

$$\overleftrightarrow{G}_{mm} \approx k^2(\hat{y}\otimes\hat{y}+\hat{z}\otimes\hat{z})\mathcal{G}_{TE} \tag{6.62}$$

$$\mathcal{G}_{TE} \approx \sum_{\lambda} \frac{u_\lambda(z)u_\lambda(z')}{2iq_\lambda(q-q_\lambda)}, \tag{6.63}$$

where the mode functions u_λ obey the orthonormality relation (4.99). We can therefore decompose the incident fields according to

$$\vec{E}_\lambda(x=0,z,\omega) = u_\lambda(z)\int \mathrm{d}z'\, u_\lambda(z')\overleftrightarrow{\mathbb{1}}_\perp\cdot\vec{E}_{in}(x=0,z',\omega). \tag{6.64}$$

Propagating these fields in x then gives

$$\vec{E}_\lambda(x,z,\omega) = \vec{E}_\lambda(0,z,\omega)e^{iq_\lambda x}\Theta(x), \tag{6.65}$$

where Θ is the Heaviside step function. The total field is then obtained by adding

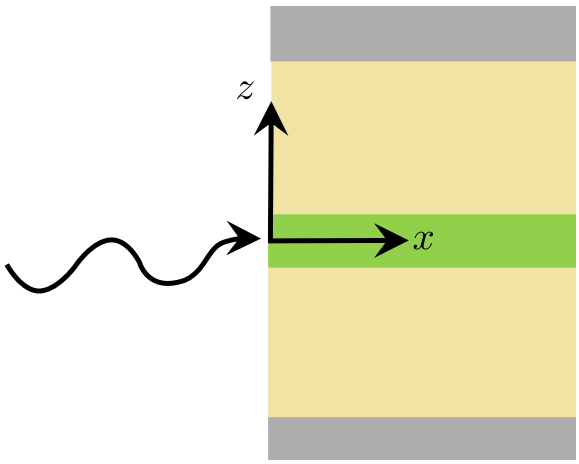

Figure 6.3: Coordinate geometry for front coupling to a thin-film nanostructure. The beam propagates directly parallel to the layers. The broken translational symmetry in x at the incident plane means that the x Fourier components of the incident beam are no longer conserved, compared to grazing incidence.

together the individual modes,

$$\vec{E}(x, z, \omega) = \sum_{\lambda} \vec{E}_{\lambda}(0, z, \omega) e^{iq_{\lambda}x} \Theta(x). \tag{6.66}$$

The magnetic field can be obtained using an identical procedure.

6.3 Linear response and bandwidth considerations

A single shot from a synchrotron contains only a few resonant photons, and as such the number density of resonant photons is far smaller than the number density of resonant nuclei, giving an extremely low excitation fraction. As such we may consider the linear response of the system, where we take the excited state population as zero, and the ground state to be in its thermal distribution. At room temperature, this is approximately a uniform distribution across the ground eigenstates, giving

$$\begin{aligned} \hat{\Pi}_{\mu\nu}(\vec{r}, t) &\approx 0 \\ \hat{\Pi}_{jk}(\vec{r}, t) &\approx \delta_{jk} \frac{\mathbb{1}}{2I_g + 1}. \end{aligned} \tag{6.67}$$

Upon linearization, only the excited-ground transition equations remain, given by

$$\begin{aligned} \partial_t \hat{\Pi}_{\mu j}(\vec{r}, t) = &\left(i(\Delta_\mu - \Delta_j) - \frac{\gamma}{2}\right) \hat{\Pi}_{\mu j}(\vec{r}, t) \\ &- \frac{im_0}{\hbar(2I_g + 1)} \vec{d}^{\,*}_{\mu j} \cdot \hat{B}(\vec{r}, t) e^{-i\omega_0 t}, \end{aligned} \tag{6.68}$$

$$\begin{aligned} \partial_t \hat{\Pi}_{j\mu}(\vec{r}, t) = &\left(-i(\Delta_\mu - \Delta_j) - \frac{\gamma}{2}\right) \hat{\Pi}_{j\mu}(\vec{r}, t) \\ &+ \frac{im_0}{\hbar(2I_g + 1)} \vec{d}_{\mu j} \cdot \hat{B}(\vec{r}, t) e^{i\omega_0 t}. \end{aligned} \tag{6.69}$$

This has the Fourier space solution

$$\hat{\Pi}_{\mu j}(\vec{r},\omega) = \frac{m_0}{2I_g+1}\frac{1}{\hbar(\omega+\Delta_\mu-\Delta_j-i\frac{\gamma}{2})}\vec{d}^{\,*}_{\mu j}\cdot\hat{B}(\vec{r},\omega-\omega_0), \tag{6.70}$$

for the negative frequency operator, and

$$\hat{\Pi}_{j\mu}(\vec{r},\omega) = -\frac{m_0}{2I_g+1}\frac{1}{\hbar(\omega-\Delta_\mu+\Delta_j+i\frac{\gamma}{2})}\vec{d}_{\mu j}\cdot\hat{B}(\vec{r},\omega+\omega_0) \tag{6.71}$$

for the positive frequency operator.

6.3.1 Bandwidth considerations and the rotating wave approximation

To derive the Fourier space equation of motion of the field, we required the use of the Kramers-Kronig relations. These involve integrals over all frequencies, and make use of the analyticity of the Green's function with respect to frequency. These relations are broken for the rotating wave approximation, which is why we did not consider making it at the Hamiltonian level as is usually done. However, the nuclear transitions have a bandwidth far smaller than the Green's function in frequency space, and as such, the rotating wave approximation will hold in the linear regime. Therefore, we make the rotating wave approximation at the level of (6.71) and (6.70).

Rotating wave approximation

We first split the magnetization into 'positive' and 'negative' frequency components,

$$\hat{m}(\vec{r},t) = e^{-i\omega_0 t}\hat{m}_+(\vec{r},t) + \text{h.c.} \tag{6.72}$$

$$\hat{m}_+(\vec{r},t) = m_0\sum_{\mu j}\hat{\Pi}_{j\mu}(\vec{r},t). \tag{6.73}$$

We can see that the positive frequency envelope $\hat{m}_+$ has the Fourier space expression

$$\hat{m}_+(\vec{r},\omega) = -\overleftrightarrow{\chi}_+(\omega)\cdot\hat{B}(\vec{r},\omega+\omega_0), \tag{6.74}$$

where the positive frequency component of the nuclear susceptibility tensor can be obtained from (6.71),

$$\overleftrightarrow{\chi}_+(\omega) = \frac{m_0^2}{2I_g+1}\sum_{\mu,j}\frac{\vec{d}^{\,*}_{\mu j}\otimes\vec{d}_{\mu j}}{\hbar(\omega-\Delta_\mu+\Delta_j+i\frac{\gamma}{2})}. \tag{6.75}$$

The field can be expanded into 'positive' and 'negative' frequency components as before,

$$\hat{B}(\vec{r},t) = e^{-i\omega_0 t}\hat{B}_+(\vec{r},t) + \text{h.c.}, \tag{6.76}$$

where the positive and negative components are the same as defined in (5.54). However, although these components are positive and negative with respect to *noise current* frequency ν, due to the interaction with the nuclei the scattered 'positive' field will contain negative components with respect to *physical* frequency ω.

Taking a Fourier transform of (6.76) we obtain

$$\hat{B}(\vec{r},\omega) = \hat{B}_+(\vec{r},\omega-\omega_0) + \hat{B}_-(\vec{r},\omega+\omega_0). \tag{6.77}$$

Substituting (6.77) into (6.74) we obtain

$$\hat{m}_+(\vec{r},\omega) = -\overleftrightarrow{\chi}_+(\omega)\cdot\left(\hat{B}_+(\vec{r},\omega) + \hat{B}_-(\vec{r},\omega+2\omega_0).\right) \tag{6.78}$$

As we have eliminated the plane wave phase factors, the Fourier transforms of the envelopes are concentrated at $\omega \approx 0$. However, we can see that the negative frequency field is coupled in the range $\omega \approx -2\omega_0$, which we assume to be far outside the bandwidth of the field envelope. Thus, the rotating wave approximation in our case reads,

$$\hat{m}_+(\vec{r},\omega) \approx -\overleftrightarrow{\chi}_+(\omega)\cdot\hat{B}_+(\vec{r},\omega). \tag{6.79}$$

Similarly, expressing the scattered field given by (6.32) as

$$\hat{B}_{sc}(\vec{r},t) = e^{-i\omega_0 t}\hat{B}_{sc,+}(\vec{r},t) + \text{h.c.}, \tag{6.80}$$

we can make the same bandwidth argument to show

$$\hat{B}_{sc,+}(\vec{r},\omega) \approx -\mu_0\rho_N\int \mathrm{d}^3r'\,\overleftrightarrow{G}_{mm}(\vec{r},\vec{r}',\omega+\omega_0)\cdot\hat{m}_+(\vec{r},\omega), \tag{6.81}$$

$$\hat{B}_{sc,-}(\vec{r},\omega) \approx -\mu_0\rho_N\int \mathrm{d}^3r'\,\overleftrightarrow{G}_{mm}(\vec{r},\vec{r}',\omega-\omega_0)\cdot\hat{m}_-(\vec{r},\omega). \tag{6.82}$$

Dispersion of the Green's function

The resonant bandwidth of the nuclei is incredibly small, on the order of 10^{-12} times the transition frequency. As such, we may consider a Taylor expansion of the Green's function around ω_0, and keep only the lowest order terms of relevance.

We will express the Green's function in terms of an envelope and phase,

$$\overleftrightarrow{G}_{mm}(\vec{r},\vec{r}',\omega) = \overleftrightarrow{g}(\vec{r},\vec{r}',\omega)e^{i\phi(\vec{r},\vec{r}',\omega)}. \tag{6.83}$$

Expanding to first order in both envelope and phase gives

$$\begin{aligned}\overleftrightarrow{G}_{mm}(\vec{r},\vec{r}',\omega) = &\left[\overleftrightarrow{g}(\vec{r},\vec{r}',\omega_0) + (\omega-\omega_0)\frac{\partial\overleftrightarrow{g}}{\partial\omega}\bigg|_{\omega=\omega_0} + \mathcal{O}\left((\omega-\omega_0)^2\right)\right]\\ &\times\exp\left(i\phi(\vec{r},\vec{r}',\omega_0) + (\omega-\omega_0)\frac{\partial\phi}{\partial\omega}\bigg|_{\omega=\omega_0} + \mathcal{O}\left((\omega-\omega_0)^2\right)\right)\end{aligned} \tag{6.84}$$

For a homogeneous medium, this expansion can be done in terms of the overall Green's function,

$$\overleftrightarrow{G}_0(\vec{r},\vec{r}',\omega) = \left(\overleftrightarrow{\mathbb{1}} - \frac{1}{n^2k^2}\nabla\otimes\nabla\right)\frac{e^{ink|\vec{r}-\vec{r}'|}}{4\pi|\vec{r}-\vec{r}'|} \tag{6.85}$$

where n is the medium refractive index, while for a waveguide, this expansion should be done with respect to each guided mode Green's function in (4.81).

Envelope dispersion

We first consider the effects of the envelope dispersion. Substituting (6.84) into (6.81), and keeping the phase constant, we can see that the result is an equation of the form

$$\hat{B}_{sc,+}(\vec{r},\omega) \approx -\mu_0\rho_N \sum_{n=0}^{\infty} \int \mathrm{d}^3 r'\, \omega^n \frac{\partial^n \overleftrightarrow{g}}{\partial \omega^n}\bigg|_{\omega=\omega_0} e^{i\phi(\vec{r},\vec{r}',\omega_0)} \cdot \hat{m}_+(\vec{r},\omega) \tag{6.86}$$

Fourier inverting, we obtain

$$\hat{B}_{sc,+}(\vec{r},t) = -\mu_0\rho_N \sum_{n=0}^{\infty} i^n \int \mathrm{d}^3 r'\, \frac{\partial^n \overleftrightarrow{g}}{\partial \omega^n}\bigg|_{\omega=\omega_0} e^{i\phi(\vec{r},\vec{r}',\omega_0)} \cdot \frac{\partial^n}{\partial t^n}\hat{m}_+(\vec{r},t). \tag{6.87}$$

We can see that the lowest order term gives the Markov approximation, coupling the field instantaneously to the nuclei, while the higher order terms give non-Markov couplings to the derivatives of the field, therefore introducing history effects.

Phase dispersion

We now focus our attention to the phase term $\phi(\vec{r},\vec{r}',\omega)$. Overall, as we can see from (6.85), within a medium with refractive index n, the field has a phase factor of

$$e^{in\omega|r-r'|/c}. \tag{6.88}$$

Therefore, in a homogeneous medium, as is applicable to nuclear forward scattering for example, we must consider at minimum a linear dispersion in the phase. For a guided mode, the dispersion can be evaluated numerically by considering the frequency dependence of a pole of the Green's function.

Including the effect of linear dispersion of the phase in (6.86) gives

$$\hat{B}_{sc,+}(\vec{r},\omega) \approx -\mu_0\rho_N \sum_{n=0}^{\infty} \int \mathrm{d}^3 r'\, \omega^n \frac{\partial^n \overleftrightarrow{g}}{\partial \omega^n}\Big|_{\omega=\omega_0} \times \exp\left(i\phi(\vec{r},\vec{r}',\omega_0) + i\omega\frac{\partial\phi}{\partial\omega}\Big|_{\omega=\omega_0}\right)\cdot \hat{m}_+(\vec{r},\omega). \tag{6.89}$$

Upon Fourier inversion, we can see that this will involve terms of the form

$$\int \frac{\mathrm{d}\omega}{2\pi} \exp\left[-i\omega t + i\omega\frac{\partial\phi}{\partial\omega}\Big|_{\omega=\omega_0}\right] f(\omega) = f\left(t - \frac{\partial\phi}{\partial\omega}\Big|_{\omega=\omega_0}\right) \tag{6.90}$$

where $f(\omega)$, $f(t)$ are the Fourier and time domain forms of the function being inverted.

In particular, for a homogeneous medium, the phase dispersion is simply

$$\frac{\partial\phi}{\partial\omega}\Big|_{\omega=\omega_0} = \frac{n}{c}|\vec{r}-\vec{r}'|, \tag{6.91}$$

and thus the linear dispersion of the phase simply gives (6.87) with the appropriate retarded time in the arguments,

$$\hat{B}_{sc,+}(\vec{r},t) \approx -\mu_0\rho_N \sum_{n=0}^{\infty} i^n \int \mathrm{d}^3 r'\, \frac{\partial^n \overleftrightarrow{g}}{\partial \omega^n}\bigg|_{\omega=\omega_0} e^{i\phi(\vec{r},\vec{r}',\omega_0)} \cdot \frac{\partial^n}{\partial t^n}\hat{m}_+(\vec{r},t-\frac{n}{c}|\vec{r}-\vec{r}'|). \tag{6.92}$$

A second order dispersion will introduce Gaussian broadening in time, but as effects beyond linear dispersion will be negligible in the problems we consider in Chapters 7 and 8, we need not consider this for our purposes. With this, we have defined the general solution for the linear response regime, including the possibility of dispersive effects. Thus, we will now proceed to consider the applications of these solutions to our topics of interest. We will begin with the effect of inhomogeneities to grazing incidence in the following chapter.

Chapter 7

Grazing incidence

In this chapter, we consider the effects of both beam and hyperfine inhomogeneities on the collective spectra of grazing incidence thin-film cavities. Experimentally obtainable beam divergences are of comparable order of magnitude to the angular width of a cavity resonance. Therefore, in Section 7.1 we analyse the effects of beam divergence on the observed energy spectra. Following this, in Section 7.2, we examine the effect of inhomogeneous hyperfine interactions on the energy spectra, taking collective Dicke dynamics into account.

7.1 Effect of angular divergence on collective spectra

In current theoretical models for grazing incidence scattering, the incident beam is considered incredibly well collimated, such that it can be approximated as a plane wave. The incident beam therefore excites a single spatial Fourier mode of the waveguide. The accuracy of this approximation depends on the relative sizes of the beam width in momentum space, to the width of a guided mode pole. In particular, it must be the case that the spatially Fourier transformed Green's function at the nuclear position is approximately constant over the Fourier width of the beam.

Even though realistic input beams have divergences on the order of a few tens of µrad, a typical guided mode pole is of comparable angular width. As such, the different spatial Fourier components will have different collective couplings, and the resulting energy spectrum must consider the average over the incident spatial Fourier modes. In addition, it is not always possible to maintain a consistent angle of incidence in an experiment. Especially at higher intensities, heating of the sample and monochromators, as well as radiation pressure on the sample, can result in an angle of incidence drift between shots.

Therefore, in order to model these effects, in Section 7.1.1, we derive the photo-detection rate taking into account a distribution of angles of incidence. Then, in Section 7.1.2 we demonstrate the effects of beam divergence and angular drift on the observed energy spectra. We use as a point of experimental comparison experimental data from beam-time ID HC-4028, ID18 at ESRF, November 2018, that underwent significant angular drift.

7.1.1 Photo-detection rate

The photo-detection rate per unit area at a point detector located $\vec{r}_d$ is given by the detector efficiency multiplied by the number density of photons within the bandwidth of the detector [60, Sec. 16.1]. The number density of a narrowband field can be taken as intensity of the electromagnetic field incident at the detector location, divided by the mean energy per photon, and thus we obtain:

$$\frac{\mathrm{d}P_d(t)}{\mathrm{d}A} = \frac{\eta}{\hbar\omega_0} I(\vec{r}_d, t) = \frac{\eta c}{2\hbar\omega_0\epsilon_0} \left\langle \vec{E}_-(\vec{r}_d, t) \cdot \vec{E}_+(\vec{r}_d, t) \right\rangle, \tag{7.1}$$

where η is the detector efficiency, and we have noted that the nuclear response bandwidth is far smaller than the photon energy, and is thus narrowband, allowing us to approximate all incident photons as having energy $\hbar\omega_0$.

If we consider now a finite size detector, whose area is given by the surface $S(\vec{s})$, the photo detection rate is simply the integral of (7.1) over the detector surface,

$$P_d(t) = \frac{\eta}{\hbar\omega_0} \int_S \mathrm{d}^2 s \, I(\vec{s}, t). \tag{7.2}$$

If the detector is sufficiently large compared to the beam radius, we can assume the entire photon count of the beam is captured, and take the limit $S \to \mathbb{R}^2_\parallel$, i.e. take the detector area to be the entire plane transverse to the beam axis,

$$P_d(t) = \frac{\eta}{\hbar\omega_0} \int_{\mathbb{R}^2_\parallel} \mathrm{d}^2 s \, I(\vec{s}, t). \tag{7.3}$$

Using the beam coordinates of Section 6.2.1, such that $\hat{z}$ is along the beam axis, we can expand the field on the detector plane into spatial Fourier components

$$\vec{E}_+(\vec{s}, z_d, t) = \int \frac{\mathrm{d}^2 q}{(2\pi)^2} e^{i\vec{q}\cdot\vec{s}} \vec{E}_+(\vec{q}, z_d, t), \tag{7.4}$$

where z_d is the detector plane coordinate. Substituting back into (7.3), we obtain

$$P_d(t) = \frac{\eta c}{2\hbar\epsilon_0} \int \frac{\mathrm{d}^2 q}{(2\pi)^2} \left\langle \vec{E}_-(\vec{q}, z_d, t) \cdot \vec{E}_+(\vec{q}, z_d, t) \right\rangle. \tag{7.5}$$

Therefore, the photo-detection rate is simply the integral of the photo-detection rate for each Fourier mode.

Experimentally, the energy spectrum of the scattered field is measured by using a thin analyser foil mounted on an oscillating Doppler drive. The foil acts as a bandpass filter with bandwidth on the order of γ, with the Doppler shift of the oscillation shifting the filter peak. The full temporal response of this setup has been analysed in great detail by Heeg [73], who demonstrated that the time integrated photon counts of such a foil, for suitable time gating, is directly proportional to the energy spectrum of the thin-film response. Therefore, for our purposes it is sufficient to model the Doppler drive as an ideal frequency filter. This has the Fourier domain transmission response

$$T_{drive}(\omega, \Delta) = T_0 \delta(\omega - \Delta), \tag{7.6}$$

where Δ is the detuning of the analyser Doppler drive, and T_0 the transmission coefficient. In time domain we therefore have

$$T_{drive}(\tau, \Delta) = T_0 e^{-i\Delta\tau}. \tag{7.7}$$

The field incident on the detector is given by the convolution of the scattered field with the analyser,

$$E_+(\vec{q}, z_d, t) = \int \mathrm{d}\tau_b \, T_{drive}(t - \tau_a, \Delta)\vec{E}_{sc}(\vec{q}, z_d, \tau_b). \tag{7.8}$$

Using this notation, we can see that the detection rate from a given Fourier component is given by

$$\begin{aligned} P_d(q, t) \propto \int \mathrm{d}\tau_a \, \mathrm{d}\tau_b \, T_{drive}(t - \tau_a, \Delta)^* T_{drive}(t - \tau_b, \Delta) \\ \times \left\langle \vec{E}_{sc,-}(\vec{q}, z_d, \tau_a)\vec{E}_{sc,+}(\vec{q}, z_d, \tau_b) \right\rangle \\ = |T_0|^2 \int \mathrm{d}\tau_a \, \mathrm{d}\tau_b \, e^{i\Delta(\tau_a - \tau_b)} \left\langle \vec{E}_{sc,-}(\vec{q}, z_d, \tau_a) \cdot \vec{E}_{sc,+}(\vec{q}, z_d, \tau_b) \right\rangle. \end{aligned} \tag{7.9}$$

The scattered field in the linear regime is given by the convolution of the reflectivity with the incident field, times the phase factor $e^{i\phi_{dw}}$ accounting for the propagating from waveguide to detector,

$$\vec{E}_{sc,+}(\vec{q}, z_d, \tau_b) = e^{i\phi_{dw}} \int \mathrm{d}\tau_d \, \overleftrightarrow{R}(\vec{q}, \tau_b - \tau_d) \cdot \vec{E}_{in,+}(\vec{q}, z_w, \tau_d), \tag{7.10}$$

where z_w is the z coordinate of the waveguide top layer. Therefore, the linear response follows the same photon statistics as the incident beam. In particular, if we assume multiplicative noise, such as phase noise, we have

$$\left\langle E^i_{in,-}(\vec{q}, z, t)E^j_{in,+}(\vec{q}, z, t') \right\rangle = \alpha^i_{in}(\vec{q}, z, t)^* \alpha^j_{in}(\vec{q}, z, t) g_1(t - t'), \tag{7.11}$$

where g_1 is the normalized first order correlation function of the noise, and α_{in} is the average envelope of the beam. Because we must evaluate quantities involving cumbersome contractions over polarization tensors, we have labelled the polarization indices i, j explicitly. Substituting (7.10) and (7.11) into (7.9), we obtain

$$\begin{aligned} P_d(q, t) \propto |T_0|^2 \int \left(\prod_{\mu=a,b,c,d} \mathrm{d}\tau_\mu \right) \Big(e^{i\Delta(\tau_a - \tau_b)} R^{ij}(\vec{q}, \tau_a - \tau_c)^* R^{ik}(\vec{q}, \tau_b - \tau_d) \\ \times \alpha^j_{in}(\vec{q}, \tau_c)^* \alpha^k_{in}(\vec{q}, \tau_d) g_1(\tau_c - \tau_d) \Big). \end{aligned} \tag{7.12}$$

Expanding into Fourier components and integrating over the intermediate times gives

$$P_d(q, \Delta) \propto |T_0|^2 \mathcal{R}^{jk}(\vec{q}, \Delta) I^{jk}_{eff}(\Delta), \tag{7.13}$$

where

$$\mathcal{R}^{jk}(\vec{q}, \Delta) = R^{ij}(\vec{q}, \Delta)^* R^{ik}(\vec{q}, \Delta), \tag{7.14}$$

and the effective intensity tensor is the convolution of the coherent intensity with the Fourier transformed coherence function,

$$I^{jk}_{eff}(q,\Delta) = \frac{c}{2\epsilon_0}\int \frac{\mathrm{d}\omega}{2\pi}\alpha^{j}_{in}(\vec{q},\Delta-\omega)^{*}\alpha^{k}_{in}(\vec{q},\Delta-\omega)g_1(\omega). \tag{7.15}$$

One can clearly see that for a fully coherent beam this reduces to the Fourier transformed intensity. For a sufficiently broad band excitation, we can assume I_{eff} is constant as a function of q. At this stage, we note that the measured intensity consists of the average of many shots, and thus is insensitive to the nature of any angular spread. Specifically, (7.15) holds for both short time angular spread i.e. due to the intrinsic beam divergence of a single shot, and long time angular spread, i.e. an angle of incidence drift between shots.

We therefore finally obtain for the photo-detection rate

$$P_d = \frac{\eta c}{\hbar\omega_0\epsilon_0}|T_0|^2\int \frac{\mathrm{d}^2 q}{(2\pi)^2}\mathcal{R}^{jk}(\vec{q},\Delta)I^{jk}_{eff}(q). \tag{7.16}$$

7.1.2 Numerical example

To begin with, we shall evaluate the full width at half maximum (FWHM) angular width of a guided mode. Splitting the guided mode wave-vector into real and imaginary parts, we have

$$\frac{1}{q-q_r+iq_i} \tag{7.17}$$

for the Fourier space response of a pole in the Green's function. The input field is specified by its angle of incidence,

$$q = k_0\cos\theta. \tag{7.18}$$

We therefore have

$$q_r = k_0\cos\theta_0 \tag{7.19}$$

as the angular representation of the pole resonance angle. Let us now consider an incident field with a small deviation from this resonant angle,

$$q = k_0\cos(\theta_0+d\theta). \tag{7.20}$$

We then have

$$q \approx k_0\cos\theta_0 - k_0\sin\theta_0 d\theta, \tag{7.21}$$

for sufficiently small $d\theta$. The Lorentzian response as a function of $d\theta$ is then given by

$$\frac{1}{q-q_r+iq_i} = \frac{1}{-k_0\sin\theta\delta\theta+iq_i}. \tag{7.22}$$

The full width at half maximum is therefore given by

$$\delta\theta = \frac{q_i}{k_0\sin\theta_0}. \tag{7.23}$$

Now that we have the angular widths, we can proceed to consider the reflectivity observable, and how the relation between angular width of the resonances, and angular divergence of the beam affects these.

Reflectivity

As an example system, we consider a cavity with structure Pt (1.8 nm) / C (20.58 nm) / Stainless steel (0.53 nm) / C (24.45 nm) / Pt (15 nm). Such a cavity was used at beam-time ID HC-4028, ID18 at ESRF, November 2018. For convenience, we will refer to this structure by the name it was assigned during the experiment, 'Cavity E'.

The goal of this experiment was to demonstrate exceptional points in the collective hyperfine spectrum, as the magnetic field of the nuclei was increased [99]. However, due to a larger than expected inhomogeneous quadrupole distribution in the steel layer, as well as angular instability during the experiment, the effect was not observable. The beam divergence could be configured between 20 µrad and 200 µrad, and 30 µrad was the final selection. However, as we shall see, this is not enough to explain the observed angular broadening. As each synchrotron shot has on the order of single digit or less of average resonant photon counts per shot, even typical repetition rates of hundreds of ns require on the order of an hour or more to obtain statistically adequate photon counts. Thus, even a minor angular drift can accumulate significantly over this duration, and one should in general consider fitting a larger angular deviation that what was configuration.

Figure 7.1 gives the resonant angles and angular widths of the first three guided modes of Cavity E, while Figure 7.2 gives its Fourier transformed Green's function evaluated at the layer coordinate, with a typical experimental FWHM highlighted. It is clear to see that the angular widths are of comparable size to the beam divergences, and as such it is questionable if a single mode approximation is valid. In particular, for the first guided mode, the collective Lamb shift varies enormously over the incident beams angular width, and thus the spectrum will not resemble the single mode solution at all. This is illustrated dramatically in Figure 7.3, which shows the theoretical reflectivity for a two-level resonant layer coupled to the first guided mode, taking into account the incident beam divergence. As low as a 20 µrad beam divergence still results in a greatly exaggerated reflectivity wing, and gives the impression of a lower collective broadening than actually occurs. The effect is far more dramatic at 200 µrad, with the spectrum distorted into appearing as a narrow Fano profile.

Even with the larger angular width, there is a noticeable effect on the third guided mode, Figure 7.4. The apparent collective Lamb shift and broadening is less strongly reduced until the most extreme beam divergences, however the contrast of the Fano profile is reduced at larger beam divergences, giving the impression of a higher cavity loss rate than is actually the case for the guided mode. As a result, if one were to attempt fitting experimental data for this scenario, without taking into account the beam divergence, one would make erroneous conclusions for the cavity structure.

This is illustrated by the experimental energy spectra for Cavity E, Figures 7.7 and 7.8. This spectrum exhibited an isotropic quadrupole distribution, of approximately 1.99γ mean and 0.37γ FWHM, and isomer shift of 1.98γ. In order to qualitatively fit the experimental spectra, a beam divergence on the order of 50 µrad was required.

Thus, in this section, we have demonstrated that the single mode approximation is not always valid at current experimental conditions. It is therefore crucial for theoretical predictions, and fits to experimental data compute the effects of a divergent beam, or erroneous conclusions can be drawn.

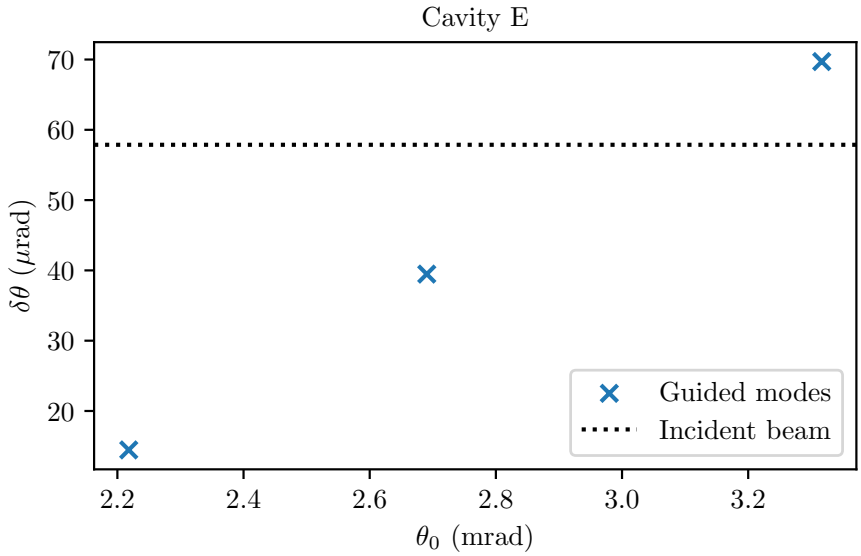

Figure 7.1: Angular positions and widths of the first three guided modes of Cavity E. Highlighted is the observed total angular spread of 57.87 µrad, which includes the 30 µrad beam divergence as well as the effect of angular instability.

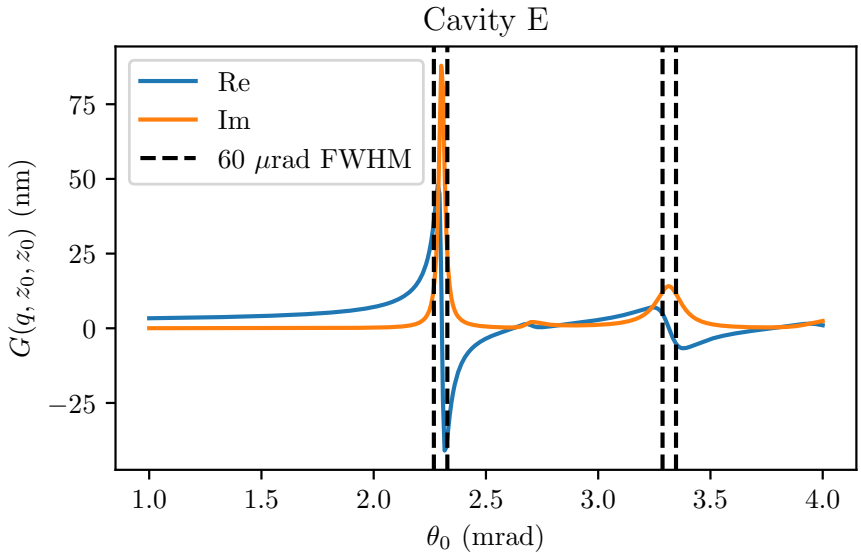

Figure 7.2: Fourier transformed Green's function of Cavity E, evaluated at the resonant layer. Real part is proportional to the collective Lamb shift, while the imaginary part is proportional to the super-radiant broadening. Highlighted are a 60 µrad interval around the peak location for the two strongly coupled guided modes, illustrating that the self-interaction of the nuclei is not constant within the spatial bandwidth of the input beam.

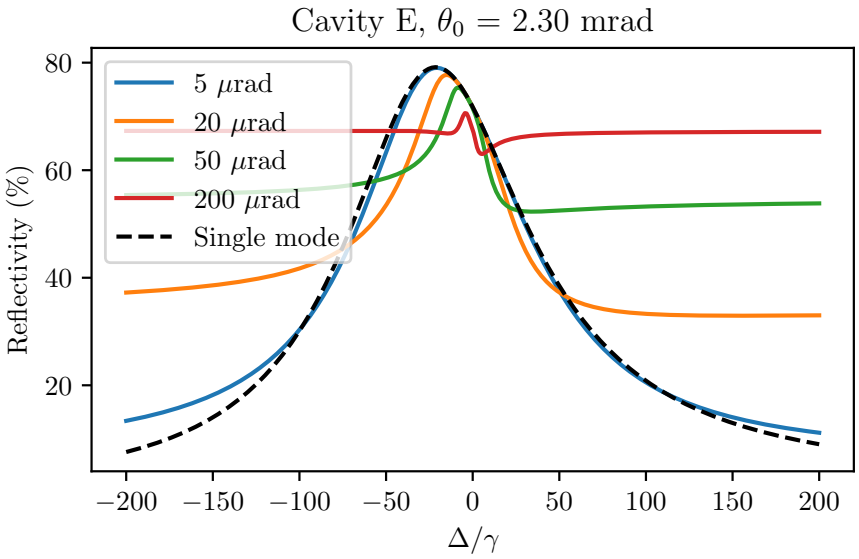

Figure 7.3: Divergence averaged reflectivity for beam incident at the first guided mode. Due to the incredibly narrow resonance, Figure 7.2, even relatively small beam divergences result in large distortions of the spectrum.

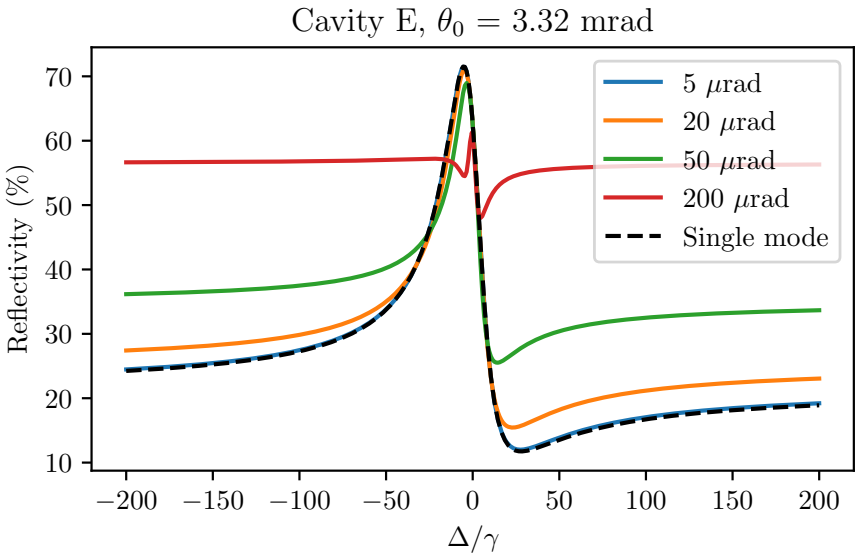

Figure 7.4: Divergence averaged reflectivity for beam incident at the first guided mode. Due to the larger angular width of the resonance, Figure 7.2, the effect is qualitatively less dramatic than Figure 7.3, nevertheless it is strong enough that one must clearly factor this in to curve-fitting and theoretical predictions.

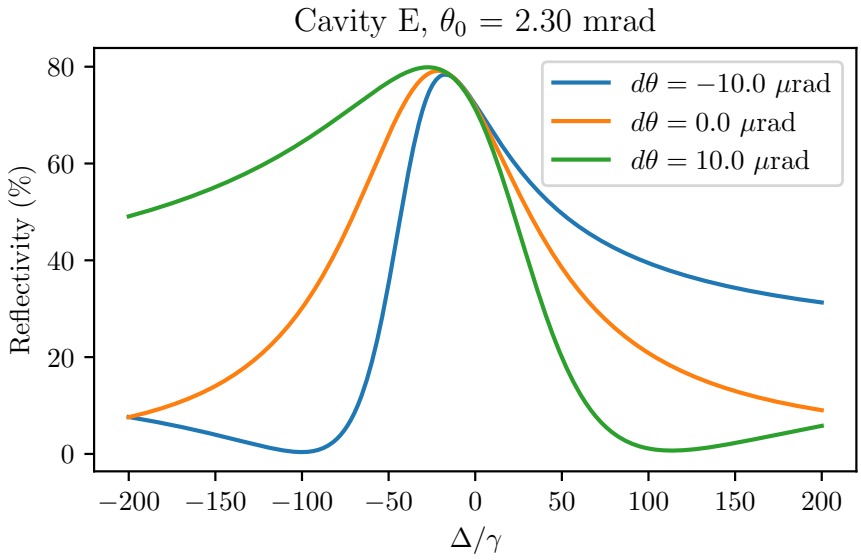

Figure 7.5: Sample of three of the reflectivity components that are averaged for a 20 µrad beam divergence, incident at the first guided mode. Due to the dramatic change in collective Lamb shift seen in Figure 7.2, the spectra for angular deviation either side of the peak are mirrored, and thus the average distorts the line-shape completely.

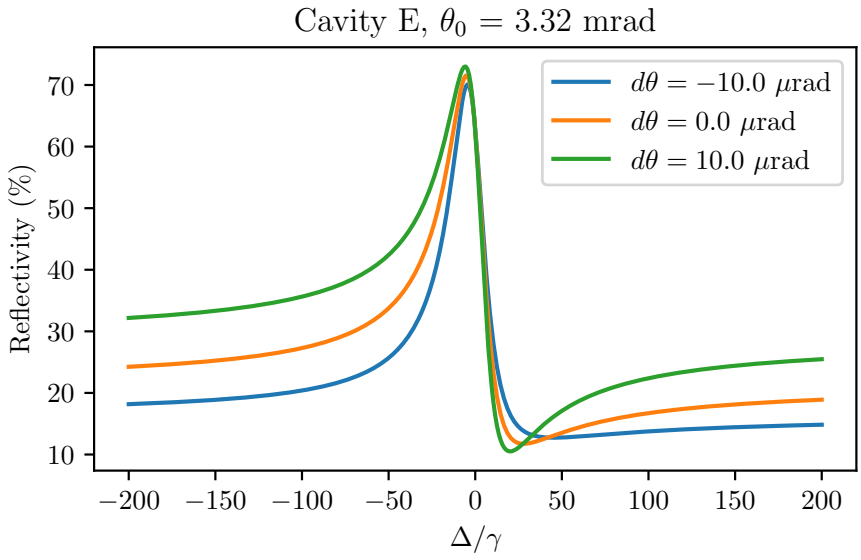

Figure 7.6: Sample of three of the reflectivity components that are averaged for a 20 µrad beam divergence, incident at the third guided mode. As one deviates from the resonance, the contrast of the Fano profile reduces, and thus the average of the spectra gives a misleadingly low contrast for the peak location.

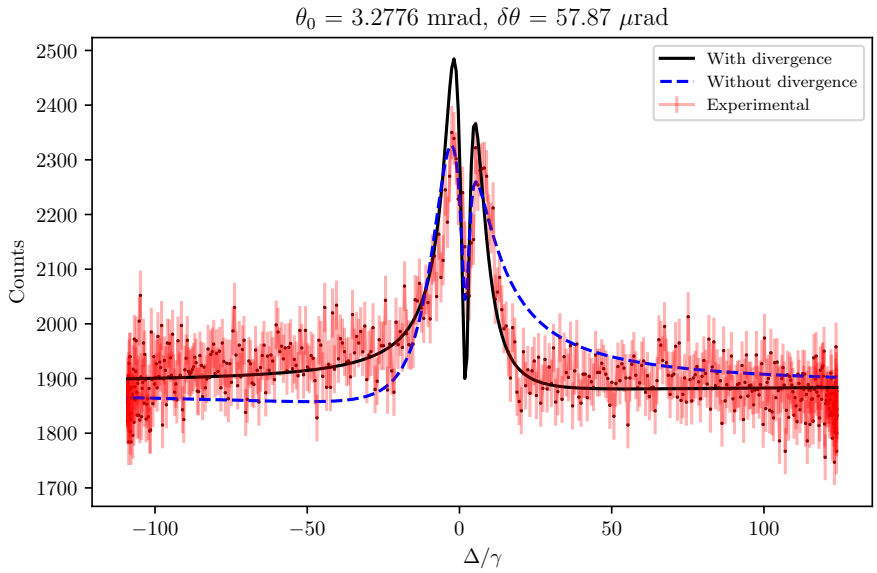

Figure 7.7: Experimental data for cavity E, measured close to third guided mode resonance. The hyperfine spectrum exhibited an isotropic quadrupole splitting, with a distribution of widths. A qualitative fit was only possible taking beam divergence into account. Fitting the low contrast centre of the peaks remains a challenge however.

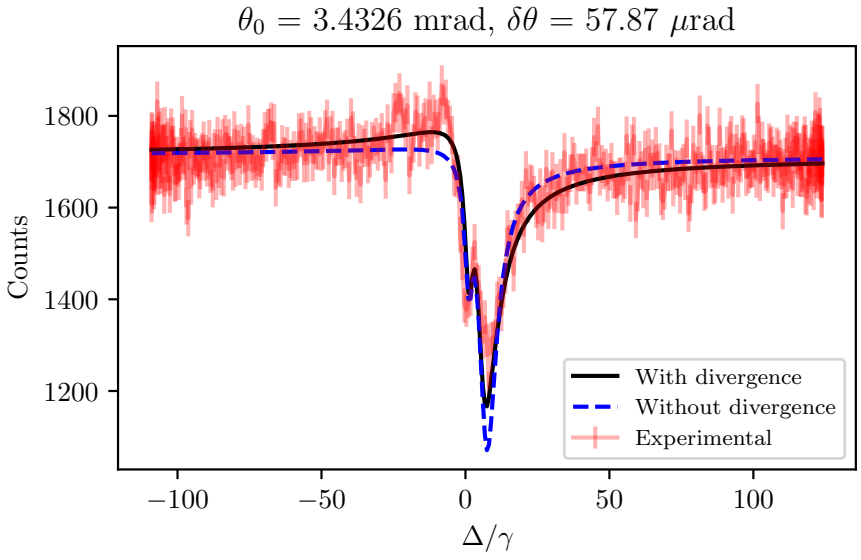

Figure 7.8: Experimental data for cavity E, measured slightly away from third guided mode resonance.

7.2 Superradiance and inhomogeneous hyperfine fields

In this section, we will consider the effects of inhomogeneous hyperfine distributions on the collective response of nuclei in grazing incidence. For a single Fourier mode interacting with identical nuclei, the grazing incidence equations of motion reduce to the Dicke model. However, the layers of the thin-film nano-structures are formed through vacuum sputter deposition, and thus have inhomogeneous hyperfine fields throughout their extent. Nevertheless, in Appendix B.1 we demonstrate that for such systems, we can use the coherent average of the individual susceptibilities to model the inhomogeneous broadening. Therefore, the positive frequency field evaluated at the resonant layer obeys the equation

$$\begin{aligned}\vec{B}_+(q,z_0,\omega) &= \vec{B}_{in}(q,z_0,\omega) \\ &\quad - \mu_0 k_0^2 L \rho_N \mathcal{G}_{TE}(q,z_0,z_0,\omega_0) \overleftrightarrow{\mathbb{1}} \cdot \overleftrightarrow{\chi}(\omega) \cdot \vec{B}_+(q,z_0,\omega), \end{aligned} \tag{7.24}$$

where for a probability distribution $p(\vec{\nu})$ of n hyperfine parameters $\vec{\nu}$ we have

$$\overleftrightarrow{\chi}_+(\omega) = \int \mathrm{d}^n \nu \, p(\vec{\nu}) \overleftrightarrow{\chi}_+(\vec{\nu},\omega), \tag{7.25}$$

with $\overleftrightarrow{\chi}(\vec{\nu},\omega)$ the susceptibility evaluated for a particular set of parameters.

We wish to find the collective susceptibility of the nuclear ensemble. To do this, we first define the dimensionless response tensor

$$\overleftrightarrow{\mathcal{F}}(\omega) = \frac{1}{f_0} \overleftrightarrow{\mathbb{1}}_\perp \cdot \overleftrightarrow{\chi}_+(\omega) \cdot \overleftrightarrow{\mathbb{1}}_\perp, \tag{7.26}$$

$$f_0 = \frac{2\pi f_{LM}}{1+\alpha} \frac{2I_e+1}{2I_g+1} \frac{\mu_0}{k_0^3}, \tag{7.27}$$

where the factor of f_0 eliminates the overall prefactor of χ. Additionally, projection onto the polarization subspace allows us to eliminate these projectors from the rest of the equations of motion. Let us also define the collective enhancement factor,

$$\begin{aligned}\zeta &= k_0^2 L f_0 \rho_N \mathcal{G}_{TE}(q,z_0,z_0,\omega_0) \\ &= -f_0 \rho_N L G_{mm}(q,z_0,z_0,\omega_0). \end{aligned} \tag{7.28}$$

The field is then given by

$$\vec{B}_+(q,z_0,\omega) = \vec{B}_{in}(q,z_0,\omega) - \zeta \overleftrightarrow{\mathcal{F}}(\omega) \cdot \vec{B}_+(q,z_0,\omega). \tag{7.29}$$

This then has the solution

$$\vec{B}(q,z_0,\omega) = \left(\overleftrightarrow{\mathbb{1}} + \zeta \overleftrightarrow{\mathcal{F}}(\omega) \right)^{-1} \cdot \vec{B}_{in}(q,z_0,\omega). \tag{7.30}$$

For systems with isotropic response tensors, we can treat $\mathcal{F}(\omega)$ as scalar, and this can be simplified to

$$\vec{B}(q,z_0,\omega) = \frac{\vec{B}_{in}(q,z_0,\omega)}{1+\zeta \mathcal{F}(\omega)}. \tag{7.31}$$

Finally, the scattered response is given by

$$\vec{B}_{sc}(q,z_0,\omega) = -\zeta \overleftrightarrow{\mathcal{F}}(\omega) \cdot \left(\overleftrightarrow{\mathbb{1}} + \zeta \overleftrightarrow{F}(\omega) \right)^{-1} \cdot \vec{B}_{in}(q,z_0,\omega). \tag{7.32}$$

Thus, for the collective susceptibility, we obtain,

$$\overleftrightarrow{\chi}_{coll}(\omega) = \chi_0 \overleftrightarrow{F}(\omega) \cdot \left(\overleftrightarrow{\mathbb{1}} + \zeta \overleftrightarrow{\mathcal{F}}(\omega)\right)^{-1}, \tag{7.33}$$

$$\chi_0 = \frac{\zeta}{\mu_0 \rho_N}. \tag{7.34}$$

For the rest of this chapter, we will consider the collective susceptibility only, and therefore refer to this simply as χ from now on. The single particle susceptibilities of the individual nuclei are implicitly contained in $F(\omega)$.

For the particular case of a two-level system, the nuclear response tensor is isotropic (see Appendix B.3), and can be treated as scalar. Thus we have

$$\mathcal{F}(\omega) = \frac{\gamma_0}{\omega + i\gamma_0}, \tag{7.35}$$

where for convenience we have labelled the half width at half maximum (HWHM) line-width as $\gamma_0 = \gamma/2$. The collective response is then given by

$$\chi(\omega) = \chi_0 \frac{\mathcal{F}(\omega)}{1 + \zeta\mathcal{F}(\omega)} = \chi_0 \frac{\gamma_0}{\omega + i\gamma_0 + \zeta\gamma_0}. \tag{7.36}$$

If we define

$$J + i\Gamma = \zeta\gamma_0, \tag{7.37}$$

we can see that this gives us the expected collective Lamb shift and broadening,

$$\chi(\omega) = \frac{\chi_0}{\omega + i\gamma_0 + J + i\Gamma}. \tag{7.38}$$

Now that we have seen how to obtain the collective response, let us proceed in the following sections to consider some explicit examples of collective responses for inhomogeneously broadened systems.

7.2.1 Gaussian broadening for two level systems

As an illustrative example, we consider a layer of resonant Mössbauer nuclei with a Gaussian distribution of the isomer shift δ. Such Gaussian distributions of hyperfine parameters are typical of amorphous solids [100–102]. For simplicity, we will consider the other hyperfine splittings to be negligible.

The isomer shift affects all excited states equally, and the distribution does not affect the dipole vectors or the natural line-widths. As we are taking the other hyperfine splittings to be negligible, all states with a given nuclear spin I are degenerate, and we can model the system as having a single transition. As a result, the susceptibility is isotropic. We therefore find that the average nuclear response tensor is given by

$$\mathcal{F}(\omega) = \int \mathrm{d}\delta\, p(\delta) \frac{\gamma_0}{\omega - \delta + i\gamma_0}. \tag{7.39}$$

With a Gaussian distribution,

$$p(\delta; \bar{\delta}, \sigma) = \frac{1}{\sqrt{2\pi\sigma^2}} \exp\left(-\frac{(\delta - \bar{\delta})^2}{2\sigma^2}\right), \tag{7.40}$$

this evaluates to a Voigt profile [103, Eq. 7.19],

$$\mathcal{F}(\omega) = f_0 \frac{\gamma}{\sqrt{2}\sigma} w\left(\frac{\omega - \bar{\delta} + i\gamma_0}{\sqrt{2}\sigma}\right), \tag{7.41}$$

where

$$w(z) = -i\sqrt{\pi}\exp\left(-z^2\right)(\mathrm{erfh}(z) - i). \tag{7.42}$$

The collective susceptibility is then given by

$$\chi(\omega) = \chi_0 \frac{\mathcal{F}(\omega)}{1 + \gamma_0^{-1}(J + i\Gamma)\mathcal{F}(\omega)}. \tag{7.43}$$

The interaction of the coherent collective coupling J, and the broadening σ is particularly interesting. Unlike the case of purely collective broadening Γ, for significant distribution widths σ the coherent coupling factor J no longer acts as a simple Lamb shift. Indeed, if J were to act as a Lamb shift one would expect instead a susceptibility of

$$\chi(\omega) = \chi_0 \mathcal{F}(\omega + J + i\Gamma), \tag{7.44}$$

with a simple translation and broadening. Instead, the peak of the spectrum is shifted slightly further than it would be in the absence of the Gaussian broadening, and is asymmetrically distorted. This is shown in Fig. 7.10 which presents the ratio $|\chi(\omega)/\chi_0|^2$ as a function of ω for three distributions widths σ.

At this point we find it interesting to compare our linear regime results with the work of Javanainen *et al* [104, 105] and Jenkins *et al* [106], who have examined the effect of inhomogeneous broadening on strongly coupled atomic clouds near saturation. In this regime, local spatial correlations become significant, and permutation symmetry no longer applies. They found that the local correlations in homogeneously broadened systems suppresses the Lorentz-Lorenz and collective Lamb shifts, while inhomogeneous broadening restores the super-radiant mean field dynamics [104]. We note that the case of inhomogeneous broadening shows some qualitative similarity to our linear regime result, Fig. 7.10, where we observe a larger peak shift for inhomogeneous broadening vs. the unbroadened case.

For illustrative purposes, we have used values of J, Γ in the range $(0-10)\gamma$, $(3-5)\gamma_0$, typical of x-ray cavities. For example, using the dyadic Green's function to simulate the single line spectrum, we find the cavity in Figure 7.9 has $J = 8.5\gamma_0$ and $\Gamma = 3.36\gamma_0$ at an incident angle of 2.32 mrad, corresponding to just below the first reflection minimum. Going exactly to the first minimum gives $J = 5.5\gamma_0$, and increases Γ significantly to $\Gamma = 18.6\gamma_0$. At an angle of 3.35 mrad, corresponding to the third reflection minimum, we have $J = 1.79\gamma_0$ and $\Gamma = 3.37\gamma_0$. Typical hyperfine distribution widths are between $(0-5)\gamma_0$. In optical contexts (for example Doppler broadening in atomic clouds, or size inhomogeneity in quantum dots), we would expect that the distribution widths could be substantially larger.

For significant distribution widths $\sigma \gg \gamma_0$, the line shape is that of a broad, almost Gaussian profile. However, as the collective coupling J is increased, as well as being shifted and skewed, the effective line-width tends to that of the incoherent coupling Γ. Figure 7.11 illustrates this behaviour for increasing coherent collective coupling J.

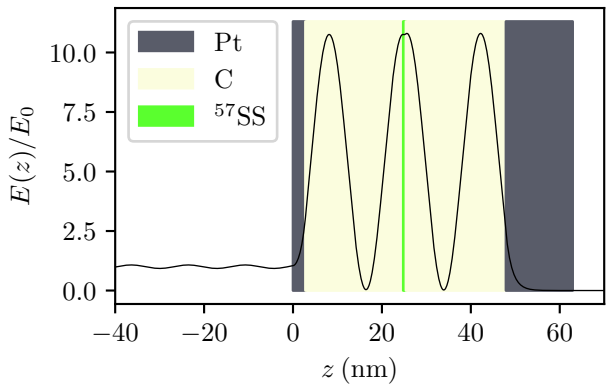

Figure 7.9: Field profile in a typical grazing incidence cavity, driven at the third guided mode. Cavity structure is Pt 2.8 nm/C 22 nm/ ^{57}SS 0.6 nm/ C 22.5 nm/Pt 15 , where ^{57}SS refers to ^{57}Fe enriched stainless steel.

7.2.2 Interference effects for magnetic splitting

Let us now consider the case of magnetic splitting in ^{57}Fe with no isomer shift and an x-ray field which drives the two $m_e - m_g = 0$ transitions as shown in Figure 2.1. The energies of these two transitions are detuned by $\pm\phi = \pm\frac{1}{2}(\mu_e - \mu_g)B_{\rm hf}$, where μ_g, μ_e are the nuclear magnetic dipole moments for the ground and excited states respectively. For a single Fourier mode interacting with identical nuclei, the grazing incidence equations of motion reduce to the Dicke model. In particular, in the linear regime, one can assign Bosonic operators to the collective transition operators [107],

$$\sum_i \hat{\Pi}^{(i)}_{\mu j} e^{iqx_i} \approx \sqrt{\frac{N}{2I_e+1}} b_{\mu j}, \tag{7.45}$$

where q is the incident wave-vector, and N is the total number of nuclei. These Bosonic operators obey [107]

$$[b_{\mu j}, b^\dagger_{\mu' j'}] = \delta_{\mu\mu'}\delta_{jj'}. \tag{7.46}$$

As we have two participating transitions, we will label them b_1, b_2. It can be shown that these collective transition operators then obey the equation of motion [107]

$$H = \hbar\phi(b_1^\dagger b_1 - b_2^\dagger b_2) - \hbar J(b_1^\dagger + b_2^\dagger)(b_1 + b_2) + \hbar\Omega(b_1^\dagger + b_2^\dagger) + \text{h.c} \tag{7.47}$$

with Lindblad operator

$$L[\rho] = -\gamma_0 \sum_{i=1,2} \mathscr{L}[\rho, b_i^\dagger, b_i] - \Gamma \sum_{i,j=1,2} \mathscr{L}[\rho, b_i^\dagger, b_j]. \tag{7.48}$$

The superradiant response of such a system was investigated by Kong and Pálffy [38] using an eigenvalue method. It was found that if the splitting ϕ is less than the incoherent part of the collective coupling Γ, the contributions from the two transitions interfere. The resulting spectrum has an interference dip in the peak, similar to

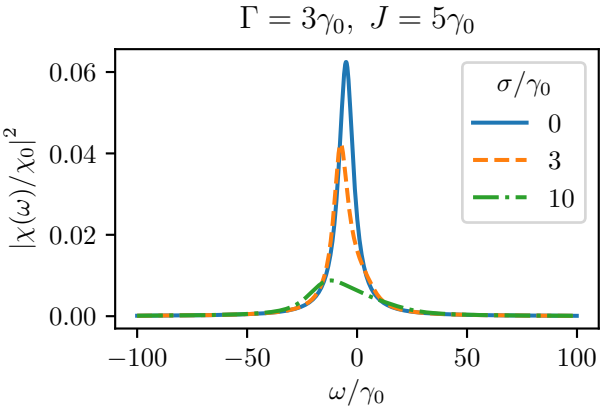

Figure 7.10: Collective spectrum $|\chi(\omega)/\chi_0|^2$ as a function of the frequency ω for $J = 5\gamma_0$ and three different distribution widths σ. The peak is shifted further as the broadening is increased, and the shape is distorted.

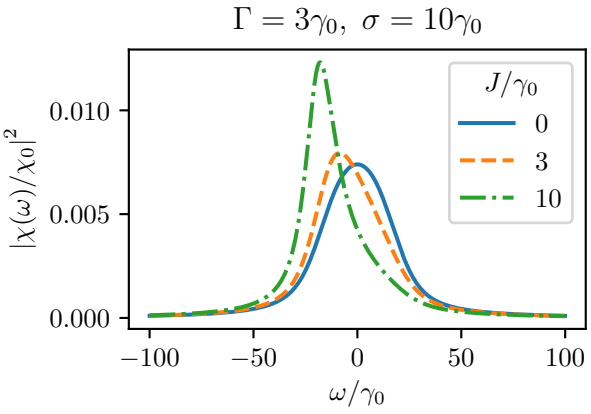

Figure 7.11: Collective spectrum $|\chi(\omega)/\chi_0|^2$ as a function of the frequency ω for $\sigma = 10\gamma_0$ and three different collective coupling values J. With increasing coherent collective coupling J the shape of the spectrum is distorted asymmetrically, and the effective line-width tends to Γ.

electromagnetically induced transparency (EIT) [10], with the collective coupling J playing the role of a control field. In addition, the coherent part of the collective coupling, J, was found not to act as a simple Lamb shift, but in fact non-trivially couple with the magnetic splitting, producing asymmetric, Fano-like spectra.

We now consider this system with the addition of a Gaussian distribution of magnetic field strengths across the sites. For a given site with splitting ϕ, the response matrix is given by [38]

$$\mathcal{F}(\omega;\phi) = \frac{2\gamma(\omega+i\gamma_0)}{(\omega+i\gamma_0)^2-\phi^2}. \tag{7.49}$$

In the case of a completely uniform magnetic field, the collective susceptibility is therefore given by

$$\chi(\omega) = \chi_0 \frac{2\gamma_0(\omega+i\gamma_0)}{(\omega+i\gamma_0)^2+2(J+i\Gamma)(\omega+i\gamma_0)-\phi^2}. \tag{7.50}$$

This has two poles in the denominator,

$$\omega_\pm = -i\gamma_0 - J - i\Gamma \pm \sqrt{(J+i\Gamma)^2+\phi^2}. \tag{7.51}$$

When the collective coupling is completely incoherent, $J = 0$, the discriminant becomes $\sqrt{\phi^2-\Gamma^2}$. We can see that if $\phi < \Gamma$, the argument of the square root becomes negative, and the poles become purely imaginary, describing overlapping Lorentzians with differing linewidths. This results in an EIT like dip. This behaviour is illustrated in Fig. 7.12 which presents the susceptibility ratio $|\chi(\omega)/\chi_0|^2$ as a function of ω for four different values of the Gaussian distribution width σ.

If we now consider the magnetic splitting to have a Gaussian distribution of width σ, and mean $\bar{\phi}$, applying Equations (7.25) and(7.41) gives

$$\begin{aligned}\mathcal{F}(\omega) &= \int \mathrm{d}\phi\, p(\phi;\bar{\phi},\sigma)F(\omega;\phi)\\ &= \frac{\gamma_0}{\sqrt{2}\sigma}\left(w\left(\frac{\omega-\bar{\phi}+i\gamma_0}{\sqrt{2}\sigma}\right)+w\left(\frac{\omega+\bar{\phi}+i\gamma_0}{\sqrt{2}\sigma}\right)\right),\end{aligned} \tag{7.52}$$

with $w(z)$ given by Equation (7.42). The susceptibility is as before given by

$$\chi(\omega) = \chi_0 \frac{\mathcal{F}(\omega)}{1+\gamma_0^{-1}(J+i\Gamma)\mathcal{F}(\omega)}. \tag{7.53}$$

The overall envelope of the spectrum resembles that of the homogeneous case, and if the distribution width σ is narrow compared with Γ, $\bar{\phi}$, we can see that the intensity minimum is still resolvable. However, increasing the distribution width gradually flattens the dip, and results in a flat, broad peak as shown in Figure 7.12.

More interesting is the effect of different strengths of the coherent collective coupling J. Rather than acting as a simple Lamb shift, the overall spectral shape is changed. One peak is flattened as the other increases, with large J resulting in a completely asymmetric picture with only a single one of the contributions being resolved. This can be seen in Figure 7.13 which presents the same dependence as Figure 7.12 but this time for different values of J. While the peak locations are somewhat shifted, the shapes are distorted as well, and the location of the minimum

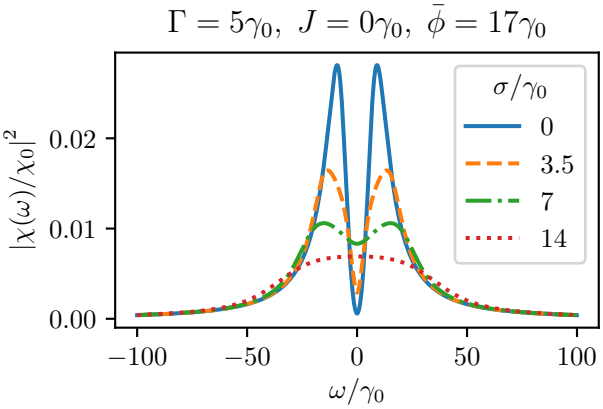

Figure 7.12: Comparison of collective spectrum $|\chi(\omega)/\chi_0|^2$ as a function of the frequency ω for $\Gamma = 5\gamma_0$, $J = 0$, with mean splitting $\bar{\phi} = 17\gamma_0$ and various values of distribution width σ. As the distribution width increases, the dip is washed out to a very flat and broad peak.

is unchanged. This is in contrast to the single line case, where J acts as a pure Lamb shift.

This holds even when the distribution width is large enough that the minimum is not resolved, as shown in Fig. 7.14. For vanishing collective coupling, $J = 0$, the two peaks are merged, and the effective linewidth is very broad. Increasing J results in the left peak growing while the right peak diminishes, and for significant J only the left peak is individually resolved, with the line-width approaching 2Γ. The result is an increase in the effective resolution of the spectrum, with an energy shift. As the coherent coupling strength is controlled via the angle of incidence of the driving field [39, 74], this provides a mechanism for mechanical control of the line-width of such a sample.

To understand this, we consider the matrix form of the corresponding equation of motion,

$$M \begin{pmatrix} b_1(\omega) \\ b_2(\omega) \end{pmatrix} = \begin{pmatrix} \Omega(\omega) \\ \Omega(\omega) \end{pmatrix} \tag{7.54}$$

with

$$M = (J + i\Gamma) \begin{pmatrix} 1 & 1 \\ 1 & 1 \end{pmatrix} + \begin{pmatrix} \phi + i\gamma_0 & 0 \\ 0 & -\phi + i\gamma_0 \end{pmatrix}. \tag{7.55}$$

and $\Omega(\omega) = \hbar^{-1} m_0 B_{in}(\omega)$.

If J is large enough compared with ϕ, γ_0, we may treat the second term as a small perturbation of the first. The eigenvectors of M are then given by

$$\hat{e}_\pm = \frac{1}{\sqrt{2}} \begin{pmatrix} 1 \\ \pm 1 \end{pmatrix} + \mathcal{O}(\phi), \tag{7.56}$$

with eigenvalues

$$\lambda_+ = 2(J + i\Gamma) + \mathcal{O}(\phi), \quad \lambda_- = \mathcal{O}(\phi) \tag{7.57}$$

The driving term couples to b_1, b_2 equally, and is thus proportional to $\hat{e}_+$. Therefore, only the symmetric state $\hat{e}_+$ is strongly driven, and we will expect to see a single peak,

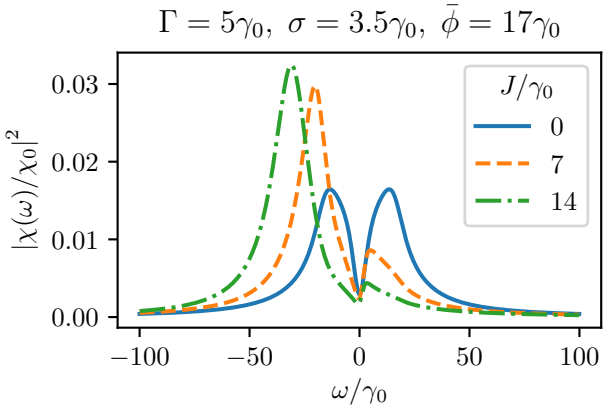

Figure 7.13: Comparison of collective spectrum $|\chi(\omega)/\chi_0|^2$ as a function of the frequency ω for small incoherent coupling $\Gamma = 5\gamma_0$, a small distribution width value $\sigma = 3.5\gamma_0$, mean splitting $\bar{\phi} = 17\gamma_0$ and varying values of coherent collective coupling J.

with a Lamb shift of $2J$ and a broadening of 2Γ. If the collective broadening Γ is significantly lower than the distribution width σ, we will then see a reduction in the effective line-width. This has potential applications in samples with significant magnetic texture, with the beam angle of incidence on the sample being used to control the collective coupling, and hence the effective line-width.

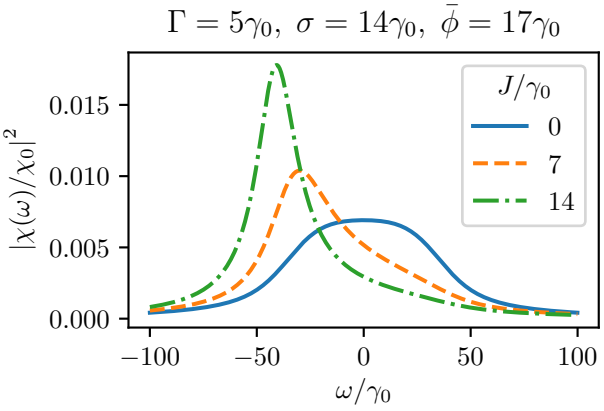

Figure 7.14: The same as Fig. 7.13 but here for a wider distribution width $\sigma = 14\gamma_0$.

Chapter 8

Forward scattering

In this chapter, we demonstrate how nuclear forward scattering can be modelled in the Green's function approach. We begin in Section 8.1 with a re-derivation of ordinary nuclear forward scattering within the Green's function approach, such that we may use it as a point of comparison with waveguide front coupling. By doing so, we demonstrate that the same model that describes collective Rabi oscillation in the atomic optics case [16, 108–110] also applies to the dynamical beat of nuclear forward scattering, and thus these two terms describe the same phenomenon.

Following this, in Section 8.2 we analyse waveguide front coupling, and demonstrate how this leads to analogous equations of motion to nuclear forward scattering in the single mode regime. We then proceed to consider the multiple mode regime, and consider two extremes of coupling strength: one where electronic scattering is far larger than nuclear scattering, and one where it is far smaller. Using perturbation theory, we show that in the strong nuclear scattering regime, the mode coupling to the nuclei leads to formation of a single opaque mode, with the remaining modes being transparent to the nuclei.

Finally, in Section 8.3, we study in depth the interference effects that occur in the two mode regime, and demonstrate that this can be used to implement models of super-radiance and sub-radiance from atomic optics.

8.1 Nuclear forward scattering in the Green's function approach

We will begin by demonstrating how the ordinary nuclear forward scattering equations can be derived using the Green's function approach. For simplicity, we will work in free space, however in a homogeneous medium one simply needs to substitute

$$k = \frac{\omega}{c} \rightarrow k = \frac{n\omega}{c}, \tag{8.1}$$

where n is the refractive index of the medium.

We begin with the dyadic Green's function for free space,

$$\overleftrightarrow{G}(\vec{r}, \vec{r}', \omega) = \int \frac{\mathrm{d}^3 q}{(2\pi)^3} \frac{\overleftrightarrow{\mathbb{1}} - \hat{q} \otimes \hat{q}}{q^2 - k^2} e^{i\vec{q}\cdot(\vec{r}-\vec{r}')}. \tag{8.2}$$

The corresponding magnetic Green's function is given by

$$\begin{aligned}\overleftrightarrow{G}_{mm}(\vec{r},\vec{r}',\omega) &= \nabla\times\overleftrightarrow{G}(\vec{r},\vec{r}',\omega)\times\nabla' \\ &= -\int\frac{\mathrm{d}^3q}{(2\pi)^3}q^2\frac{\overleftrightarrow{\mathbb{1}}-\hat{q}\otimes\hat{q}}{q^2-k^2}e^{i\vec{q}\cdot(\vec{r}-\vec{r}')},\end{aligned} \tag{8.3}$$

where we have used

$$\hat{q}\times\hat{q}=0, \tag{8.4}$$

$$\hat{q}\times\overleftrightarrow{\mathbb{1}}\times\hat{q}=-(\overleftrightarrow{\mathbb{1}}-\hat{q}\otimes\hat{q}). \tag{8.5}$$

We consider an incident beam propagating in the positive x direction, and uniform in the y,z plane,

$$\hat{B}_{in}(\vec{r},t)=e^{-i(\omega_0 t-k_0 x)}B_0(x,t)\hat{e}, \tag{8.6}$$

where $\hat{e}$ is the polarization vector of the incident beam, and $B_0(x,t)$ the slowly varying beam envelope. We can similarly replace the scattered field and nuclear magnetization as a slowly varying envelope times plane wave phase,

$$\hat{B}_{sc,+}(x,\omega)\to\hat{B}_{sc,+}(x,\omega)e^{ik_0x}, \tag{8.7}$$

$$\hat{m}_{+}(x,\omega)\to\hat{m}_{+}(x,\omega)e^{ik_0x}. \tag{8.8}$$

As the incident beam is uniform in y,z, so is the induced nuclear magnetization, and thus the scattered response envelope is given by

$$\begin{aligned}\hat{B}_{sc,+}(x,\omega) &= \mu_0\rho_N\int\mathrm{d}^3r'\,e^{-ik_0(x-x')}\overleftrightarrow{G}_{mm}(\vec{r},\vec{r}',\omega)\cdot\overleftrightarrow{\chi}_{+}(\omega)\cdot\hat{B}_{+}(x',\omega) \\ &= \mu_0\rho_N\int\mathrm{d}x'\,\overleftrightarrow{G}_{1D}(x-x',\omega)\cdot\overleftrightarrow{\chi}_{+}(\omega)\cdot\hat{B}_{+}(x',\omega),\end{aligned} \tag{8.9}$$

where

$$\begin{aligned}\overleftrightarrow{G}_{1D}(x-x',\omega) &= \int\mathrm{d}y'\,\mathrm{d}z'\,\overleftrightarrow{G}_{mm}(\vec{r}-\vec{r}',\omega) \\ &= -\int\frac{\mathrm{d}q}{2\pi}q^2\frac{\overleftrightarrow{\mathbb{1}}-\hat{x}\otimes\hat{x}}{q^2-k^2}e^{iq(x-x')}.\end{aligned} \tag{8.10}$$

This can be evaluated using contour integration. In order to enforce outward propagating boundary conditions, we displace the pole at $q=k$ to $k+i0^+$, and $q=-k$ to $-k-i0^+$. We then close contour in the positive upper half plane for $x>x'$, and the lower half plane for $x<x'$. This gives

$$\overleftrightarrow{G}_{1D}(x-x',\omega)=-\frac{ik}{2}(\overleftrightarrow{\mathbb{1}}-\hat{x}\otimes\hat{x})e^{ik|x-x'|} \tag{8.11}$$

As discussed in Section 6.3.1, we must consider the dispersion of the Green's function over the resonant bandwidth of the nuclei. Firstly, we can see that the phase has the linear dispersion discussed in Section 6.3.1, that cannot be neglected, in order to properly account for the retarded time.

Secondly, we see that the prefactor of k has a linear dispersion, leading to the series expansion

$$\overleftrightarrow{G}_{1D}(x-x',\omega+\omega_0)\approx-\overleftrightarrow{\mathbb{1}}_{\perp}\frac{ik_0}{2}e^{ik_0|x-x'|+i\omega c^{-1}|x-x'|}\left(1+\frac{\omega}{\omega_0}+\mathcal{O}\left(\frac{\omega^2}{\omega_0^2}\right)\right). \tag{8.12}$$

Since the resonant bandwidth is on the order of $10^{-12}\omega_0$, we can safely neglect the dispersion in the envelope. We therefore have the following equation of motion for the scattered field envelope:

$$\hat{B}_{sc,+}(x,\omega) = \frac{i\mu_0 k_0 \rho_N}{2} \int \mathrm{d}x'\, e^{i(k_0+\frac{\omega}{c})|x-x'|} e^{-ik_0(x-x')} \hat{m}_+(x',\omega). \tag{8.13}$$

There are two contributions: the forward scattering contribution from $x' < x$, and the back scattering from $x' > x$. The back scattering contribution will have a phase factor in the integrand of $e^{-2ik_0x'}$, which we assume is outside the bandwidth of our envelopes. We therefore neglect the back scattering,

$$\hat{B}_{sc,+}(x,\omega) \approx \frac{i\mu_0 k_0 \rho_N}{2} \int_0^x \mathrm{d}x'\, e^{i\frac{\omega}{c}(x-x')} \hat{m}_+(x',\omega). \tag{8.14}$$

Inverting to time domain, we obtain the nuclear forward scattering equation in integral form,

$$\hat{B}_{sc,+}(x,t) = \frac{i\mu_0 \rho_N k_0}{2} \int_0^x \mathrm{d}x'\, \hat{m}_+(x', t - c^{-1}(x-x')). \tag{8.15}$$

Taking a spatial derivative gives

$$\partial_x \hat{B}_{sc,+}(x,t) = \frac{i\mu_0 \rho_N k_0}{2} \hat{m}_+(x,t) - c^{-1}\partial_t \hat{B}_{sc,+}(x,t), \tag{8.16}$$

which can be rearranged to give a paraxial Maxwell's equation for the field envelope,

$$(\partial_x + c^{-1}\partial_t)\hat{B}_+(x,t) = \frac{i\mu_0 \rho_N k_0}{2} \hat{m}_+(x,t), \tag{8.17}$$

where we have used the fact that the input field is the homogeneous solution,

$$(\partial_x + c^{-1}\partial_t)\hat{B}_{in}(x,t) = 0, \tag{8.18}$$

to substitute the scattered field with the total field.

The time derivative from the retarded time can be eliminated with the coordinate transformation

$$t \to t_r = t - \frac{x}{c}, \tag{8.19}$$

$$x \to x, \tag{8.20}$$

$$\partial_t \to \partial_{t_r}, \tag{8.21}$$

$$\partial_x \to \partial_x - c^{-1}\partial_{t_r}. \tag{8.22}$$

We finally obtain

$$\partial_x \hat{B}_+(x,\tau) = \frac{i\mu_0 \rho_N k_0}{2} \hat{e}_{in}^* \cdot \hat{m}_+(x,\tau), \tag{8.23}$$

with $\hat{m}(x,\tau)$ obeying the nuclear Bloch equations (6.14) through (6.17), under the substitution $\partial_t \to \partial_{t_r}$.

8.1.1 Fourier space solution

Using the Fourier space expression for the magnetization

$$\hat{m}_+(x,\omega_r) = -\overleftrightarrow{\chi}_+(\omega_r)\cdot\hat{e}_{in}\hat{B}_+(x,\omega_r), \tag{8.24}$$

we have

$$\partial_x\hat{B}_+(x,\omega_r) = -i\frac{k_0}{2}F(\omega_r)\hat{B}_+(x,\omega_r), \tag{8.25}$$

where ω_r is the Fourier dual of the retarded time t_r, and the dimensionless response function

$$F(\omega) = \mu_0\rho_N\hat{e}^*_{in}\cdot\overleftrightarrow{\chi}_+(\omega)\cdot\hat{e}_{in}. \tag{8.26}$$

The solution of this equation of motion is

$$\hat{B}_+(x,\omega_r) = \exp\left(-i\frac{k_0x}{2}F(\omega_r)\right)\hat{B}_{in}(0,\omega_r), \tag{8.27}$$

where we have used the fact that the scattered field at the initial position $x = 0$ is zero, to rewrite the boundary condition in terms of $\hat{B}_{in}$ only. For a broadband pulse, we can approximate the Fourier transformed field as uniform over the bandwidth of the nuclei, and take

$$\hat{B}_{in}(0,t_r) \approx \frac{B_{in}}{\Gamma_{in}}\delta(t_r), \tag{8.28}$$

where Γ_{in} is the bandwidth of the incident field.

8.1.2 Two level solution in time domain

Under the two level regime, using equation (B.31) we obtain

$$F(\omega) = \rho_N\frac{\sigma_0}{k_0}\cdot\frac{f_{LM}}{1+\alpha}\cdot\frac{2I_e+1}{2I_g+1}\cdot\frac{\gamma/2}{\omega+i\gamma/2} = \rho_N\frac{\sigma_{rad}}{k_0}\frac{\gamma/2}{\omega+i\gamma}, \tag{8.29}$$

where we have defined the partial radiative cross-section

$$\sigma_{rad} = \frac{2I_e+1}{2I_g+1}\frac{\sigma_0}{1+\alpha}. \tag{8.30}$$

Thus we see that the response function is identical to that of Kagan [68, eq. 3.1, 3.2], demonstrating that macroscopic Green's function formalism can reproduce results of the single photon scattering theory. The solution to (8.27), (8.28), (8.29) is given by [68, 79]

$$\hat{B}_+(x,t_r) = \frac{B_{in}}{\Gamma_{in}}\left(\delta(t_r) - e^{-\gamma t_r/2}\gamma\xi\frac{J_1(2\sqrt{\xi\gamma t_r})}{\sqrt{\xi\gamma t_r}}\right), \tag{8.31}$$

where J_1 is a Bessel function of the first kind, and

$$\xi = \frac{\rho_N\sigma_{rad}xf_{LM}}{4} \tag{8.32}$$

is the dimensionless 'effective resonant length' [68, 70]. We note that the only difference between our solution and Kagan's is the substitution of the real time with the retarded time, which is to be expected as Kagan considered thin foils, and thus neglected propagation delays.

8.1.3 Comparison to collective Rabi oscillations

In the atomic optics literature, the oscillation in the scattered field of dense ensembles of atoms is referred to as 'collective Rabi oscillation' [16, 108–110]. The theoretical models used to describe this use the Green's function coupled dipole-dipole approach, and as such are equivalent to the model we have considered in this section. In particular, Svidzinsky [16] derived the solution for collective Rabi oscillations due to a plane wave excitation of a dense linear chain of atoms, and obtained the same expression as (8.31). As he included the effects of time delay in his model, his expression also included the retarded time delay. Thus, we can clearly see that the dynamical beat of nuclear forward scattering is the same phenomenon as collective Rabi oscillation, and can be modelled using the same Green's function approach.

8.2 Waveguide forward scattering

We now turn our attention back to the multi-layer waveguide. We will demonstrate that under front coupling, such that a single resonant mode is excited, the resulting equations of motion result in forward scattering equations similar to those of 8.1.

8.2.1 Two-dimensional problem

We consider an incident pulse propagating along x, that is uniform along y. The resonant nuclei are placed in a thin layer of thickness L in the plane $z = z_0$. We assume the layer is sufficiently thin that we can take the nuclei to have a delta distribution in the z coordinate.

Due to the uniformity in y, and the thin layer, we may substitute

$$\hat{m}(\vec{r}, t) \to L\delta(z - z_0)\hat{m}(x, t) \tag{8.33}$$

$$\hat{B}(\vec{r}, t) \to \hat{B}(x, z, t), \tag{8.34}$$

thus making the problem two-dimensional.

The scattered positive frequency field of the nuclei satisfies

$$\hat{B}_{sc,+}(x, \omega) = -\mu_0 \rho_N L \iint \mathrm{d}x' \, \mathrm{d}y' \, \overleftrightarrow{G}_{mm}(x - x', y - y', z, z_0, \omega) \cdot \hat{m}_+(x, \omega). \tag{8.35}$$

The Fourier representation of $\overleftrightarrow{G}_{mm}(\vec{r}, \vec{r}')$ in Cartesian coordinates is explicitly

$$\overleftrightarrow{G}_{mm}(x - x', y - y', z, z', \omega) = \iint_{-\infty}^{\infty} \frac{\mathrm{d}q_x}{2\pi} \frac{\mathrm{d}q_y}{2\pi} e^{iq_x(x-x')} e^{iq_y(y-y')} \overleftrightarrow{G}_{mm}(q_x, q_y, z, z', \omega), \tag{8.36}$$

where we distinguish between the Fourier and real space quantities by their argument.

Due to cylindrical symmetry, the Green's function can be written in the form

$$\overleftrightarrow{G}_{mm}(q_x, q_y, z, z', \omega) = U(\phi_q) \overleftrightarrow{G}_{mm}(q, 0, z, z', \omega) U(\phi_q)^{\dagger}, \tag{8.37}$$

where $U(\phi)$ is a rotation matrix, and

$$q_x = q \cos(\phi_q), \quad q_y = q \sin(\phi_q). \tag{8.38}$$

Integrating out the y' coordinate gives

$$\int \mathrm{d}y'\, e^{iq_y(y-y')} = 2\pi\delta(q_y)e^{iq_y y}. \tag{8.39}$$

To evaluate the integral over the Dirac delta, we make use of the following pull-back identity,

$$\int \mathrm{d}^n r\, f(\vec{r})\delta(g(\vec{r})) = \int_\Omega \mathrm{d}\mu(\vec{s})\, \frac{f(\vec{s})}{|\nabla g|}, \tag{8.40}$$

where Ω is the surface defined by $g(\vec{r}) = 0$, and $\mathrm{d}\mu(\vec{s})$ is the induced surface measure with respect to the choice of surface parameterization $\vec{s}$. In our case, $g(q, \phi_q) = q\sin(\phi_q)$, with the zero hyper-surface given by the line $\phi_q = 0$. The induced surface measure is merely the Euclidean measure $\mathrm{d}q$. We also have

$$\nabla g = \sin(\phi_q)\hat{\phi}_q + \cos(\phi_q)\hat{q}, \quad |\nabla g| = 1. \tag{8.41}$$

Thus, we have the following identity,

$$\int \mathrm{d}^2 q\, \delta(q\sin(\phi_q))f(q, \phi_q) = \int_{-\infty}^{\infty} \mathrm{d}q\, f(q, 0). \tag{8.42}$$

Finally, applying this to our Green's function allows us to obtain the effective two-dimensional Green's function for the resonant layer,

$$\overleftrightarrow{G}_{2D}(x - x', z, z', \omega) = \int_{-\infty}^{\infty} \frac{\mathrm{d}q}{2\pi} e^{iq(x-x')} \overleftrightarrow{G}_{2D}(q, z, z', \omega), \tag{8.43}$$

where

$$\overleftrightarrow{G}_{2D}(q, z, z', \omega) = \overleftrightarrow{G}_{mm}(q, 0, z, z', \omega) \approx -k^2 \overleftrightarrow{G}(q, 0, z, z', \omega). \tag{8.44}$$

With the relevant Green's function in hand, let us now examine the nucleus-field coupling.

8.2.2 Coupling to nuclei

We begin with the mode decomposition of the waveguide Green's function,

$$\overleftrightarrow{G}_{2D}(q, z, z', \omega) = -k^2 \sum_\lambda \int \frac{\mathrm{d}q}{2\pi} \overleftrightarrow{G}_\lambda(\vec{q}, z, z', \omega) e^{i\vec{q}\cdot(\vec{r}_\parallel - \vec{r}'_\parallel)} - k^2 \overleftrightarrow{G}_{rad}(q, z, z', \omega). \tag{8.45}$$

As per Chapter 4, we have

$$\overleftrightarrow{G}_\lambda(q, z, z', \omega) = \frac{\overleftrightarrow{g_\lambda}(z, z', \omega)}{q - q_\lambda(\omega)} + \text{c.c.}, \tag{8.46}$$

where q_λ is the wave-vector of the mode, and the residue is given by

$$\overleftrightarrow{g_\lambda}(z, z', \omega) \approx \overleftrightarrow{\mathbb{1}}_\perp \frac{i}{2q_\lambda} u_\lambda(z, \omega) u_\lambda(z', \omega), \tag{8.47}$$

where u_λ is the mode function normalized according to (4.99). Due to the normalization, the product $u_\lambda(z)u_\lambda(z')$ has the dimension of inverse length, thus $\overleftrightarrow{g_\lambda}$ is dimensionless.

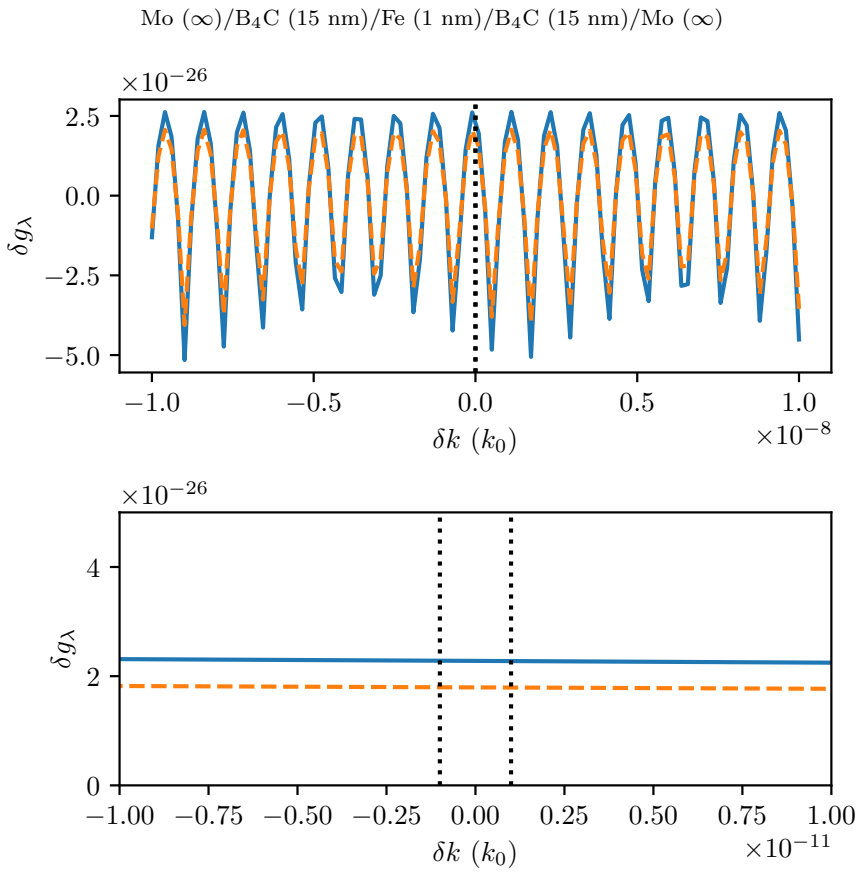

Figure 8.1: Dispersion of first guided mode residue for a molybdenum waveguide, with nuclear bandwidth highlighted and zoomed in bottom panel. We can see that there is no conceivably observable dispersion.

As one can see in Figures 8.1 and 8.2, the dispersions of both the mode residue g_λ and mode wave-vector q_λ are negligible over the resonant bandwidth of the nuclei, with a fractional variation on the order of 10^{-6} for q_λ and essentially zero for g_λ. We can therefore take

$$\overleftrightarrow{G}_\lambda(q, z, z', \omega) \approx \overleftrightarrow{G}_\lambda(q, z, z', \omega_0). \tag{8.48}$$

We will therefore drop the frequency argument of u_λ, q_λ etc. from our notation, and assume they are evaluated at ω_0.

The magnetic field can be expanded into the basis of eigenmodes,

$$\hat{B}_+(x, z, t) = \sum_\lambda \hat{B}_\lambda(x, t) u_\lambda(z) + \hat{B}_{rad}(x, z, t), \tag{8.49}$$

and due to the orthonormality of eigenmodes, we can see that the scattered response

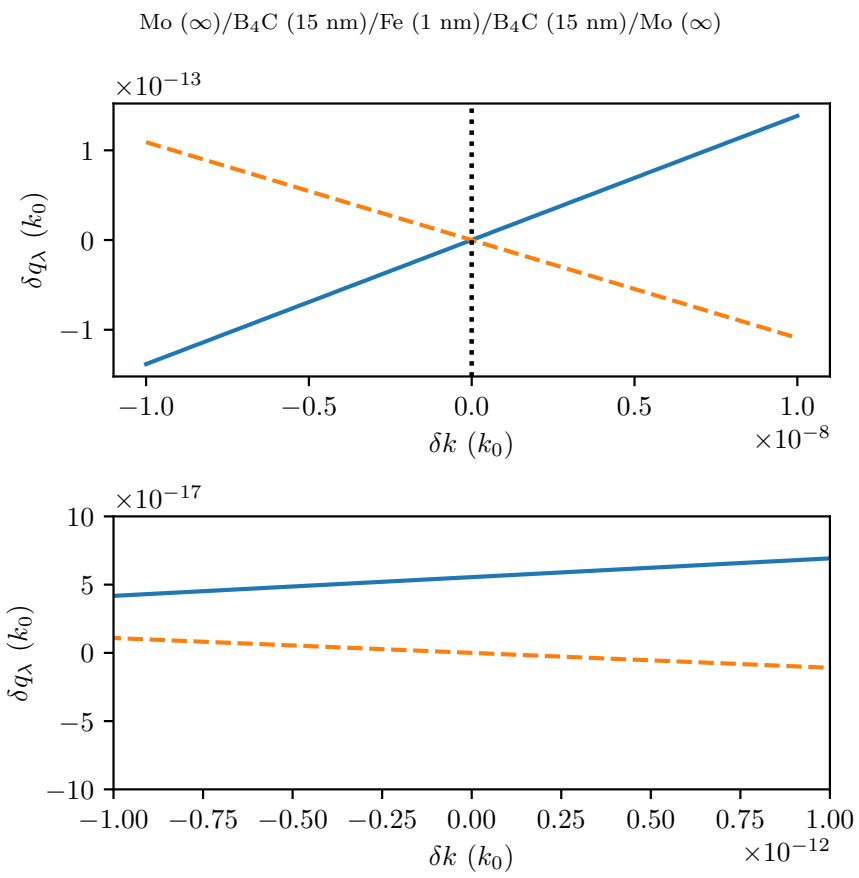

Figure 8.2: Dispersion of first guided mode wave-number for a molybdenum waveguide, with nuclear bandwidth highlighted and zoomed in bottom panel. There is only a small linear dispersion of approximately $10^{-6}k_0$, and thus the corresponding phase velocity is exceedingly large. As such, propagation delays can be neglected.

of each mode is given by

$$\hat{B}_{sc,\lambda}(x,\omega) = \mu_0 \rho_N L \frac{ik_0^2}{2q_\lambda} u_\lambda(z_0) \int \mathrm{d}x'\, e^{iq_\lambda|x-x'|} \overleftrightarrow{\mathbb{1}}_\perp \cdot \hat{m}_+(x',\omega). \tag{8.50}$$

In turn, the magnetization is given by

$$\hat{m}_+(x,\omega) = -\overleftrightarrow{\chi}_+(\omega) \cdot \sum_\lambda u_\lambda(z_0)\hat{B}_\lambda(x,\omega). \tag{8.51}$$

Thus, the magnetization is coupled to each resonant mode proportional to the value of its mode function at the resonant layer, as expected. We will now proceed to derive and solve the equation of motion of a single mode waveguide, which is the simplest model to consider.

8.2.3 Single mode solution

If the waveguide is sufficiently thin, only the first one or two modes are supported. The nuclear layer can then be placed at the anti-node of the fundamental mode, with higher modes suppressed. Then, one can neglect the other modes, and consider the single mode problem.

In this regime, we find that

$$\hat{B}_\lambda(x,\omega) = -i\frac{k_0^2 L}{2q_\lambda}F(\omega)u_\lambda(z_0)^2\int_0^x \mathrm{d}x'\, e^{iq_\lambda(x-x')}\hat{B}_\lambda(x,\omega), \tag{8.52}$$

with $F(\omega)$ the response function defined in (8.29).

We can see our first figure of merit: the relative coupling strength. We saw that for nuclear forward scattering, the prefactor was

$$-\frac{ik_0}{2}F(\omega), \tag{8.53}$$

while for front coupling it is given by

$$-\frac{ik_0^2 L}{2q_\lambda}u_\lambda(z_0)^2F(\omega). \tag{8.54}$$

The dimensionless relative coupling strength is therefore

$$\zeta_\lambda = u_\lambda(z_0)^2\frac{k_0 L}{2q_\lambda} = g_\lambda(z_0,z_0)k_0 L, \tag{8.55}$$

and we can interpret this as the ratio of the guided mode cross-section to the free-space cross-section.

To transform (8.52) into (8.27), we first eliminate the exponential from the integrand by defining

$$\beta(x,\omega) = e^{-iq_\lambda x}\hat{B}_\lambda(x,\omega). \tag{8.56}$$

Substituting into (8.52) and taking a spatial derivative gives

$$\partial_x\beta(x,\omega) = -\frac{ik_0\zeta_\lambda}{2}F(\omega)\beta(x,\omega). \tag{8.57}$$

This then has the solution

$$\beta(x,\omega) = \exp\left(-\frac{ik_0 x\zeta}{2}F(\omega)\right)\beta(0,\omega). \tag{8.58}$$

Adding back the phase from (8.56) gives

$$\hat{B}_\lambda(x,\omega) = \exp\left(iq_\lambda x - \frac{ik_0 x\zeta}{2}F(\omega)\right)\hat{B}_\lambda(x,\omega). \tag{8.59}$$

This can be solved via Kagan's method, to obtain

$$B_\lambda(x,t) = \frac{B_{in}}{\Gamma_{in}}e^{iq_\lambda x}\left(\delta(t) - e^{-\gamma t/2}\gamma\xi_\lambda\frac{J_1(2\sqrt{\xi_\lambda\gamma t})}{\sqrt{\xi_\lambda\gamma t}}\right), \tag{8.60}$$

where now the guided mode 'effective resonant length' is given by

$$\xi_\lambda = \frac{\rho_N \sigma_{rad} x \zeta_\lambda f_{LM}}{4}. \tag{8.61}$$

We can see the primary differences are the scaling of the effective resonant length with the mode factor ζ_λ, the guided mode envelope, and the absence of retardation effects. Indeed, the incredibly small dispersion of the resonant wavevector over the nuclear bandwidth implies that that guided modes have a propagation speed enormously larger than c, on the order of 10^6 times faster! However, we bear in mind that this is a group velocity, and as such is only an apparent velocity, much like a shadow from a moving light source can be observed to have arbitrarily large speeds when projected sufficiently far from the source. If one considers the full frequency response of the problem, outside the resonant bandwidth, Kramers-Kronig consistency enforces causality.

We are therefore to interpret this incredibly large group velocity as reflecting the large mismatch in bandwidth between the waveguide and the nuclei: the waveguide is broad-band, and has a dispersion on far larger frequency scales, and therefore emission into the guided mode equilibrates much faster than the decay of the nuclear coherence. As such, the time delay between the emission and absorption of radiation from nuclei placed at different x coordinates has a negligible effect on the steady state behaviour of the system, which is reflected as a group velocity much larger than c.

8.2.4 Multiple modes

For multiple resonant modes, we find

$$B_\lambda(x,\omega) = -iF(\omega)\frac{k_0^2 L}{2p_\lambda} u_\lambda(z_0) \sum_{\lambda' \in \Lambda} u_{\lambda'}(z_0) \int_0^x \mathrm{d}x'\, e^{iq_\lambda(x-x')} B_{\lambda'}(x',\omega), \tag{8.62}$$

where Λ is the set of modes. Taking a spatial derivative and multiplying by the mode function gives

$$u_\lambda(z_0)\partial_x B_\lambda(x,\omega) = i \sum_{\lambda' \in \Lambda} K_{\lambda\lambda'}(\omega) u_{\lambda'}(z_0) B_{\lambda'}(x,\omega), \tag{8.63}$$

where

$$K_{\lambda\lambda'}(\omega) = Q_{\lambda\lambda'} - M_{\lambda\lambda'}(\omega), \tag{8.64}$$

$$Q_{\lambda\lambda'} = q_\lambda \delta_{\lambda\lambda'} \tag{8.65}$$

$$M_{\lambda\lambda'}(\omega) = \zeta_\lambda \frac{k_0}{2} F(\omega). \tag{8.66}$$

Here, we have split the coupling matrix into guided mode electronic part Q, and nuclear part M. We have neglected the effect of dispersion as its magnitude is absurdly low over the resonant bandwidth of the nuclei.

For convenience, we will introduce bra-ket notation for the mode functions. Specifically, we can write

$$|B(x,z_0,\omega)\rangle = \sum_{\lambda \in \Lambda} B_\lambda(x,z_0,\omega)\,|\lambda\rangle\,. \tag{8.67}$$

In this notation, one can see that

$$B_\lambda(x, z_0, \omega) = \langle \lambda | B(x, z_0, \omega) \rangle \,, \tag{8.68}$$

while the total field is given by

$$B(x, z_0, \omega) = \langle + | B(x, z_0, \omega) \rangle \,, \tag{8.69}$$

where N_Λ is the number of modes, and

$$|+\rangle = \sum_{\lambda \in \Lambda} |\lambda\rangle \,. \tag{8.70}$$

Using this notation, is clear to see that M is a rank one matrix,

$$M(\omega) = \frac{k_0}{2} F(\omega) \, |\zeta\rangle\langle +| \tag{8.71}$$

where

$$|\zeta\rangle = \sum_{\lambda \in \Lambda} \zeta_\lambda \, |\lambda\rangle \,. \tag{8.72}$$

As such, the only non-trivial right eigenvector is $|\zeta\rangle$ itself, with eigenvalue

$$\frac{k_0}{2} F(\omega) \sum_{\lambda \in \Lambda} \zeta_\lambda \,. \tag{8.73}$$

The remaining eigenvectors are trivial (i.e. zero eigenvalue), and span the kernel (i.e. right null space) of $M(\omega)$. As such, their choice of basis is completely arbitrary, and can be obtained using the Gram-Schmidt process.

The left eigenvectors are similarly given by $\langle +|$ with the same eigenvalue as $|\zeta\rangle$, and the remaining eigenvectors spanning the co-kernel (i.e. left null space).

8.2.5 Strong coupling regime

Let us consider a regime where $|Q| \ll |M|$, such that we can approximate it as a small perturbation. This is the 'strong coupling' regime, i.e. the nuclear scattering is much stronger than the electronic scattering.

As the null vectors of M are degenerate, we must take care with our choice of perturbation. In addition, M is not symmetric, and therefore its eigenvectors do not form an orthonormal basis. However, for perturbation purposes, we only require that the eigenvectors of our *initial* matrix are orthonormal, and we are free to have a non-symmetric perturbation. The null space of M has an orthonormal basis, and is also orthogonal to $|S\rangle\langle S|$, where

$$|S\rangle = \frac{1}{\sqrt{N_\Lambda}} \, |+\rangle \,, \tag{8.74}$$

is the normalized symmetric state, with N_Λ the number of modes. Therefore,

$$\{|S\rangle\} \cup \ker(M), \tag{8.75}$$

where $\ker(M)$ denotes the null space of M, is an orthonormal basis.

To handle the degeneracy, as well as the non-symmetric nature of M, we will use the diagonal of M, Q with respect to the symmetric basis as our initial matrix. Defining the projectors

$$P_l = |l\rangle\langle l|\,, \tag{8.76}$$
$$P_S = |S\rangle\langle S|\,, \tag{8.77}$$
$$P_S + \sum_{l\in\ker(M)} |l\rangle\langle l| = \mathbb{1}, \tag{8.78}$$

We first decompose M according to

$$M = P_S M P_S + V_Q, \tag{8.79}$$

where we note that as $|l\rangle$ is a null vector,

$$P_l M P_l = 0. \tag{8.80}$$

Q is decomposed as,

$$Q = Q_{\ker(M)} + Q_S + V_Q, \tag{8.81}$$
$$Q_{\ker(M)} = \sum_l P_l Q P_l, \tag{8.82}$$
$$Q_S = P_S Q P_S. \tag{8.83}$$

Our initial matrix is then explicitly given by

$$H = Q_{\ker(M)} + Q_S - P_S M P_S \tag{8.84}$$

with the perturbation given by

$$V = V_Q - V_M. \tag{8.85}$$

At this stage we note that by construction, H is symmetric and non-degenerate, and therefore its eigenvectors are orthonormal. As such, we can use ordinary perturbation theory, even though the perturbation V is not symmetric.

Using ϵ as a perturbation parameter, the problem we wish to solve is

$$(H + \epsilon V)\,|S\rangle = k_S\,|S\rangle\,, \tag{8.86}$$
$$(H + \epsilon V)\,|l\rangle = k_l\,|l\rangle\,, \tag{8.87}$$
$$k_S = \sum_n \epsilon^n k_S^{(n)}, \tag{8.88}$$
$$k_l = \sum_n \epsilon^n k_l^{(n)}, \tag{8.89}$$
$$|S\rangle = \sum_n \epsilon^n \left|S^{(n)}\right\rangle, \tag{8.90}$$
$$|l\rangle = \sum_n \epsilon^n \left|l^{(n)}\right\rangle. \tag{8.91}$$

To zeroth order, the eigenvectors of the full interaction matrix K will therefore simply be the eigenvalues of H, and by construction the eigenvalues of the left

eigenvalues of M. In particular, $|S\rangle$ will be an eigenvector, and the corresponding mode has the solution

$$B_S(x,z,\omega) = \langle 1|U|B(x,z,\omega)\rangle = \langle 1|U|S\rangle\, e^{ik_S^{(0)}(\omega)x} B_S(0,z,\omega), \tag{8.92}$$

where explicitly we have

$$k_S^{(0)}(\omega) = -\frac{k_0}{2}\xi_\zeta F(\omega) + q_S^{(0)}, \tag{8.93}$$

$$\xi_\zeta = \sum_\lambda \zeta_\lambda, \tag{8.94}$$

$$q_S^{(0)} = \langle S|Q|S\rangle = \frac{1}{N_\Lambda}\sum_{\lambda\in\Lambda} q_\lambda, \tag{8.95}$$

We can see that this state is 'opaque': it has a dynamical beat, with an enhanced effective resonant length that is the sum of each individual modes resonant length. The electronic contribution is simply the mean of each mode's wave-vector and refractive index.

On the other hand, the remaining modes are left null vectors of $M(\omega)$,

$$\langle l|\, M(\omega) = 0, \tag{8.96}$$

and therefore have the solution

$$B_l(x,z,\omega) = \langle l|U|B(x,z,\omega)\rangle = e^{ik_l^{(0)}(\omega)x} B_l(0,z,\omega), \tag{8.97}$$

$$k_l^{(0)}(\omega) = q_l^{(0)}, \tag{8.98}$$

$$q_l^{(0)} = \langle l|Q|l\rangle\,, \tag{8.99}$$

$$n_l^{(0)} = \langle l|\mathcal{N}|l\rangle\,. \tag{8.100}$$

We can see that to zeroth order, the null vectors are 'transparent': they do not interact with the nuclei at all, and therefore propagate only with their corresponding electronic contributions.

We can then in principle continue this process for higher order corrections, but this is less qualitatively useful due to the frequency dependence of the perturbation, and as such we will stop here, and instead proceed to explicitly analyse the solution for a wave-guide with two-modes as a case study.

8.3 Super-radiance and sub-radiance for two mode coupling

In this section, we consider a two mode waveguide, and a spatially patterned resonant layer. Specifically, let us assume that the nuclei within the resonant layer are placed in micro-strips of width w, located at coordinates (x_n, z_0), where z_0 is the overall resonant layer z coordinate, and x_n is the location of the nth micro-strip centre along the x axis. For strips that are sufficiently narrow compared to the gradient of the envelopes of the guided modes, the nuclei in each strip will experience a uniform envelope, and we can then take the number density of resonant nuclei to be

$$\rho(\vec{r}) = \rho_N w L \delta(z - z_0) \sum_n \delta(x - x_n). \tag{8.101}$$

The scattered response in mode λ from the n micro-strip is given by

$$\begin{aligned} B^{(n)}_{sc,\lambda}(x,\omega) = -i\frac{k_0 w}{2} F(\omega)\zeta_\lambda \Theta(x - x_n) e^{iq_\lambda (x-x_n)} \\ \times \left(B^{(n)}_{sc,1}(x_n,\omega) + B^{(n)}_{sc,2}(x_n,\omega) + B^{(n-1)}(x_n,\omega) \right) \end{aligned} \tag{8.102}$$

where $B^{(n-1)}$ is the total field including the scattering of all previous micro-strips,

$$\begin{aligned} B^{(n-1)}(x,\omega) =& B_{in,1}(0,\omega)e^{iq_1 x} + B_{in,2}(0,\omega)e^{iq_2 x} \\ &+ \sum_{m=1}^{n} \left(B^{(n-m)}_{sc,1}(x,\omega) + B^{(n-m)}_{sc,2}(x,\omega) \right), \end{aligned} \tag{8.103}$$

$$B^{(0)}(x,\omega) = B_{in}(x,\omega), \tag{8.104}$$

with B_{in} the input field. For convenience, we have dropped the explicit notation of the layer z coordinate, z_0. We can see the total fields obey the recurrence relation

$$B^{(n)}(x,\omega) = B^{(n-1)}(x,\omega) + B^{(n)}_{sc}(x,\omega), \tag{8.105}$$

$$B^{(n)}_{sc}(x,\omega) = B^{(n)}_{sc,1}(x,\omega) + B^{(n)}_{sc,2}(x,\omega). \tag{8.106}$$

Equation (8.102) can be solved by evaluating at the position of the nth microstrip,

$$B^{(n)}_{sc,1}(x_n,\omega) = -\zeta_1 f(\omega)(B^{(n)}_{sc,1}(x_n,\omega) + B^{(n)}_{sc,2}(x_n,\omega) + B^{(n-1)}(x_n,\omega)), \tag{8.107}$$

$$B^{(n)}_{sc,2}(x_n,\omega) = -\zeta_2 f(\omega)(B^{(n)}_{sc,1}(x_n,\omega) + B^{(n)}_{sc,2}(x_n,\omega) + B^{(n-1)}(x_n,\omega)), \tag{8.108}$$

$$f(\omega) = \frac{ik_0 w F(\omega)}{2}. \tag{8.109}$$

We thus have the recursive solution for $x_n \le x \le x_{n+1}$,

$$B^{(n)}_{sc,1}(x_n,\omega) = -\frac{\zeta_1 f(\omega)}{1 + (\zeta_1 + \zeta_2) f(\omega)} B^{(n-1)}(x_n,\omega), \tag{8.110}$$

$$B^{(n)}_{sc,2}(x,\omega) = -\frac{\zeta_2 f(\omega)}{1 + (\zeta_1 + \zeta_2) f(\omega)} B^{(n-1)}(x_n,\omega), \tag{8.111}$$

$$B^{(n)}_{sc}(x,\omega) = -(\zeta_1 e^{iq_1(x-x_n)} + \zeta_2 e^{iq_2(x-x_n)}) \frac{f(\omega)}{1 + (\zeta_1 + \zeta_2) f(\omega)} B^{(n-1)}(x_n,\omega), \tag{8.112}$$

$$B^{(n)}(x,\omega) = B^{(n-1)}(x,\omega) + B^{(n)}_{sc}(x,\omega). \tag{8.113}$$

Let us now turn our attention to the envelope of the scattered field,

$$A(x) = \zeta_1 e^{iq_1 x} + \zeta_2 e^{iq_2 x}, \tag{8.114}$$

We decompose the wave-vectors into mean and difference, as well as real and imaginary parts, and the resonant lengths into modulus and phase,

$$q_1 = \bar{q} + \delta q + i\bar{\kappa} + i\delta\kappa, \tag{8.115}$$
$$q_2 = \bar{q} - \delta q + i\bar{\kappa} - i\delta\kappa, \tag{8.116}$$
$$\bar{q} = \frac{1}{2}\,\mathrm{Re}(q_1 + q_2), \tag{8.117}$$
$$\bar{\kappa} = \frac{1}{2}\,\mathrm{Im}(q_1 + q_2), \tag{8.118}$$
$$\delta q = \frac{1}{2}\,\mathrm{Re}(q_1 - q_2), \tag{8.119}$$
$$\delta\kappa = \frac{1}{2}\,\mathrm{Im}(q_1 - q_2), \tag{8.120}$$
$$\zeta_1 = |\zeta_1|e^{i\phi_1} = |\zeta_1|e^{i(\bar{\phi}+\delta\phi)}, \tag{8.121}$$
$$\zeta_2 = |\zeta_2|e^{i\phi_2} = |\zeta_2|e^{i(\bar{\phi}-\delta\phi)}, \tag{8.122}$$
$$\bar{\phi} = \frac{1}{2}(\phi_1 + \phi_2), \tag{8.123}$$
$$\delta\phi = \frac{1}{2}(\phi_1 - \phi_2). \tag{8.124}$$

For an ideal waveguide, ζ_1, ζ_2 are purely real. However, in the presence of loss, they have a small imaginary part and thus $\phi_1, \phi_2 \neq 0$, but are small.

The common phase can then be factored out,

$$\bar{A}(x) = A(x)e^{-i(\bar{q}+i\bar{\kappa})x - i\bar{\phi}} = |\zeta_1|e^{i[(\delta q + i\delta\kappa)x + \delta\phi]} + |\zeta_2|e^{-i[(\delta q + i\delta\kappa)x + \delta\phi]}. \tag{8.125}$$

The modulus of this envelope is then given by

$$\begin{aligned} |\bar{A}(x)|^2 &= |\zeta_1|^2 e^{2\delta\kappa x} + |\zeta_2|^2 e^{-2\delta\kappa x} + 2|\zeta_1||\zeta_2|\,\mathrm{Re}(e^{i[(\delta q + i\delta\kappa)x + i\delta\phi]}) \\ &= |\zeta_1|^2 e^{2\delta\kappa x} + |\zeta_2|^2 e^{-2\delta\kappa x} + 2|\zeta_1||\zeta_2|\cos(\delta q x + \delta\phi)\cosh(\delta\kappa x). \end{aligned} \tag{8.126}$$

In practice, as we shall see in the following section, the imaginary parts of q_1, q_2 are very close. We will therefore assume $\delta\kappa \approx 0$, valid for sufficiently short distances. For distances long enough for the mismatch in attenuation to be an issue, the overall attenuation will be strong regardless, so in practice the effect is negligible.

Thus, for negligible attenuation mismatch, (8.126) reaches an extremum for positions

$$\delta_q x + \delta\phi = \pi n \quad n \in \mathbb{Z}. \tag{8.127}$$

Consider a strip placed at $x_0 = 0$. Let the strips ahead of it be placed at locations

$$x_n = \frac{\pi n - \delta\phi}{\delta q}, \quad n > 0. \tag{8.128}$$

The unattenuated envelope reaches its maximum amplitude of

$$|\bar{A}(x_n)|^2 = (|\zeta_1| + |\zeta_2|)^2. \tag{8.129}$$

However, consider now the scattered field from x_1. The path difference is then given by

$$x_n - x_1 = \frac{\pi(n-1)}{\delta q}, \tag{8.130}$$

which is off target with the anti-nodes of the scattered field from x_1 by a distance of $\delta\phi/\delta q$. Therefore, it is impossible to place all the micro-strips to be completely constructive with each other unless $\delta\phi = 0$. In practice, as we shall see, for realistic waveguides this effect is small, and over the attenuation length of the cavity modes we can consider all micro-strips to be perfectly constructive.

Let us turn our attention now to destructive interference. This occurs when the beat term is zero,

$$\delta q x + \delta\phi = \pi(n + \frac{1}{2}) \quad n \in \mathbb{Z}. \tag{8.131}$$

Thus, the scattered field from a strip at $x = 0$ is completely out of phase with strips placed at locations

$$x_n = \frac{\pi(n + \frac{1}{2}) - \delta\phi}{\delta q}, n > 0. \tag{8.132}$$

At these locations, the unattenuated scattered amplitude reaches its minimum value of

$$|\bar{A}(x_n)|^2 = (|\zeta_1| - |\zeta_2|)^2. \tag{8.133}$$

As we shall see, it is possible in practice to achieve $|\zeta_1|$, $|\zeta_2|$ very close to each other, and thus achieve a very high level of destructive interference. However, note it is not possible to get total destructive interference at all positions in a periodic array: consider three micro-strips placed $\pi/2\delta q$ apart. The second strip is transparent to the first, due to the fact that the scattered field of the first strip is completely destructively interfered. The third strip is transparent to the second. However, the third strip is located $\pi/\delta q$ from the first, and thus the first strips field is maximal! Nevertheless, this demonstrates an intriguing subradiant phenomenon: a period array of micro-strips at $\pi/2\delta q$ spacing can be divided into two, non-interacting ensembles!

8.3.1 Evaluating the response of periodic arrays

We will now demonstrate how the scattered response of a periodic array can be evaluated in the ideal scenario, $\zeta_1 = \zeta_2 = \zeta$, (which implies $\delta\phi = 0$) and $\delta\kappa = 0$.

The common $e^{i(\tilde{q}+i\tilde{\kappa})x}$ phase is eliminated by defining

$$\beta_i(x,\omega) = e^{-i(\tilde{q}+i\tilde{\kappa})x} B_i(x,\omega), \tag{8.134}$$

where B_i refers to any of the fields, total, scattered, input, etc. Equations (8.110), (8.111), (8.112), (8.113) then read

$$\beta^{(n)}_{sc,1}(x,\omega) = -\frac{\zeta f(\omega) e^{i\delta q(x-x_n)}}{1+2\zeta f(\omega)} \beta^{(n-1)}(x_n,\omega), \tag{8.135}$$

$$\beta^{(n)}_{sc,2}(x,\omega) = -\frac{\zeta f(\omega) e^{-i\delta q(x-x_n)}}{1+2\zeta f(\omega)} \beta^{(n-1)}(x_n,\omega), \tag{8.136}$$

$$\beta^{(n)}_{sc}(x,\omega) = -\frac{2\zeta \cos(\delta q(x-x_n))}{1+2\zeta f(\omega)} \beta^{(n-1)}(x_n,\omega), \tag{8.137}$$

$$\beta^{(n)}(x,\omega) = \beta^{(n-1)}(x,\omega) - \frac{2\zeta \cos(\delta q(x-x_n))}{1+2\zeta f(\omega)} \beta^{(n-1)}(x_n,\omega). \tag{8.138}$$

In particular, we have

$$\beta^{(n)}(x_{n+1},\omega)=\beta^{(n-1)}(x_{n+1},\omega)-\frac{\zeta\cos(2\delta q\delta x)}{1+2\zeta f(\omega)}\beta^{(n-1)}(x_n,\omega), \tag{8.139}$$

for arrays spaced at periodic intervals of width δx.

Constructive interference

For constructive interference, we place the micro-strips at locations

$$x_n=\frac{\pi n}{\delta q}. \tag{8.140}$$

Let us define b to be the values of the total field sat the periodic locations,

$$b^{(m)}(\omega)=\beta^{(m)}(x_m,\omega). \tag{8.141}$$

We note that since

$$\cos(\delta q\delta x)=\cos(\pi)=-1, \tag{8.142}$$

the periodically evaluated total fields obey the recurrence relation

$$\begin{aligned} b^{(m)}(\omega)&=\left(\cos(\delta q\delta x)-\frac{2\zeta\cos(\delta q\delta x)}{1+2\zeta f(\omega)}\right)b^{(m-1)}(\omega) &(8.143)\\ &=\frac{-1}{1+2\zeta f(\omega)}b^{(m-1)}(\omega)\\ b^{(0)}(\omega)&=\beta(0,\omega). &(8.144)\end{aligned}$$

This then has the solution

$$b^{(m)}(\omega)=\frac{(-1)^m}{(1+2\zeta f(\omega))^m}\beta_{in}(0,\omega). \tag{8.145}$$

The mth scattered field, evaluated at arbitrary positions, is therefore given by

$$\beta_{sc}^{(m)}(x,\omega)=-2\zeta\cos(\delta qx)\frac{(-1)^m}{(1+2\zeta f(\omega))^m}\Theta(x-x_m) \tag{8.146}$$

Thus, the total field after scattering from N strips in total is given by

$$B(x,\omega)=B_{in}(x,\omega)-e^{i(\tilde{q}+i\tilde{\kappa})x}2\zeta\cos(\delta qx)f(\omega)\sum_{m=1}^{N}\frac{(-1)^m}{(1+2\zeta f(\omega))^m}B_{in}(0,\omega). \tag{8.147}$$

In particular, if we set the waveguide outlet to an anti-node, the output field is given by

$$B_{out}(x_{out},\omega)=e^{i(\tilde{q}+i\tilde{\kappa})x_{out}}\frac{(-1)^N}{(1+2\zeta f(\omega))^N}B_{in}(0,\omega). \tag{8.148}$$

This lets us directly define the transmission coefficient,

$$T(\omega)=\frac{B_{out}(x_{out},\omega)}{B_{in}(0,\omega)}=T_0\frac{1}{(1+2\zeta f(\omega))^N}, \tag{8.149}$$

where $T_0 = (-1)^N e^{i(\tilde{q}+i\tilde{\kappa})x_{out}}$ is the bare waveguide transmittance. We can see that the total nuclear transmittance is the product of the transmittances of the individual micro-strips,

$$T(\omega) = T_0 \prod_{i=1}^{N} T_{nuc}(\omega), \tag{8.150}$$

$$T_{nuc} = \frac{1}{1 + 2\zeta f(\omega)}. \tag{8.151}$$

Let us now consider explicitly the response of a two-level system,

$$f(\omega) = \frac{i\gamma/4}{\omega + i\gamma/2} k_0 w. \tag{8.152}$$

The nuclear transmittance is then given by

$$T_{nuc} = \frac{1}{1 + 2\zeta f(\omega)} = \frac{\omega + i\gamma/2}{\omega + i\gamma/2 + i\zeta\gamma k_0 w/2}. \tag{8.153}$$

Assume for the time being that ζ is purely real. This would be the case for propagation in a homogeneous lossless medium. This function then reaches its minimum when $\omega = 0$,

$$T_{nuc} \to \frac{1}{1 + \zeta k_0 w/2} \leq 1. \tag{8.154}$$

Therefore, we can see that this corresponds to the attenuation of the incident field by the resonant absorption of a single microstrip, which is enhanced by the strip width w due to super-radiance. Due to the waveguide attenuation, not all the attenuated input field is converted to nuclear excitation, and we will now carefully consider the efficiency of nuclear absorption.

The first strip absorbs $1 - T_{nuc}(\omega)$ of the beam. The transmission to the second strip is $T_{nuc}(\omega)T_\delta$, where the waveguide transmission between the strips is given by

$$T_\delta = -e^{i(\tilde{q}+i\tilde{\kappa})\delta x}, \quad \delta x = \frac{\pi}{\delta q}. \tag{8.155}$$

Therefore, the second strip absorbs $T_{nuc}(\omega)T_\delta(1 - T_{nuc}(\omega))$. In general, the nth strip absorbs a factor of

$$(T_{nuc}(\omega)T_\delta)^{n-1}(1 - T_{nuc}(\omega)). \tag{8.156}$$

The total absorption is then

$$(1 - T_{nuc}(\omega)) \sum_{n=1}^{N} (T_{nuc}(\omega)T_\delta)^{n-1} = (1 - T_{nuc}(\omega)) \frac{(T_{nuc}(\omega)T_\delta)^N - 1}{T_{nuc}(\omega)T_\delta - 1}. \tag{8.157}$$

As $|T_{nuc}(\omega)T_\delta| < 1$, this reaches a limit of

$$\frac{1 - T_{nuc}(\omega)}{1 - T_{nuc}(\omega)T_\delta}, \tag{8.158}$$

as $N \to \infty$, corresponding to the maximal absorption efficiency. In particular, if $T_\delta \to 1$, one reaches perfect absorption.

As $\omega \to \infty$, the nuclear transmittances tend to 1. Therefore, as with nuclear forward scattering, the time response will consist of a prompt response, corresponding to the bare waveguide transmittance, and a delayed response from the nuclear excitation. The form of the delayed response in Fourier space is given by

$$R(\omega) = \frac{(\omega + i\gamma/2)^N}{(\omega + i\gamma/2 + J + i\Gamma)^N} - 1, \tag{8.159}$$

where

$$J + i\Gamma = i\frac{\zeta k_0 w \gamma}{2}. \tag{8.160}$$

Let us define $\nu = \omega + i\gamma/2 + J + i\Gamma$. We then have

$$R(\nu) = \frac{(\nu - \nu_0)^n - \nu^n}{\nu^n} = \sum_{m=0}^{n-1} \binom{n}{m} \left(-\frac{\nu_0}{\nu}\right)^{n-m}, \tag{8.161}$$

where $\nu_0 = J + i\Gamma$. The time domain form is then given by

$$R(t) = e^{i(J+i\gamma/2+i\Gamma)t} \sum_{m=0}^{n-1} \binom{n}{m} (-\nu_0)^{n-m} \int_{i\gamma/2+i\Gamma-\infty}^{i\gamma/2+i\Gamma+\infty} \frac{\mathrm{d}\nu}{2\pi} e^{-i\nu t} \frac{1}{\nu^{n-m}}. \tag{8.162}$$

Since the contour lies above all poles, the response is non-zero only for $t > 0$. Therefore, closing the contour in the lower half plane for $t > 0$, and noting that

$$\int_{i\gamma/2+i\Gamma-\infty}^{i\gamma/2+i\Gamma+\infty} \frac{\mathrm{d}\nu}{2\pi} e^{-i\nu t} \frac{1}{\nu^l} = (-i)^l \frac{t^{l-1}}{(l-1)!}\Theta(t), \tag{8.163}$$

we have

$$\begin{aligned} R(t) &= i\nu_0 e^{i(J+i\gamma/2+i\Gamma)t} \sum_{m=0}^{n-1} \binom{n}{m} \frac{1}{(n-m-1)!} (i\nu_0 t)^{n-m-1}\Theta(t) \\ &= i\nu_0 e^{i(J+i\gamma/2+i\Gamma)t} \sum_{m=0}^{n-1} \binom{n}{n-m-1} \frac{1}{m!} (i\nu_0 t)^m. \end{aligned} \tag{8.164}$$

In particular, we recognize the sum as a generalized Laguerre polynomial,

$$\sum_{m=0}^{n-1} \binom{n}{n-m-1} \frac{1}{m!} (i\nu_0 t)^m = L_{n-1}^{(1)}(-i\nu_0 t) \tag{8.165}$$

Therefore, the delayed response has the compact expression

$$R(t) = i\nu_0 e^{i(J+i\gamma/2+i\Gamma)t} L_{n-1}^{(1)}(-i\nu_0 t). \tag{8.166}$$

As n gets large, the leading term in $L_{n-1}^{(1)}(x)$ approaches

$$\binom{n}{n-m-1} \frac{1}{m!} \sim n^m \frac{n}{m!(m+1)!}, \quad n \to \infty. \tag{8.167}$$

We then have asymptotically

$$n \sum_{m=0}^{n-1} \frac{(i\nu_0 n t)^m}{m!(m+1)!} \sim n \frac{\sqrt{n} J_1\left(2\sqrt{-in\nu_0 t}\right)}{\sqrt{-in\nu_0 t}}, \quad n \to \infty. \tag{8.168}$$

In particular, when the Lamb shift is vanishing, $J = 0$, we obtain $\nu_0 = i\Gamma$, and thus

$$L_{n-1}^{(1)}(\Gamma t) \sim n \frac{J_1\left(2\sqrt{n\Gamma\nu_0 t}\right)}{\sqrt{n\Gamma t}}. \tag{8.169}$$

The delayed response is then given by

$$R(t) \sim -n\Gamma e^{-(\gamma/2+\Gamma)t} \frac{J_1\left(2\sqrt{n\Gamma t}\right)}{\sqrt{n\Gamma t}}. \tag{8.170}$$

Combining with the prompt response, we obtain

$$\delta(t) - n\Gamma e^{-(\gamma/2+\Gamma)t} \frac{J_1\left(2\sqrt{n\Gamma t}\right)}{\sqrt{n\Gamma t}}, \tag{8.171}$$

which we can see is identical to the forward scattering of a bulk layer, with the addition of an overall collective broadening.

Now that we have explored the forward scattering of a constructively interfering array of micro-strips, let us turn our attention to the case of destructive interference.

Destructive interference

For destructive interference, the condition for the inter-strip spacing is

$$\delta x = \frac{\pi}{2\delta q}. \tag{8.172}$$

Let us consider two strips placed δx apart. The total field after scattering from the first strip is given by

$$\beta^{(1)}(x, \omega) = (1 - \frac{2\zeta f(\omega)\cos(\delta q x)}{1 + 2\zeta f(\omega)})\beta_{in}(x, \omega). \tag{8.173}$$

Evaluating this at the position of the second strip, we obtain

$$\beta^{(1)}(\delta x, \omega) = \beta_{in}(\delta x, \omega), \tag{8.174}$$

due to destructive interference. Therefore, the second strip does not experience the scattered radiation of the first! On the other hand, if we place a third strip at $x = 2\delta x$, the scattered field of the second is vanishing, but we obtain

$$\beta^{(1)}(2\delta x, \omega) = \left(-1 + \frac{2\zeta f(\omega)}{1 + 2\zeta f(\omega)}\right), \tag{8.175}$$

due to the fact that $2\delta x \delta q = \pi$. Therefore, we can see that in general, if we have periodic array spaced δx apart, we can divide them into even and odd positions, which each scatter independently, and constructively with each other. The even scattered field is zero whenever the odd is maximal, and vice versa, therefore the final observed scattered field is that of only half the strips, with the corresponding resonant length that of only half the total number! Thus, this geometry is subradiant.

8.3.2 Numerical example

As a numerical study, we will consider a waveguide with Molybdenum cladding layers, a 1 nm iron layer, and 15.8 nm of B_4C filler on either side of the resonant layer. This wave-guide illustrates all the features developed in this chapter, and thus we will use it as our illustrative example. The numerically obtained parameters for this waveguide are summarized in Table 8.1.

Parameter	Value
δq	$152.12\,\mathrm{mm}^{-1}$
$\pi/\delta q$	$20.65\,\mu\mathrm{m}$
$\delta\kappa$	$-1.88\,\mathrm{mm}^{-1}$
$Q_{beat} = \lvert\delta q/\delta\kappa\rvert$	80.78
$Q_{atten} = \lvert\delta q/\bar{\kappa}\rvert$	45.91
$\bar{Q} = \sqrt{Q_{beat}Q_{atten}}$	60.90
$\bar{q} - k_0$	$-0.3832\,\mu\mathrm{m}^{-1}$
$\bar{\kappa}$	$3.31\,\mathrm{mm}^{-1}$
ξ_1	$2.7311\times10^{-4} + 2.6046\times10^{-6}i$
ξ_3	$2.7425\times10^{-4} - 4.3168\times10^{-6}i$
$B_1(0,\omega)/B_{in}$	$5.4906 - 1.9194\times10^{-3}i$
$B_3(0,\omega)/B_{in}$	$0.614\,61 - 1.8194\times10^{-2}i$
$\delta\phi$	0.0252 rad
$\lvert\xi_1/\xi_3\rvert$	0.99576
$(J + i\Gamma)/\gamma$	$6.4056\times10^{-4} + 0.204\,77i$

Table 8.1: Summary of two-mode coupling parameters, for the dominant modes $\lambda = 1, 3$ in a molybdenum waveguide. All quantities are evaluated at resonant layer centre. Waveguide structure is Mo (∞)/ B_4C (15.8 nm)/ ^{57}Fe (1 nm)/ B_4C (15.8 nm)/ Mo (∞)

First, we illustrate the guided and leaky mode profiles in Figures 8.3 and 8.4, as a function of layer depth. This waveguide supports three guided modes, but only the even modes, i.e. those that are symmetric upon reflections about z_0, have appreciable magnitude when evaluated at the nuclear layer. The leaky modes have similar magnitudes to the guided modes, however their attenuation is far larger, which can be observed in Figure 8.5. This figure illustrates the location of the guided modes, leaky modes and branch cut in the complex q plane. Due to the larger attenuation of the leaky modes, their corresponding residues are suppressed by a proportional factor. This can be clearly seen in Figure 8.6, which shows the Fourier transformed Green's function along the real q axis. The dominant contribution by far is that of the two even guided modes, $\lambda = 1, 3$, and the rest can be treated as a constant background, renormalizing the single particle decay rate.

To evaluate the expansion coefficients for the resonant fields, we assume a broadband input, and thus take the incident field on the front plane to be constant. We therefore have

$$B_\lambda(0,\omega) = B_{in}\int_{-\infty}^{\infty} \mathrm{d}z\, u_\lambda(z). \tag{8.176}$$

The resultant input field at the resonant layer is illustrated in Figure 8.7. Clearly visible is the beat pattern resulting from the interference of the two modes. The

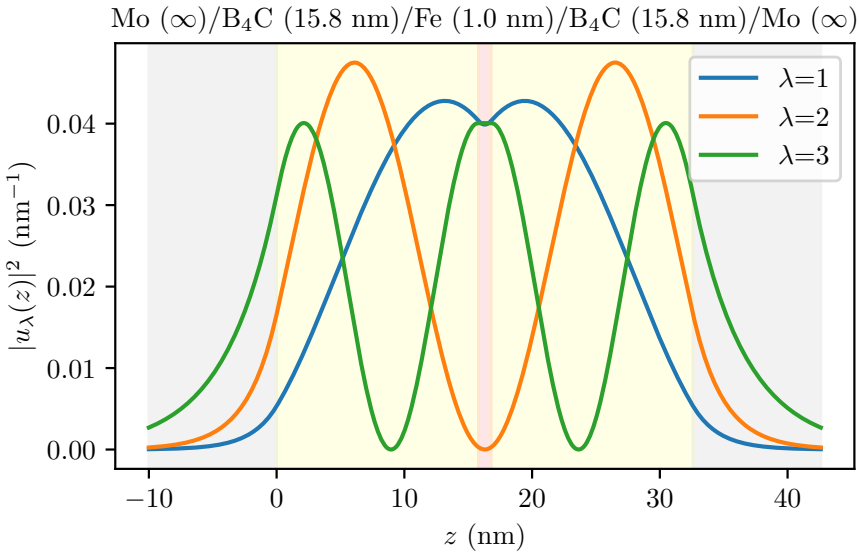

Figure 8.3: Normalized amplitudes of the guided modes of a molybdenum waveguide. Only the first two even modes, $\lambda = 1, 3$ couple to the thin nuclear layer, giving us a two mode geometry. The layer widths have been optimized for the two modes to couple almost exactly equally to the resonant layer, giving a strong interference beat in their collective radiation field.

first guided mode has a larger relative amplitude due to the fact that it oscillates less within the waveguide core, and as such has a larger component in the uniform input profile.

From Table 8.1, we can see that the wavelength of the interference beat between the two guided modes is approximately 20 µm. On the other hand, the attenuation lengths are much smaller, on the millimetre scale. This motivates the definition of two Q factors for the system. The first is the 'beat Q factor',

$$Q_{beat} = \frac{\delta q}{\delta \kappa}. \tag{8.177}$$

This is to be qualitatively interpreted as the number of beats that occur before the attenuation mismatch causes visibility to diminish significantly. For this waveguide, it has a value of approximately 81. The second is the 'attenuation Q factor',

$$Q_{atten} = \frac{\delta q}{\bar{\kappa}}, \tag{8.178}$$

which measures the number of beats that occur before overall attenuation dissipates the field. For this waveguide, it is lower than Q_{beat}, with a value of approximately 46. We take the overall Q factor for the collective mode to be the geometric mean of these two Q factors, as both the overall attenuation and attenuation mismatch should be minimized to optimize the cavity for long range sustained collective interference. For this waveguide, the geometric mean gives an overall Q factor of approximately 61. The effects of both attenuation mismatch and overall attenuation is clearly illustrated in Figure 8.8, which illustrates how the attenuation mismatch causes the

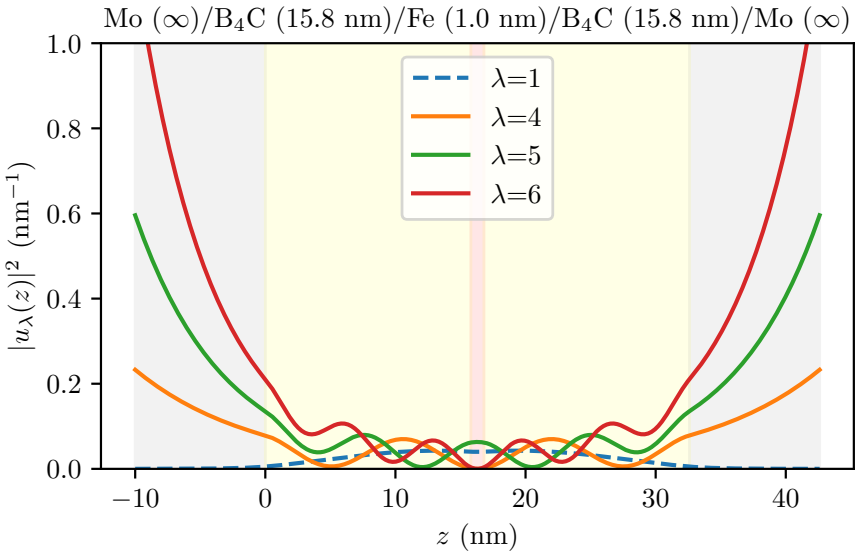

Figure 8.4: Normalized amplitudes of the first few leaky modes of a molybdenum waveguide, which correspond to resonances of the radiative modes. Superimposed, and dashed, is the amplitude of the first guided mode, $\lambda = 1$. The exponential divergence of the leaky modes is clearly visible, demonstrating their nature as an asymptotic expansion for the near field. Although the leaky modes have amplitudes of similar magnitude to the guided modes at the resonant layer (red shading), Figures 8.5 and 8.6 demonstrate how the overall coupling strength is suppressed by their large attenuation.

relative strengths of the constituent fields to diverge throughout the waveguide, and thus reduces the visibility of the interference beat.

To evaluate the effect of the phase mismatch between the guided modes, which evaluates to approximately $\delta\phi = 0.0252\,\text{rad}$, we consider the difference between perfect constructive interference, and one that is slightly off target by $\delta\phi$. This gives

$$1 - \cos(0.0252) \approx 0.03\%. \tag{8.179}$$

As such, this is negligible, especially compared with the effects of attenuation mismatch.

Let us now compare the constructive and destructive scattering ensembles, for an equivalent total combined strip thickness, Figure 8.9. One can clearly see that the constructive ensemble reaches a larger maximum, while the destructive ensemble has a greatly suppressed interference beat due to the out of phase emission of the two sub-ensembles. However, due to the attenuation mismatch, the effect is not perfect, and the contrast in peak field strength between the two ensembles is not as high as the ideal case.

Due to the narrow strip width, and the relatively large wavelength of the interference beat, the field envelope is very uniform over the strip's longitudinal extent. For a 1 µm strip, the change in amplitude is approximately

$$1 - \cos(1/20) \approx 0.12\%. \tag{8.180}$$

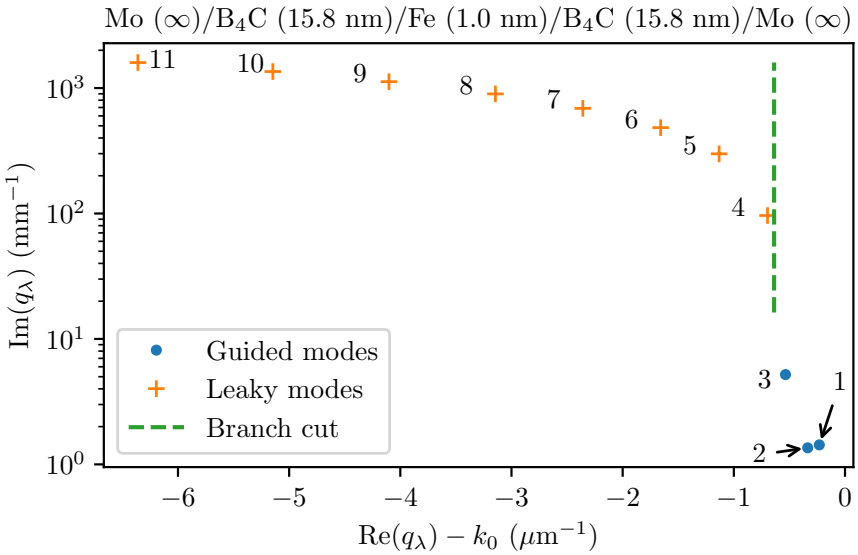

Figure 8.5: Relative mode wave-numbers and radiative mode branch cut for molybdenum waveguide. One can clearly see that leaky modes and guided modes are separated by the branch cut. The leaky modes are significantly attenuated compared to the guided modes, and as such are only relevant at very close range, on the order of 1 µm.

Thus, we can consider the strip to follow Dicke model dynamics. This can easily be seen by the response of a single strip,

$$-\frac{2\zeta f(\omega)}{1+2\zeta f(\omega)}, \tag{8.181}$$

which is identical in form to the collective response of a grazing incidence Dicke mode from Section 7.2. Compared to a bulk layer scattering, this results in an additional overall collective Lamb shift and broadening, however the effect is small, approximately 0.2γ for the broadening, and negligible Lamb shift.

Let us now consider the regime of minimized attenuation mismatch. If this could be achieved, the constructively interfering micro-strips would act as very strong absorbers of resonant X-rays, Figure 8.10. This figure illustrates the maximal absorption efficiency as a function of frequency for vanishing attenuation mismatch, reaching a peak efficiency of approximately 75% for a 1 µm strip. However, in practice, the effect of attenuation mismatch reduces this to the order of 60% or less. This can be seen in Figure 8.11, which shows the effect of micro-strip width on the peak saturation reached by the scattered field. Reducing the strip width reduces the ensemble size, and hence the Dicke super-radiance, resulting in a smaller cross-section. As a result, narrow strips reach a smaller peak saturation before attenuation becomes significant. There is a trade-off to be made however, between the strength of the Dicke super-radiance and the uniformity of the field across the strips longitudinal extent, with wider strips experienced a less uniform field envelope. As such, one cannot increase the strip size much beyond

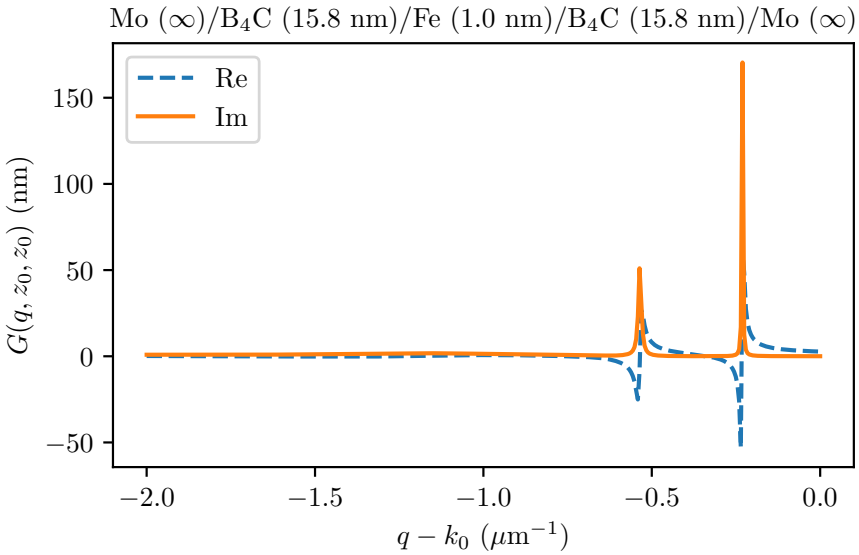

Figure 8.6: Fourier transformed Green's function of a molybdenum clad waveguide, evaluated at resonant layer position. One can clearly see that only two modes couple with any appreciable amplitude to the nuclei, with the leaky modes heavily suppressed by attenuation.

Qualitatively, the absorption spectra resemble those of nuclear forward scattering [68], as we saw in equations (8.166), (8.171), the nuclear forward scattering spectrum is reached as the limit of large strip number. This is illustrated in Figure 8.12, which compares the Laguerre polynomial response of a finite number of strips, to the large N Bessel function limit. One can see that for larger strip numbers the Bessel function limit approximates the Laguerre response for longer times.

Finally, let us examine the two-dimensional field profiles of the scattered field, Figures 8.13 and 8.14. One can see that the scattered fields in both the constructive and destructive cases reach similar peak magnitudes, however for the destructive field the field is redistributed slightly outside the layer. Of interest however is the phase shift of the interference beats undergone by the constructive field as it crosses an anti-node of the third guided mode, which is not the case with the destructive field. This effect could be interesting to explore when considering multiple resonant layers, with an interplay between the phase mismatch of two layers placed on either side of the third guided mode anti-nodes.

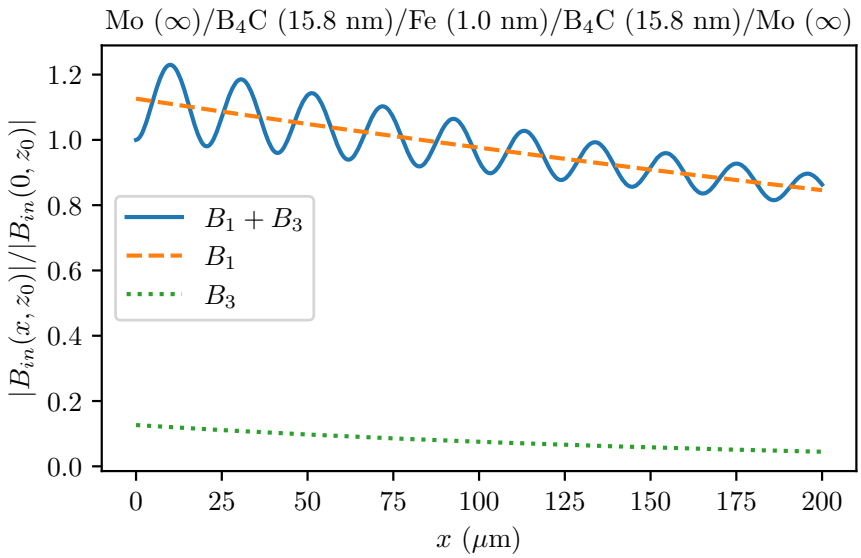

Figure 8.7: Amplitudes of input fields, evaluated at the layer depth z_0, as they propagate through the waveguide. Note the long attenuation lengths. The interference between the two modes is visible as a beat pattern with a wavelength of approximately 20 µm. Field is normalized by total field at beginning of resonant layer; as the input fields are initially out of phase, peak values with this choice of normalization are greater than one.

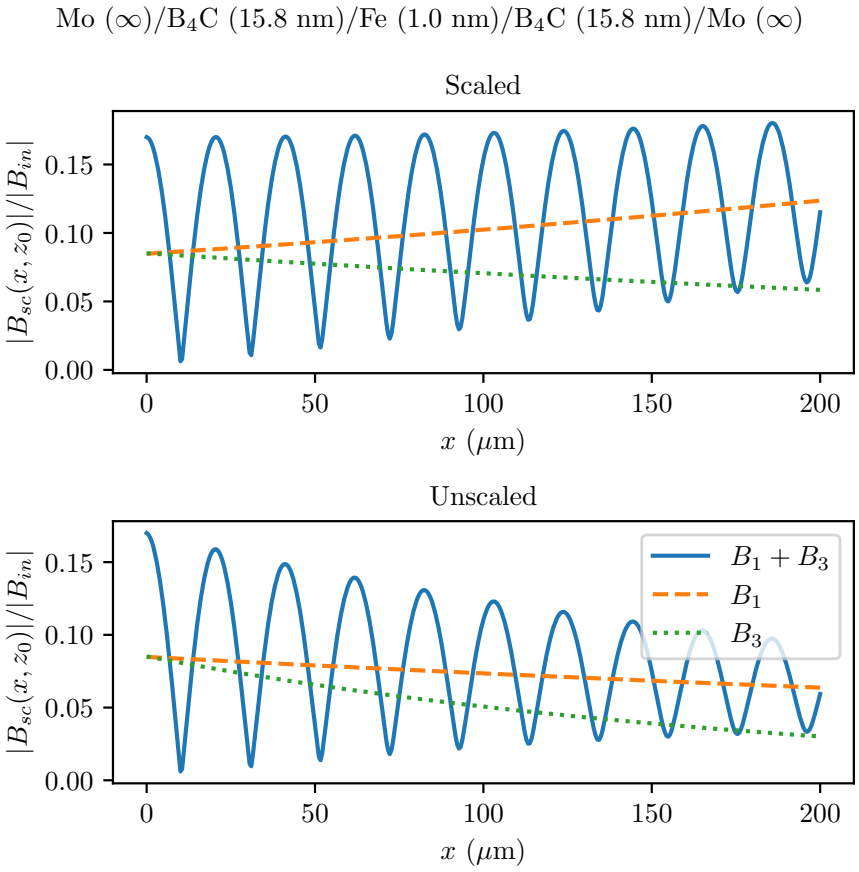

Figure 8.8: On-resonance scattered field for a single micro-strip, both scaled to remove the overall attenuation (top), and unscaled (bottom). One can observe both the interference beat of the two participating modes. As the collective mode is the symmetric superposition of the two participating modes, a mismatch in the attenuation lengths causes the scattered field to gradually drift out of the collective mode, clearly visible as the reduced visibility of the interference beats.

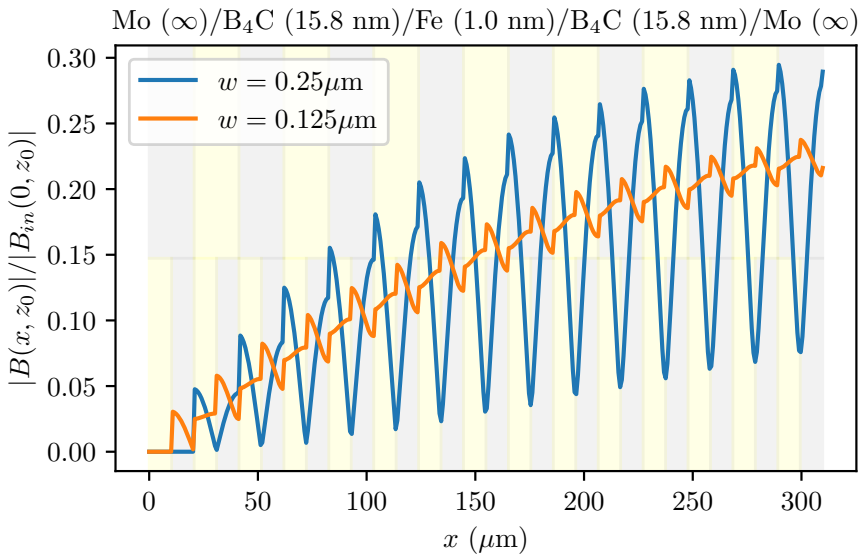

Figure 8.9: Comparison of super-radiant (blue) and sub-radiant (orange) geometries, with identical combined strip thickness. The super-radiant state reaches a higher peak scattered intensity, but displays the pronounced beat of the collective interference. The sub-radiant geometry displays a suppressed beat, due to the out of phase emission of the two sub-ensembles. Shading displays strip locations for constructive (top) and destructive (bottom) geometries.

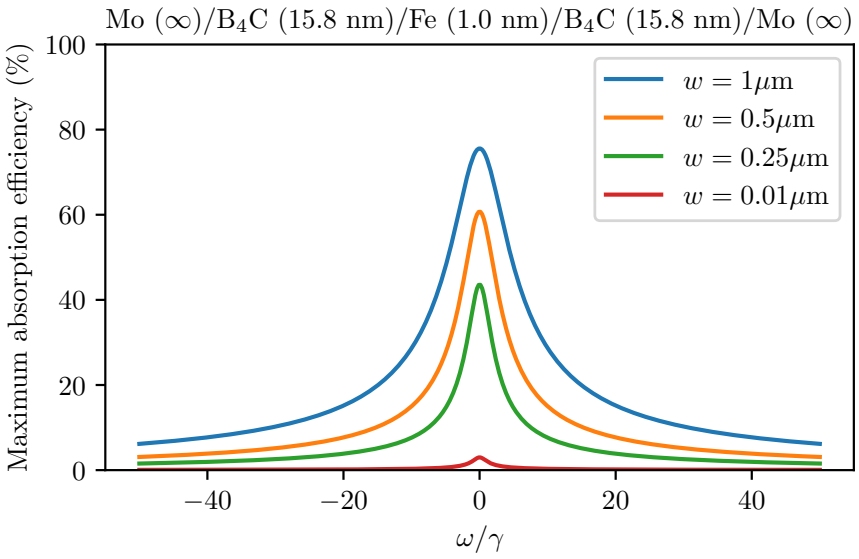

Figure 8.10: Ideal maximal absorption efficiency for constructively interfering micro-strips of various widths. Increasing the strip width beyond approximately 1 µm would violate the assumption of uniform illumination across a strip's extent, and thus we consider this as our upper bound. At 1 µm, a single strip absorbs approximately 17% of resonant light. Transmission between the strips is approximately 93%. Clearly visible is the significant super-radiant broadening, presenting an enhanced total Mössbauer cross-section.

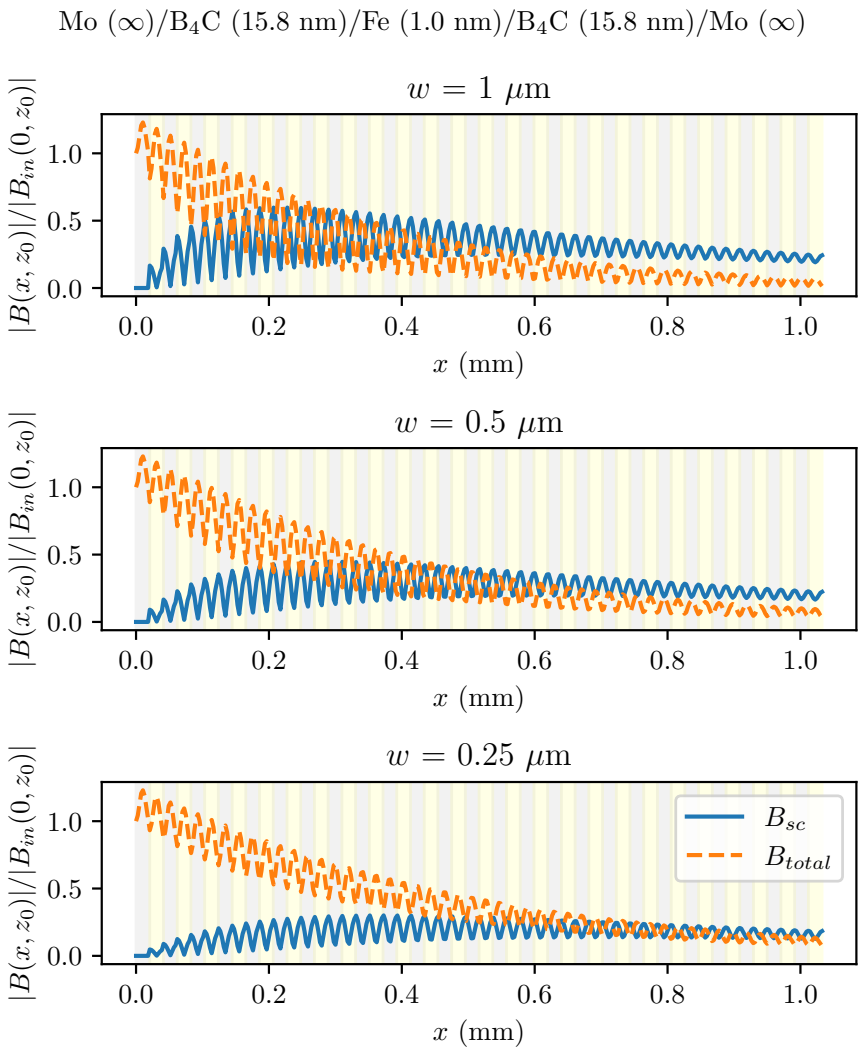

Figure 8.11: Effect of micro-strip width on saturation of constructively interfering strips. Contrast of shading used to illustrate strip locations, with narrow strips (width not illustrated) located at the edge of each shading transition. Strips are kept at same spacing, corresponding to a single beat length. Peak saturation is quickly reached, at about 100 μm, corresponding to 5 strips. Increasing strip width increases the collective cross-section, and thus saturation is reached closer to the incident plane, and with larger intensity.

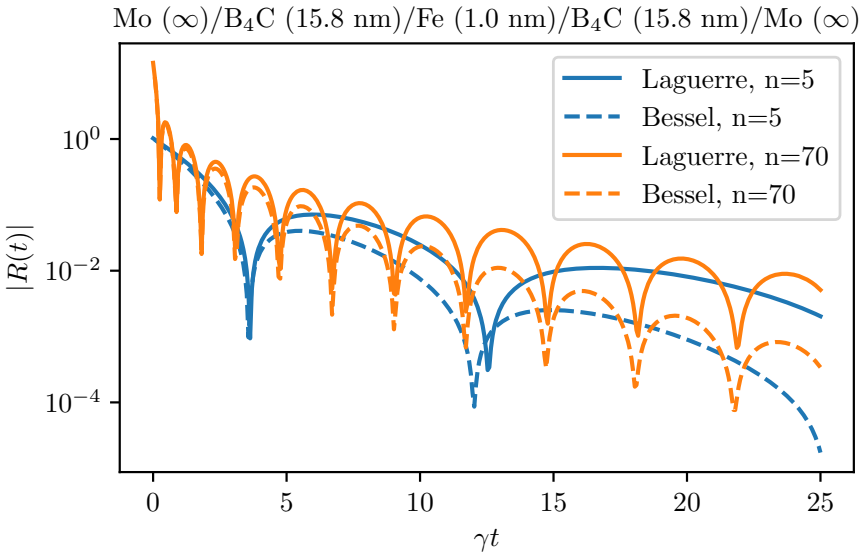

Figure 8.12: Comparison of Laguerre solution for microstrip temporal response (solid) and Bessel function limit (dashed), for equivalent total resonant length. The responses match for short times. For larger numbers of strips, the dynamical beat of the Bessel function response matches the Laguerre response qualitatively for longer durations, however the decay of a Bessel response is more rapid.

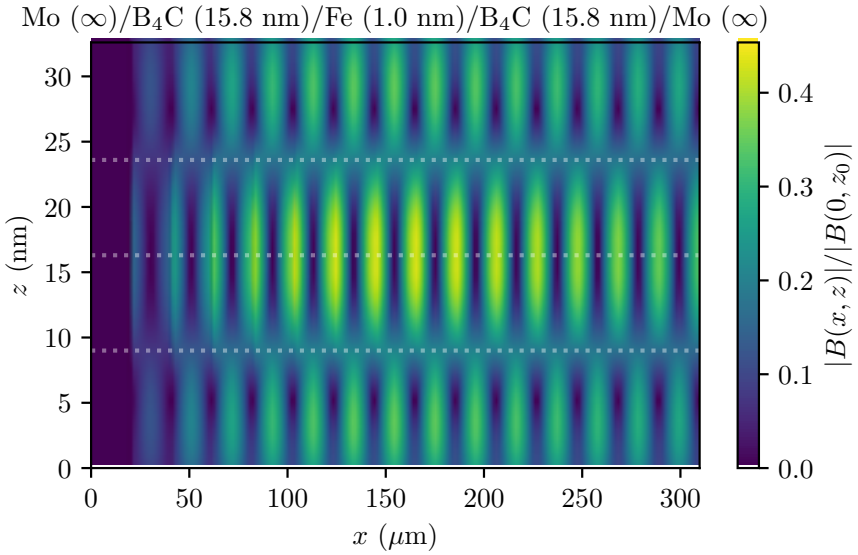

Figure 8.13: Two-dimensional field profile of scattered field from constructively interfering strips. Highlighted in white are the anti-nodes of the participating modes (Figure 8.3), with the nuclear strips located at the central anti-node. The first mode only has a single anti-node at the centre, while the other has three anti-nodes. The scattered field undergoes a phase shift as one crosses these anti-nodes in the z direction.

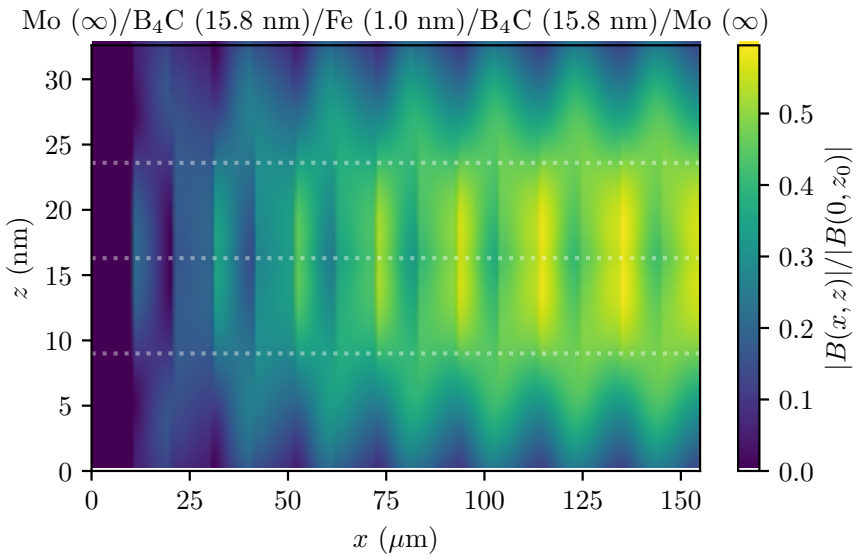

Figure 8.14: Two-dimensional field profile of scattered field from destructively interfering strips. Highlighted in white are the anti-nodes of the participating modes. The scattered field does not experience a significant interference beat, and thus the phase shift at the anti-nodes is greatly suppressed compared with Figure 8.13.

Chapter 9

Conclusions and outlook

9.1 Green's function formalism for Mössbauer nuclei

In Chapters 3, 4 and 6 we used the Grüner-Welsch quantization to demonstrate that the coupling of the electromagnetic field to Mössbauer nuclei in general linear macroscopic media obey Maxwell-Bloch equations. Specifically, the field obeys the macroscopic Maxwell-Equations with the nuclear magnetization as a source, and the nuclei obey the isomeric equivalent of the optical Bloch equations. Thus, we can describe the scattered field of the nuclei via the dyadic Green's function of the macroscopic Maxwell's equations for the medium, and we were able to use the well known spectral properties of the slab waveguide Green's function to derive analytic expressions for the guided mode propagation.

Outlook

While we have only considered slab geometries in this work, exact expressions and spectral expansions for the dyadic Green's function are known for many other experimentally interesting geometries. For example, solutions for cylindrical and spherical multi-layers are known [82], and thus one could evaluate if Mössbauer nuclei embedded in nanowires or nano-spheres could have desirable properties.

On the other hand, for less symmetric geometries, exact solutions are not known, and one must use numerical methods to obtain the quasi-normal modes. Radiative boundary conditions pose a considerable challenge. However, if the geometry involves entirely lossy media, attenuation allows one to consider finite volumes, and the numerics become far more amenable. This could be useful for analysing geometries with periodic voids, to create effective optical potentials.

In addition, while we have neglected tapered waveguides in this work, Chen *et al.* [56] have demonstrated that they could be used to focus the guided mode, and thus enhance the local field, with the possibility of attaining nuclear inversion. This work was done using the paraxial Maxwell's equations to solve the propagation of the field, which assumes that the envelope of the field is slowly varying in the transverse direction. As such, this may not necessarily be a good approximation in the limits of extreme focusing. On the other hand, any taper would have to occur on a longitudinal length scale much larger than the wavelength of the field, and additionally, the difference in refractive indices at X-ray wavelength are small. Thus, it is possible that a Born series could be used to obtain its Green's function,

starting with the Green's function for a slab waveguide, and treating the taper as a perturbation.

9.2 Inhomogeneity in grazing incidence X-ray quantum optics

In Chapter 7, we considered the effects of two kinds of inhomogeneity on grazing incidence energy spectra. We first considered angular broadening, and showed that angular instability during an experiment can result in distortion of the spectral features in such a way that one could draw erroneous conclusions about the hyperfine interactions in a sample.

We have demonstrated that angular divergences can lead to significant deviations from single mode behaviour in grazing incidence, and the potential for erroneous estimates for hyperfine parameters and cavity structures when using grazing incidence scattering as a measurement technique. This also demonstrates a trade-off between intensity and single mode excitation: focusing the beam tighter for a larger intensity necessarily increases the beam divergence, and thus poses a limitation on the field strengths that can be achieved in the single mode regime.

Next, we considered the role of inhomogeneous broadening in Dicke model super-radiance. We demonstrated that rather than acting as a frequency shift and overall broadening, the collective Lamb shift and super-radiant decay rate act in novel ways as a collective all to all coupling between the nuclei. This all to all coupling can overcome the effects of inhomogeneous broadening due to hyperfine parameter distributions, and the limit of strong collective coupling leads to an effectively single line spectrum, i.e. the collective mode dominates.

Outlook

Since commonly used beam parameters have a divergence that is to be considered broad relative to the resonance widths of the thin film cavities, one cannot assume in general that a single Fourier mode is excited. Future theoretical predictions should therefore take beam divergence into account, especially when fitting to experimental data.

The situation with inhomogeneous broadening however, is not so pessimistic. The combination of various collective and hyperfine parameters results in a wide range of available line-shapes, as well as a degree of control using the angle of incidence.

9.3 X-ray quantum optics of Mössbauer waveguides

In Chapter 8, we developed the theory for the interaction of guided modes of a thin film waveguide with a thin layer of Mössbauer nuclei placed within. The resulting equations of motion were shown to be analogous to nuclear forward scattering, with the effective resonant length being scaled by the mode amplitude at the nuclear layer and inverse of the mode wave-vector.

We then considered the role played by coupling to multiple modes, and showed that a thin layer of nuclei only emits to a single, symmetric combination of the available modes.

In a waveguide with only two available modes, we showed that as the scattered field of the nuclei is emitted into a superposition of the two modes, the resulting radiation pattern has an interference beat. If the nuclei are structured in micro-strips, the positioning of the strips can be manipulated to interact with each other constructively or destructively as desired.

Outlook

We have demonstrated that front coupling geometry provides true two-dimensional geometric control in the quantum optics of Mössbauer nuclei. As a result, models from the visible optics community, involving the coupling of guided modes to atoms structured in arrays, or two-dimensional arrangements, are now viable to implement in the Mössbauer regime.

For example, placing micro-strips at nodes allows for one to consider neighbouring pairs as effectively non-interacting, but next nearest neighbour pairs as strongly interacting. An auxiliary layer of micro-strips could potentially be used to reintroduce coupling between nearest neighbours via cross-layer scattering, and thus implement asymmetric hopping models with Mössbauer nuclei. This raise the prospect of the experimental investigation of the associated topological phenomena [111–114] in a manner free from thermal noise, with minimal inhomogeneous broadening.

The possibility of two-dimensional structures on the other hand, bring to mind the atomic mirror array [19, 22]. In this geometry, the interference of collective radiation in a two-dimensional sub-wavelength grid of atoms leads them to act as a mirror to resonant light. While at first glance it would seem this is impossible to implement with Mössbauer nuclei, due to incredibly small wavelength of the transitions, we saw in the two mode case that it is in fact the *difference* in wavelengths between guided modes that sets the length scale for the interference effects, and thus, a similar effect might be achievable in a waveguide setting.

Finally, due to the sputter deposition process for the creation of the thin-films, we are limited to polycrystalline layers and thus forward scattering only. On the other hand, if monocrystalline layers could be achieved experimentally, one could potentially match the longitudinal wavelength of a guided mode to a Bragg resonance of the guided layer, which would introduce back-scattering, and thus bidirectional propagation.

Appendix A

Radiative modes

In this Appendix, we study the radiative modes, and justify neglecting them in our equations of motion. The radiative modes correspond to the branch cut of Section 4.2, and form a continuum. They are physically interpreted as modes which propagate out into the capping layers, as opposed to being confined within the core of the waveguide like the guided modes. In Figure A.1, we can see that this results in a Fano-like profile peaked at the radiative branch cut $\mathrm{Re}(n_{top})k_0$. Although there is no exact general analytical solution that we know of for the Fourier inversion of this profile, we may nevertheless seek an appropriate approximate solution.

One such method is to seek a sum of poles that would approximate G_{rad} along the real q axis. The resulting approximation can be Fourier inverted to give a sum of decaying exponentials, plus a possible background contribution. The problem with this however, is that this approximation is in general inconsistent with the analytic continuation of G_{rad} into the imaginary q plane. However, as G_{rad} has a branch cut, which is avoided by our integration contour, we are free to chose poles which lie on this branch cut, and not affect the analytic properties of the contour interior. This corresponds to approximating the branch cut as a series of zeros and poles, and is thus a rational function approximation method.

Thus, our Ansatz for the approximation is

$$\overleftrightarrow{G}_{rad}(q, z_0, z_0, \omega) \approx \overleftrightarrow{\mathbb{1}}_{\perp} \sum_{\lambda \in \Lambda_{eff}} \frac{g_\lambda}{k_0} \cdot \frac{1}{q/k_0 - \mathrm{Re}(n_{top}) + i\beta_\lambda} + \overleftrightarrow{\mathbb{1}}_{\perp} \sum_{l} \frac{g_{rad}^{(l)}}{k_0} \left(\frac{q}{k_0}\right)^l , \tag{A.1}$$

where Λ_{eff} is the set indexing our effective radiative modes, $\beta_\lambda > 0$ is the displacement along the vertical branch-cut contour, and we have made a series expansion with coefficients $g_{rad}^{(l)}$ for the background, which is an entire function.

In Figure A.2, we can see the largest 4 pole contributions to this approximation, for a waveguide with structure Mo/B_4C (24 nm) /^{57}Fe (1 nm)/ B_4C (24 nm)/Mo, with the background overlaid. The background is constant over the spatial bandwidth of interest, and as such will result in a collective Lamb shift and broadening of the propagating nuclear polariton. Specifically, if we consider contribution to the

two-level equation of motion, (B.39), from the flat radiative background, we obtain

$$i\frac{m_0^2}{3\hbar}\,\mathrm{tr}\left\{\overleftrightarrow{\mathbb{1}_\perp}\right\}\mu_0\rho_N k_0 L g_{rad}^{(0)}\int \mathrm{d}x'\int\frac{\mathrm{d}q}{2\pi}e^{iq(x-x')}\hat{\Pi}_{ge}(x',\omega) \tag{A.2}$$

$$=if_{LM}\Gamma_{rad.}(\mathscr{M}1, I_e\to I_g)\frac{2}{3}\cdot\frac{\rho_N}{k_0^3}k_0 L g_{rad}^{(0)}\hat{\Pi}_{ge}(x,\omega) \tag{A.3}$$

$$=(i\Delta_{coll.}-\Gamma_{coll.})\hat{\Pi}_{ge}(x,\omega). \tag{A.4}$$

For front coupling, these are quite small. For example for the cavity in Figure A.2, the collective broadening is approximately 0.05% of $\Gamma_{rad.}$, and the Lamb shift 0.37% of $\Gamma_{rad.}$. Since approximately 90% of the single particle line-width is due to internal conversion, we can see this contribution is negligible.

The pole contributions themselves couple negligibly to the nuclei, having an effective resonant length that is 3 to 4 orders of magnitude smaller than that of the dominant two modes. Therefore, we can safely neglect the radiative modes, and consider only the dominant guided and leaky modes.

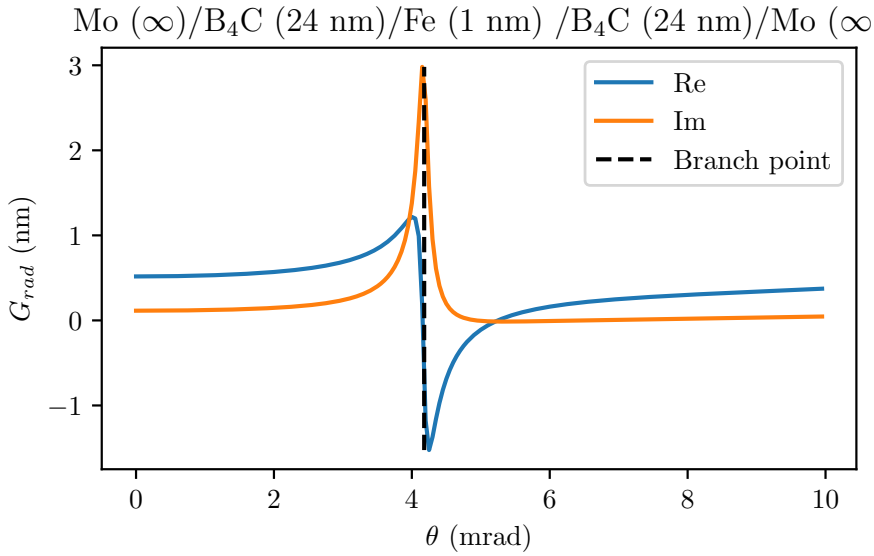

Figure A.1: Radiative Fourier space Green's function evaluated at the resonant layer, $G_{rad}(q = k_0\cos\theta, z_0, z_0, \omega)$ for a Molybdenum based waveguide. One can clearly see a Fano like profile along the real q axis, concentrated around $q = \mathrm{Re}(n_{\mathrm{Mo}})k_0$, corresponding to the branch cut contribution.

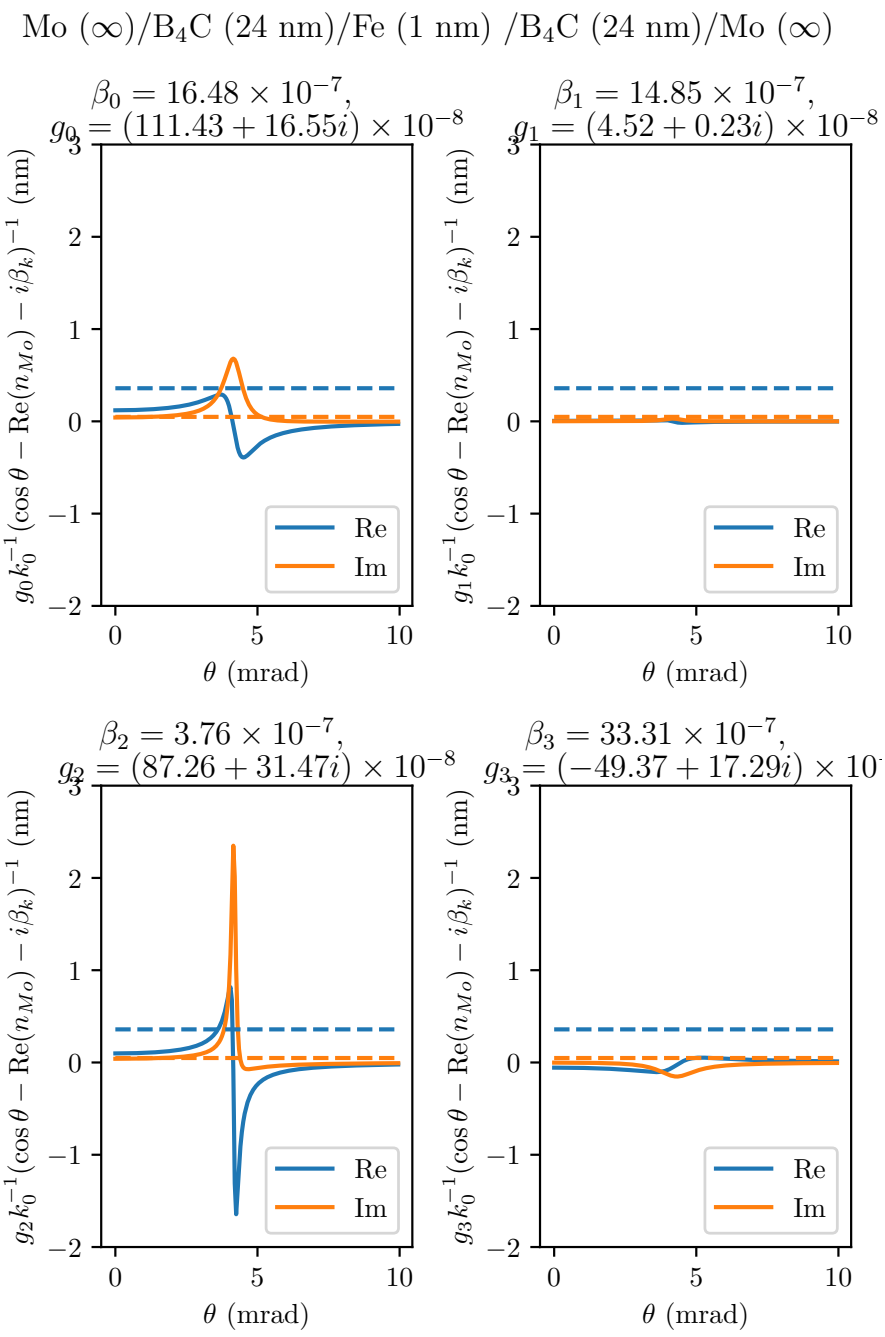

Figure A.2: Individual poles used to approximate the branch cut contribution of Figure A.1 (solid line), overlaid with the broad-band background (dashed line). The background results in a collective Lamb shift of $0.37\% \times \Gamma_{rad.}$, and collective broadening of $0.05\% \times \Gamma_{rad.}$. The residue and hence effective resonant length of each pole is 3 to 4 orders of magnitude smaller than that of the dominant guided modes.

Appendix B

Specific forms of the susceptibility tensor

In this Appendix, we derive specific forms of the susceptibility tensor that are required in the main body of the work.

Experimentally, thin film waveguides are formed through a sputter deposition process. As such, the resonant layer is polycrystalline in practice, and each crystal grain will have a random orientation and structure. Therefore, there is a probabilistic distribution of hyperfine parameters throughout the sample, and we must take this into account. Therefore, in Section B.1, we show that the susceptibility tensor in these circumstances can be obtained by averaging over the hyperfine distribution. We then specialize this in Section B.2 for isotropic distributions, to show that this reduces to a sum of Lorentzians multiplied by an isotropic polarizability tensor.

Finally, in Section B.3, we consider the limit of zero hyperfine splittings, to obtain the necessary pre-factors for the resulting single line susceptibility, as well as for the two-level Bloch equations.

B.1 Derivation of average susceptibility tensor

Suppose the hyperfine interaction is parameterized by a parameter N-vector $\vec{s}$, with probability distribution $p(\vec{s})$,

$$\int p(\vec{s})\, \mathrm{d}^N s = 1. \tag{B.1}$$

For each parameter vector, we can write the Hamiltonians for the excited and ground states in the form

$$H_e(\vec{s}) = \sum_\mu \hbar \Delta_\mu(\vec{s}) \left|\mu, \vec{s}\right\rangle\!\left\langle \mu, \vec{s}\right|, \tag{B.2}$$

$$H_g(\vec{s}) = \sum_j \hbar \Delta_j(\vec{s}) \left|j, \vec{s}\right\rangle\!\left\langle j, \vec{s}\right|, \tag{B.3}$$

where $\left|\mu, \vec{s}\right\rangle$ is the μth excited eigenstate of $H_e(\vec{s})$, $\Delta_\mu(\vec{s})$ its corresponding eigenvalue, and analogous for j.

The response tensor is then given by

$$\chi_+(\omega,\vec{s}) = \frac{m_0^2}{2I_g+1}\sum_{\mu,j}\frac{\vec{d}_{\mu j}(\vec{s})^*\otimes\vec{d}_{\mu j}(\vec{s})}{\hbar(\omega-\Delta_\mu(\vec{s})+\Delta_j(\vec{s})-i\frac{\gamma}{2})}, \tag{B.4}$$

where $\vec{d}_{\mu j}(\vec{s})$ is the dimensionless transition dipole vector.

Consider a geometry that has translational symmetry along the y axis, and a line of inhomogeneous nuclei located at x_0, z_0, that extends along the y coordinate. The response of this slice to a beam that is uniform in y is given by

$$B_{sc}(\vec{r},\omega) = \\ -\mu_0\rho_N\int \mathrm{d}y'\,\overleftrightarrow{G}_{mm}(x,x_0,y-y',z,z_0,\omega_0)\cdot\overleftrightarrow{\chi}_+(\omega,\vec{s}(y'))\cdot\vec{B}_{in}(x_0,z_0,\omega), \tag{B.5}$$

where we have expressed the inhomogeneity as a spatially dependent hyperfine parameter vector. Fourier transforming the y coordinate, we have

$$B_{sc}(x,q,z,\omega) = -\mu_0\rho_N\overleftrightarrow{G}_{mm}(x,x_0,q,z,z_0,\omega_0)\cdot\overleftrightarrow{\chi}_{avg}(\omega,q)\cdot\vec{B}_{in}(x_0,z_0,\omega), \tag{B.6}$$

where

$$\overleftrightarrow{\chi}_{avg}(\omega,q) = \int \mathrm{d}y'\,e^{-iqy'}\overleftrightarrow{\chi}_+(\omega,\vec{s}(y')). \tag{B.7}$$

Let us suppose that the bandwidth of the Fourier transformed Green's function is sufficiently narrow, such that e^{iqy} is approximately constant over a single crystal grain, and that the grains are approximately equally size. We can then take the integral to be given by the sum

$$\int \mathrm{d}y'\,e^{-iqy'}\overleftrightarrow{\chi}_+(\omega,\vec{s}(y')) \approx \delta y\sum_{i=1}^{M}\overleftrightarrow{\chi}_+(\omega,\vec{s}_i)e^{iqy_i}, \tag{B.8}$$

where M is the number of grains in the integral, $\vec{s}_i$ is the hyperfine parameter vector at the ith grain, y_i its location, and δy the domain size. Let us consider a coarse graining of the hyperfine parameters: we tile the hyperfine parameter space with N-cubes of size δs^N, and approximate all parameter vectors within an N-cube as equal to the cube centre. We can then collect all terms with the same coarse grained parameter vector together, to get

$$\int \mathrm{d}y'\,e^{-iqy'}\overleftrightarrow{\chi}_+(\omega,\vec{s}(y')) \approx \delta y\sum_{\vec{n}}\overleftrightarrow{\chi}_+(\omega,\vec{s}_{\vec{n}})\sum_{i_{\vec{n}}}e^{iqy_{i_{\vec{n}}}}, \tag{B.9}$$

where $\vec{n}$ labels the N-cubes, and $i_{\vec{n}}$ labels the crystal grains that have approximately the same hyperfine parameters $\vec{s}_{\vec{n}}$. Since these grains are randomly distributed, the sum over the phases will be approximately zero, unless $q=0$, in which case we have

$$\sum_{i_{\vec{n}}} = m_{\vec{n}}, \tag{B.10}$$

where $m_{\vec{n}}$ is the number of sites in the parameter bucket $\vec{s}_n$. We then have

$$\int \mathrm{d}y'\,e^{-iqy'}\overleftrightarrow{\chi}_+(\omega,\vec{s}(y')) \approx \begin{cases} M\delta y\sum_{\vec{n}}\overleftrightarrow{\chi}_+(\omega,\vec{s}_{\vec{n}})\frac{m_{\vec{n}}}{M}, & q=0,\\ 0, & \text{otherwise.}\end{cases} \tag{B.11}$$

For large enough samples, $m_{\vec{n}}/M$ tends toward the probability of finding a hyperfine parameter within the corresponding N-cube. Finally, we take the limit $M \to \infty$, and simultaneously $\delta s \to 0$, as a larger extent of nuclei can be divided into finer and finer sub-ensembles. The prefactor $M\delta y$ tends towards the total y extent of the nuclei, while the sum tends towards an integral over the probability distribution of hyperfine parameters. Therefore, we have the continuum limit

$$\overleftrightarrow{\chi}_{avg}(\omega, q) \approx 2\pi\delta(q) \int \mathrm{d}^N\vec{s}\, p(\vec{s})\overleftrightarrow{\chi}_{+}(\omega, \vec{s}). \tag{B.12}$$

While the proof presented here is somewhat ad hoc, it can be made rigorous using Lebesgue integration and the theory of random processes. Thus, an inhomogeneous ensemble driven by a uniform beam, will have a uniform scattered field, with the response tensor given by the average of the individual response tensors of the hyperfine distribution.

B.2 Isotropic hyperfine distributions

A common situation to encounter is that of polycrystalline samples with random orientations of the crystal grains. Let us suppose that a single grain has excited and ground state Hamiltonians

$$H_e = \sum_{\mu} \hbar\Delta_\mu \left|\mu\right\rangle\!\left\langle\mu\right|, \tag{B.13}$$

$$H_g = \sum_{j} \hbar\Delta_j \left|j\right\rangle\!\left\langle j\right|, \tag{B.14}$$

with the notation as per Chapter 5. A single such grain has susceptibility tensor given by (6.75),

$$\overleftrightarrow{\chi}_{+,0}(\omega) = \frac{m_0^2}{2I_e+1} \sum_{\mu,j} \frac{\vec{d}^{\,*}_{\mu j} \otimes \vec{d}_{\mu j}}{\hbar(\omega - \Delta_\mu + \Delta_j + i\frac{\gamma}{2})}. \tag{B.15}$$

Let us consider the reference coordinates to be that of this initial grain. The response of another grain, with a different orientation, can be found by a rotation of $\overleftrightarrow{\chi}_{+}$ through the corresponding Euler angles α, β, γ that relate the local hyperfine coordinates to that of the initial grain,

$$\overleftrightarrow{\chi}_{+}(\omega, \alpha, \beta) = R(\alpha, \beta, \gamma)\overleftrightarrow{\chi}_{+,0}(\omega)R(\alpha, \beta, \gamma)^{\dagger}, \tag{B.16}$$

where R is the Euler rotation matrix in polarization space. Since the polarization space is an irreducible representation of $SO(3)$ with $l = 1$, we have

$$R(\alpha, \beta, \gamma)_{q,q'} = D^1_{q,q'}(\alpha, \beta, \gamma), \tag{B.17}$$

where q, q' denotes the matrix elements of the rotation in terms of spherical basis vectors, and D is the Wigner rotation matrix.

Expanding the dipole vectors in the spherical vector basis via (5.13),

$$\vec{d}_{\mu j} = \sum_{q} C(1q, \mu \to j)\hat{e}_q, \tag{B.18}$$

we have

$$\overleftrightarrow{\chi}_+(\omega,\alpha,\beta,\gamma) = \frac{m_0^2}{2I_e+1}\sum_{\mu,j}\sum_{q,q'}\sum_{k,k'} C(1q,\mu\to j)C(1q',\mu\to j)\hat{e}_k\otimes\hat{e}_{k'} \times D^1_{k,q}(\alpha,\beta,\gamma)D^1_{q',q_2}(\alpha,\beta,\gamma)^*. \quad \text{(B.19)}$$

We now take the average over the isotropic distribution. The probability measure for Euler angles is simply the normalized Haar measure for the rotation group $SO(3)$, which is given by

$$\int \mathrm{d}\mu(\alpha,\beta,\gamma) = \frac{1}{8\pi^2}\int_{-\pi}^{\pi}\mathrm{d}\alpha\int_{-\frac{\pi}{2}}^{\frac{\pi}{2}}\sin\beta\,\mathrm{d}\beta\int_{-\pi}^{\pi}\mathrm{d}\gamma\,. \quad \text{(B.20)}$$

We therefore have the averaged response

$$\overleftrightarrow{\chi}_{avg}(\omega) = \int \mathrm{d}\mu(\alpha,\beta,\gamma)\,\overleftrightarrow{\chi}_+(\omega,\alpha,\beta,\gamma). \quad \text{(B.21)}$$

Using the orthogonality of Wigner matrices,

$$\int \mathrm{d}\mu(\alpha,\beta,\gamma)\,D^l_{q,k}(\alpha,\beta,\gamma)D^{l'}_{q',k'}(\alpha,\beta,\gamma)^* = \frac{1}{2l+1}\delta_{q,q'}\delta_{k,k'}\delta_{l,l'} \quad \text{(B.22)}$$

we finally arrive at

$$\overleftrightarrow{\chi}_{avg}(\omega) = \frac{\overleftrightarrow{\mathbb{1}}}{3}\sum_{\mu,j}\frac{m_0^2}{\hbar(\omega-\Delta_\mu+\Delta_j+i\frac{\gamma}{2})}. \quad \text{(B.23)}$$

B.3 Reduction to two level system

In the absence of hyperfine splittings, the susceptibility tensor is given by

$$\overleftrightarrow{\chi}_+(\omega) = \frac{m_0^2}{2I_g+1}\sum_{m_e,m_g}\frac{\vec{d}^*_{m_em_g}\otimes\vec{d}_{m_em_g}}{\hbar(\omega+i\gamma/2)}, \quad \text{(B.24)}$$

where we have chosen the angular momentum basis for the ground and excited states. We can evaluate the polarization dyadic by first expanding in terms of Wigner 3j symbols,

$$\sum_{m_e,m_g}\vec{d}_{m_em_g}\otimes\vec{d}^*_{m_em_g} = (2I_e+1)\sum_{q,q'}\sum_{m_e,m_g}\hat{e}_q\otimes\hat{e}^*_{q'}\begin{pmatrix}I_e & I_g & 1\\ -m_e & m_g & q\end{pmatrix}\begin{pmatrix}I_e & I_g & 1\\ -m_e & m_g & q'\end{pmatrix} \quad \text{(B.25)}$$

$$= \frac{2I_e+1}{3}\sum_q \hat{e}_q\otimes\hat{e}_q$$

$$= \frac{2I_e+1}{3}\overleftrightarrow{\mathbb{1}},$$

where we have used the 3j orthogonality relation

$$\sum_{m_e,m_g}\begin{pmatrix}I_e & I_g & 1\\ -m_e & m_g & q\end{pmatrix}\begin{pmatrix}I_e & I_g & 1\\ -m_e & m_g & q'\end{pmatrix} = \frac{1}{3}\delta_{qq'}. \quad \text{(B.26)}$$

We also note that as the decay rate of the elastic scattering channel is given by

$$\Gamma_{elas}(\mathscr{M}1, I_e \to I_g) = \frac{\mu_0 k_0^3}{3\pi\hbar}\mathscr{B}(\mathscr{M}1, I_e \to I_g) f_{LM}, \tag{B.27}$$

and we also have

$$m_0^2 = f_{LM}\mathscr{B}(\mathscr{M}1, I_e \to I_g) \tag{B.28}$$

$$\Gamma_{elas}(\mathscr{M}1, I_e \to I_g) = \frac{1}{1+\alpha}\gamma, \tag{B.29}$$

from before, that we can write

$$m_0^2 = \frac{3\pi\hbar}{k_0^3}\cdot\frac{f_{LM}}{1+\alpha}\gamma. \tag{B.30}$$

The susceptibility is therefore given by

$$\overleftrightarrow{\chi}_+(\omega) = \overleftrightarrow{\mathbb{1}}\frac{2I_e+1}{2I_g+1}\frac{2\pi}{\mu_0 k_0^3}\cdot\frac{f_{LM}}{1+\alpha}\cdot\frac{\gamma/2}{\omega+i\gamma/2}. \tag{B.31}$$

The scattered response will therefore have the same polarization as the field driving it. Furthermore, for all three geometries of grazing incidence, forward scattering, and waveguide front coupling, the polarization space of the Green's function is approximately parallel to the plane perpendicular to the propagation direction, i.e.

$$\overleftrightarrow{G}_{mm}(\vec{r}, \vec{r}', \omega_0) \approx (\overleftrightarrow{\mathbb{1}} - \hat{k}\otimes\hat{k})G_{mm}(\vec{r}, \vec{r}', \omega_0). \tag{B.32}$$

As such, as the polarization of the incident field is entirely preserved, we can therefore write the total field as

$$\hat{B}_+(\vec{r}, t) \to \hat{B}_+(\vec{r}, t)e^{-i(\omega_0 t - k_0 x)}\hat{e}_{in}, \tag{B.33}$$

where $\hat{B}_+$ is now the scalar field envelope, and $\hat{e}_{in}$ the polarization of the incident beam.

The 'two level' nuclear operators then can be defined as

$$\hat{\Pi}_{ee} = \sum_{m_e}\hat{\Pi}_{m_e m_e}, \tag{B.34}$$

$$\hat{\Pi}_{eg} = \sum_{m_e m_g}\hat{\Pi}_{m_e m_g}\vec{d}^*_{m_e m_g}\cdot\hat{e}_{in}, \tag{B.35}$$

$$\hat{\Pi}_{gg} = \sum_{j}\hat{\Pi}_{jj}. \tag{B.36}$$

The nuclear Bloch equations (6.14) through (6.17) then become

$$\partial_t\hat{\Pi}_{ee}(x,t) = -\gamma\hat{\Pi}_{ee}(x,t) + \frac{im_0}{\hbar}\left(\hat{\Pi}_{eg}(\vec{r},t)\hat{B}_+(x,t) - \hat{\Pi}_{ge}(x,t)\hat{B}_-(x,t)\right) \tag{B.37}$$

$$\partial_t\hat{\Pi}_{gg}(x,t) = \gamma\hat{\Pi}_{ee}(x,t) - \frac{im_0}{\hbar}\left(\hat{\Pi}_{eg}(x,t)\hat{B}_+(x,t) - \hat{\Pi}_{ge}(x,t)\hat{B}_-(x,t)\right) \tag{B.38}$$

$$\partial_t\hat{\Pi}_{eg}(x,t) = -\frac{\gamma}{2}\hat{\Pi}_{eg}(x,t) + \frac{im_0}{\hbar}\left(\hat{\Pi}_{ee}(x,t) - \hat{\Pi}_{gg}(x,t)\right)\hat{B}_-(x,t). \tag{B.39}$$

$$\partial_t\hat{\Pi}_{ge}(x,t) = -\frac{\gamma}{2}\hat{\Pi}_{ge}(x,t) - \frac{im_0}{\hbar}\left(\hat{\Pi}_{ee}(x,t) - \hat{\Pi}_{gg}(x,t)\right)\hat{B}_+(x,t). \tag{B.40}$$

Appendix C

Conventions and formulae

C.1 Conventions

Fourier transforms

As we deal extensively with partial Fourier transforms, a notation to distinguish all possible combinations of spatial and temporal Fourier transform would be cumbersome. Therefore, for all Fourier transforms, we distinguish between a function $f(\vec{r}, t)$ and its corresponding transform $f(\vec{k}, \omega)$ etc. by the function arguments.

For time domain Fourier transforms, the convention we use for the forward and backward transforms is

$$f(\omega) = \int_{-\infty}^{\infty} \mathrm{d}t\, e^{i\omega t} f(t), \tag{C.1}$$

$$f(t) = \int_{-\infty}^{\infty} \frac{\mathrm{d}\omega}{2\pi} e^{-i\omega t} f(\omega). \tag{C.2}$$

For spatial domain Fourier transforms, we use the corresponding convention,

$$f(\vec{q}) = \int_{\mathbb{R}^3} \mathrm{d}^3 r\, e^{-i\vec{q}\cdot\vec{r}} f(\vec{r}), \tag{C.3}$$

$$f(\vec{r}) = \int_{\mathbb{R}^3} \frac{\mathrm{d}^3 q}{(2\pi)^3} e^{i\vec{q}\cdot\vec{r}} f(\vec{q}). \tag{C.4}$$

With this convention a plane wave with positive frequency ω and wave-vector $\vec{k}$, travelling in the positive $\hat{k}$ direction reads

$$e^{-i\omega t + i\vec{k}\cdot\vec{r}}. \tag{C.5}$$

A Hermitian operator separated into positive and negative frequency components reads

$$\psi(t) = \psi_+(t) + \psi_-(t), \tag{C.6}$$

$$\psi_+(t) = \psi_-(t)^\dagger, \tag{C.7}$$

$$\psi_+(t) = \int_0^{\infty} \frac{\mathrm{d}\omega}{2\pi} e^{-i\omega t} \psi_+(\omega), \tag{C.8}$$

$$\psi_+(\omega) = \int_{-\infty}^{\infty} \mathrm{d}t\, e^{i\omega t} \psi(t), \quad \omega > 0. \tag{C.9}$$

In particular, for a free Bosonic annihilation operator b, with Hamiltonian given by

$$H = \hbar\omega b^\dagger b, \tag{C.10}$$
$$[b, b^\dagger] = 1, \tag{C.11}$$

the Heisenberg evolution of the operator is given by

$$b(t) = b(0)e^{-i\omega t}. \tag{C.12}$$

Therefore, we identify

$$b_+ = b, \quad b_- = b^\dagger. \tag{C.13}$$

Wigner symbols, Clebsch-Gordan coefficients

For the Clebsch-Gordan coefficients, we have chosen to denote

$$C(lq, I_e, m_e \to I_g, m_g) = \left\langle I_g, m_g, l, q \middle| I_e, m_e \right\rangle \tag{C.14}$$

and use the Condon-Shortley phase convention, such that the coefficients are real.

For the Wigner 3j symbols, we use the convention of Edmonds, [115, eq. 3.7.3]

$$\begin{pmatrix} j_1 & j_2 & j_3 \\ m_1 & m_2 & m_3 \end{pmatrix} = \frac{(-1)^{j_1 - j_2 - m_3}}{\sqrt{2j_3 + 1}} \langle j_1, m_1, j_2, m_2 | j_3, m_3 \rangle . \tag{C.15}$$

With this convention, the Wigner-Eckart theorem reads [115, eq. 5.4.1]

$$\langle j', m' | T^{(k)}_q | j, m \rangle = (-1)^{j' - m'} \begin{pmatrix} j' & k & j \\ -m' & q & m \end{pmatrix} \langle j' || T^{(k)} || j \rangle . \tag{C.16}$$

C.2 Useful formulae

In Section 5.2, we defined the expansion coefficients

$$C(lq, \mu \to j) = \sqrt{2I_e + 1} \sum_{m_e, m_g} (-1)^{I_e - m_e} \langle \mu | I_e, m_e \rangle \left\langle I_g, m_g \middle| j \right\rangle \begin{pmatrix} I_e & 1 & I_g \\ -m_e & q & m_g \end{pmatrix}, \tag{C.17}$$

and the rate fractions

$$\mathcal{R}(\lambda l, \mu \to j) = \sum_q |C(lq, \mu \to j)|^2. \tag{C.18}$$

We will now evaluate the sums over their arguments. To do so, we will use the following identity of Wigner symbols,

$$\sum_{m_i, m_j} \begin{pmatrix} j_1 & j_2 & j_3 \\ m_1 & m_2 & m_3 \end{pmatrix} \begin{pmatrix} j_1 & j_2 & j_3 \\ m_1 & m_2 & m_3' \end{pmatrix} = \frac{\delta_{m_k m_k'}}{2j_k + 1}, \tag{C.19}$$

where ijk is any permutation of 123, and we have assumed the triangle conditions of j_1, j_2, j_3 are satisfied. The identity can be obtained from their orthogonality

relation in m_1, m_2, and permutation of columns. Applying this identity to the rate coefficients gives

$$\begin{aligned}\sum_{q,\mu} C(lq,\,\mu\to j)C(lq,\,\mu\to j') &= (2I_e+1)\sum_{m_e,m_g}\sum_{m_e',m_g'}(-1)^{m_e'-m_e}\langle I_e,\,m_e|\mu\rangle\left\langle\mu\middle|I_e,\,m_e'\right\rangle\\ &\quad\times\left\langle j'\middle|I_g,\,m_g'\right\rangle\langle I_g,\,m_g|j\rangle\begin{pmatrix}I_e & l & I_g\\ -m_e & q & m_g\end{pmatrix}\begin{pmatrix}I_e & l & I_g\\ -m_e' & q & m_g'\end{pmatrix}\\ &= (2I_e+1)\sum_{q,m_e}\sum_{m_g,m_g'}\left\langle j'\middle|I_g,\,m_g'\right\rangle\langle I_g,\,m_g|j\rangle\\ &\qquad\times\begin{pmatrix}I_e & l & I_g\\ -m_e & q & m_g\end{pmatrix}\begin{pmatrix}I_e & l & I_g\\ -m_e & q & m_g'\end{pmatrix}\\ &= \frac{2I_e+1}{2I_g+1}\sum_{m_g}\left\langle j'\middle|I_g,\,m_g\right\rangle\langle I_g,\,m_g|j\rangle\\ &= \frac{2I_e+1}{2I_g+1}\delta_{jj'}.\end{aligned}\tag{C.20}$$

Similarly, we have

$$\begin{aligned}\sum_{q,j} C(lq,\,\mu\to j)C(lq,\,\mu'\to j) &= (2I_e+1)\sum_{m_e,m_g}\sum_{m_e',m_g'}(-1)^{m_e'-m_e}\langle I_e,\,m_e|\mu'\rangle\left\langle\mu\middle|I_e,\,m_e'\right\rangle\\ &\quad\times\left\langle j\middle|I_g,\,m_g'\right\rangle\langle I_g,\,m_g|j\rangle\begin{pmatrix}I_e & l & I_g\\ -m_e & q & m_g\end{pmatrix}\begin{pmatrix}I_e & l & I_g\\ -m_e' & q & m_g'\end{pmatrix}\\ &= (2I_e+1)\sum_{q,m_g}\sum_{m_e,m_e'}\langle I_e,\,m_e|\mu'\rangle\left\langle\mu\middle|I_e,\,m_e'\right\rangle\\ &\qquad\times\begin{pmatrix}I_e & l & I_g\\ -m_e & q & m_g\end{pmatrix}\begin{pmatrix}I_e & l & I_g\\ -m_e' & q & m_g\end{pmatrix}\\ &= \sum_{m_e}\langle I_e,\,m_e|\mu'\rangle\left\langle\mu\middle|I_e,\,m_e'\right\rangle\\ &= \delta_{\mu\mu'}.\end{aligned}\tag{C.21}$$

Bibliography

[1] M. Lucibella, "May 16, 1960: Maiman Builds First Working Laser", APS News **19** (2010).

[2] P. M. Kraus, M. Zürch, S. K. Cushing, D. M. Neumark, and S. R. Leone, "The ultrafast X-ray spectroscopic revolution in chemical dynamics", Nature Reviews Chemistry **2**, 82–94 (2018).

[3] Y. Obara, H. Ito, T. Ito, N. Kurahashi, S. Thürmer, H. Tanaka, T. Katayama, T. Togashi, S. Owada, Y.-i. Yamamoto, S. Karashima, J. Nishitani, M. Yabashi, T. Suzuki, and K. Misawa, "Femtosecond time-resolved X-ray absorption spectroscopy of anatase TiO2 nanoparticles using XFEL", Structural Dynamics **4**, 044033 (2017).

[4] T. Salditt, M. Osterhoff, M. Krenkel, R. N. Wilke, M. Priebe, M. Bartels, S. Kalbfleisch, and M. Sprung, "Compound focusing mirror and X-ray waveguide optics for coherent imaging and nano-diffraction", Journal of Synchrotron Radiation **22**, 867–878 (2015).

[5] K. Sakurai and M. Mizusawa, "Quick atomic-scale structure imaging by synchrotron x-rays: a new tool for probing realistic inhomogeneous systems", Nanotechnology **15**, S428 (2004).

[6] T. Koyama, H. Takano, S. Konishi, T. Tsuji, H. Takenaka, S. Ichimaru, T. Ohchi, and Y. Kagoshima, "Circular multilayer zone plate for high-energy x-ray nanoimaging", Review of Scientific Instruments **83**, 013705 (2012).

[7] M. Drescher, M. Hentschel, R. Kienberger, M. Uiberacker, V. Yakovlev, A. Scrinzi, T. Westerwalbesloh, U. Kleineberg, U. Heinzmann, and F. Krausz, "Time-resolved atomic inner-shell spectroscopy", Nature **419**, 803–807 (2002).

[8] K. Hämäläinen, D. P. Siddons, J. B. Hastings, and L. E. Berman, "Elimination of the inner-shell lifetime broadening in x-ray-absorption spectroscopy", Physical Review Letters **67**, 2850–2853 (1991).

[9] W.-T. Liao, C. H. Keitel, and A. Pálffy, "X-ray-generated heralded macroscopical quantum entanglement of two nuclear ensembles", Scientific Reports **6**, 33361 (2016).

[10] M. Fleischhauer, A. Imamoglu, and J. P. Marangos, "Electromagnetically induced transparency: Optics in coherent media", Reviews of Modern Physics **77**, 633–673 (2005).

[11] U. Gaubatz, P. Rudecki, S. Schiemann, and K. Bergmann, "Population transfer between molecular vibrational levels by stimulated Raman scattering with partially overlapping laser fields. A new concept and experimental results", The Journal of Chemical Physics **92**, 5363–5376 (1990).

[12]R. H. Dicke, "Coherence in Spontaneous Radiation Processes", Physical Review **93**, 99–110 (1954).

[13]M. Tavis and F. W. Cummings, "Exact Solution for an N-Molecule—Radiation-Field Hamiltonian", Physical Review **170**, 379–384 (1968).

[14]A. Svidzinsky and J.-T. Chang, "Cooperative spontaneous emission as a many-body eigenvalue problem", Phys. Rev. A **77**, 043833 (2008).

[15]A. A. Svidzinsky, J.-T. Chang, and M. O. Scully, "Cooperative Spontaneous Emission of N Atoms: Many-Body Eigenstates, the Effect of Virtual Lamb Shift Processes, and Analogy with Radiation of N Classical Oscillators", Physical Review A **81**, 053821 (2010).

[16]A. A. Svidzinsky, "Nonlocal effects in single-photon superradiance", Physical Review A **85**, 013821 (2012).

[17]R. Friedberg and J. T. Manassah, "Effects of including the counterrotating term and virtual photons on the eigenfunctions and eigenvalues of a scalar photon collective emission theory", Physics Letters A **372**, 2514–2521 (2008).

[18]J. T. Manassah, "Cooperative radiation from atoms in different geometries: decay rate and frequency shift", Advances in Optics and Photonics **4**, 108–156 (2012).

[19]J. Rui, D. Wei, A. Rubio-Abadal, S. Hollerith, J. Zeiher, D. M. Stamper-Kurn, C. Gross, and I. Bloch, "A subradiant optical mirror formed by a single structured atomic layer", Nature **583**, 369–374 (2020).

[20]A. Asenjo-Garcia, J. D. Hood, D. E. Chang, and H. J. Kimble, "Atom-light interactions in quasi-one-dimensional nanostructures: a green's-function perspective", Phys. Rev. A **95**, 033818 (2017).

[21]A. Asenjo-Garcia, M. Moreno-Cardoner, A. Albrecht, H. J. Kimble, and D. E. Chang, "Exponential improvement in photon storage fidelities using subradiance and "selective radiance" in atomic arrays", Phys. Rev. X **7**, 031024 (2017).

[22]D. E. Chang, L. Jiang, A. V. Gorshkov, and H. J. Kimble, "Cavity QED with atomic mirrors", New Journal of Physics **14**, 063003 (2012).

[23]F. Vagizov, V. Antonov, Y. V. Radeonychev, R. N. Shakhmuratov, and O. Kocharovskaya, "Coherent control of the waveforms of recoilless γ-ray photons", Nature **508**, 80–83 (2014).

[24]R. Coussement, Y. Rostovtsev, J. Odeurs, G. Neyens, H. Muramatsu, S. Gheysen, R. Callens, K. Vyvey, G. Kozyreff, P. Mandel, R. Shakhmuratov, and O. Kocharovskaya, "Controlling Absorption of Gamma Radiation via Nuclear Level Anticrossing", Physical Review Letters **89**, 107601 (2002).

[25]Y. V. Radeonychev, I. R. Khairulin, F. G. Vagizov, M. Scully, and O. Kocharovskaya, "Observation of Acoustically Induced Transparency for γ-Ray Photons", Physical Review Letters **124**, 163602 (2020).

[26]O. Kocharovskaya, R. Kolesov, and Y. Rostovtsev, "Coherent optical control of Mössbauer spectra", Physical Review Letters **82**, 3593–3596 (1999).

[27]X. Zhang, W.-T. Liao, A. Kalachev, R. Shakhmuratov, M. Scully, and O. Kocharovskaya, "Nuclear quantum memory and time sequencing of a single γ photon", Physical Review Letters **123**, 250504 (2019).

[28] J. Haber, X. Kong, C. Strohm, S. Willing, J. Gollwitzer, L. Bocklage, R. Rüffer, A. Pálffy, and R. Röhlsberger, "Rabi oscillations of X-ray radiation between two nuclear ensembles", Nature Photonics **11**, 720–725 (2017).

[29] X. Kong and A. Pálffy, "Stopping Narrow-Band X-Ray Pulses in Nuclear Media", Physical Review Letters **116**, 197402 (2016).

[30] R. Röhlsberger, H.-C. Wille, K. Schlage, and B. Sahoo, "Electromagnetically induced transparency with resonant nuclei in a cavity", Nature **482**, 199–203 (2012).

[31] K. P. Heeg, H.-C. Wille, K. Schlage, T. Guryeva, D. Schumacher, I. Uschmann, K. S. Schulze, B. Marx, T. Kämpfer, G. G. Paulus, R. Röhlsberger, and J. Evers, "Vacuum-Assisted Generation and Control of Atomic Coherences at X-Ray Energies", Physical Review Letters **111**, 073601 (2013).

[32] K. P. Heeg, A. Kaldun, C. Strohm, C. Ott, R. Subramanian, D. Lentrodt, J. Haber, H.-C. Wille, S. Goerttler, R. Rüffer, C. H. Keitel, R. Röhlsberger, T. Pfeifer, and J. Evers, "Coherent X-ray-optical control of nuclear excitons", Nature **590**, 401–404 (2021).

[33] K. P. Heeg, C. Ott, D. Schumacher, H.-C. Wille, R. Röhlsberger, T. Pfeifer, and J. Evers, "Interferometric phase detection at x-ray energies via Fano resonance control", Physical Review Letters **114**, 207401 (2015).

[34] K. P. Heeg, J. Haber, D. Schumacher, L. Bocklage, H.-C. Wille, K. S. Schulze, R. Loetzsch, I. Uschmann, G. G. Paulus, R. Rüffer, R. Röhlsberger, and J. Evers, "Tunable Subluminal Propagation of Narrow-band X-Ray Pulses", Physical Review Letters **114**, 203601 (2015).

[35] K. P. Heeg, A. Kaldun, C. Strohm, P. Reiser, C. Ott, R. Subramanian, D. Lentrodt, J. Haber, H.-C. Wille, S. Goerttler, R. Rüffer, C. H. Keitel, R. Röhlsberger, T. Pfeifer, and J. Evers, "Spectral narrowing of x-ray pulses for precision spectroscopy with nuclear resonances", Science **357**, 375–378 (2017).

[36] R. Röhlsberger, K. Schlage, B. Sahoo, S. Couet, and R. Rüffer, "Collective Lamb Shift in Single-Photon Superradiance", Science **328**, 1248–1251 (2010).

[37] A. I. Chumakov, A. Q. R. Baron, I. Sergueev, C. Strohm, O. Leupold, Y. Shvyd'ko, G. V. Smirnov, R. Rüffer, Y. Inubushi, M. Yabashi, K. Tono, T. Kudo, and T. Ishikawa, "Superradiance of an ensemble of nuclei excited by a free electron laser", Nature Physics **14**, 261–264 (2018).

[38] X. Kong and A. Pálffy, "Collective radiation spectrum for ensembles with Zeeman splitting in single-photon superradiance", Physical Review A **96**, 033819 (2017).

[39] K. P. Heeg and J. Evers, "X-ray quantum optics with Mössbauer nuclei embedded in thin-film cavities", Physical Review A **88**, 043828 (2013).

[40] O. Diekmann, D. Lentrodt, and J. Evers, "Inverse design approach to x-ray quantum optics with Mössbauer nuclei in thin-film cavities", Physical Review A **105**, 013715 (2022).

[41] I. Nam et al., "High-brightness self-seeded X-ray free-electron laser covering the 3.5 keV to 14.6 keV range", Nat. Photon. **15**, 435–441 (2021).

[42] Y. Shvyd'ko, V. Blank, and S. Terentyev, "Diamond x-ray optics: Transparent, resilient, high-resolution, and wavefront preserving", MRS Bulletin **42**, 437–444 (2017).

[43]D. H. Bilderback, S. A. Hoffman, and D. J. Thiel, "Nanometer spatial resolution achieved in hard x-ray imaging and laue diffraction experiments", Science **263**, 201–203 (1994).

[44]A. Iida and K. Hirano, "Kirkpatrick-Baez optics for a sub-μm synchrotron x-ray microbeam and its applications to x-ray analysis", Nuclear Instruments and Methods in Physics Research Section B: Beam Interactions with Materials and Atoms **114**, 149–153 (1996).

[45]C. G. Schroer and B. Lengeler, "Focusing hard x rays to nanometer dimensions by adiabatically focusing lenses", Phys. Rev. Lett. **94**, 054802 (2005).

[46]H. Mimura, S. Handa, T. Kimura, H. Yumoto, D. Yamakawa, H. Yokoyama, S. Matsuyama, K. Inagaki, K. Yamamura, Y. Sano, K. Tamasaku, Y. Nishino, M. Yabashi, T. Ishikawa, and K. Yamauchi, "Breaking the 10 nm barrier in hard-x-ray focusing", Nature Physics **6**, 122–125 (2009).

[47]R. Huang and D. H. Bilderback, "Single-bounce monocapillaries for focusing synchrotron radiation: modeling, measurements and theoretical limits", Journal of Synchrotron Radiation **13**, 74–84 (2006).

[48]X. Zeng, F. Duewer, M. Feser, C. Huang, A. Lyon, A. Tkachuk, and W. Yun, "Ellipsoidal and parabolic glass capillaries as condensers for x-ray microscopes", Appl. Opt. **47**, 2376–2381 (2008).

[49]M. Zwanenburg, J. Bongaerts, J. Peters, D. Riese, and J. van der Veen, "Focusing of coherent x-rays in a tapered planar waveguide", Physica B: Condensed Matter **283**, 285–288 (2000).

[50]F. Pfeiffer, C. David, M. Burghammer, C. Riekel, and T. Salditt, "Two-dimensional x-ray waveguides and point sources", Science **297**, 230–234 (2002).

[51]A. Jarre, C. Fuhse, C. Ollinger, J. Seeger, R. Tucoulou, and T. Salditt, "Two-dimensional hard x-ray beam compression by combined focusing and waveguide optics", Phys. Rev. Lett. **94**, 074801 (2005).

[52]S. P. Krüger, H. Neubauer, M. Bartels, S. Kalbfleisch, K. Giewekemeyer, P. J. Wilbrandt, M. Sprung, and T. Salditt, "Sub-10nm beam confinement by x-ray waveguides: design, fabrication and characterization of optical properties", Journal of Synchrotron Radiation **19**, 227–236 (2012).

[53]H.-Y. Chen, S. Hoffmann, and T. Salditt, "X-ray beam compression by tapered waveguides", Applied Physics Letters **106**, 194105 (2015).

[54]S. Hoffmann-Urlaub, P. Höhne, M. Kanbach, and T. Salditt, "Advances in fabrication of x-ray waveguides", Microelectronic Engineering **164**, 135–138 (2016).

[55]T. Salditt, S. Hoffmann, M. Vassholz, J. Haber, M. Osterhoff, and J. Hilhorst, "X-ray optics on a chip: guiding x-rays in curved channels", Phys. Rev. Lett. **115**, 203902 (2015).

[56]Y.-H. Chen, P.-H. Lin, G.-Y. Wang, A. Pálffy, and W.-T. Liao, "Transient nuclear inversion by x-ray free electron laser in a tapered x-ray waveguide", Physical Review Research **4**, L032007 (2022).

[57]L. M. Lohse, A. Negi, A. Panchwanee, O. Leupold, I. Sergeev, P. Andrejić, A. Pálffy, T. Salditt, and R. Röhlsberger, "Nuclear forward scattering in a single mode x-ray waveguide", (in preparation).

[58] Y. O. Dudin, L. Li, F. Bariani, and A. Kuzmich, "Observation of coherent many-body Rabi oscillations", Nature Physics **8**, 790–794 (2012).

[59] R. L. Mössbauer, "Kernresonanzfluoreszenz von gammastrahlung in Ir191", Zeitschrift für Physik **151**, 124–143 (1958).

[60] D. A. Steck, *Quantum and Atom Optics*, (Jan. 26, 2019) http://steck.us/teaching.

[61] H. Weiss and H. Langhoff, "Observation of one phonon transitions in terbium by nuclear resonance fluorescence", Physics Letters A **69**, 448–450 (1979).

[62] J. P. Hannon and G. T. Trammell, "Mössbauer Diffraction. I. Quantum Theory of Gamma-Ray and X-Ray Optics", Physical Review **169**, 315–329 (1968).

[63] J. P. Hannon and G. T. Trammell, "Mössbauer Diffraction. II. Dynamical Theory of Mössbauer Optics", Physical Review **186**, 306–325 (1969).

[64] J. P. Hannon, N. J. Carron, and G. T. Trammell, "Mössbauer diffraction. III. Emission of Mössbauer gamma rays from crystals. A. General theory", Physical Review B **9**, 2791–2809 (1974).

[65] J. P. Hannon, G. T. Trammell, M. Blume, and D. Gibbs, "X-Ray Resonance Exchange Scattering", Physical Review Letters **61**, 1245–1248 (1988).

[66] J. Hannon and G. Trammell, "Coherent γ-ray optics", Hyperfine Interactions **123**, 127–274 (1999).

[67] Y. Kagan, A. M. Afanas'ev, and I. P. Perstnev, "Theory of resonance bragg scattering of y quanta by regular crystals", Soviet Physics-JETP **27**, 819 (1968).

[68] Y. Kagan, A. M. Afanas'ev, and V. G. Kohn, "On excitation of isomeric nuclear states in a crystal by synchrotron radiation", Journal of Physics C: Solid State Physics **12**, 615–631 (1979).

[69] Y. Kagan, "Theory of coherent phenomena and fundamentals in nuclear resonant scattering", Hyperfine Interactions **123**, 83–126 (1999).

[70] Y. V. Shvyd'ko, "Nuclear resonant forward scattering of x rays: Time and space picture", Physical Review B **59**, 9132–9143 (1999).

[71] Y. V. Shvyd'ko, T. Hertrich, U. van Bürck, E. Gerdau, O. Leupold, J. Metge, H. D. Rüter, S. Schwendy, G. V. Smirnov, W. Potzel, and P. Schindelmann, "Storage of Nuclear Excitation Energy through Magnetic Switching", Physical Review Letters **77**, 3232–3235 (1996).

[72] W. Sturhahn and V. Kohn, "Theoretical aspects of incoherent nuclear resonant scattering", Hyperfine Interactions **123**, 367–399 (1999).

[73] K. P. Heeg, "X-Ray Quantum Optics With Mössbauer Nuclei In Thin-Film Cavities" (Ruprecht-Karls-Universität Heidelberg, Heidelberg, Germany, 2014).

[74] D. Lentrodt, K. P. Heeg, C. H. Keitel, and J. Evers, "Ab initio quantum models for thin-film x-ray cavity QED", Physical Review Research **2**, 023396 (2020).

[75] X. Kong, D. E. Chang, and A. Pálffy, "Green's-function formalism for resonant interaction of x rays with nuclei in structured media", Physical Review A **102**, 033710 (2020).

[76] H. T. Dung, L. Knöll, and D.-G. Welsch, "Resonant dipole-dipole interaction in the presence of dispersing and absorbing surroundings", Phys. Rev. A **66**, 063810 (2002).

[77]T. Gruner and D.-G. Welsch, "Green-function approach to the radiation-field quantization for homogeneous and inhomogeneous Kramers-Kronig dielectrics", Physical Review A **53**, 1818–1829 (1996).

[78]L. Novotny and B. Hecht, *Principles of nano-optics*, 2nd ed. (Cambridge University Press, Cambridge, 2012), 564 pp.

[79]G. Smirnov, "General properties of nuclear resonant scattering", Hyperfine Interactions **123/124**, 31–77 (1999).

[80]M. S. Tomaš, "Green function for multilayers: Light scattering in planar cavities", Physical Review A **51**, 2545–2559 (1995).

[81]P. Johansson, "Electromagnetic green's function for layered systems: applications to nanohole interactions in thin metal films", Phys. Rev. B **83**, 195408 (2011).

[82]S. Y. Buhmann, *Dispersion Forces I*, Vol. 247, Springer Tracts in Modern Physics (Springer, Berlin, Heidelberg, 2012).

[83]G. W. Hanson and A. B. Yakovlev, *Operator Theory for Electromagnetics: an Introduction* (Springer New York, New York, NY, 2002).

[84]J. D. Jackson, *Classical Electrodynamics*, 3rd ed. (Wiley, Hoboken, NY, 1998), 832 pp.

[85]T. Schoonjans, A. Brunetti, B. Golosio, M. Sanchez del Rio, V. A. Solé, C. Ferrero, and L. Vincze, "The xraylib library for X-ray–matter interactions. Recent developments", Spectrochimica Acta Part B: Atomic Spectroscopy **66**, 776–784 (2011).

[86]C. Vassallo, "Radiating normal modes of lossy planar waveguides", Journal of the Optical Society of America **69**, 311–316 (1979).

[87]E. W. Weisstein, *Argument Principle*, `https://mathworld.wolfram.com/ArgumentPrinciple.html` (visited on 10/20/2022).

[88]H. Blok, J. M. Splunter, and H. G. Janssen, "Leaky-wave modes and their role in the numerical evaluation of the field excited by a line source in a non-symmetric, inhomogeneously layered, slab waveguide", Applied Scientific Research **41**, 223–236 (1984).

[89]M. J. N. V. Stralen, K. F. I. Haak, and H. Blok, "On the classification of discrete modes in lossy planar waveguides: the modal analysis revisited", Optical and Quantum Electronics **29**, 243–262 (1997).

[90]J. Hu and C. R. Menyuk, "Understanding leaky modes: slab waveguide revisited", Advances in Optics and Photonics **1**, 58 (2009).

[91]R. Smith, G. Forbes, and S. Houde-Walter, "Unfolding the multivalued planar waveguide dispersion relation", IEEE Journal of Quantum Electronics **29**, 1031–1034 (1993).

[92]P. T. Kristensen, C. Van Vlack, and S. Hughes, "Generalized effective mode volume for leaky optical cavities", Optics Letters **37**, 1649 (2012).

[93]K. M. Lee, P. T. Leung, and K. M. Pang, "Dyadic formulation of morphology-dependent resonances I Completeness relation", Journal of the Optical Society of America B **16**, 1409 (1999).

[94]P. T. Leung and K. M. Pang, "Completeness and time-independent perturbation of morphology-dependent resonances in dielectric spheres", Journal of the Optical Society of America B **13**, 805 (1996).

[95] E. M. Purcell, "Proceedings of the American Physical Society", Physical Review **69**, 681 (1946).

[96] P. Ring and P. Schuck, *The Nuclear Many-Body Problem*, Texts and Monographs in Physics (Springer, Berlin, Heidelberg, 1980), 718 pp.

[97] M. Bhat, "Nuclear Data Sheets for A = 57", Nuclear Data Sheets **85**, 415–536 (1998).

[98] E. W. Weisstein, *Sokhotsky's Formula*, https://mathworld.wolfram.com/SokhotskysFormula.html (visited on 10/30/2022).

[99] X. Kong, "Collective Effects of Nuclei in Single X-Ray Photon Superradiance" (Ruprecht-Karls-Universität Heidelberg, Heidelberg, Germany, 2016).

[100] T. E. Sharon and C. C. Tsuei, "Magnetism in Amorphous Fe-Pd-P Alloys", Physical Review B **5**, 1047–1064 (1972).

[101] A. M. Van Diepen and T. J. A. Popma, "Mössbauer effect and magnetic properites of an amorphous Fe2O3", Le Journal de Physique Colloques **37**, 755 (1976).

[102] G. Férey, A. Leclerc, R. de Pape, J. Mariot, and F. Varret, "Caracterisation d'une variete amorphie de FeF3 : etude thermique, magnetique et Mössbauer", Solid State Communications **29**, 477–480 (1979).

[103] *NIST digital library of mathematical functions*, http://dlmf.nist.gov/, Release 1.0.28 of 2020-09-15, F. W. J. Olver, A. B. Olde Daalhuis, D. W. Lozier, B. I. Schneider, R. F. Boisvert, C. W. Clark, B. R. Miller, B. V. Saunders, H. S. Cohl, and M. A. McClain, eds.

[104] J. Javanainen, J. Ruostekoski, Y. Li, and S.-M. Yoo, "Shifts of a Resonance Line in a Dense Atomic Sample", Phys. Rev. Lett. **112**, 113603 (2014).

[105] J. Javanainen, J. Ruostekoski, Y. Li, and S.-M. Yoo, "Exact electrodynamics versus standard optics for a slab of cold dense gas", Phys. Rev. A **96**, 033835 (2017).

[106] S. D. Jenkins, J. Ruostekoski, J. Javanainen, R. Bourgain, S. Jennewein, Y. R. P. Sortais, and A. Browaeys, "Optical Resonance Shifts in the Fluorescence of Thermal and Cold Atomic Gases", Phys. Rev. Lett. **116**, 183601 (2016).

[107] P. Andrejić and A. Pálffy, "Superradiance and anomalous hyperfine splitting in inhomogeneous ensembles", Physical Review A **104**, 033702 (2021).

[108] T. S. do Espirito Santo, P. Weiss, A. Cipris, R. Kaiser, W. Guerin, R. Bachelard, and J. Schachenmayer, "Collective excitation dynamics of a cold atom cloud", Physical Review A **101**, 013617 (2020).

[109] C. Glosser, B. Shanker, and C. Piermarocchi, "Collective Rabi dynamics of electromagnetically coupled quantum-dot ensembles", Physical Review A **96**, 033816 (2017).

[110] J. Stanojevic and R. Côté, "Many-body Rabi oscillations of Rydberg excitation in small mesoscopic samples", Physical Review A **80**, 033418 (2009).

[111] M. Milićević, T. Ozawa, P. Andreakou, I. Carusotto, T. Jacqmin, E. Galopin, A. Lemaître, L. Le Gratiet, I. Sagnes, J. Bloch, and A. Amo, "Edge states in polariton honeycomb lattices", 2D Materials **2**, 034012 (2015).

[112] P. St-Jean, V. Goblot, E. Galopin, A. Lemaître, T. Ozawa, L. L. Gratiet, I. Sagnes, J. Bloch, and A. Amo, "Lasing in topological edge states of a one-dimensional lattice", Nature Photonics **11**, 651 (2017).

[113]W.-P. Su, J. R. Schrieffer, and A. J. Heeger, "Soliton excitations in polyacetylene", Physical Review B **22**, 2099–2111 (1980).

[114]A. J. Heeger, S. Kivelson, J. R. Schrieffer, and W.-P. Su, "Solitons in conducting polymers", Reviews of Modern Physics **60**, 781–850 (1988).

[115]A. R. Edmonds, *Angular Momentum in Quantum Mechanics* (Princeton University Press, Dec. 31, 1957).

Acknowledgements

I would like to express my sincerest gratitude to my supervisor, Prof. Dr. Adriana Pálffy. Working with her has been an absolute pleasure, and she has always gone above and beyond to create a great working environment for her entire group. From her, I have learned so much about all aspects of scientific work, not only regarding my research, but also presentation and writing too. Despite having to manage two changes of scientific position, two small children, her husband having to be in Paris for work every second week, she has managed to always find the time and energy to devote herself fully to her scientific work, and the duties of supervision. I especially wish to congratulate her on her new professorship at Julius-Maximilians-Universität Würzburg, and I am excited to see how the group will grow over the next few years.

I extend my deepest thanks to Honarprof. Dr. Christoph Keitel for his support during my time at Max Planck Institut für Kernphysik (MPIK), and for offering me the position and funding to work as part of IMPRS-QD.

I am deeply grateful to Prof. Dr. Michael Hartmann for hosting me at his chair during my time at Friedrich-Alexander-Universität Erlangen-Nürnberg as part of TRR306 QuCoLiMa.

I would like to thank Prof. Dr. Maurits Haverkort for reading my thesis and writing the second referee report.

I would like to thank the further members of my examination committee, Prof. Dr. Werner Aeschbach and PD Dr. Robert Moshammer for their interest in my thesis.

I extend my sincerest thanks to the secretaries who have guided me through the depths of German bureaucracy during the course of my studies, Sibel Babacan and Ludmila Hollmach at MPIK, and Anja Stöckigt and Erika Rutscheidt at TRR306 QuCoLiMa. They have been a tremendous help, and I thank their patience for dealing with my terrible organizational skills.

I am deeply grateful to SFB1225 Isoquant for their role in funding my studies during my time at MPIK.

I am deeply grateful to TRR306 QuCoLiMa for funding the last year of my studies. During my time at QuCoLiMa I have seen many interesting talks, and had many great discussions about the physics of quantum collectivity. In particular, I wish to acknowledge the project leaders of Area C04, Prof. Dr. Ralf Röhlsberger and Prof. Dr. Joachim von Zanthier. They are truly great scientists, and their talks and discussions are always incredibly informative and thought-provoking.

I wish to extend special thanks to Leon M. Lohse, who has been my main collaborator on the waveguide project. Working with him has been an absolute joy, and I look forward to our publications together.

I wish to acknowledge PD Dr. Jörg Evers, and his research group at MPIK, especially Dr. Killian Heeg and Dr. Dominik Lentrodt. Their work in the field of X-ray quantum optics has paved the way for the rest of us, and it is always exciting to see what interesting and novel ideas they have, both theoretical and experimental. In particular during our participation in beam-time ID 11008029 at P01 at PETRA III, August 2020, I had many interesting scientific discussions with Dominik and we shared many interesting ideas with each other.

I wish to acknowledge the members of Prof. Dr. Ralf Röhlsbergers group at PETRA III, especially Olaf Leupold, Ilya Sergeev and Lars Bocklage. I have learned much about experimental X-ray physics from them.

I wish to acknowledge my former colleagues and lunch/coffee companions at MPIK, Zoltán Harman, Natalia Oreshkina, Naveen Kumar, Antonino Di Piazza, Oleg Skoromnik, Tobias Wistisen, Vincent Debierre, Chunhai Lyu, Maitreyi Sangwal and Igor Valueev. They made every day at MPIK an absolute joy.

I wish to acknowledge in particular my fellow IMPRS-HD students, and great friends and travel companions, Halil Çakir, Daniel Bakucz-Canario, Sergei Kobzak, Kamil Dzikowski, Archana Sampath and Michael Quin. I have many fond memories of our journeys together, and I hope we can make many more in the future.

I wish to acknowledge the members of Adriana's group during my studies, Xiangjin Kong, Yuanbin Wu, Pavlo Bilous and Brendan Nickerson. I wish to extend a special thanks to Tobias Kirschbaum for his friendship and for translating my abstract, and wish him the best of luck for his newly begun doctoral studies.

I wish to acknowledge my friends and flatmates in Heidelberg, Ana Muñoz-Verdu, Bahar Melis Çoban, and Milena Schellenberger. I miss our lockdown shenanigans and our raccoon family. In particular, I wish to extend my deepest thanks to the Schellenberger family for hosting me at their home during the initial lockdown days of the COVID-19 pandemic.

I wish to acknowledge the EMBL canteen for fueling my time at MPIK with their incredible food.

I wish to acknowledge Coffee Nerd in Heidelberg and Süß und Würzig in Erlangen for fueling my caffeine addiction.

I wish to acknowledge the pīwauwau rock wren for bird of the year.

Finally, I extend my deepest love and gratitude to my family: my father Nebojša, my mother Jasmina, my sister Natalija, my grandparents Branko, Marka and Dara, and all of my extended family. I could not have done this without their support.